Investigation of the role of ionising radiation on corrosion and related phenomena that occur in light water reactors

A thesis submitted to the University of Manchester for the degree of
DOCTOR OF ENGINEERING
In the Faculty of Science and Engineering

Elizabeth H Parker-Quaife

School of Chemistry

University of Manchester

2019

Contents

List of Figures

List of Tables

List of Appendices

Word count: 64820

List of Nomenclature and Acronyms

HT – High temperature

HP – High pressure

LWR – Light Water Reactor

NPP - Nuclear Power Plant

PWR – Pressurised Water Reactor

AOA – Axial offset Anomaly

CIPS – CRUD induced Power Shifts

CRUD – Corrosion Related Unidentified Deposit

PKA – Primary Knock-on Atom

SRIM – Stopping and Range of Ions in Matter

$\sigma(X)$ – Probability event X occurring

SS – Stainless steel

Cr – Chromium

Ni – Nickel

Fe – Iron

Element $^{n+}$ – Charge of the ion

[----] – Concentration of species in brackets

$[H_2]_{D,}$ Dissolved hydrogen concentration

$[O_2]_D$ – Dissolved Oxygen Concentration,

EC – Electrical Conductivity

Fe_2O_3 – Haematite

Fe_3O_4 – Magnetite

FeO – Wustite

H_2O_2 – Hydrogen Peroxide

XPS – X-ray Photoelectron Spectroscopy

SEM – Scanning Election Microscopy

EDS – Electron Dispersive Spectroscopy

GI-XRD – Grazing Incidence X-Ray Diffraction

XRD – X-ray Diffraction Spectroscopy

TEM – Transmission Electron Microscopy

STEM – HAADF – Scanning Transmission Electron Microscopy – High Annular Dark-field Imaging

TEM – SEAD Transmission Electron Microscopy – Selected Area Diffraction

TPD – Thermal Programmed Desorption

ICP-MS Inductively Coupled Plasma Mass

ppb – Parts per billion

ppm – Parts per million

H_2O – Water

$^{\bullet}OH$ – Hydroxyl radical

H^+ – Proton

e_{aq}^- – Solvated electron

HO^- – Hydroxyl ion

$H^{\bullet}$ – Hydrogen radical

Fe^{2+} – Ferrous ion

Fe^{3+} – Ferric ion

LET – Linear Energy Transfer

PTFE – Polytetrafluoroethylene

PEEK – Polyether ether ketone

ECP- Electrochemical corrosion Potential

OCP – Open circuit potential

E_{corr} Electrochemical corrosion potential

SHE- Standard Hydrogen Electrode

G – G value

V- Volts

eV- Electron volts

P – Partial vapour pressure of adsorbate gas in equilibrium with the surface at 77.4 K

P_o – Saturated pressure of adsorbate gas, in pascals

V_a – Volume of gas adsorbed at standard temperature and pressure (STP)

V_m – Volume of gas adsorbed at STP

S_{total} / S_{BET} – Surface area parameters

N – Avogadro's constant

$E_{subscript}$ – Energy of subscript term

Φ – A work function in an equation

K, L, M – Refers to types of orbital transition

d – Interlayer spacing

Tp – Peak temperature

BH – Rate of heating in kelvin

R – Gas constant

A – Absorbance

E – Extinction coefficient $M^{-}1cm^{-1}$

C – Concentration of absorbate M

l – Pathlength

R_p – Polarisation resistance

nM – Nano molar

mM – Milli molar

ηm – Nanometer

Abstract

Investigation of the role of ionising radiation on corrosion and related phenomena that occur in light water reactors.

Elizabeth Parker-Quaife, University of Manchester, Engineering Doctorate, 2019

The corrosion of materials used within Light Water Reactors (LWRs) can lead to release, transport and deposition of generated corrosion products. The build-up of these corrosion products is termed CRUD. CRUD build-up causes operational issues within reactor primary circuits affecting reactor safety and efficiency. Understanding the effects of radiation on corrosion and its related phenomena is essential when considering new build plants and lifetime extension programs. This work is part of a larger project by Rolls Royce PLC that aims to model the chemistry of PWR systems and is tasked with providing insight and experimental data of corrosion and CRUD behaviour under radiation conditions. This work investigated the effects of radiation on the corrosion of nuclear material and how corrosion products interact with products from the radiolysis of LWR coolant.

Direct examination of the corrosion process under exposure to radiation is logistically difficult. This work reports the successful design, development and implementation of a High Temperature and High Pressure (HTHP) facility that can be used in conjunction with either a ɣ-radiation source or an accelerator providing heavy ion radiation. This work enables studies of both water radiolysis and corrosion in simulated LWR conditions. As far as the participants of this project are aware, this equipment is the only one of its kind that allows for the multifunctionality it gives. Results of the design and commission processes are outlined and highlight key design decisions and the consequences of these. The oxidation of SS 316 under ɣ-irradiation conditions was undertaken which showed γ-irradiation exposure during oxidation has a measurable effect on oxide type and thickness.

The interactions between corrosion and radiolysis products were investigated building on previous studies in this field; iron oxides were γ-irradiated in the presence of hydrogen peroxide. The results of this study show complex behaviour that is a result of both reactions at the oxide | solution interface and those in bulk aqueous phase.

The impact of this work and its place in the larger project at Rolls Royce is discussed, giving recommendations on what should be considered when modelling these systems.

Declaration

No portion of the work referred to in the thesis has been submitted in support of an application for another degree or qualification of this or any other university or other institute of learning.

Copyright statement

Acknowledgements

As with all research projects, the work presented in this thesis would not be possible without the support of my advisory team, staff, my colleagues and peers across the departments I have the opportunity to work within. (The Dalton Cumbrian Facility, the EngD centre, Materials Performance Centre and at the Rad Lab at The University of Notre Dame). I would like to give a special thanks for the support of my academic supervisor Prof. Simon Pimblott for his constant encouragement and patience towards my curiosity driven research. I would like to thank Dr Fabio Scenini and Dr Jonathan Duff for their help, guidance and technical support. I would like to extend my thanks to Dr Andy Banks, Dr Lara-Jane Pegg and Dr Andrew Powell for their industrial guidance. Dr David Stanley thank you for the support throughout the EngD program you advise, and patience has been invaluable.

I wish to acknowledge support (including an EngD studentship to EPQ) from the Engineering and Physical Sciences Research Council (grant number EP/G037426/1) and Rolls Royce Plc.

Personal Acknowledgments

I am not sure I can begin to adequately describe how the process of getting my EngD has allowed for my continuous development as both an individual, and as a member of the scientific community. But I would like to try, many of those acknowledged here will appreciate the attempt. The process of obtaining a doctorate has been demanding in a multitude of ways, challenging my sense of self, personal and professional relationships. Ultimately it has led to the realisation that no problem is unsolvable, that things can always be reframed, redefined, and difficulties overcome. Throughout my doctorate I have had the opportunity to travel to so many places, Japan, America, Spain, Italy, and those are just those where conferences or workshops were held. These opportunities have let me explore aspects of myself I did not know existed. Running around a Japanese university campus at 4 am due to jetlag is an incredibly surreal experience. These experiences, well if you had asked me if they were possible when I was a child I would have flatly refuted. I did not expect to be where I am now, doing what I am now, I just knew that I wanted to learn, learn and learn some more. I can tell you I am nowhere near done, there is so much still to know and understand, stating my curiosity is never-ending, honestly it’s probably the ultimate Sisyphean task.

I have been lucky to have met many people throughout this process, academically, professionally and in my personal life. With many connections made, each giving fresh perspectives on the science and ways in which to decompress and debrief after intense meanderings on the afore mentioned science. These connections have been made across many cities, time zones and unbelievable some of the best problem solving has been transatlantic. I have been pleasantly surprised by the willingness of others to help out and provide support in all aspects of being a doctoral candidate. Who would have thought a doctorate in nuclear engineering would have provided such riches?

Thank you to those of you that have provided academic know how. To those who challenged me when my thoughts went off on a tangent or missed the point completely you helped me get back on top of things. You have provided a much-needed sounding board, direction, and knowledge, thank you for passing on your skills and experience. Without this I would not be ready to take on new challenges, without this I am not sure I would have managed to complete the mammoth task that is a doctoral degree.

Thank you to those who always showed me unfaltering kindness in our hotchpotch work places, I know that I have needed extra help with managing the strain of my project. You always knew where to have patience, and when to take a risk and assert the importance of self-care, taking time to readjust. It has been invaluable. I am a stronger more stable person because of this. Thank you is not enough, but it is all the English language has to offer.

Those of you who in my professional life who crossed over to being pillars of support in my personal life and those of you who became or remained pillars of support in my personal life, gosh aren't you all everyday heroes. You everyday heroes come from many aspects of my life, some are friends, others colleagues and peers. In the ranks are members of my family, stoic and constantly adapting to my ever-increasing vocabulary and obscure opinions. I know supporting someone through the processes of getting a doctorate is hard enough, but add 9 house moves, relationship evolutions and changes, along with an ADHD diagnosis, and my demonstrative nature I have no idea how you all managed. But you have, and I do not have the words to express how much I needed you and am grateful that you have been there. You've encouraged me at every stage, providing places to be myself, (to explore what that means) and never failing to make sure I know you care when I did not, when I do not believe it. Thank you to those of you who have encouraged my creative aspects, thank you for listening to my rants about digital photography, those on

the rewards of analogue processes and cameras. Thank you for patience while I recited early angsty poems and being present for the evolution to something more refined. Thank you to those of you that sat patiently while I sketched things to collect my thoughts, emotions, well really just while I collected myself. I appreciate you all for letting me be excited when maybe there was nothing to be excited about, after all I am a scientist, possibly an engineer, not an awarding winning artist.

It's impossible to name you, as you are much more to me than names. Also, the nature of ADHD would mean that I would inevitably forget someone, realise, point it out and cause offense. I have always endeavoured to avoid offense, never leaving anyone out (really just aiming to sell out my funeral). So rather than list you, I will let you include yourself if you feel that any of the above resonated with you, let it be known I appreciate you all an immense amount. I would not have been able to do this without you. Any of it, I am where I am today because you all showed me that it is okay to ask for support, to ask for help, that it won't weaken me to do so. It strengthens me. It enlightens me. It makes me, me.

Chapter 1: Project overview and industrial relevance

When considering lifetime extension of nuclear power plants (NPPs) and new build design, the minimisation and mitigation of material degradation processes is essential. The nuclear industry relies on a variety of materials in the construction of NPPs with a limited selection of metal alloys within the reactor systems, including stainless steels and nickel-based alloys. Selection is based of the material's physical properties and its predicted lifetime; a material selection is a compromise of many factors including minimisation on material degradation pathways. Several degradation processes that can affect the integrity of the metals include; creep, corrosion, stress fracture and metallic sensitisation. The consequences of these included reduced lifetime of the metals and altered properties i.e. metal failure and reduced reactor efficiency. Understanding these failure mechanisms could lead to increased reactor lifetime in current reactors and better material selection for future fleets.

This project fits within a larger program at Rolls Royce PLC where the mechanisms of corrosion and its related processes is under way. This project incorporates several smaller experimental and theoretical studies with the aim to build a predictive model of the primary and secondary circuits in Pressurised Water Rector (PWR) systems. Specifically, this large-scale project aims to model the behaviour of CRUD (Corrosion Related Unidentified Deposit), how it is transported around the primary circuit and the affects these phenomena have on the chemistry of the water-based coolant systems. It is hoped that these models will aid design and implementation of new plants and their operational procedures in future. The project aims and objectives for this EngD project were outlined and amended when required in conjunction with Rolls Royce. This project aimed to provide input data to support this CRUD modelling and time was spent at Rolls Royce working alongside research scientists and engineers to make sure the work was relevant and how it could be incorporated into the larger program. Although the work reported here has relevancy to both PWR and Boiling Water Reactor (BWR) systems, as a sponsor Rolls Royce has more interest in its application in specific PWR systems and how experimental programs can support predictive modelling.

This thesis outlines work that probes the degradation via corrosion of materials employed in PWRs. The design and development of a High Temperature High Pressure (HTHP) recirculation facility designed at the University of Manchester was undertaken during this

project and the effects of radiation on corrosion and related processes was investigated. This work aims to add to the understanding of corrosion mechanisms and subsequent processes due to the presence of radiation. And to provide experimental data that can be used to inform the development of predictive models, forecasting reactor lifetime and the investigation of scenarios that are encountered during reactor operation. This work also intends to contribute further to the fundamental understanding of corrosion processes, with the possibility of informing material selection and design in future.

Firstly, the literature surrounding this work is outlined and is covers several categories, literature relevant to radiation processes, the corrosion of nuclear materials and literature relevant to studying simulated reactor conditions. **Chapter 2** introduces nuclear energy and its place in the UKs energy arena, **Chapter 3** introduces radiation chemistry. **Chapter 4 Sections 4.1-4.7** discuss the fundamentals of corrosion and the study of corrosion processes at high temperature and under simulated LWR conditions. **Chapter 4, Section 4.8** is a literature review published in the Nuclear Plant Chemistry conference proceedings (NPC 2016) outlining the literature that informed the study into corrosion and radiolysis product interactions. **Chapter 5** summarises the experimental and analytical techniques used throughout this work. **Chapter 6, Section 6.1** gives an overview of the design process and **Section 6.2** is an equipment and method development discussion. This is in paper format, outlining the design and deployment of the High temperature and High pressure (HTHP) facility undertaken during this EngD project; it focuses on the commissioning and proof of principle studies. **Chapter 6, Section 6.3** outlines a corrosion study undertaken where stainless steel 316 (SS 316) samples were oxidised at 288 °C with and without gamma irradiation. **Chapter 7, Section 7.1** gives detail of the method development for a study probing interaction between corrosion and radiolysis products giving details of the study once the experimental method was refined. **Chapter 7, Section 7.2** reports the results from a set of experiments investigating the interactions between corrosion and radiolysis products. **Chapter 8** concludes the work undertaken giving its industrial relevance and impact as well as suggesting possible direction for further works. Supplementary work is then given in the appendixes.

Project Aims and objectives

Aims:

- Develop an understanding of how radiation effects corrosion of a stainless steel 316 over a series of temperatures and pressures leading to those of PWR system.
- To investigate corrosion mechanisms; corrosion product release and subsequent interactions.

Objectives:

- Design and deployment of a high temperature and pressure (HTHP) set up that can be used for the investigation of radiolysis and corrosion behaviours;
- Investigation of the corrosion of nuclear materials under radiation exposure
- Development of an experimental method that enables the interaction between radiolysis and corrosion products to be investigated;
- Collect data that can inform industrial modelling programs that aim to predict the behaviour of CRUD in PWR primary coolant circuits.

Chapter 2: The United Kingdom's energy arena

2.1 Nuclear Power Plants and electricity generation

Globally, electric energy production utilises a variety of power generating systems, civil nuclear power generates around 11% of total energy produced, utilising around 450 nuclear power plants (NPPs). The current global nuclear fleet deploys various reactors types including Pressurised Water Reactors (PWRs), Boiling Water Reactors (BWRs), Advanced Gas cooled Reactors (AGRs) and Pressurised Heavy Water Reactors (PHWRs). PWR and BWR systems account for upwards of 80% of world reactor fleet and are classified as Light Water Reactors (LWRs).[1] Of these Pressurised Water Reactors (PWRs) account for 65 % of the in-operation reactor fleet and BWRs up to 20%.[1-3] Both BWR and PWR systems utilise the fission of uranium in thermactor core with light water as a moderator and coolant.

In PWR systems the reactor core sits within the primary coolant system providing both cooling and moderation of the core by water. A schematic of a typical PWR system can be seen in **Figure 2.1-1** (diagram is taken from the U.S.NRC and the primary circuit is labelled 2).[4] The secondary circuit generates steam through an exchange of heat with the primary circuit, this steam is then used in a turbine system producing electricity.

BWR systems involve a single circuit providing cooling and steam generation, a typical BWR system can be seen in **Figure 2.1-2** (diagram is taken from the U.S.NRC).Water in BWR systems is at lower pressure so will boil when temperatures in the core reach 285 °C; typical operation allows for 12-15% of water to be at the top of the core as steam (which gives a lower moderating effect). This steam then passes through drying plates and directly into the turbines where electricity is generated.

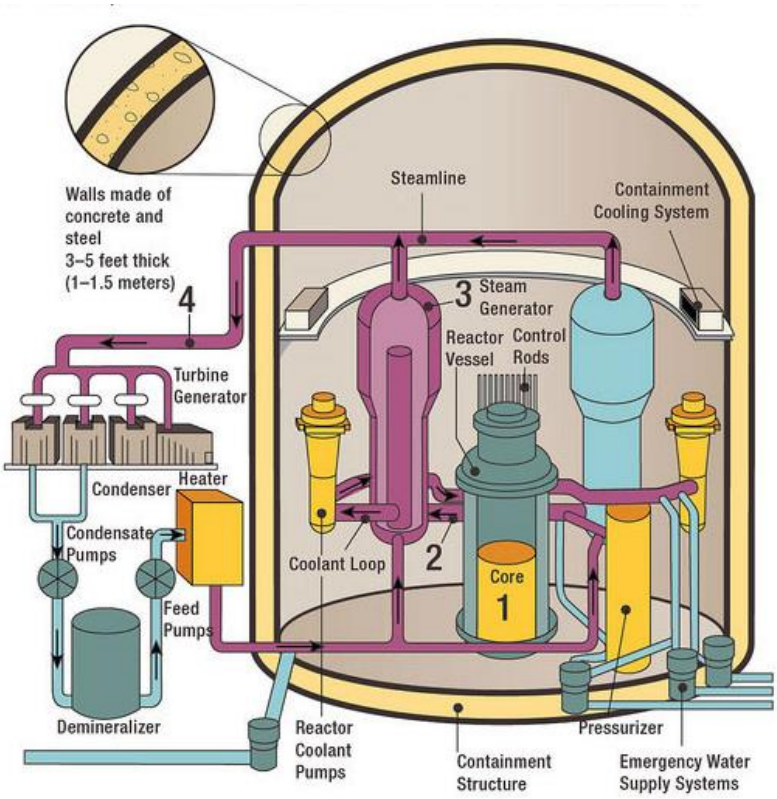

Figure 2.1-1. Outline of a typical PWR system. 1) The core inside the reactor vessel creates heat; 2) Pressurized water in the primary coolant loop carries the heat to the steam generator; 3) Inside the steam generator, heat from the primary coolant loop vaporizes the water in a secondary loop, producing steam; 4) steam passes into the steam turbines

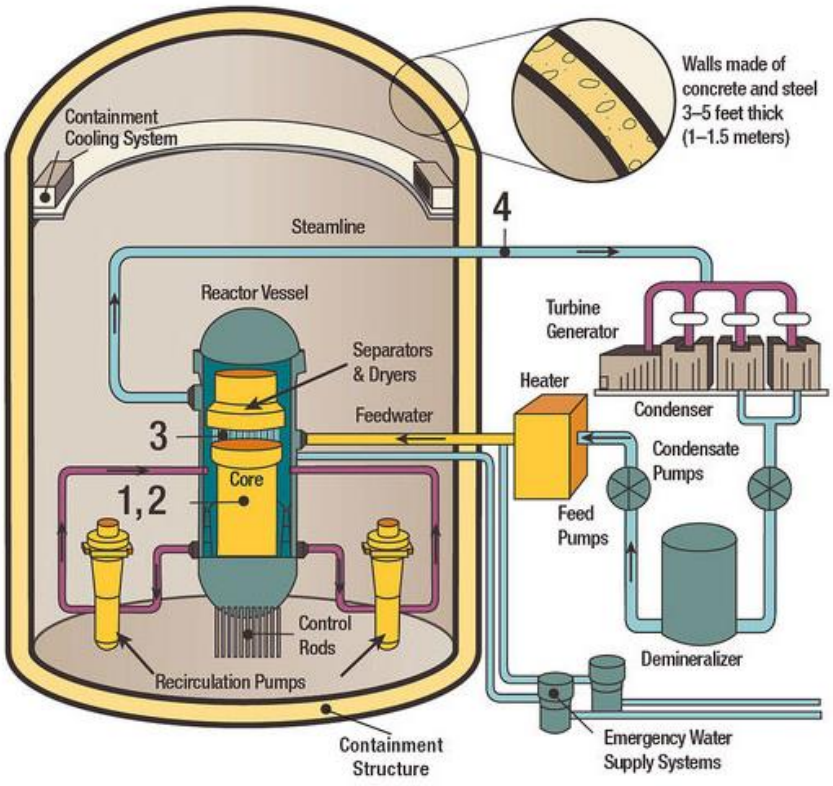

Figure 2.1-2. Outline of typical BWR 1) Reactor core that generates heat 2) A steam and water mixture is produced from the water coolant, moving upwards absorbing heat 3) Steam-water mixture enters a two-stage moisture separation before it enters the steam line 4) The steam line directing it to the main turbine where electricity is generated

The United Kingdom currently has an electricity generating capacity is 106 GWe and it is projected that by 2035 the minimum requirement will need to increase to 137 GWe. The UK employs a diverse energy mix; coal and gas, nuclear and renewable sources, nuclear power currently meets 21% of the national energy demand from 14 AGRs located over 6 sites and 1 PWR at Sizewell B. Half this capacity is expected to be shut down by 2025 with the rest closing by 2035.[5-8] **Table 2.1-1**. outlines the reactor types, their current capacity and their expected lifetime. **Figure 2.1-3** shows the current generating capacity, the increase needed to meet future demand and the contribution of this that is expected to be delivered by nuclear.[9]

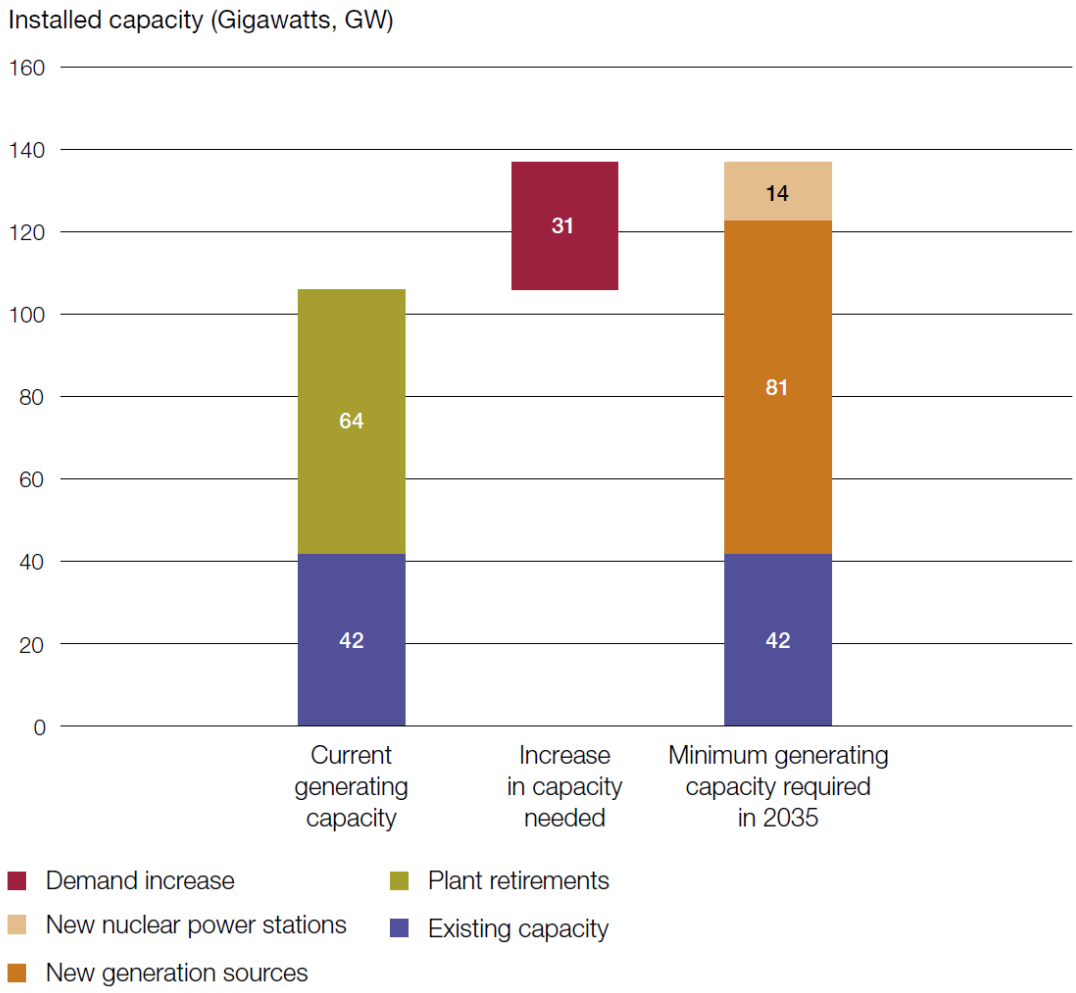

Figure 2.1-3. Graph to show the current electricity gernerating capacity in the UK and the predicted increase in capacity and how it will be met.

The UK has committed to build 14-16 GW of new nuclear build to replace the retiring plants, this is to include up to 12 plants over five sites.[6-9] The reactor designs being considered unlike the current fleet, are all light water reactor designs. There are three PWR designs; the Framatome EPR, Westinghouse AP1000 and General Nuclear system HPR1000 alongside one advanced BWR design to be supplied by Hitachi GE.[6] The infographic in **Figure 2.1-4** shows the current reactor sites and where the new builds are expected to be built.[10]

Table 2.1-1. Table of the current UK nuclear plant fleet, with type, operating capacity and expected shut down timescale

Plant	Type	Present Capacity MWe net	First power	Expected shutdown
Dungeness B 1&2	AGR	2 x 520	1983 & 1985	2028
Hartlepool 1&2	AGR	595,585	1983 & 1984	2024
Heysham I 1&2	AGR	580, 575	1983 & 1984	2024
Heysham II 1&2	AGR	2 x 610	1988	2030
Hinkley point B 1&2	AGR	475, 470	1976	2023
Hunterston B 1&2	AGR	475, 485	1976 & 1977	2023
Torness 1&2	AGR	590, 595	1988 & 1989	2030
Sizewell B	PWR	1198	19965	2035

Figure 2.1-4. Map of the site for current and future nuclear power plants

The work presented in this thesis aims to contribute to design, development and lifetime extension of nuclear reactors, when considering the use of nuclear energy in the future of the United Kingdom's energy arena.

The work presented is relevant to both PWR and BWR systems as both encounter issues related to corrosion related materials degradation. The work outlined in this thesis aims to contribute to the understanding of these corrosion mechanisms and corrosion product behaviour with a primary focus on simulated PWR conditions. The reasons for this are two-fold, these systems are most relevant to Rolls Royce (the company that sponsored the presented EngD project) and that the plants planned for the UK market are predominantly PWRs. Saying this there are similarities in the LWR systems so some of the more fundamental work presented here has applications more relevant to BWR systems. The basis for a thorough understanding of the effects of radiation on corrosion is the fundamental knowledge of both the corrosion mechanisms and the radiolysis

processes that occur in primary coolant circuit systems. Once these are in place the in-situ processes can be investigated. **Chapters 3 and 4** discuss the literature relevant to radiation chemistry, the radiolysis process and corrosion of materials used in the nuclear industry. **Chapter 4 Section 4.8** outlines the literature of subsequent interactions between corrosion and radiolysis products

References

1. Bethel Afework, Jordan Hanania, Kailyn Stenhouse and J. Donev, Pressurized water reactor https://energyeducation.ca/encyclopedia/Pressurized_water_reactor, 2019).
2. Nuclear Power Reactors, http://www.world-nuclear.org/information-library/nuclear-fuel-cycle/nuclear-power-reactors/nuclear-power-reactors.aspx, 2018).
3. Bethel Afework, Jordan Hanania, Kailyn Stenhouse and J. Donev, Boiling water Reactor https://energyeducation.ca/encyclopedia/Boiling_water_reactor, 2018).
4. U.S.NRC, *Journal*, 2015.
5. W. N. Association, Nuclear Power in the United Kingdom http://www.world-nuclear.org/information-library/country-profiles/countries-t-z/united-kingdom.aspx, (accessed January 2019, 2019).
6. N. AMRC, UK new build plans http://namrc.co.uk/intelligence/uk-new-build-plans/, (accessed January 2019, 2019).
7. H. Government, *Nuclear Industrial Strategy - The UK's Nuclear Future* HM Government 2013.
8. H. Government, *Sustaining Our Nuclear Skills*, HM Government, 2015.
9. C. a. A. General, *Nuclear Power in the UK* National Audit Office 2016.
10. H. Government, Map of nuclear power stations in the UK, https://www.gov.uk/government/publications/map-of-nuclear-power-stations-in-the-uk, (accessed Feburary 2019, 2019).

Chapter 3: Introducing radiation chemistry

3.1 The interactions of radiation with matter

As previously described, LWRs utilise the fission of uranium in the reactor core which generates a series of radioactive nuclei that decay releasing ionising radiation. The most common of these are α, β, and γ radiation, accelerated charged particles and short wave electromagnetic radiation.[1] The radiation produced during fission goes on to cause a cascade of reactions within the materials it interacts with; such as coolant (water) and the structural materials of the coolant circuit. Radiation chemistry may be defined as 'the science of the chemical effects brought about by the absorption of ionising radiation.' [2] The energies of the radiation tend to be in the order of keV or MeV (in magnitude) and the ionisation or excitation of matter will go on to produce a radiation track of products. Ionising radiation can be split into two groups: the light group and heavy group. The light containing electron-positron, muons, X and γ-rays and the heavy including protons, α-particles and fission fragments.[1] These may be further categorised; 1) charged particles (e-, e+, α, etc); 2) uncharged particles (n); and 3) electromagnetic radiation (γ).[1, 3] If a collision occurs resulting in ionisation, an ion pair is produced (an electron and the positive ion), and the electron from this may induce secondary ionisation reactions. The chemical response to radiation is dependent on the composition of the medium it interacts with and the energy that is deposited. The main energy transfer processes in these reactions is loss through the collision of the radiation with electrons in the medium and examples of this are shown in **Figure 3.1-1.** The energy transferred from the radiation will depend on type, with heavy ions being able to deposit energy in 'stages,' and γ either passing through the material or being absorbed via a single process. The absorption of radiation by matter is illustrated in **Figure 3.1-1,** comparing the absorption of ultraviolet light photons and α-particles by matter.[4]

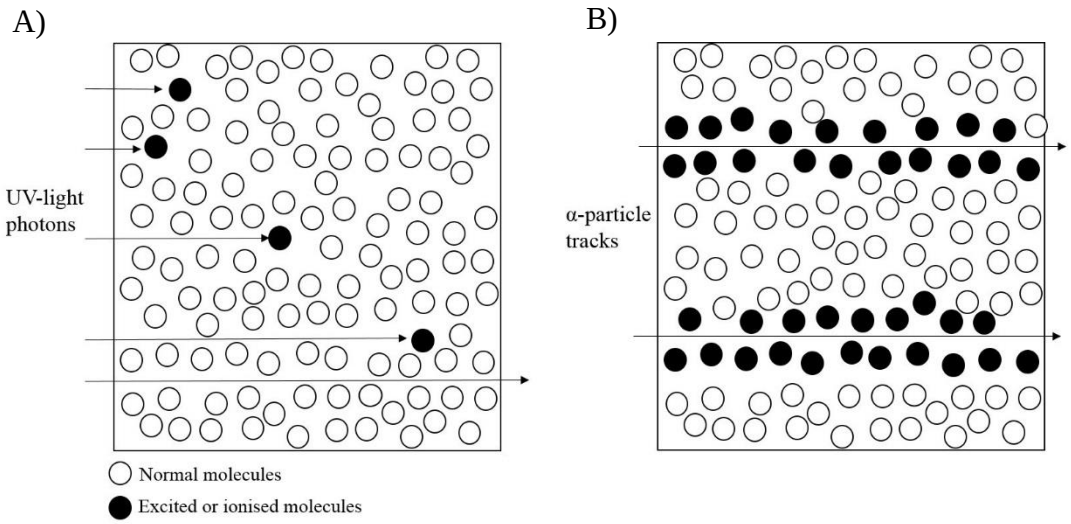

Figure 3.1-1. Absorption of radiation by matter a) ultraviolet light photons b) alpha particles.

The energy loss during an interaction of ionising radiation with matters is referred to as the Linear Energy Transfer (LET), the rate of which is defined by the amount of energy absorbed by matter within a specific length travelled 'the total energy lost per unit path'.[3-5] In processes involving photons energy is absorbed via a single process, or the photons pass through the materials, in these cases the term LET is used to describe the electrons produced by the γ-absorption and its subsequent generation of secondary electrons. The LET values for radiation processes increase in the following order:

LET increases

γ rays, high energy electrons
low-energy electrons
protons
deuterons
α particles
heavy ions (ionised N, O, etc)
fission fragments

To give more context to the interactions of radiation with matter the types of radiation encountered in LWR systems should be described in more detail. When considering the distance penetrated by radiation the higher the LET the lower the penetration path. The

characteristics of these radiation types is summarised in **Table 3.1-1** and is followed by a more in-depth description.

Table 3.1-1. Type and characteristics of various types of radiation

Radiation type	Characteristics	Range	What will shield it
Alpha (α)	2 protons, 2 neutrons, +2 charge	2 – 5 cm in air	Paper or outer layers of skin
Beta (β)	Small mass, -1 charge	< 10 m	Plastic or glass
Gamma (γ)	No charge or mass	<35 m	Lead, steel, concrete
Neutrons (η)	No charge, small mass	> 35 m	Water, concrete, plastic

α-particles

Radionuclei that have undergone decay may emit α-particles which are nuclei of helium atoms that have lost both electrons and have a charge of +2. α-particle energies are dependent on the radioactive element they are released from. Energy is lost in small amounts via inelastic collisions with electrons in their path, which cause ionisation and excitation processes in a somewhat straight pathway through the matter it is interacting with.[4]

β-decay

β-decay can be described as either fast electrons or positrons emitted by radioactive nuclei and have energy from zero to E_β that are characteristic of the element they are emitted from.[4] β-decay occurs when a neutron is converted to a proton (or the opposite) to give a more favourable ratio of proton to neutrons, the energy loss is shared between ejected particles and the decaying atom.

ɣ-rays

ɣ-rays are electromagnetic radiation with short wavelengths in the range of 3×10^{-9} to 3×10^{-11} cm, radioactive nuclei emit single monoenergetic ɣ-rays or a small number photons of discrete energies.[4] ɣ-rays are often referred to as photons and are emitted by the

relaxation of excited nuclei with no subsequent change in neutron or positron number. Their interaction with matter occurs in a single process with all the energy or part of the incident ɣ-rays lost during the collision process and the remainder transmitted with their full incident energies.

Neutrons

Neutrons are uncharged so do not produce ionisation themselves but interact with atomic nuclei and may result in ionisation predominately from protons or heavy ions produced by these interactions. Neutrons are highly penetrating and interact with nuclei by elastic scattering, inelastic scattering, nuclei reaction and capture depending on the energy of the incident neutron.[4] It is valid to study neutron interactions by using heavy ions and protons as these are produced in neutron interactions.

The focus of the research in this project is understanding the effects of ɣ-radiation on corrosion processes and their subsequent corrosion products. Gamma radiation can be treated as photons, when these pass through a substance they can interact with nuclei or electrons and the likelihood of the interaction and the energy lost in the interaction is dependent on the atomic number of the medium and the energy of the incident photon. The three main interactions photons have with matter are the photoelectric effect, the Compton effect and pair production.

The photoelectric effect

Incident photons will interact with atomic electrons, transferring some of or all of their energy and are then emitted. This is known as the photoelectric effect. The interacting electron is ejected from the atomic shell with energy equal to the incident energy minus the binding energy of the electron. Due to conservation laws, the absorbing atom will recoil and thus it is not possible for free electrons to interact with photons via the photoelectric effect. The vacancy created by the ejected electron will be filled by electrons from outer shells, with energy emitted by x-rays or auger electrons.

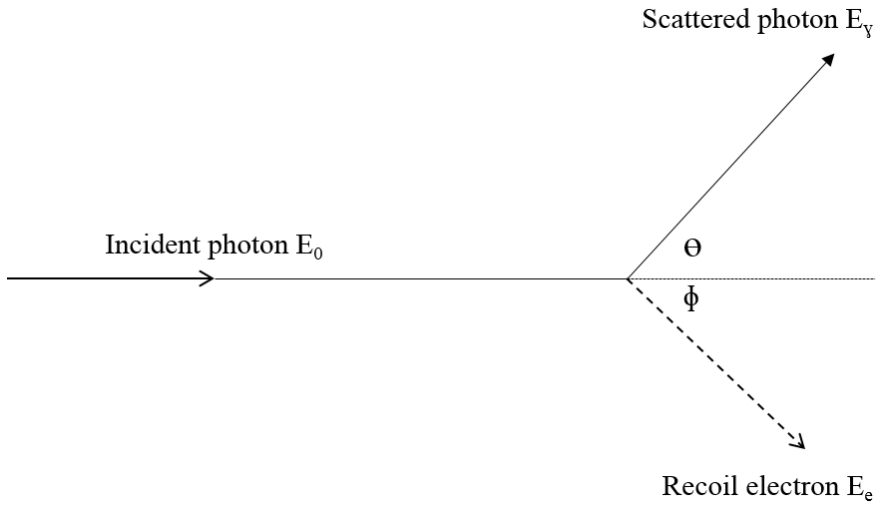

Figure 3.1-2. A simple representation of the Compton Effect recreated from Spinks and Woods.

The Compton effect

In the Compton effect, the interaction of photon with a loose or free shell electron is possible, resulting in the electron being accelerated and photon is deflected (direction of photon will change) with a reduced energy.[5] An illustration of the Compton effect is represented in **Figure 3.1-2** which is a recreation of work by Spinks and Woods.[4]

Pair production

Pair production occurs for higher energy photons that have energies of more than 1.02 MeV. In this process, the incident photon is completely absorbed by the atomic nucleus (occasionally an electron). This results in the production of a positron and an electron which have energies equal to half the incident energy minus resting energies of the particles. The positron will eventually combine with an electron, and two ɣ-rays with 0.51 MeV energy are produced. (Pair production is represented in **Figure 3.1-3** a recreation from Spinks and Woods). The processes in which ɣ-radiation interact with

matter results in secondary electrons (or fast-moving electrons), these can cause ionisation and excitation of further electrons in the absorbing material. These interact with matter in three discrete ways, electromagnetic radiation, elastic scattering and inelastic scattering.

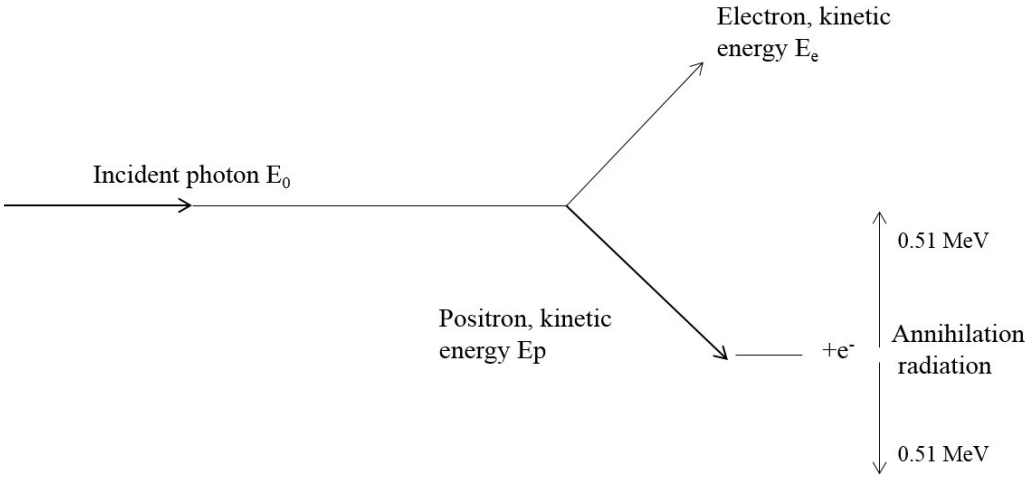

Figure 3.1-3. A representation of pair production recreated from Spinks and Woods.

The absorption and scattering of radiation during interaction processes is known as attenuation and is dependent on material composition and individual incident photon energies. The probability of interactions is proportional to the attenuation coefficient of a material and this is known as a materials cross section, σ. The attenuation behaviour of a material can be used to predict the type of interaction that may occur with matter. An important application is radiation shielding where materials are selected for their ability to 'block' or minimise radiation exposure to personal and equipment.

The absorption and scatter of photons by these processes' contributions to the overall attenuation coefficient of a material. The absorption coefficients for photoelectric effect, Compton effect and pair production are summed to give an overall absorption coefficient. When this is added to the scattering coefficients it gives the overall attenuation coefficient for the material. The attenuation of photons by a material is dependent on the materials atomic weight, density and thickness as well as the energy of individual photons. The distance travelled by a photon is based on the probability of encountering a particle in the

matter (the absorption cross section) and as distance travelled increases the likelihood of interaction also increases. The attenuation of radiation by a material can be measured experimental by using a known gamma-ray source and measuring the intensity of radiation after interaction with the absorbing material. A typical experimental set up can be seen in **Figure 3.1-4** reproduction of work by Spinks and Woods.[4]

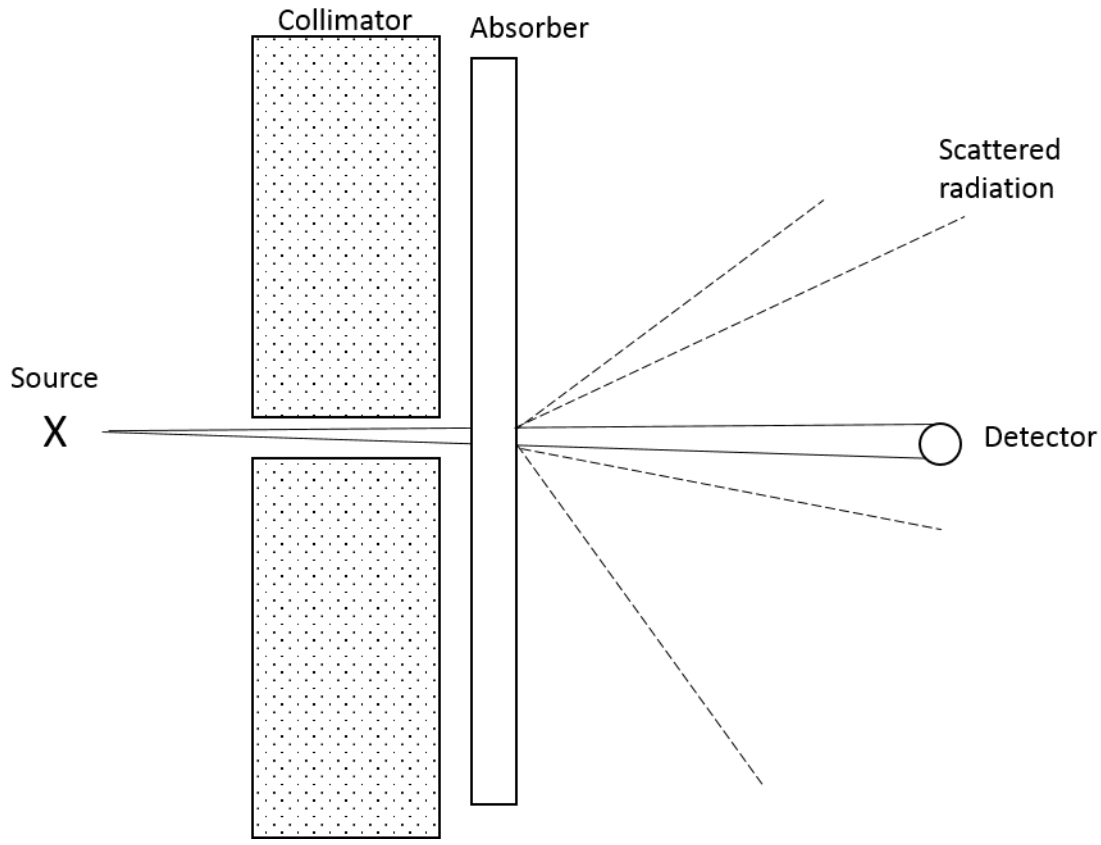

Figure 3.1-4. Typical attenuation experimental set up. Reproduction of diagram by Spinks and Woods.

Under these narrow beam conditions with a collimated source the intensity measured by the detector is mathematically defined as

$$I = I_0 e^{-\mu x} \qquad \textbf{(3.1-1)}$$

where I_0 is the intensity measured in the absence of an absorber, x the thickness of the absorber and μ the total linear absorption coefficient:

$$\boldsymbol{\mu = \tau + \sigma + \kappa} \qquad \textbf{(3.1-2)}$$

And τ, σ and κ are the absorption coefficients for the photoelectric, Compton and pair production processes. It is important to consider these factors when designing and implementing experiments as the attenuation behaviour of a structural material will affect the dose received by target systems. It is also possible for the attenuation behaviour to induce unintended chemistry in experimental systems so this should be considered when exploring the approach taken in experimental programs.

3.2 The effects of radiation on materials

The effects of radiation discussed so far have focused on the ionising processes that may occur and the attenuation affects these may have. In metallic materials such as those used as structural components of nuclear reactors, interactions with radiation can occur by other processes. If particles of radiation have sufficiently high energy the interactions with atoms of the irradiated materials can lead to disturbance of the materials lattice structure.[6] These interactions can result in lattice defect formation that may affect both microstructure and macrostructural properties. During the collisions between incident radiation and atoms, radiation will lose its energy to atoms and the following damage may occur:

1) Displacement damage – the movement of atoms from their lattice positions
2) Ion implantation or capture of particles by atomic nuclei (causing transmutation) resulting in compositional changes to the material
3) Excitation of electrons that may result in ionisation, these processes do not produce permanent damage in the materials.

The collision of an incident particle with the lattice atoms will lead to changes in the direction of path, a scattering of the incident radiation. Collisions may either be elastic where particles remain unchanged, or inelastic where the original incident energy is lost often to the lattice atoms. Mathematically the kinetic energy transferred from incident energy to the lattice atom is:

$$T = \frac{4M_1M_2}{(M_1+M_2)^2} E \sin^2 \vartheta \qquad \textbf{(3.2-1)}$$

where M_1 and M_2 are the masses of an incident particle and lattice atom at rest. E is the energy of the incident particle and ϑ the scattering angle of the radiation after collision. An atom that is 'knocked' out of its original lattice site by the incident radiation particle is known as a primary knock on atom (PKA). PKAs can have an energy from zero to maximum transfer energy (T_m) where T_m occurring with a head on collisions at an angle of collision is equal to 180 °. The formation of PKA is equivalent to the formation of a Frenkel pair, where both a vacancy and an interstitial atom are formed.[6] When a PKA has sufficiently high energy it will continue to move through the material, colliding with atoms, displacing them and causing a what is known as a collision cascade (displacement cascade), this is represented pictorial in **Figure 3.2-1**.

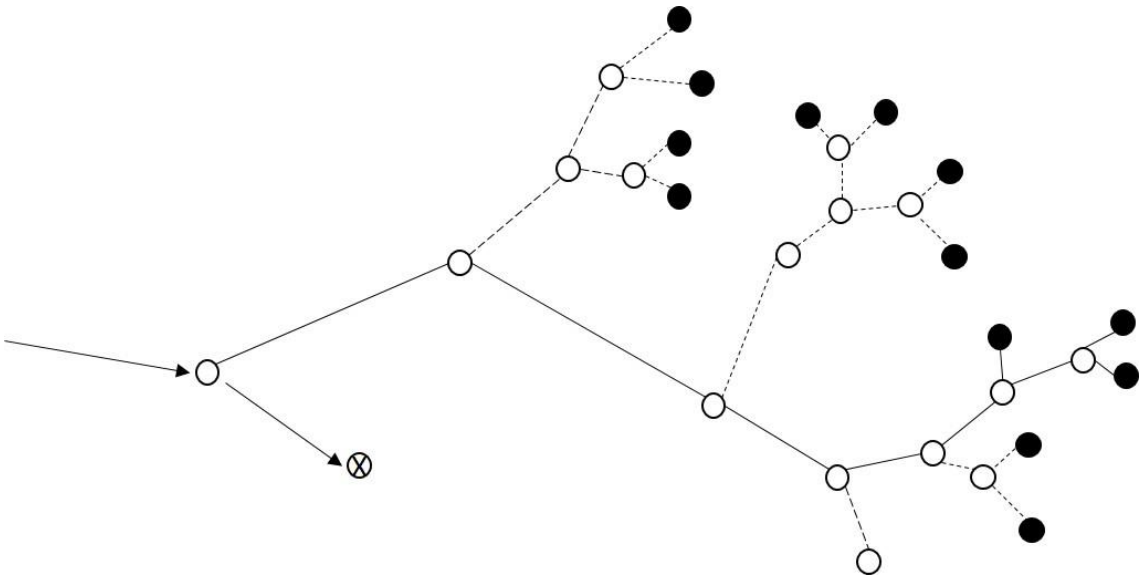

Figure 3.2-1. Schematic representation of a displacement cascade, X – impinging particle, ○ – Vacancies ●- interstitials, full line-trajectory of PKA, dashed line-trajectory of higher knock on atoms.

Behaviour in these systems (such as displacement cascades) mean that the effects incident radiation can be more complex than just the formation of a Frenkel pair. Effects include defect clusters, amorphous regions and dislocation loops.[7] It is possible for the surface of a material to be damaged by the incident radiation, with the additions of atoms to the surface, with crater and ripple formation possible.[7] Damage can be related to the initial particle impact (primary damage) and then subsequent thermalisation processes related to the collision.

One way to measure the effects of incident radiation has on matter is to measure the average number of displacement atoms per lattice atom, this is known as the dpa. It was

first defined in 1975,[8] and is now 'a widely used standard for estimating the primary damage from neutrons, ion and electrons.'[7] To calculate dpa for neutron damage, it is necessary to know the neutron flux/fluence and the effective displacement cross-section, $\sigma_d(E)$, (the probability of displacement of an atom in the target as a result of a collision in impacting radiation). $\sigma_d(E)$ can be mathematically defined as:

$$\sigma_d(E) = \int_0^\infty \sigma_s(E)\sigma(E,T)v_d(T)dT \qquad \textbf{(3.2-2)}$$

where $\sigma_s(E)$ the probability of the incident radiation colliding with an atom in the substrate, $\sigma(E, T)$ the probability of displaced atom receiving energy T and $V_d(T)$ the number of secondary displaced atoms. To calculate the dpa this probability is multiplied by flux intensity, Φ, or practically this can have values with time dependence, $\Phi_{tot}(t)$ and a normalised flux spectrum when integrated over energy, $\Psi(E,t)$ which is assumed to be constant over exposure time.[7] Considering this dpa can be calculated:

$$\text{dpa} = t_e\Phi_{tot}\int_o^\infty dE\,\sigma_d(E)\Psi(E) \qquad \textbf{(3.2-3)}$$

This brief overview of displacement damage gives information on how radiation may affect the microstructure and macrostructural properties of materials and how often this is measured by calculating the average number of displacements per atom. As ɣ-radiation is the focus of the work outlined in this thesis and the interactions of ɣ-radiation with materials does not tend to lead to displacement damage further details of displacement damage are not given.

3.3 Measuring the effects of radiation

To evaluate the effects of radiation on materials, the energy loss of incident radiation must be considered and then it can be compared to any chemical or physical changes seen in the irradiated system.

When considering charged particles, the specific energy loss of the particle into the target medium may be defined as the stopping power $\hat{S}$,

$$\hat{S} = \frac{dE_{loss}}{dx}\ (J/m) \qquad \textbf{(3.3-1)}$$

where *x* is the distance travelled by the particle.[4, 5] The stopping power is a function relating the particle velocity and changes as the particle is slowed down. LET was defined earlier as the energy lost per unit length mathematically it can be defined as:

$$\text{LET} = \frac{dE_{abs}}{dx} \qquad \textbf{(3.3-2)}$$

LET is related to stopping power:

$$\frac{dE_{loss}}{dx} = \frac{dE_{abs}}{dx} + E_x \quad \textbf{(3.3-3)}$$

And the difference E_x is the energy lost due to electromagnetic radiation.[3] Both LET and stopping power can only give quantitative information on the average energy lost as they assume continuous slowing of the particles. These do not give quantitative information about the concentration of reactive species generated. For quantitative information the interaction of radiation must be related to the system response, the yield of a radiation induced reaction can be measured. The response to the radiation absorbed (energy) is related to its radiation-chemical yield and can be defined by *G Value* of the reaction. It may be simply defined as 'a measure of the chemical yield.[9] The *G Value* describes the number of molecules exhibiting change per 100eV of energy absorbed.[4, 5, 9, 10]

$$G = \frac{M}{N} \times \frac{100}{W} \quad \textbf{(3.3-4)}$$

where, W (eV) = the mean energy required to form an ion pair in the material which assumed to be 32.5eV per ion pair, the equation reduces to:

$$G = \frac{3M}{N} \quad \textbf{(3.3-5)}$$

The SI unit representation is defined as the moles of material formed or changed by an energy absorption of 1 joule; 1 molecule per 100 eV = 0.136 μmol J^{-1} or 1 mol J^{-1} = 9.649 x 10^6 per 100 eV.[3, 4] With the symbol *g*(x) referring to number per 100 eV and G(X) to mol J^{-1}. The mean energy deposited into system can be described as the dose received or absorbed dose. *Absorbed dose (D)* is the average amount of radiation absorbed per unit mass[3, 5]:

$$D = \frac{dE_{abs}}{dm} \quad \textbf{(3.3-6)}$$

where $E_{abs} = E_{in} - E_{out}$

The SI unit for *absorbed dose* is the *Gray* (Gy) and is 1 Gy = 1 J/kg and *dose rate* can be defined as the absorbed rate per unit time, and its units are Gy/s. An older unit for *absorbed dose* is the *Rad* which is the dose that causes 100 ergs of energy to be absorbed by 1 g of material. Dosimetry techniques allow the chemical response of a system to be assessed based on the measured response in a known reaction.

Dosimetry measures a sources radiation dose by calibration of the dosimeter's response, there are many types of dosimeter such as chemical and solid-state dosimeters. A

dosimeter may detect the radiation itself as in the case of heavy ions or the response for the lighter and non-ionising radiation types (such as γ and neutrons). Measurements of dose for ɣ-radiation is discussed here. Chemical dosimetry is a convenient way to measure the dose rate of a system but does require knowledge of the radiation-chemical yield of the system and is compared to the response of primary dosimeter. According Spinks and Woods if a chemical dosimeter is to be used the response should be:[4]

1) Proportional to absorbed dose over a wide range of values (doses)
2) Independent of the absorbed dose rate
3) Independent of the energy and LET of the radiation
4) Independent of temperature, and
5) Reproducible

An established chemical solution dosimeter is the use of Fricke solution; Vertes *et al.* describe it as 'the best-known liquid chemical dosimeter suggesting it that this system is 'widely used for calibration purposes.'[5] Fricke dosimetry uses a solution of Ferrous Sulphate and monitors radiation by the oxidation of the ferrous ion at low pH given that oxygen is present. The effects of radiation on the Fricke solution are well documented and assume Fe^{3+} interacts with the radiolysis products of water. Other dosimeters include solid state dosimeters that use UV-Vis spectroscopy to observe absorbance changes due to irradiation and doses determined using a look up table.

3.4 Radiolysis processes

Radiation, the types, behaviour, their possible interactions and consequences have briefly been described. The following sections aim to describe the importance of the interactions experienced between the materials present and the coolant of LWR primary circuits. Water radiolysis process is introduced now, and literature related to investigating primary circuit conditions and how they affect the corrosion of nuclear materials is discussed in **Chapter 4: Sections 4.1 to 4.8.**

LWR systems use water as a coolant and moderator in the reactor core and a variety of additives are used to control the chemical and radiation induced processes that occur. These processes within the coolant circuit are affected by radiation processes and the products of these. The presence of additives, surfaces and corrosion processes will also affect the radiation processes. Radiation chemistry plays an important role in nuclear engineering research with the goal to bring clarity to radiolytically driven processes. An

important factor is the effects of radiation on the coolant in the coolant circuit, in the simplest form, this is water. The splitting of water by electromagnetic radiation (light) is termed photolysis and produces hydrogen and water. The dissociation of water by ionising radiation is more complicated and is termed radiolysis. The decomposition of water exposed to ionising radiation results in chemically active species, composing of ions and radicals and it can be summarised as the following.[4, 5]

$$H_2O \longrightarrow HO^{\bullet}, e_{aq}^{-}, H^{\bullet}, HO_2^{\bullet}, H_2O_2, H_2, H^{+} \quad \textbf{(3.4-1)}$$

The routes to these radiolysis processes are outlined in **Figure 3.4-1** which is a recreation based on work by Buxton as well as work by Spinks and Woods.[4, 11]

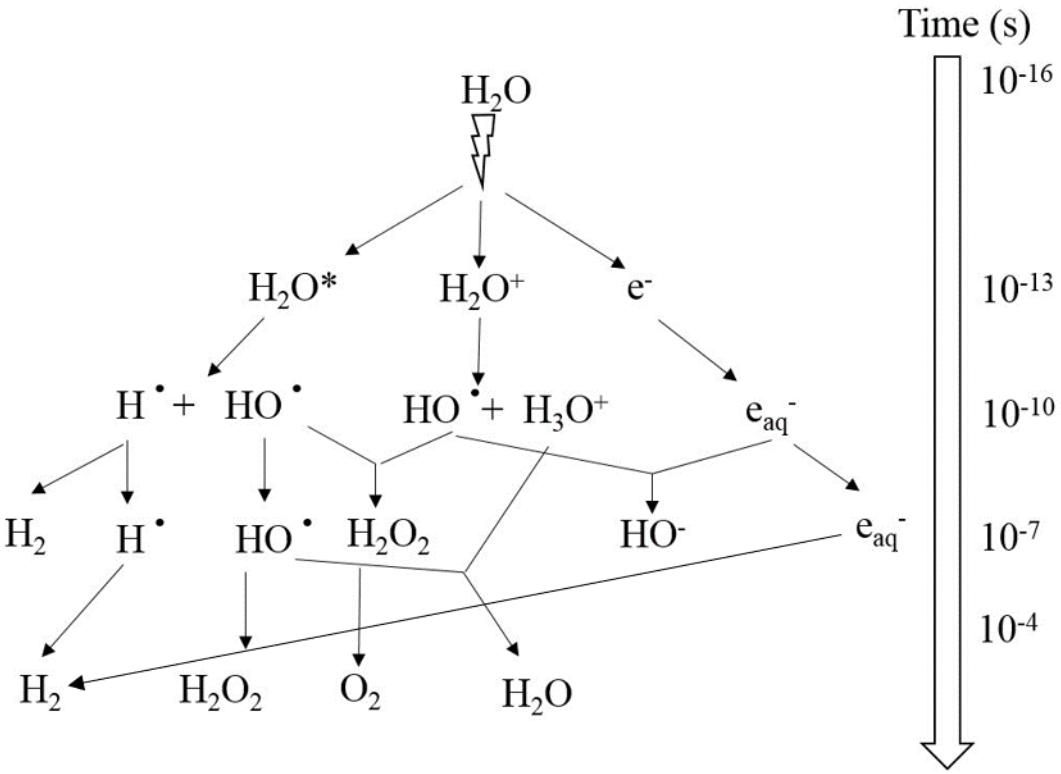

Figure 3.4-1. The radiolysis process with timescales, created from work by Buxton and Spinks and Woods.

Radiolysis products can be spilt into oxidising (H_2O_2, •OH and HO_2•) and reducing species (e^-_{aq}, H• and H_2), and will cause changes in the redox behaviour of the coolant.[12 13] Of particular interest, are hydrogen peroxide and molecular H_2 due to their redox activity and their relatively long half-lives. Long term studies will often start with investigating the effects of these products on corrosion before progressing to the more complex in-situ radiation studies. Studies that investigate the behaviour of these corrosion phenomena may be separated into the initial corrosion of the materials and then the release, transport

and deposition of the corrosion products and their subsequent behaviour. **Chapter 4, Sections 4.1-4.5** discuss general corrosion mechanisms of metals, **Section 4.6** gives an overview of how these CRUD related issues affect reactor operation and revenue. **Section 4.7** looks at how corrosion mechanisms may be investigated under simulated reactor conditions. Finally, **Section 4.8** discusses the literature surrounding the interactions between corrosion and radiolysis products.

References

1. A. Mozumder, *Fundamentals of Radiation Chemistry*, Academic Press, USA, 1999.
2. S. C. Lind, *Radiation Chemistry of Gases*, Reinhold, 1961.
3. G. Choppin, J. Liljenzin, J. Rydberg and C. Ekberg, *Radiochemistry and Nuclear Chemistry*, Elsevier, United States of America, 4 edn., 2013.
4. J. W. T. Spinks and R. J. Woods, *An Introduction to Radiation Chemistry*, John Wiley & Sons, United States of America, 3 edn., 1990.
5. A. Vertes, S. Nagy, Z. Klencsar, R. G. Lovas and F. Rosch, *Handbook of Nuclear Chemistry*, Springer, London, 2 edn., 2011.
6. in *Materials Science Monographs*, eds. J. Koutský and J. Kočik, Elsevier, 1994, vol. 79, pp. 22-65.
7. K. Nordlund, A. E. Sand, F. Granberg, S. J. Zinkle, R. Stoller, R. S. Averback, T. Suzudo, L. Malerba, F. Banhart, W. J. Weber, F. Willaime, S. Dudarev and D. Simeone, *Primary Radiation Damage in Materials*, 2015.
8. M. J. Norgett, M. T. Robinson and I. M. Torrens, *Nuclear Engineering and Design*, 1975, **33**, 50-54.
9. K. H. Lieser, *Nuclear and Radiochemistry*, Wiley-VCH, Germany, 2 edn., 2001.
10. M. Burton, *Discussion Faraday Society*, 1952, **12**, 317.
11. M. M. M. S. Maurizot, T. Douki, J. Belloni *Radiation Chemistry: From Basics to Appliactions in Materials and Life Sciences*, EDP Sciences, France, 2008.
12. C. C. Lin, Y. J. Kim, L. W. Niedrach and K. S. Ramp, *CORROSION*, 1996, **52**, 618-625.
13. K. Ishigure, T. Nukii and S. Ono, *Journal of Nuclear Materials*, 2006, **350**, 56-65.

Chapter 4: Corrosion of nuclear materials

The structural materials used in LWRs undergo degradation and of the possible routes corrosion is prevalent and is experienced in many forms including: general corrosion, stress corrosion cracking, flow assisted corrosion and irradiation enhanced corrosion. This chapter explores the literature associated with general corrosion processes, the corrosion of nuclear materials with and without simulated LWR conditions.

4.1 The corrosion processes

Metallic corrosion is a degradation method that occurs by electrochemical redox processes, where a metal (M) loses electrons, thus becoming an electropositive species as shown in **Equation(4.1-1)**.[1] The loss of electrons means that this species is oxidised, the oxidation state of the species increases. Due to the conservation laws, the electrons generated in the reaction must be deposited elsewhere. The incorporation of an electron into another chemical species is known as a reduction reaction.[1] The electron acceptor may be another metal, a proton, water or even oxygen, dependent on the system.

$$\mathrm{M} \rightarrow \mathrm{M}^{n+} + n\mathrm{e}^{-} \qquad \textbf{(4.1-1)}$$

For corrosion to proceed there must be an electrochemical potential difference between the oxidising and reducing species (allowing for energy transfer). An electron will move to the lower energy state within the system but there must be no resulting net electrical charge accumulation within the system.[1] Corrosion can be described in terms of electronic levels and the study of these electronic levels is electrochemistry. Understanding the movement of the electrons in this system allows for studies into the energetics and the kinetics of corroding systems. Metals have a continuous band structure, in which electrons may move freely, with a band gap between the occupied and unoccupied levels. A visualisation of this can be seen in **Figure 4.1-1.** The maximum energy at which an electron sits is called the Fermi Energy, E_F.[2] In electrochemical studies the ability for a material to move electrons makes the species a conductor. The Fermi level may be influenced by external application of voltage; this will add or remove electrons from the conductor.[2] In a system where the oxidation and reduction (O/R) species are connected electrons may move from one species to the other, from an occupied orbital to one that is not occupied. From valence to conductance bands, with the energy between this called the band gap. The electronic energies of these levels can be considered in terms of electrode potentials. The energies of the orbitals correspond to the redox potentials; in

Figure 4.1-1 the electron transfer is shown in terms of energy levels for a reduction and oxidation processes. The electrode potential can be seen as movement of electrons between internal energy levels in the system.[2] It may also be seen as the movement of these electrons between the surface and its environment, when an equilibrium is reached this movement causes a net electrical charge, a potential difference between the two phases.[3]

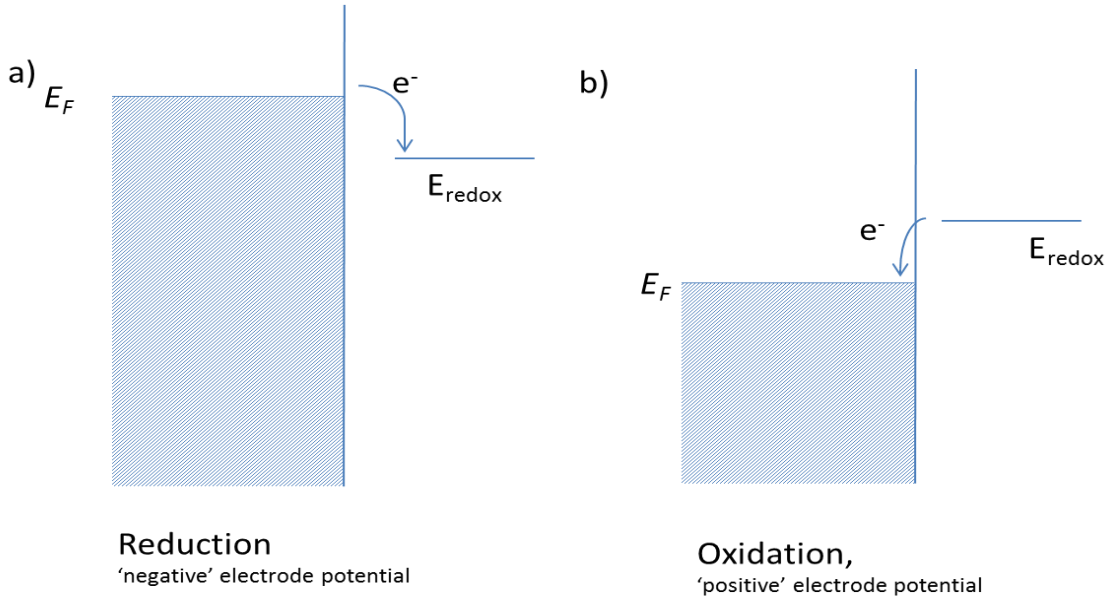

Figure 4.1-1. Diagram to show the electron movement in redox processes regarding electronic levels within materials.

Electrode potential measurements allow for monitoring of systems and can give information on corrosion. The redox process can be split into two half equations, the reduction and the oxidation equations. These half equations each have an electrode potential, which is measured in terms of a standard electrode the basic equations are outlined in **Equations (4.1-2) and (4.1-3)** M is the oxidised species, the metal and N is the electron acceptor, either a metal, oxygen, hydrogen etc determined by the system type. The difference between the two half equations is the system electrode potential, and in corrosion it is the corrosion potential (E_{corr}) **(Equation (4.1-4))** The electrode potentials are given in terms of a standard, in most cases the standard hydrogen electrode (SHE), the potential of the SHE is set at zero, and comparison to this allows for a series to be defined. **Equation (4.1-5)** shows the reaction occurring at the SHE.

$$M \rightarrow M^{n+} + ne^{-} \qquad oxidation \qquad \textbf{(4.1-2)}$$

$$N^{n+} + ne^{-} \rightarrow N \qquad reduction \qquad \textbf{(4.1-3)}$$

$$M + N^{n+} \rightarrow M^{n+} + N \qquad Over\ all\ redox \quad (E_{cor}) \qquad \textbf{(4.1-4)}$$

A standard electrode potential for a system is measured in comparison to the SHE and tabulated.

$$2\mathrm{H}^+ + 2e^- \rightarrow \mathrm{H}_2 \qquad \textbf{(4.1-5)}$$

The electrochemical series is formed utilising these equations, with noble metal being less likely to corrode having positive electrode potentials, and materials prone to corrosion having a more negative potential. A simplified electrochemical series is listed in **Table 4.1-1,** these values are recorded at standard conditions, 298 K, 1 atm pressure and effective concentrations of 1 mol/L.[4] These standard electrode potentials are redox potentials and may be broken down into their substituent half equations.

The electrode potential of a system can be related to the overall standard electrode via the Nernst equations seen in **Equation (4.1-6)** (when ideality is assumed). Where Q is the reaction quotient, a measurement of the activity of a system or the concentration of the redox species.

$$E_{cell} = E^0{}_{cell} - \frac{R\mathrm{T}}{z\mathrm{F}} \ln Q \qquad \textbf{(4.1-6)}$$

The Nernst equation gives the ability to predict or calculate the system's electrode potential if species concentration is known, or vice versa, if electrode potentials are known species concentrations or activities can be calculated. The Nernst equation gives a basis for electrochemical techniques, measurements and monitoring methods.

Table 4.1-1. Electrochemical series

Element	Redox	*E°* ***(volts)***	
Lithium	$Li^+ + e^- \rightleftharpoons Li(s)$	- 3.040	Most reactive
Potassium	$K^+ + e^- \rightleftharpoons K(s)$	- 2.936	
Calcium	$Ca^{2+} + 2e^- \rightleftharpoons Ca(s)$	- 2.868	
Sodium	$Na^+ + e^- \rightleftharpoons Na(s)$	- 2.714	
Magnesium	$Mg^{2+} + 2e^- \rightleftharpoons Mg(s)$	- 2.360	
Aluminium	$Al^{3+} + 3e^- \rightleftharpoons Al(s)$	- 1.677	
Zinc	$Zn^{2+} + 2e^- \rightleftharpoons Zn(s)$	- 0.762	
Chromium	$Cr^{3+} + 3e^- \rightleftharpoons Cr(s)$	- 0.740	
	$Cr^{2+} + 2e^- \rightleftharpoons Cr(s)$	- 0.890	
Iron	$Fe^{2+} + 2e^- \rightleftharpoons Fe(s)$	- 0.440	
Cadmium	$Cd^{2+} + 2e^- \rightleftharpoons Cd(s)$	- 0.402	
Cobalt	$Co^{2+} + 2e^- \rightleftharpoons Co(s)$	- 0.282	
Nickel	$Ni^{2+} + 2e^- \rightleftharpoons Ni(s)$	- 0.236	
Cadmium	$Cd^{2+} + 2e^- \rightleftharpoons Cd(s)$	- 0.402	
Hydrogen	$2H^+ + 2e^- \rightleftharpoons H_2(g)$	0.000	
Copper	$Cu^+ + e^- \rightleftharpoons Cu(s)$	+ 0.518	
	$Cu^{2+} + 2e^- \rightleftharpoons Cu(s)$	+ 0.339	
Iron	$Fe^{3+} + e^- \rightleftharpoons Fe^{2+}(aq)$	+ 0.77	
Silver	$Ag^+ + e^- \rightleftharpoons Ag(s)$	+ 0.799	
Mercury	$Hg^{2+} + 2e^- \rightleftharpoons Hg(l)$	+ 0.852	
Platinum	$Pt^{2+} + 2e^- \rightleftharpoons Pt(s)$	+ 1.180	
Gold	$Au^{2+} + e^- \rightleftharpoons Au(s)$	+ 1.690	Least reactive metal

Electrochemical behaviour will vary with system conditions, a consideration that is often made is the pH of the system. Clark and Cohen first published work reporting E against pH for chemical systems and work was extended by many others, with these plots often referred to as Pourbaix diagram signalling significant work done in this area by M. Pourbaix.[5-7] E-pH diagrams may have non-redox full reactions where there are no changes in oxidation numbers of the elements, (represented by vertical lines) and redox half reactions where there is an exchange of electrons, (represented by horizontal sloped lines). Half equations must be combined to give reactions where a change in oxidation state is represented and electrons are cancelled out, an overall electrode potential value for a reaction may be calculated by the taking the difference in the E values in the half equations.[7] All E-pH diagrams will have dashed sloped lines that reflect the E value changes for HOH species, with the upper line representing the reaction in **Equation (4.1-7)** and lower the reaction outlined in **Equation (4.1-8)**

$4e^- + 4H^+ + O_2 \rightarrow 2HOH$ E = 1.23 – 0.059 pH **(4.1-7)**

And

$2e^- + 2H^+ \rightarrow H_2$ E= 0.00 – 0.059 pH **(4.1-8)**

For predicting the likelihood of a species interacting with water at a given pH a vertical 'cut' is made at the proper E values, and species are indicated below and above these cuts. The vertical cuts are known as electron ladders. A reaction may be thermodynamically predicted using the E-pH diagrams of the elements involved, where the electrode potentials from reactants E-pH diagram are combined with that of water to form in what is referred an 'electron ladder' which is ordered by decreasing E. The species on lower rungs must be combined with upper species giving intermediates and these equations balanced, when all system factors are considered reactions tend to correlate with experimental observations.[7] **Figure 4.1-2** gives the E-pH diagram for water alongside the couples of common reducing and oxidising agents, diagram by Schweitzer and Pesterfield.[7]

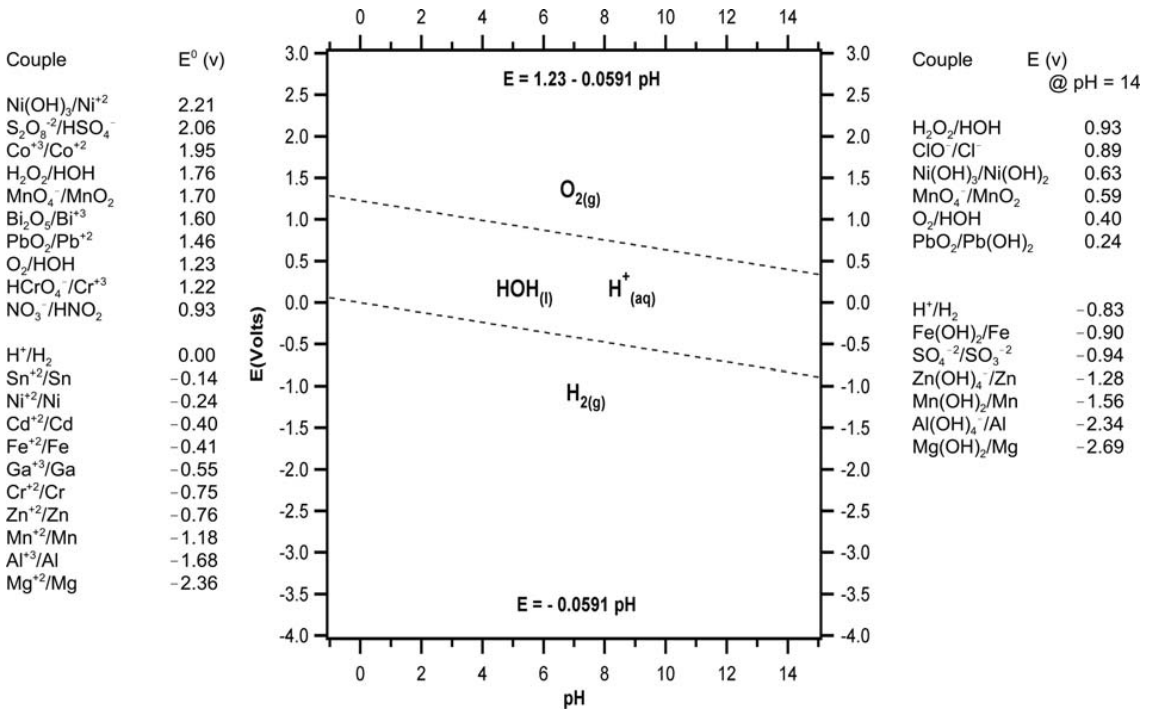

Figure 4.1-2. E-pH diagram for water systems with commonly used oxidants and reductants. Soluble species and most solids are hydrated. Diagram taken from work by Schweitzer and Pesterfield.[7]

As corrosion behaviour is dictated by the movement of electrons it is important to consider the affects that radiation may have on the electron movement in these materials, or if the materials promote the splitting of water via their involvement in redox processes. Materials can be insulators, conductors or semi-conductors depending on their electronic band structure, with the ability of electron movement from the valence band to the conductance band dictating this behaviour. A large band gap means a material is an insulator, smaller gaps, semi-conductors and conductors have no or very small band gaps. If a material has a band gap that aligns with the reduction (EH_2/H^+) and oxidation (EO_2/H_2O) potentials of water, they may act as a catalyst promoting the splitting of water. The splitting of water by light or ionising radiation generate a hole and a 'hot electron.' With semiconductors and metals there is the possibility of the electrons near the metal surface being scavenged therefore, removing electrons from participating in further radiolysis processes. This is an important consideration when considering the effects of radiation on corrosion mechanisms and the interaction of products with radiolysis products. Work by Renault *et al.* proposes a mechanism for electron scavenging at metal surfaces a production of this mechanism can be seen in **Figure 4.1-3**.[8]

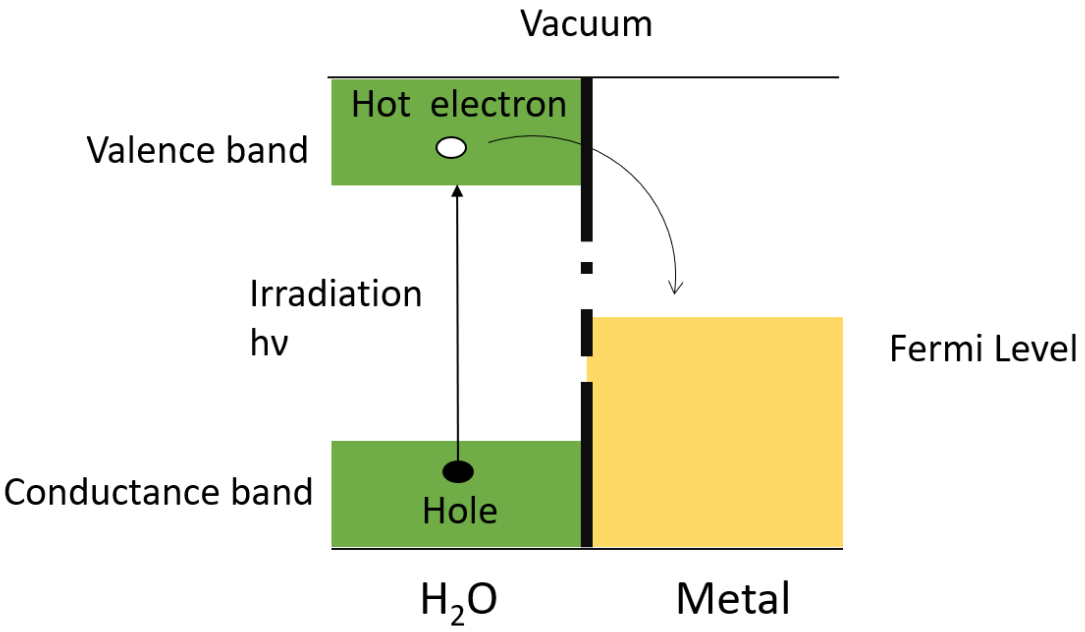

Figure 4.1-3. Proposed mechanism for electron scavenging near metal surface, showing the water electronic structure.

The possibility of the transfer of electrons from water to materials highlights the importance of understanding the oxide present on a materials surface, its composition (and its valence band structure) and how this may dictate its redox behaviour and therefore its ability to scavenge electrons generated in radiolysis processes.

Corrosion of LWR related structural materials

Current PWR and BWR coolant systems employ a variety of austenitic stainless steels and nickel alloys (Inconels) with older fleets using mild steels and cladding materials include zircaloy. PWRs primary circuit structural materials including austenitic and 300 series stainless steels and nickel alloys (600, 690 and 800) with typical compositions for these materials given in **Table 4.1-2.**[9, 10 11-13] **Table 4.1-3** gives the estimated surface area of each material used in the coolant circuits of BWR, PWR and CANDU – PHWR reactors showing the diversity of materials used within these systems, which leads to the complexity of corrosion behaviour that is observed in these systems.

Table 4.1-2. Composition of typical materials used in LWR primary circuits. Values that do not have a range are the maximum value expected in these materials

Alloy	Composition elements										Other
	Fe	Cr	Ni	C	Mn	Si	P	S	Mo	W	
S 316	Bal	16-18	10-14	0.08	2	1	0.045	0.003	2.0-3.0	n/a	
SS316 L	Bal	16-18	10-14	0.03	2	1	0.045	0.003	2.0-3.0	n/a	n/a
SS 304	Bal	18-20	8-11	0.08	2	0.75	0.045	0.03	n/a	n/a	N 0.1
Ni alloy 690	7-11	27-31	Bal	0.05	0.5	0.5	0.02	0.015			Cu 0.5, Ti 0.5, Al 0.5
Ni alloy 600	6-10	14-17	Bal	0.15	1	0.5	n/a	0.015			Ci 0.5
Ni alloy 800	39.5	19-23	Bal	0.1	1.5	1	n/a	0.015	n/a	n/a	Cu 0.75, Ti 0.6, Al 0.6

Table 4.1-3 Surface area in contact with coolant in typical water-cooled reactor plants

Material Type	Surface area of coolant circuit		
	BWR	PWR	CANDU-PHWR
Stainless steel	44	5	-
Inconel 600, 800 or Monel	-	75	77
Carbon Steel	8	-	10
Zircaloy	48	20	13

The general corrosion of these LWR materials create a double layered oxide with a 'normal spinel chromite' ($FeCr_2O_4$) inner layer, with a non-stoichiometric nickel ferrite ($Ni_xFe_{3-x}O_4$) outer layer sometimes referred to as nickel rich magnetite. The corrosion processes of mild and stainless steels at elevated temperatures was the focus of early investigations, with J. Robertson summarising the possible mechanisms to the multi-layer oxide growth exhibited by these materials.[14, 15] It was suggested that corrosion occurs via a diffusion induced current, with steel systems being able to exhibit currents due to electron and/or proton movement as well as the application of external currents to induce

oxidation.[14, 15] The varied current types explain a materials ability to grow multiple oxide films with the diffusion of ions across layers and grain boundaries determining the rate of corrosion.[15] Robertson then went on to summarise the oxidation of stainless steels at elevated temperatures.[14]

4.2 Mild steel corrosion

Robertson describes the microstructure of the oxide layers in mild steel, explaining that the oxide films can differ in both oxidation state and grain size in his 1989 paper.[15] A duplex system grows with an inner layer of small grain size due to the spatial confinement by the outer layer during growth. The outer layers in these systems are unconfined thus have larger grains and may grow outwardly.[15] For mild steel corrosion in an aqueous system, Robertson summarised the literature that previously outlines the aqueous corrosion such as the Castle-Masterson model. The Castle-Masterson model suggest the rate determining step for corrosion is the diffusion of aqueous iron to the outer oxide layer; the pore model describes the diffusion of the iron to the outer layer. Robertson goes on to describe the gaseous oxidation model for corrosion where the outer layer ion grows at an oxide-gas boundary by outward transportation of metal and inner layer growth is by inwards transportation of oxygen. The aqueous model is somewhat insufficient in describing the corrosion process and therefore Robertson proposes another model that describes the formation of duplex layers providing an inner layer is in place.[15] The paper combines models to describe the corrosion via a ‘grain boundaries pore model’.[15] Pores are created within the oxide layers because of the mismatch in grain size, with gaps between grains leading to micropores. These micropores allow for transport of metal ions as well as the transport of redox species (oxygen and hydrogen). This model is discussed in terms of corrosion rates with a dependence on temperature and pH, which is limited by the solid-state diffusion of Fe ions along grain boundaries of the oxide layer. The ion diffusion process is discussed in terms of movement through oxide layers, along the grains and though pores in the films. As the reactions throughout corrosion are driven by electrochemical behaviour, the transport of ions and reducing species may be enhanced by a supplied current, and the diffusion of ions themselves also generates a current. Understanding the type of current produced can aid films stoichiometry identification. There are three possible current types in these system, external current, electron transfer

(oxidation current) and a proton current. The system cycles between these current types depending on system conditions. **Figure 4.2-1** shows the transfer diffusion and current possibilities for a steel corrosion system.

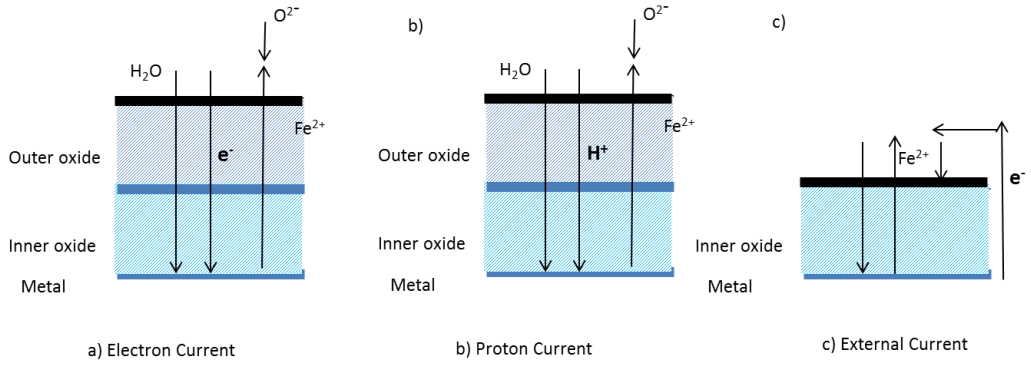

Figure 4.2-1. Diagram to show the different diffusion models and current production modes in steel corrosion systems. Diagram replicated from Robertson paper. a) The electronic current, movement of electrons through the oxides; b) proton current, movement of H^+ across the oxide; c) an external applied current causing the movement of ions and electrons.

The different current types enable the various oxide film composition; Fe_3O_4 may be produced using hydrogen or electronic current and the thickness of this oxide layers is dependent on its Pilling- Bedworth ratio, ν, which is 2.1 for this particular oxide[14]. The Pilling-Bedworth ratio is a description of the ratio of the oxide cell volume with respect to the elementary cell volume of the equivalent metal where the oxide has been created.

$$Rpb = \frac{V_{oxide}}{V_{metal}} = \frac{M_{oxide}\, x\, \rho_{metal}}{n\, x\, M_{metal} x\, oxide} \qquad \textbf{(4.2-1)}$$

where M is the atomic mass, n the number of atoms of metal per molecule of the oxide, p is the density of them and V the molar volume of oxide metal. A $R_{pb} < 1$ gives a layer that is not protective, at around 2 the oxide can chip off and gives no real protective effect but a R_{pb} of between 1 and 2 predicts an oxide that creates a passivating layer that protects the metal from further surface oxidation.[16] The effects of these ratios has on oxide type and porosity is represented in **Figure 4.2-2.**[16]

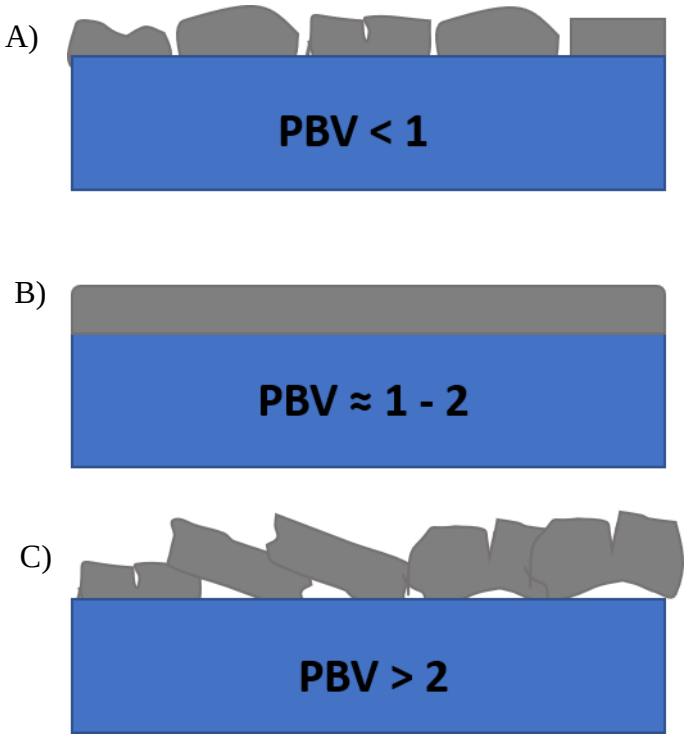

Figure 4.2-2. Diagram to show the effect of the Pilling Bedworth ratio on oxide type and protectiveness. A) R_{pb} < 1 shows the non-protective oxide, B) shows a R_{pb} of between 1 and 2 where the oxide creates a passivating layer that protects the metal from further surface oxidation C) shows a R_{pb}> 2 where the oxide chips off exposing the metal and gives little protective effect.

The oxide structure and layering can be predicted using the Pilling-Bedworth ratio alongside chemical oxidation equations. For steels, iron may be directly oxidised to produce the inner oxide layer without transfer of ions and reducing species with the rest of the Fe being oxidised to Fe^{2+}. These Fe^{2+} ions diffuse out towards the outer layer, with electrons diffusing to provide a counter current allowing for conservation laws. The Fe^{2+} forms either Fe_3O_4 or γ- FeOOH (with surface hydration), γ- FeOOH has been proposed as a passive layer in these systems. When hydrated, the ability to supply electrons reduces so proton counter currents occur and hydrogen is evolved at the oxide-metal interface.[15] At elevated temperature the surface will dehydrate, and electronic conductance will dominate once more (work by Tomlinson and Cory supports this) with the proportion of H_2 evolved at the oxide-metal interface decreasing after 350 ˚C.[17] The mechanistic detail in this paper supports the 'grain boundary pore model' and suggests corrosion rate is limited by the outwards diffusion of metal ions along grain boundaries. The systems dependence on temperature and pH (which is discussed in length) also supports this

model which unifies the previous aqueous and gaseous models. Robertson discusses in a 1991 paper the mechanism for corrosion of stainless steels.[14]

4.3 Stainless steel corrosion

Stainless steels differ from mild steels due by inclusion of alloying elements such as; Ni, Cr and possibly Manganese (Mn). The inclusion of these means the oxide films that grow during corrosion will have different compositions than those formed in mild steels. The grain boundary model can be applied to corrosion of stainless steels, a 1991 paper by Robertson summarises the corrosion mechanism for ferritic and austenitic stainless steels using this model as an example.[14] Corrosion at lower temperatures leads to a Cr_2O_3 layer which is formed via tunnelling of the oxidation species- the diffusion of anions towards the metal | oxide interface. Once the tunnelling thickness is exceeded, the film growth is dependent on diffusion rates of the ions. The diffusion rates of the ions commonly found in stainless steels are listed in order below.[14]

$$Mn^{2+} > Fe^{2+} > Co^{2+} > Ni^{2+} >> Cr^{3+}$$

The rate determining step is ion diffusion across the layers via solid state diffusion, and so, the rate of film growth depends on this. A duplex film grows in these systems, with

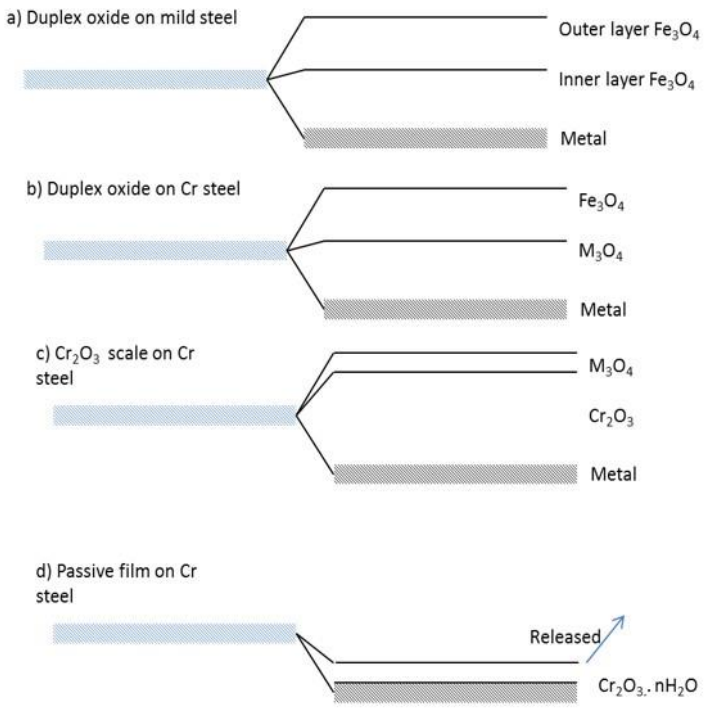

Figure 4.3-1. Scheme to show the possible oxide film on mild and Cr steels. a) Duplex oxide present on mild steels, showing the different iron oxides; b) Stainless steel films, duplex oxides; c) Stainless steel showing that there is a possibility of a Cr_2O_3 film. Recreation of work by Robertson *et al.*

the inner layer forming by inward diffusion of water along the micropores and the outward diffusion of metal ions along grain boundaries. **Figure 4.3-1** compares the oxide films present in stainless and mild steel.[14]

In stainless steels, the addition of chromium gives enhanced corrosion resistance due to its relatively low diffusion rate compared to the other metal ions present. Cr may be oxidised to form a passive layer which remains the inner most oxide layer. The oxidation of Cr generates Cr_2O_3 oxide and this is not readily released into the system, preferring to stay attached to the metal interface forming the inner layer.[14] It is possible for an outer M_3O_4 layer to form, where M may be Fe or Ni etc. The outer layer may release into the solution (an important phenomenon) and release rate is thus tied into the corrosion rate. Total corrosion rate is independent of the presence of this outer layer and is dependent temperature and pH. Corrosion can be described in terms of anionic and cationic processes, with the inner Cr-rich oxide growth by anionic transport.[14] The metal-oxide interface moves towards the surface base, Ni and Fe are transported through the inner layer and may dissolve into the water by cation release. A possible fate for these dissolved ions is position forming an outer oxide layer with mixed oxide layers also due to the alloying elements present.[18]

PWR conditions are more complicated than those summarised in the work by Robertson due to the presence of chemical additives and a mixed radiation field. A more recent paper into the corrosion of stainless steels by Wren *et al.* attempts to address some of these complexities. These studies investigate the electrochemical behaviour of these materials and utilised electron diffraction to probe the structure and composition of the corrosion products formed when steels are exposed to borated solutions. It is reported that the oxide at the metal interface is Fe_3O_4 with a spinel structure and on the outer layer being γ-Fe_2O_3 at the solution interface.[19] More recent work shows that the structure of the film layers can vary greatly: from amorphous layers to crystalline Fe_3O_4 and γ- Fe_2O_3, suggesting new structures with altered cation vacancy geometries.[19 20] The paper also highlights the difference the system conditions can make, stating that electrochemical studies using NaOH gave oxide films including $Fe(OH)_2$, Fe_3O_4, FeOOH and γ-Fe_2O_3[19, 21] (citing work by Hugot *et al.* a study that utilised cyclic voltammetry and Raman spectroscopy).[21] Wren *et al.* stated there is debate over types of oxides formed and how they are formed, and the condition of the system; pH, redox conditions and temperature will vary the corrosion considerably.

4.4 Nickel alloy corrosion

Due to initial differences in composition, the corrosion mechanism of nickel-based alloys is different as are the subsequent corrosion products. Studies into Ni corrosion suggest that there is also a dependence on pH, temperature and system potential, and that oxides produced vary.[22] The oxides produced include NiO, Ni_2O_3 NiOOH and $Ni(OH)_2$ due to the variable oxidation states accessible to Ni.[23] The alloying of Nickel with varying weight percentages of chromium and iron, along with other alloying elements (e.g. manganese and carbon) leads to the Inconels, austenitic nickel alloys. The oxide formation for Inconel-type alloys leads to a complex layer structure. A suggested structure for this is shown in **Figure 4.4-1**, which also shows the fate of these oxides. The species present in an oxidised Inconel system include mixed nickel ferrites and iron-nickel chromite. Just like stainless steels, it is possible to have a multi-layered oxide film due to the difference in diffusion coefficients of the alloying elements. In Inconel corrosion there is an inner chromium rich layer and an outer layer that forms from the precipitation of dissolved ions from solution when the solubility limit of the solution is exceeded.[24] J Park suggests (in a 2004) paper the route to this duplex layer and explains the process in terms of diffusion coefficients and precipitation reactions.[24] The metal ions in the layer can diffuse outwards and dissolve into the solution, and if the solution becomes saturated it will cause ions to deposit on the surface of the inner layer. Considering the relative solubility of the ions in the first layer, this 'inner layer' is initially a nickel-iron chromate, the diffusion coefficients of nickel and iron are higher than that of chromium, so they diffuse towards the surface and dissolve into the system[24] and thus leaves a chromium rich inner layer. A precipitation reaction can then occur at the inner layer/solution interface producing a nickel ferrite outer oxide layer. Park suggests the formation of this outer layer is by a salt film precipitation that has the reaction scheme:

$$xNi^{2+} + (3 - x)Fe^{2+} + H_2O \rightarrow Ni_xFe_{3-x}O_4 + 8H^+ + 2e^- \qquad \textbf{(4.4-1)}$$

Park emphasises the fact the Ni^{2+} and Fe^{2+} are from the metal and diffuse through the inner layer, dissolve into the electrolyte and precipitate on the inner layer/solution interface. The work describes this as a new and adequate descriptive model for the corrosion of the Inconel products calling it the "Diffusion-dissolution coupled model".[24] Behaviour of the corrosion products once solvated is complicated and depends heavily on environmental conditions, with this affecting ongoing corrosion behaviour. A few possibilities for corrosion mechanism of materials used in PWR systems have been reviewed here, with a few indications of the fates of the oxide layers. Stainless steels produce multilayer systems where the top layers can release into solution and the fate of the Cr containing spinels that make up part of the inner layer dependant on other conditions. Before considering the effects of radiation it is important to introduce radiation processes, radiation chemistry and its relevance in PWR systems.[22]

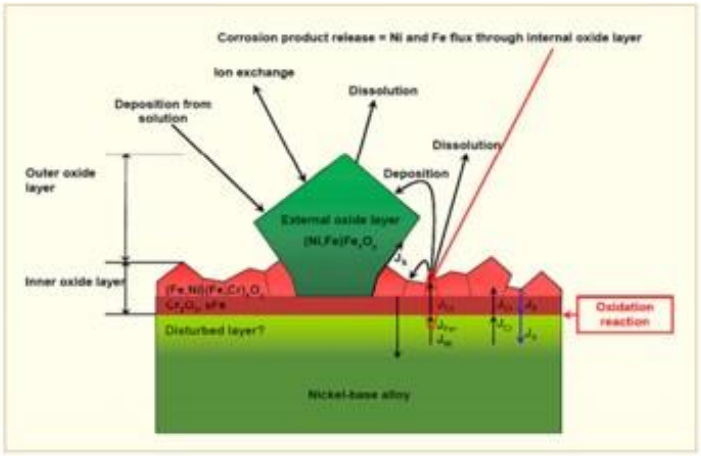

Figure 4.4-1. Schematic to show the fates and arrangement of corrosion products in a nickel-based alloy. Taken from a STUK report into the properties of oxide films.

4.5 The implications of LWR structural material corrosion

The corrosion of structural materials may lead to the release, transport and deposition of corrosion products in LWR coolant loops. The build-up of deposited corrosion products is termed CRUD and is responsible for reduced reactor performance, axial offset anomaly and increased radiation fields (if deposition occurs on the reactor core fuel rods) and in BWR systems has been known to cause enhanced localised corrosion. For PWR systems the transport and deposition of corrosion products occurs in the primary coolant circuit; which can cause issues with reactor safety and efficiency. The complex conditions within the primary coolant circuit alters corrosion behaviour of structural materials; with the transport and re-deposition of the outer-layer oxide products an ongoing issue.[25-27] Due to the single circuit design in BWR systems the release, transport and deposition of

radionuclides and corrosion products is an issue that can lead an increased radioactivity in deposited species.. Although reactivity of these species is relatively short-lived turbines must be shielded and during maintenance operations radiological protection is needed. **Table 4.5-1** gives an overview of the initial formation of corrosion products in BWR and PWR systems highlighting differences in the sources of corrosion products and the coolant environment.

Table 4.5-1. Data on the sites and sources of corrosion and deposition in typical PWR and BWR systems.

	System	
	BWR	**PWR or PHWR**
Sources	90 % from feedtrain All ferrous alloys – come Cu based alloys 10 % from coolant circuit Mostly from stainless steels	All from the coolant circuit: 4% from stainless steels 96% from SG materials – high nickel alloys
Temperature range	Feedtrain 35 – 190 Coolant 270-280	Coolant 270 – 315
Chemistry	Neutral low conductivity, oxygenated throughout	Alkaline or boric acid/ alkali buffered Hydrogenated, O_2 'free'
Elemental composition	98% Cr, Mn, Ni, Cu, Co – 0.1-0.6	Mainly Fe Ni Cr in order
Chemical	Predominately α-Fe_2O_3 up to 10% Fe_3O_4. If feed water is deoxygenated higher levels of Fe_3O_4 is possible. On stainless steel coolant surfaces spinels have been found to be: Ni-Fe_2O_4 , $NiCr_2O_4$	Predominately Fe_3O_4 spinels on stainless steel surfaces with Ni and Cr substitutions. Higher degrees of Ni substitutions on SG alloys giving $NiFe_2O_4$ as well as non-stoichiometric intermediates of $NiCrO_4$ being reported

The conditions experienced within the reactor coolant loops of LWR reactor systems can be described as harsh, with pressures up to 153 Atm and temperatures reaching 325°C, not to mention the exposure to ionising radiation, including neutron and gamma fluxes.[28] LWR coolant systems utilise water as a coolant and moderator along with the addition of chemicals that attempt to mitigate corrosion and increase neutron moderation, which further complicates the radiation and chemically induced processes within the coolant loop.[10, 29, 30]

Additives in PWR include:

- Lithium hydroxide, for control of pH controls corrosion product transport and can help reduce fuel clad corrosion;
- Hydrogen/ hydrazine (or ammonia), to supress the net radiolysis of water and to alter corrosion product solubility;
- Boric acid used as a burnable poison
- Zinc acetate to help reduce ^{60}Co incorporation to the oxide film enabling it to be removed via ion exchange, and to mitigate the extent of pressurised water SCC.

Chemistry of a BWR system is also enhanced to optimise plant performance and control stress corrosion cracking. Water quality is controlled, and plants utilise advanced chemistry regime that include hydrogen inject, zinc addition, noble metal chemical addition. These advanced chemistries are not utilised by all rector operators and when these are not undertaken, plants are described as operating under normal chemistry conditions (NWC).

4.6 The impact of corrosion on plant operations

Even with these mitigation methods issues still arise due to CRUD; of one of the most problematic is Axial offset Anomaly (AOA) as this affects the power distribution of fuel rods as well increasingly the likelihood of out of core activity. AOA/CIPS (CRUD induced power shifts) occurs via the favourable deposition of corrosion products at the top of the fuel rods caused by their retrograde solubility. This uneven CRUD build-up causes a non-uniform power distribution and affects the heat transfer coefficient of the zircalloy cladding. Corrosion particles may activate via transmutation and successive transportation of species may lead to increased out of core activity.[26, 27, 31] An example of increased activity is the generation of ^{60}Co via the transmutation of ^{58}Ni to ^{59}Co which goes on to capture a further neuron generating ^{60}Co which emits beta and subsequently gamma rays.[32, 33] ^{60}Co has been described as the dominant dose producing isotope in reactor interiors over shorter lifetimes (10 years).[32]

It is important to assess the implications of the corrosion related phenomena on plant operations and energy production. The following section will outline a few examples of how corrosion and CRUD related issues can affect reactor performance and electricity production, focusing on axial offset anomaly and fuel failure.

AOA/CIPS has been an issue with PWR reactors since it was first observed in 1989 at the Callaway plant. AOA incidents have been known to occurred globally, but the frequency is less in European reactors where CRUD levels appear to be lower.[34, 35] AOA presents many operational concerns including; enhanced corrosion, boron hideout and out of core activity increase, these issues lead to reactors operating at reduced capacity.[34-37] As well as the safety and operational concerns, these AOA related issues incur a financial cost, when AOA incidents arise the NNP as to run at reduced output, the extent of which is determined by the NNP licensor. The most extreme example of this is the 1989 incident at Callaway which lead to the rector licensor requiring the reactor to run at 70% of total capacity for about a month.[36, 37]

It is possible to estimate the cost to the operator of running at reduced power by calculating the lost revenue due to power reduction, examples of reduced reactor power due to AOA include 95, 85 and 70% of total power. The estimations given in **Table 4.6-1** are based on the average US cost of generation per Megawatt hours (MWH), assuming a price to consumer equal to the production cost. The operating costs per MWH are not readily available for UKs only current PWR system and the reactors expected to be built in the UK have operating capacities between 1000 and 2000 MWe. The values are calculated for the smallest nuclear reactor in the USA, the R.E. Ginna Nuclear Power plant which has an electricity generating capacity of 582 Megawatts and the largest, a 3,937 MW capacity. These are chosen as future UK systems will have operating capacities that lie between these.

The R.E Ginna plant running at maximum output will generates 13,968 MWH over a 24-hour period and the Palo Verde plant 94,488 MWH. According to Nuclear Energy Institute the average total generating cost for the current reactor fleet in the USA is $33.50/ MWH.[38] Using this figure is used to estimate revenue, over a 24 hour period the Ginna plant running at maximum capacity for 24 hours gives the operating cost of $467,928 per day, this may be taken as the minimum revenue cost of the electricity generated also (assuming no mark up or inclusion of initial plant build cost).[39] The Palo Verde plant running at maximum capacity produces 94,488 MWH, giving a cost/revenue value of $3,165,348. **Table 4.6-1** gives the minimum expected lost revenue for 3 scenarios; a 5%, 15%, and 30% reduction in operating power per day and per month (calculated using a 30-day month). These power reductions also mean less energy is

produced meaning other means must be found to meet consumer energy demands, impacting the energy infrastructure.

Table 4.6-1. Calculated Loss in revenue for R.E. Ginna and Palo Verde reactors at 3 possible power reductions scenarios due to AOA

Reactor type, manufacturer and design capacity	**Operating capacity 24h hours**	**Revenue at 100% operating capacity**	**Reduction in revenue running at**		
			95%	85 %	70%
R.E. Ginna New York **582 MW Westinghouse**	13,968 MWH	$467,928 per day			
Reduction in revenue per day			$23,396	$70,189	$140,378
Reduction in revenue per month			$0.70 million	$2.11 million	$4.21 million
Palo Verde, Arizona **3,937 MW Combustion engineering PWR**	94,488 MWH	$3,165,348 per day			
Reduction in revenue per day			$158,267	$474,802	$949,604
Reduction in revenue per month			$4.75 million	$14.24 million	$28.49 million

These conservative estimations show AOA caused by CRUD/ corrosion related build up may lead to lost revenue running into the millions over relatively short time scales. Another related issue that should be mentioned the failure of fuel rods due to CRUD, corrosion and debris build up this presents both economical and operational concerns. An example of fuel failure due to CRUD induced corrosion is the TMI-1 PWR rector, where 9 rods failed after 121 days at power.[34, 40] **Figure 4.6-1** presents data from the IAEA reporting the rate of fuel failure, a value which is relatively low and varies from country to country, but the average is between 10-5 and 10-4.[34, 41] With Japan having rectors operating mostly defect free over a ten-year period, this was reported in an IAEA report published in 2010 giving information on failure rate and reactor type.[41]

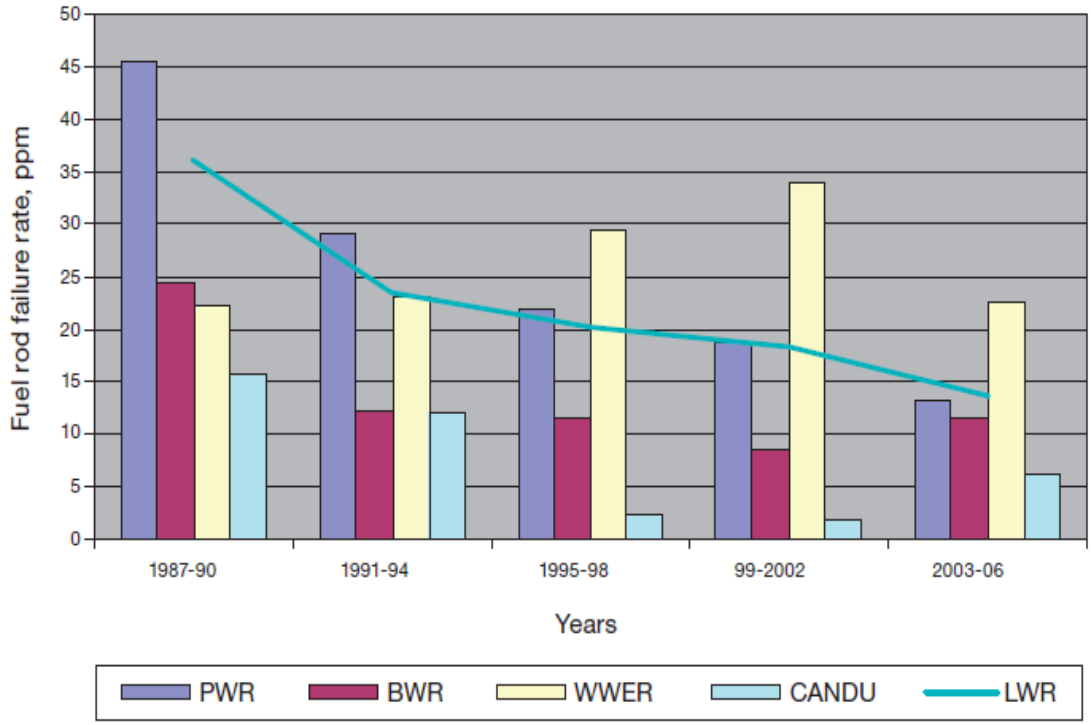

Figure 4.6-1. Graph showing the rate of fuel rod failure by reactor type over time.

The cost of failure runs into several millions per event due fuel replacement and reload and well as the cost of replacing the power cost during plant outage.[34] Unlike the cost implications caused by AOA incidents, fuel failure can require full shut down of the plant during fuel removal and replacement. Industry are striving to aim towards a zero-failure rate, which requires knowledge of these related failure mechanisms and how they may be remedied. An understanding of corrosion related phoneme will contribute the mitigation and resolution of the issues presented here amongst others. With this discussion of the general corrosion mechanisms and the implications that these may have on LWR systems,

specifically PWRS the following sections discuss previous works that have investigated corrosion of nuclear materials under simulated reactor conditions.

4.7 Corrosion under simulated LWR conditions

The literature outlined in this section reviews the understanding of corrosion processes related to those experiences in PWR primary circuits processes; with an interest in the effects of radiation on the corrosion of stainless steel. Due to the harsh nature of the nuclear environment it is very difficult to simulate fully the conditions; studies tend to focus on either emulating PWR temperatures, pressures and coolant chemistry or investigating the role radiation at varying temperatures. Although the focus of the experimental work is on gamma radiation, heavy ion and proton irradiations were considered when equipment and method were developed so the literature was given consideration, and some is included. When investigating the corrosion mechanisms for these systems, high temperature and pressure equipment is utilised (the development of these takes considerable time and resources) with variable monitoring techniques. In-situ monitoring techniques includes electrochemical measurements and monitoring system parameters, such as dissolved ionic species and dissolved gas concentration, as well as water sampling. Specimen can also be examined after the corrosion experiment; with electrochemical measurements, scanning electron and optical microscopy, X-ray diffraction techniques and X-ray photoelectron spectroscopy. A previous review by Parker-Quaife *et al.* probed this release and transport behaviour, summarising a selection of the literature regarding the interactions between corrosion and radiolysis products, along with a brief overview of some of the more prominent literature of ɣ-radiation effects on the corrosion mechanism of nuclear material. This review is presented in **Chapter 4, Section 4.8**.[42]

Summarises by Robertson give an overview of the mechanistic understanding in relation to the corrosion of stainless and mild steels at high temperatures and pressures. During the 1970s and 80s, work by Ishigure *et al.* investigated the effects of radiation of release of corrosion products, and the corrosion specimen exposed to high temperature water.[43, 44] The oxidising species generated during water radiolysis (H_2O_2, •OH and HO_2•) effect corrosion most significantly. Due to the complexity of in-situ studies some studies focus on simulating radiation conditions by adding the molecule radiolysis products such as H_2O_2 which has been shown to be suitable substitute and is a somewhat fascicle mode of investigation. Studies investigating the effects of H_2O_2 on the high temperature corrosion

of stainless steel 304 have been investigated using electrochemical techniques in situ, followed by analysis of the oxide films using various technics including SEM imaging.[45-49] Work undertaken by Wren *et al.* has investigated the effects of ɣ-radiation on corrosion alongside studies into PWR chemistry and radiolysis behaviour,[19, 50-59] Was *et al.* have investigated proton irradiation of nuclear materials under simulated PWR conditions.[60-62] Corbel *et al.* have investigated electrochemical behaviour of stainless steel in PWR primary coolant conditions under proton irradiation.[63-65]

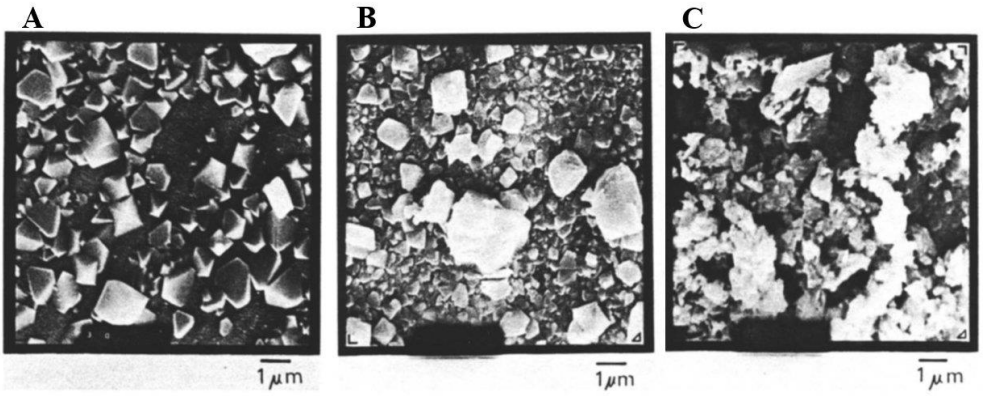

Figure 4.7-1. A) corroded at 250 °C with 20 ppb O_2 for 500 hrs at a flow rate of 20 ml/min without radiation; B) corroded for 1500 hrs at 250 °C with 20 ppb O_2 at a flow rate of 50 ml/min with ɣ-radiation; C) sample corroded under various conditions for 30,000 hrs. Taken from work by Ishigure *et al.*

The studies by Ishigure *et al.* utilised water sampling techniques and SEM imaging to probe the effects on ɣ-radiation on these processes. Coupons of 304 SS were exposed to ɣ-radiation (dose rate of 500 Gy/hr) for up to 1500 hrs at 250 °C with a varied flow rate; the focus was on the release of corrosion products. A recreation of experimental set-up can been seen in **Figure 4.7-2.**[44] Results showing that radiation enhances the release of insoluble iron in these systems, and release rates decrease with ongoing corrosion; SEM imaging were used to show the differences in the corrosion films and shows a difference in surface morphology with and without radiation.[44] The SEM images are reported in **Figure 4.7-1** and shows that the corrosion under irradiation conditions leads to a change in oxide morphology with less uniformity and smaller crystal size. **Figure 4.7-1C** shows an image of a sample exposed to varying high temperature conditions for 30,000 hours and has considerably more corrosion product deposition. This work also proposed a possible route to CRUD formation, that utilises the apparent increase the insoluble iron. The ferrous ion is released during the corrosion process with a low rate when oxygen

concentration is low. The ferrous ion is then oxidised by the radiolysis products and the ferric ion can form ferric hydroxide which goes on to dehydrate producing haematite.

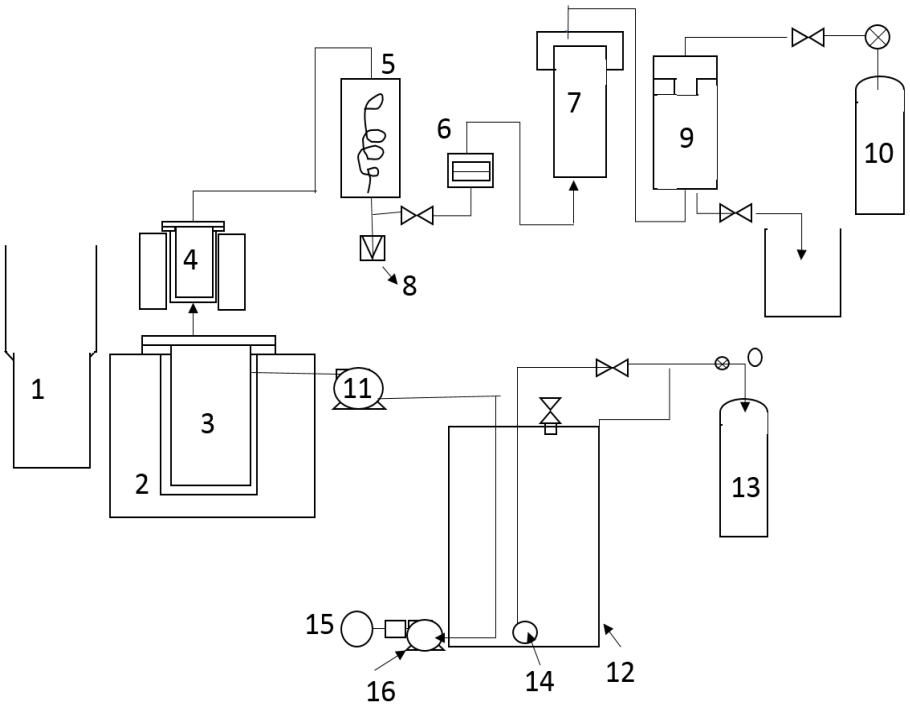

Figure 4.7-2. Reproduction of recirculation loop outline used in work undertaken by Ishigure *et al.*: (1)^{60}Co source, (2) electric furnace, (3) main autoclave, (4) autoclave for surface examining specimens, (5) cooler, (6) filter, (7) ion-exchange resins, (8) safety valve, (9) pressure controller, (10) He gas, (11) plunger pump, (12) reservoir of distilled water, (13) high purity argon gas, (14) butter, (15) O_2 monitor, (16) sensor (17) pump.

Work on the fundamental corrosion processes in SS 316 under simulated primary coolant chemistry is more limited, with minimal studies on the effects of radiation. Studies have focused on the effects of hydrogen, oxygen and surface finish on corrosion.[66-71] Early work by Kim characterised the oxide on 316 SS in 288 ^{o}C water under normal and hydrogen water chemistries cycling between conditions; normal water conditions having 200 ppb oxygen and 20 ppb hydrogen, and hydrogenated conditions 150 ppb hydrogen and 16 ppb oxygen.[66] Electrochemical measurements monitored the corrosion behaviour and TEM with EDS used to analyse the oxide post irradiation. The study showed a duplex structure with an inner chromium rich layer, and an outer layer with large particles, nickel enriched Fe_2O_4-type structure with smaller Fe_2O_3 particles, under hydrogenated conditions these small particles were Cr-enriched Fe_3O_4. Hydrogenated conditions gave a less compact oxide with larger particles when compared to normal conditions. Kim suggests that under normal water conditions, Cr-depletion occurs in the outer layer due

to oxidation of Cr.[66] The suggested oxide film structure and composition was outlined in a schematic which is recreated in **Figure 4.7-3.**

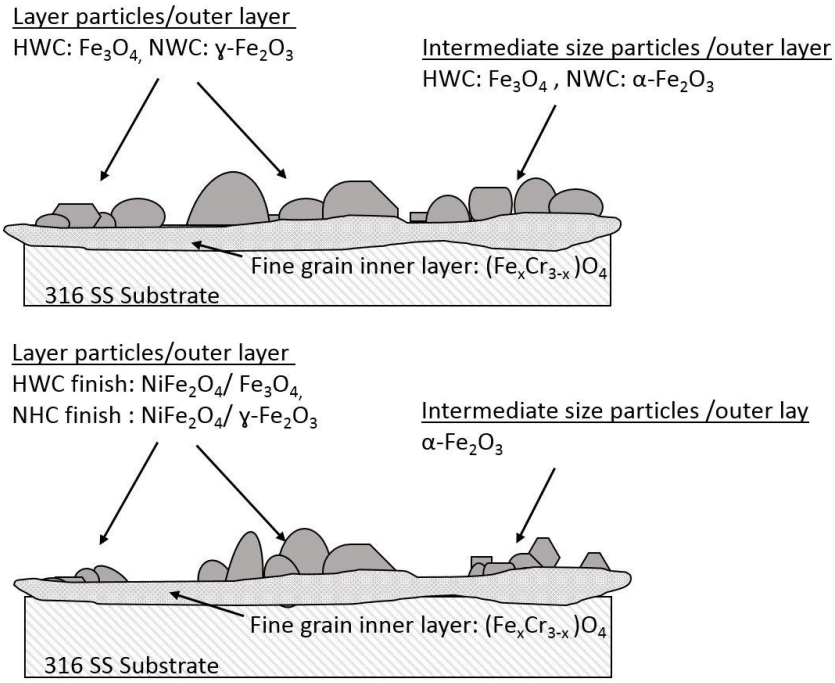

Figure 4.7-3. Schematic of corrosion films formed on SS 316 in only HWC or NWC conditions or in cycling NWC/HWC conditions at 288 °C.

Dong *et al.* studied the effect of dissolved hydrogen on corrosion of 316 nuclear grade at high temperature, varying the hydrogen concentration and characterising the oxide using, SEM, XPS with depth profiling, TEM-EDX for oxide thickness and atomic composition.[67] These systems form a double-layered oxide structure with outer layer Fe-Ni spinel with haematite oxide, and an inner layer of Fe-Cr-Ni spinel oxide with a thin $Cr(OH)_3$ layer on its surface. Increased hydrogen concentration results in the decrease of chromium in the inner layer alongside an increase in iron, this is attributed to the accelerated diffusion of Fe ion in the inner continuous layer by hydrogen.[67] Other work by Han *et al.* have looked at the effects of surface finish and modified composition on the oxidation in high temperature water with added lithium hydroxide and boric acid.[68, 69] These studies characterised the oxide using SEM, STEM-HADAFF with XRD, Raman and XPS (with depth profiling). This work supports the formation of a duplex oxide, with inner layers containing higher chromium and outer layers with iron rich spinels. Electropolishing produced a compact monolayer, suggesting enhanced oxidation resistance.[69] Modifying nickel, silicon and chromium content showed that an increased [Cr] in the alloys promoted the formation of a thin Cr-rich inner oxide layer, and that was

protective in nature hindering further growth.[68] Work by Chen *et al.* characterised the interfacial reactions and oxide films that grow on 316L stainless steel under various simulated PWR conditions, hydrogenated, deaerated and oxygenated. 316L was exposed to water containing LiOH, at 310 °C with a flow rate of 5 L/ hr at pH = 6.99.[70] This study utilised in-situ electrochemistry, SEM imaging, TEM with SEAD diffusion, STEM-HAADF imaging with EDS line scans and Raman spectroscopy. **Figure 4.7-4** shows the SEM images under the different conditions, showing a clear difference in oxide morphology with altered dissolved hydrogen and oxygen concentrations.[70] The oxide films in the deaerated and hydrogenated conditions were similar in composition, with a duplex structure and the inner layer compact and chromium rich. The outer layer spinel oxides had different morphologies dependant on conditions. The hydrogenated conditions lead to a more compact outer layer with smaller spinel structures. Oxygenated conditions lead to an oxide film with haematite outer particles and an inner layer rich in nickel. The outer oxide did not have the straight edges and planar faces seen in the other conditions.[70]

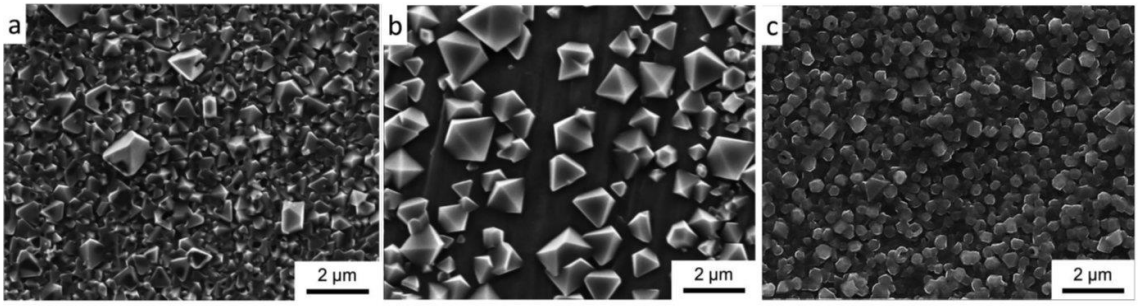

Figure 4.7-4. SEM (secondary electron image) morphologies of the oxide films formed on 316L SS exposed in various simulated PWR primary water environments: (a) hydrogenated, 500 hr, (b) deaerated, 1170 hr, and (c) oxygenated, 1012 hr. Reproduction of images reported by Chen *et al.*

The use of hydrogen peroxide in simulating radiation

As previously outlined, the effects of radiation are often simulated by the addition of hydrogen peroxide (H_2O_2). Studies like this aim to examine the effects of H_2O_2 on oxide composition, morphology, and corrosion behaviour. A few example studies outlined here focus on the effects of H_2O_2 oxidation of 304 SS as work on SS 316 is limited. Examination of the oxide film of stainless steel 304 exposed to H_2O_2, O_2 and H_2 by Kim utilised AES, SEM and TEM showing an increase in overall thickness of the oxide formed under H_2O_2 conditions than that of hydrogenated conditions.[45] The outer oxides varied for exposure conditions with α-Fe_2O_3 (200 ppb O_2), ɣ-Fe_2O_3 (200 ppb H_2O_2) and Fe_3O_4

(150 ppb). With hydrogen peroxide exposure, the chromium content of the inner oxide was less and a higher observed nickel content occurred.[45] SEM imaging shows a distinct difference in oxide appearance, changes in packing density and particle sizes. It is obvious these effects can be seen in the SEM images replicated in **Figure 4.7-5.**[45] The specimen exposed to H_2O_2 have both large crystals and smaller more amorphous oxide deposition, where the oxide appears less uniform than that of the other samples. Electrochemical corrosion potential (ECP) measurements gave a higher value for samples exposed to hydrogen peroxide. Work by Satoh *et al.* investigated the effects of hydrogen peroxide on SS 304 corrosion using a HTHP once through loop, with controlled hydrogen peroxide addition.[46-49] The corrosion was monitored using ECP and impedance measurements with samples exposed to 100 ppb of H_2O_2 or 200 ppb O_2, one following another, or the simultaneous addition. The ECP for samples exposed to H_2O_2 were larger (which follows the work by Kim than those exposed to O_2 only, a sequential exposure to O_2 after H_2O_2 showed a higher ECP value than that of samples only exposed to O_2 which was suggested to be due to the memory effects of the oxide). But the ECP of those exposed to oxygen first are not affected by the pre-exposure.[47] This suggests that exposure to H2O2 promotes corrosion irrespective of previous conditions. The resistance to oxide dissolution and the oxide films electric resistance was also determined in these studies, with smaller values for resistance to dissolution in specimen exposed to H_2O_2.[47, 48] This follows the trend outlined by Ishigure *et al.* that suggests the dissolution rate is higher in radiation conditions.

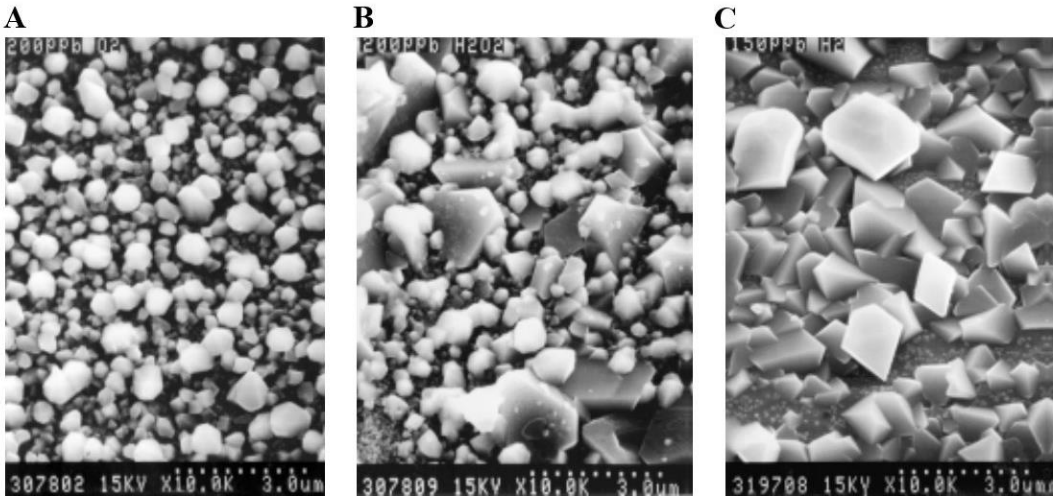

Figure 4.7-5. Two-week exposure to different water chemistries at 288 °C A) 200 ppb O_2; B) 200 ppb H_2O_2; C) 150 ppb H_2. Replication of images reported by Kim *et al.*

Comprehensive work by Wren *et al.* has progressed from investigating the effects of radiolysis products (such as hydrogen peroxide), temperature and pH on corrosion of nuclear materials, to investigating the effects of ɣ-radiation on corrosion with in-situ monitoring alongside post oxidation analysis.[50-59] The aim of these ongoing works is to get a kinetic and mechanistic understanding of the corrosion processes and incorporating this into a mechanistic model for the prediction of oxide growth and dissolution.[59] Mechanistic detail has been gained via a well-defined experimental and theoretical program first investigating simpler carbon steels,[19, 52-54, 58]followed by stainless steel alloys,[55] and the most recent work probing nickel and cobalt alloys.[51, 56, 57] These corrosion mechanisms were probed using electrochemical techniques (including cyclic voltammetry and impedance spectroscopy), SEM as well as surface techniques including Raman and X-ray Photoelectron Spectroscopy (XPS). The effects of ɣ-radiation versus H_2O_2 on the corrosion of carbon steel were investigated taking a stepwise approach, adding experimental complexity with each experiment. Firstly, a kinetic study of H_2O_2 with a potentiostaticly grown oxide film was undertaken, and then followed by the role of temperature and pH on the corrosion mechanism. Once the basic mechanism was outlined, investigations that probed the role ɣ-radiation at ambient and elevated temperatures under neutral and basic conditions were undertaken. Electrochemical studies under basic conditions (pH 10.6) gave mechanistic detail of the corrosion process, suggesting 3 distinctive potential regions for the oxide film formation and conversion, varying mechanisms between charge transfer, electron transfer and cation vacancy movement.[19, 58] The proposed mechanism was finalised in a 2009 paper, with the three keys regions being defined: Region I has a potential of -0.8V < E< -0.6V; where Fe^{I} and $Fe^{II/III}$ oxides are stable and a magnetite (Fe_3O_4) layer forms. Region II is from -0.5 v < E < -0.2V, an increase in potential and magnetite can oxidise and produce a γ-Fe_2O_3 oxide. Region III is from -0.1V < E< 0.4 V the most stable oxide in this region was γ-FeOOH over Fe_3O_4.[19] The corrosion process for the carbon steels oxidised in pH 10.6 solutions is outlined in **Figure 4.7-6** showing the proposed regions and the theorised routes to oxidation.

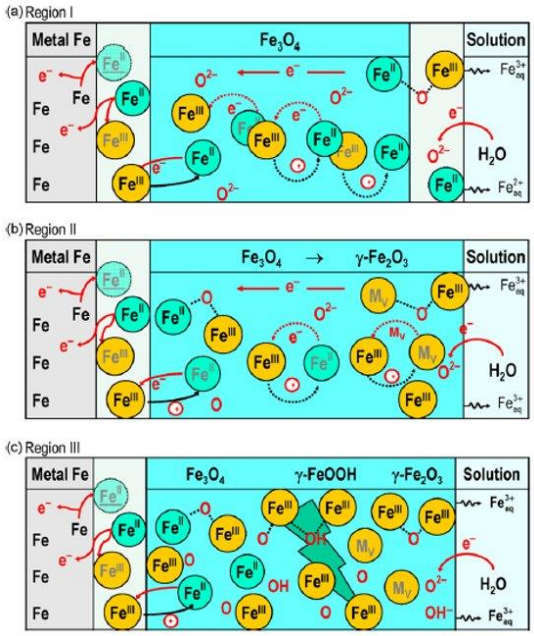

Figure 4.7-6. Diagram taken from Wren to show the corrosion mechanisms of mild steels at pH 10.6, showing the different potential regions in experienced and the mechanisms of corrosion at each outlined potential.

AES, XPS spectroscopy and SEM microscopy confirmed that oxidation under basic conditions leads to the formation of a dual layered oxide comprised of an inner layer of Fe_3O_4 and outer layer of Fe^{III} oxide/hydroxide.[19, 58] Wren *et al.* concluded from these results that the corrosion rates are likely to depend on thermodynamic contributions such as any aqueous redox species and system pH; oxidation processes of $Fe^{II/III}$ and Fe^{III} oxides are kinetically facile as oxidation potentials are close to the equilibrium potentials of the system. When considering the kinetics of H_2O_2 with the oxide an addition of 1mM H_2O_2 solution leads to the degradation of the outer oxide layer and thickening of the inner Fe_3O_4 layer, which was confirmed using Raman spectroscopy.[58] The potential regions defined these in works allows for the prediction of oxide type at specific corrosion potentials, and enables the growth of specific oxide using electrochemical techniques. These were utilised when the effects of ɣ-radiation of corrosion of carbon steel was probed.[53] The effects of temperature on these systems was investigated and the study suggested that the thermal processes such as precipitation and dissolution are affected along with thermal transformation, and oxidation at the oxide/water interface, which continues to be driven by the applied potential.[54]

Studies by Wren *et al.* investigating effects of ɣ-radiation on corrosion

The effects of ɣ-radiation on corrosion was monitored using open circuit, impedance and linear polarisation measurements; and these techniques were used to determine Ecorr and R_P values for ɣ-irradiated carbon steel. The values from ɣ-irradiations were compared to the values determine from the addition of 1 mM H_2O_2.[53, 58] Oxide films were pre-grown electrochemically (using the potential regions defined in the 2007/20009 work) and exposed to ɣ-radiation to varying total doses with a dose rate of ~6.8 $kGyh^{-1}$ (using a Gammacell 220 Excel Cobalt –60 irradiator); or H_2O_2 solutions. The potentials regions used to grow the film were as follows:

- -0.7 V for a Fe_3O_4 film,
- -0.2 V to give a Fe_3O_4/ ɣ-Fe_2O_3 mixed film
- 0.2 V gives mixture of all three a Fe_3O_4/ ɣ-Fe_2O_3 and ɣ- FeOOH.

In the irradiated systems, the electrolyte solutions were periodically tested to determine the concentration of H_2O_2, it was reported after 0.5 hr the $[H_2O_2] = 10^{-6}$ M, and at 6 hr $[H_2O_2] = 10^{-4}$ M. The steady state value for H_2O_2 was not reached due pH value being 10.6 which remained constant over the testing period. Under the presence of ɣ-radiation E_{corr} initially decreases rapidly and recovered to reach steady state in the 6-hr irradiation period. The films grown at -0.7 V needed longer irradiations before steady state E_{corr} was reached which gives some information of the stability of this oxide.[53] This study concluded that radiation conditions could be simulated in solutions by the use of H_2O_2, if compared with samples in representative concentrations of H_2O_2. It was shown that the E_{corr} and system resistance were dependent on the $[H_2O_2]$ but there was no correlation to the initial oxide film composition. Wren *et al.* concluded that from this study it may be possible to predict the corrosion rate of a steel in γ- radiation environments at pH 10.6.[53] Next in-situ corrosion tests were attempted in a static system held at 150 °C during experimental periods, this autoclave system was irradiated using a MDS Nordio Gammacell 220 Excel Cobalt-60 irradiator. Coupons of mild steel were prepared and sealed in quartz vials with neutral water or water/ LiOH solutions of pH 10.6, the addition of LiOH adjusted the pH, preparation was in an argon purged glove box to minimise pre-irradiation corrosion. These samples were irradiated with a dose rate of 6.2 kGy/hr at 150 °C for 20 or 60 hours. Once oxidised the surface oxides were examined using SEM and Raman spectroscopy, there was a clear difference in the surfaces at the different pHs, this can be shown in **Figure 4.7-7**.[55] Oxide grown at the neutral pH which shows

formation of small crystallites, it's suggested that this is typical of magnetite crystals. With the longer irradiation time the oxide surface becomes smoother there is also the presence of nano-particles covering the oxide surface that are present at both irradiation times. The oxide that is formed at the higher, more basic pH is smooth and featureless at both irradiation periods, but the nano-particles observed at the lower pH are not present. Both samples become featureless and smooth over a longer radiation exposure time their cross sections are very different, at lower pH they are more porous and less uniform. The difference in porosity and uniformity could be attributed to the change in solubility of iron at different pHs, and how this affect the rate of reaction for the oxide formation.[55] The paper also indicates that the γ-radiation experienced by the system alters the corrosion process, increasing E_{corr} and this dictates the oxide phase that forms. The paper suggests that from the SEM and the Raman data that at pH 10.6 the ionizing radiation causes a passive film formation that is a mixed oxide, containing both Fe_3O_4 and γ-Fe_2O_3. It goes on to suggest that in fact at these conditions water radiolysis may even limit carbon steel corrosion.

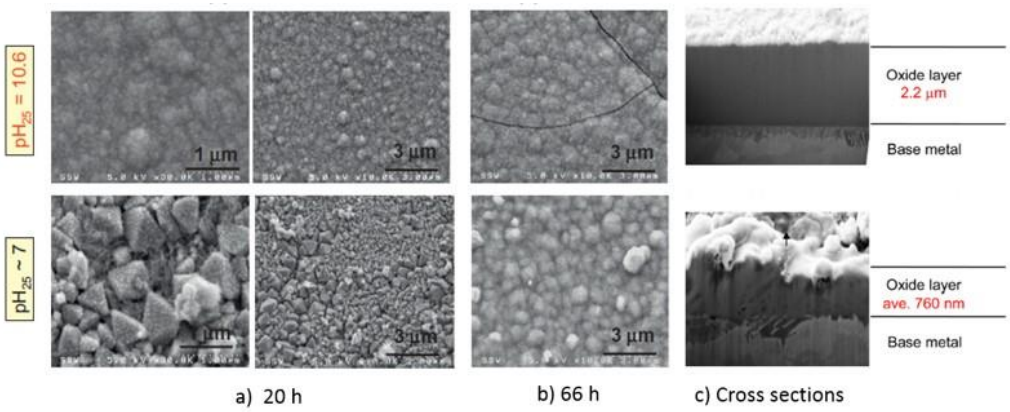

Figure 4.7-7. SEM images of the coupon surfaces a) 20 h and b) 66 h exposure to γ-radiation at 150 °C and pH 25 °C pH 10.6 (top) pH 7 (bottom) c) SEM images of the oxide cross section, pH 10.6 top and pH 7 bottom. Images taken from Wren *et al.* 2012 paper

Mild steel components are increasingly replaced by stainless steel 316 or 304 in nuclear reactor systems, so Wren *et al.* have also investigated the influence of γ- radiation 316 L corrosion. The study was implemented at room temperature in a borate buffer solution at pH 10.6 (due to the low solubility at this pH), adjusted using boric acid or sodium hydroxide. An electrochemical cell was placed inside a ^{60}Co source and cyclic voltammetry was carried out as a function of potential along with periodic

electrochemical impedance tests, the typical test lasted for 48 hours. After potentiostatic polarization measurements were complete the working electrodes were analysed using XPS, and/or SEM. Wren *et al.* produced a similar mechanistic schematic as in their previous work, identifying key electrochemical potential regions in the growth of the multi-layer oxide. This schematic (as seen in **Figure 4.7-8)** summarises the potential oxides that form in the SS 316L system, at which potential these would occur. There are 4 distinct electrochemical potential regions; with several oxidation reactions available in each region. Wren summarises the paper with a description of these regions and which is the most likely when the system is free from ionizing radiation or under its influence. Region Ox I (<-0.5V $_{SCE}$) Cr_2O_3 is converted to chromite ($FeCr_2O_4$) and an outer layer of magnetite may occur. The second oxidation region Ox II (-0.5V_{SCE} – 0 V_{SCE}) oxidation of magnetite can occur and form γ-Fe_2O_3 with oxidation of hydrate Fe^{II} species to γ-FeOOH. The reactions occurring in the same potential regions lead to competition, which affects oxide film type and subsequently its behaviour. The following two regions are at potentials above 0 V_{SCE} and are responsible for the oxidation reactions that produced a porous γ-FeOOH, then the exposed metal is oxidised. Oxide that grows at high potentials such as this are due to film fracture and repair. Chromite can form at these high potentials due to the exposure of the metal surface. The proposed mechanism for growth is shown in **Figure 4.7-8a** and the associated potential regions outlined, (the changes in ECP exhibited during the irradiations). It is valid to conclude that the mechanism of corrosion is different when the system is exposed to ɣ-radiation. The work carried out by Wren *et al.* is very comprehensive, but in-situ work is limited static corrosion studies om carbon steel at 150 °C, so there is more work to be undertaken here. Studies should be made at higher temperatures and under flowing conditions, and eventually with water chemistry equivalent to that of a PWR system.

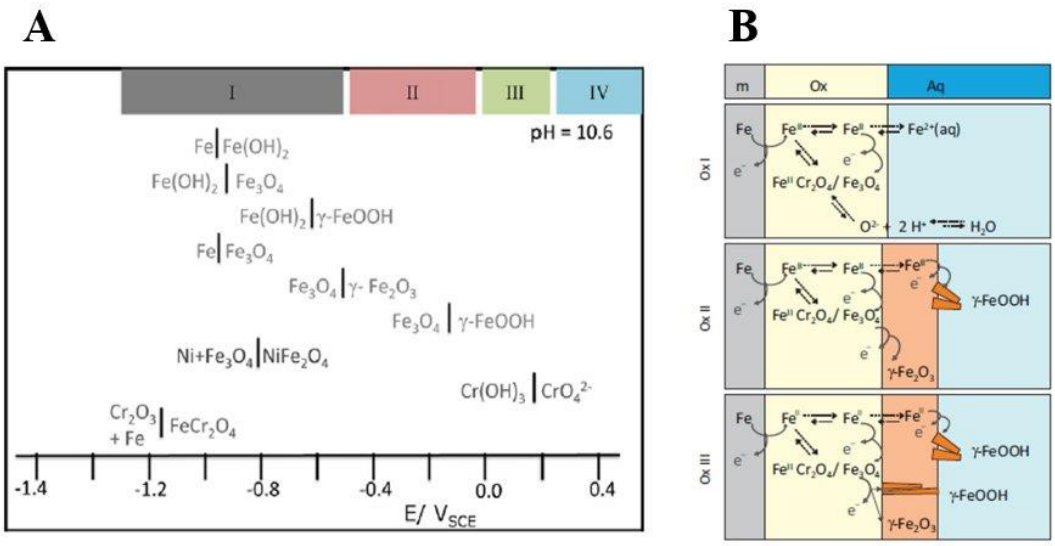

Figure 4.7-8. A) Potential profile for redox reactions in stainless steel reactions showing redox couples present in these systems and at which potential the redox reactions occur; B) Diagram to show the potential mechanisms of corrosion in a stainless-steel system and the different potentials the system cycles through. Take from Wren *et al.* 2012.

The study of both heavy ion and ɣ-radiation is not currently possible so the studies are undertaken separately. The effects of neutron damage on corrosion are simulated using heavy ions or protons in accelerator studies. Although this work does not investigate the effects of heavy ion irradiation, prominent literature is included as it helped to inform the design of the equipment during this project, and the effects of radiolysis on corrosion in these systems can give a comparative basis for ɣ-studies.

Accelerator studies

Accelerator studies reported here aim to give a brief overview of work with focus on the experimental set up. Early work by Lister *et al.* utilised a closed loop system to investigate the effects of proton irradiation on corrosion. A corrosion cell was placed down flow from an irradiated section and so the effects of radiolysed water with the material was investigated rather than any material damage, the experimental water recirculation systems are duplicated in **Figure 4.7-9**.[72] Other work used weight loss measurements to observe in-beam corrosion behaviour, as well as corrosion rate calculation of samples in beam.[73, 74] The aim of these experiments was to investigate the effects of water chemistry on corrosion mitigation. Two recirculation loops were designed one with pH and hydrogen water chemistry (HWC) control out for 304 SS, and a second using copper and steal components with no HWC control. Corrosion probes (316 L, alloy 718, Al alloys, Cu, Ta and W) were downstream from the beam, and corrosion rates were reported in respect to immersion time and appeared related to proton flux and beam current, samples in the loop without HWC having higher corrosion rates. The work concluded that corrosion of samples downstream of the proton beam may be mitigated with controlled water purity and hydrogen concentration.[74]

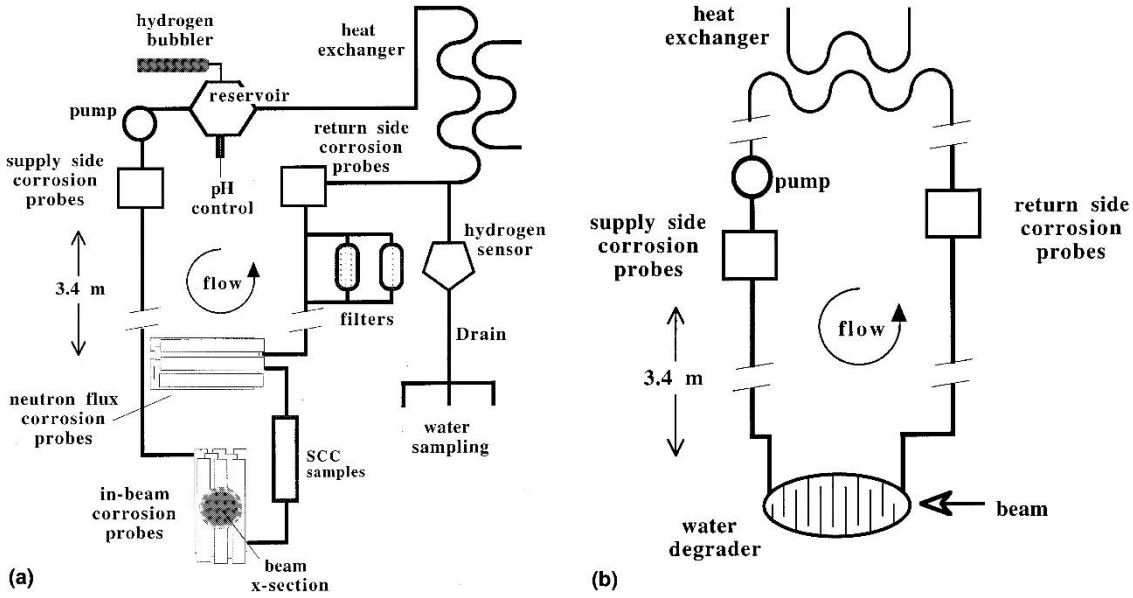

Figure 4.7-9. Duplication of the recirculation loops used in the experiments by Lillard *et al.* A) System with HWC water is exposed to the beam then circulated to the out of core probes, B) Copper and steel loop with no HWC, water is irradiated and then based through to the rest of the loop.

Studies led by Corbel build on the earlier works utilising a CERI cyclotron accelerator to investigate the effects of proton beam radiolysis on corrosion of iron, and of stainless steel 316. Techniques used were a combination of in-situ electrochemical techniques and post irradiation SEM imaging.[63-65] These studies use a static system, at HTHP the corrosion sample is used as the irradiation cell window, so proton flux is passed directly through it. The cells internal volume is 30 mL, and deaerated water containing lithium and boron was used and temperature was raised to 300 °C. A platinum reference electrode allowed for electrochemical response to be monitored throughout the exposure to 22 MeV protons (with around 6 MeV emerging at the metal/water interface).[64, 65] The experimental setup is duplicated in **Figure 4.7-10.** First, only the effect of proton irradiation was investigated with no hydrogen addition and it showed that there is an increased effected on potential with increased flux. After increased time period at 300 °C, or after several irradiations, this response lessened which was described as an ageing effect.[64] Further work using the equipment designed looked at the effects of temperature and hydrogen on the electrochemical response. This work concluded that there is an increase in potential associated with irradiation along with increased temperature ≤ 200 °C but plateaus at temperatures between 200-300 °C. Increased hydrogen concentration reduced the oxidative potential response. Sequential irradiations and exposures has an effect on electrochemical response, decreasing it without irradiation and under irradiation the oxidative response is also lessened.[65]

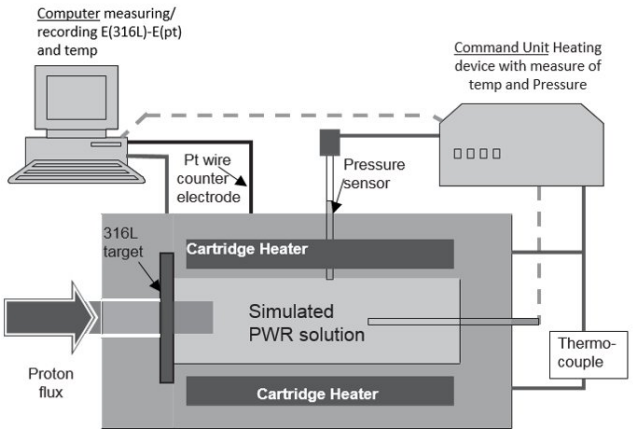

Figure 4.7-10. Replication of the high temperature and pressure cell used by Corbel *et al.* to investigate the effects of proton irradiation on SS 316 corrosion under simulated PWR chemistry.

Was *et al.* have developed a facility to observe the effects of proton irradiation on corrosion under PWR flowing conditions. Current studies have looked at the corrosion of stainless steel 316L at 320 °C under hydrogenated conditions at a flow of 15 ml/ minute.[60, 61] The SS 316 coupon made up the chamber window and a proton beam up to 3.2 MeV was passed through it. The studies have varied the time of exposure, and observed oxide changes post irradiation using SEM, TEM, XRD and Raman. Characterisation of the oxides showing that oxides exposed to proton radiation were thinner and more porous, and depleted in chromium.[60, 61] Further work has utilised pre-oxidised samples that go on to be exposed to proton irradiation in an attempt to observe which effects are radiolytically driven. The previous work was built upon with characterisation undertaken using the previously stated techniques, and mechanistic detail is determined by using data on corrosion potentials and redox reactions.[62] The examination of irradiated, unirradiated and flow regions showed a difference in oxide, with irradiated samples and samples in flow regions showing haematite in the outer oxide and chromium loss in the inner oxides. The presence of haematite in the flow and irradiated suggested that the changes in oxide are due to radiolysis products, and at that those with a long lifetime, so it as concluded that H_2O_2 generated in water radiolysis is likely to be cause of this.[62]

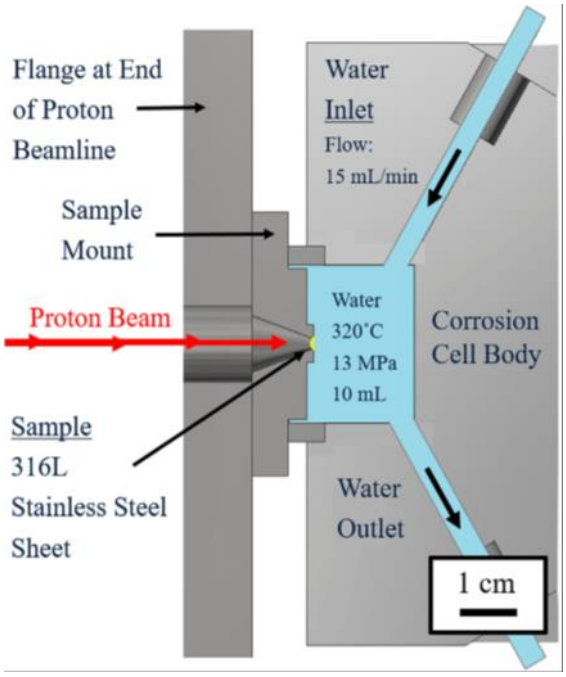

Figure 4.7-11. Schematic of the irradiation cell designed and commission by Was *et al.* used in the investigation of the effects of proton irradiation on stainless steel 316.

The literature outlined in this chapter has attempted to summarise the most prominent experimental research of the effects of radiation on corrosion and the related processes. It has outlined the scientific contributions to the current understanding of corrosion, radiation and radiolysis behaviour related to the work undertaken during the research project reported in this body of work. This research has informed the design and deployment of an a HTHP facility that is able to contribute to this field; with the ability to oxidise samples in-situ under exposure to either heavy ion or ɣ-irradiation.

The literature reviewed has shown the complexity of these studies in respect to time scale, man power, logistics and cost. The possibility to model these systems would be beneficial with data collected and advances in fundamental understanding from experimental work will contribute to the development of encompassing models. Work into modelling the corrosion[59, 62, 75] and CRUD behaviour[25, 76, 77] has been undertaken and many models exist to predict radiolysis behaviour.[78-81] The complexity of simulating PWR systems both experimentally and by modelling, means further research and understanding is required.

References

1. W. D. C. Jr, *Materials Science and Egnineering an Introduction*, John Wile & Sons, Inc. , USA, 6 edn., 2003.
2. A. M. B. C. M. A. Brett, *Electroanalysis*, Oxford University Press, New Yprl, 1 edn., 2008.
3. R. G. Compton and G. H. W. Sanders, *Electrode potentails* Oxford Univeristy Press Oxford, 1995.
4. D. C. Harris, *Quantitative Chemical Analysis*, W. H. Freeman, 2010.
5. W. M. Clark and B. Cohen, *Public Health Reports (1896-1970)*, 1923, 666-683.
6. M. Pourbaix, *Atlas of electrochemical equilibria in aqueous solutions*, National Association of Corrosion Engineers, Houston, Texas, 1974.
7. G. K. Schweitzer and L. L. Pesterfield, *The Aqueous Chemistry of the Elements*, Oxford University Press, 2010.
8. S. Moreau, M. Fenart and J. P. Renault, *Corrosion Science*, 2014, **83**, 255-260.
9. F. Cattant, D. Crusset and D. Féron, *Materials Today*, 2008, **11**, 32-37.
10. G. C. W. Comley, *Progress in Nuclear Energy*, 1985, **16**, 41-72.
11. Special-Metals, *Journal*, 2002.
12. Special-Metals, *Journal*, 2002.
13. P. Cohen, A. Research, T. C. o. Water and S. i. T. P. Systems, *The ASME Handbook on Water Technology for Thermal Power Systems*, American Society of Mechanical Engineers, 1989.
14. J. Robertson, *Corrosion Science*, 1991, **32**, 443-465.
15. J. Robertson, *Corrosion Science*, 1989, **29**, 1275-1291.
16. R. E. B. N.B. Pilling, *Journal of the Institute of Metals*, The Institute of Metals 1923.
17. N. C. L. Tomlinson, *Corrosion Science*, 1989, 939.

18. P. Rudling, R. Adamson, A. Strasser, B. Cox, F. Garzarolli and S. Odar, Biboa 2014.
19. W. Xu, K. Daub, X. Zhang, J. J. Noel, D. W. Shoesmith and J. C. Wren, *Electrochimica Acta*, 2009, **54**, 5727-5738.
20. M. F. Toney, A. J. Davenport, L. J. Oblonsky, M. P. Ryan and C. M. Vitus, *Physical Review Letters*, 1997, **79**, 4282-4285.
21. J. F. A. Hugot- Le Goff, N Boucherit, S. Joiret, J. Wilinski *Journal of Electrochemistry Society* 1990, **137**, 2684.
22. T. Laitinen, M. Bojinov, I. Betova, K. Maekelae and T. Saario, *The properties and transport phenomena in oxide films on iron, nickel, chromium and their alloys in aqueous environments*, Report STUK-YTO-TR--150, Radiation and Nuclear Safety Authority, Finland, (1999).
23. *The properties of and transport phenomena of oxide films on iron, nickel, chromium and their alloys in aqueous environmets* STUK Helsinki 1999.
24. J.-J. Park, S.-I. Pyun and S.-B. Lee, *Electrochimica Acta*, 2004, **49**, 281-292.
25. C. B. Lee, Doctor of Philosophy, Massachusetts Intitute of Technology, 1990.
26. D. H. Lister, in *Nuclear Corrosion Science and Engineering*, Woodhead Publishing, 2012, DOI: https://doi.org/10.1533/9780857095343.1.57, pp. 57-74.
27. S. Oder, Bilboa, Spain, 2014.
28. M. Le Calvar and I. De Curières, in *Nuclear Corrosion Science and Engineering*, Woodhead Publishing, 2012, DOI: https://doi.org/10.1533/9780857095343.5.473, pp. 473-547.
29. K. D. Kok, *Nuclear Engineering Handbook*, CRC Press, 2009.
30. J. R. Lamarsh, *Introduction to nuclear engineering*, Addison-Wesley Pub. Co., 1975.
31. N. Cinosi, I. Haq, M. Bluck and S. P. Walker, *Nuclear Engineering and Design*, 2011, **241**, 792-798.
32. J. Evans, E. Lepel, R. Sanders, C. Wilkerson, W. Silker, C. Thomas, K. Abel and D. Robertson, *Long-lived activation products in reactor materials*, Pacific Northwest Lab., Richland, WA (USA), 1984.
33. H. Provens, *Journal*, 2008.
34. I. A. E. AGENCY, *Water Chemistry and Clad Corrosion/Deposition Including Fuel Failures*, INTERNATIONAL ATOMIC ENERGY AGENCY, Vienna, 2013.
35. A. Strasser, H. Schroeder and K. Sheppard, *Electric Power Research Institute (EPRI): Palo Alto, CA*, 1996.
36. P. L. Frattini, J. Blok, S. Chauffriat, J. Sawicki and J. Riddle, *Nuclear Energy*, 2001, **40**, 123-135.
37. U.S.NRC, Information Notice No. 97-85: Effects of Crud Buildup and Boron Deposition on Power Distribution and Shutdown Margin, https://www.nrc.gov/reading-rm/doc-collections/gen-comm/info-notices/1997/in97085.html, (accessed 3.1.19, 2019).
38. N. E. I. Inc., *Nuclear Costs In Context*, Nuclear Energy Institute Inc., https://www.nei.org/CorporateSite/media/filefolder/resources/reports-and-briefs/nuclear-costs-context-201810.pdf, 2018.
39. U. S. E. I. Administration, How much electricity does a nuclear power plant generate?, https://www.eia.gov/tools/faqs/faq.php?id=104&t=3, (accessed 1.3.2019, 2019).

40. R. Tropasso, J. Willse and B. Cheng, presented in part at the International meeting, LWR fuel performance, Orlando, FL, 2004.
41. I. A. E. AGENCY, *Review of Fuel Failures in Water Cooled Reactors*, INTERNATIONAL ATOMIC ENERGY AGENCY, Vienna, 2010.
42. E. Parker-Quaife, F. Scenini, Andrew Banks, Andrew Powell, Lara-Jane Pegg and S. M. Pimblott, presented in part at the Nuclear Plant Chemistry International Confernece Brighton 2016.
43. K. Ishigure, H. Iksie, K. Oshmia, N. Fujita and S. Ono, *Radiation Physics and Chemistry*, 1983, **21**, 281-287.
44. M. Kawaguchi, K. Ishigure, N. Fujita and K. Oshima, *Radiation Physics and Chemistry (1977)*, 1981, **18**, 733-740.
45. Y.-J. Kim, *CORROSION*, 1999, **55**, 81-88.
46. T. Satoh, S. Uchida, J.-i. Sugama, N. Yamashiro, T. Hirose, Y. Morishima, Y. Satoh and K. Iinuma, *Journal of Nuclear Science and Technology*, 2004, **41**, 610-618.
47. J. Sugama, S. Uchida, N. Yamashiro, Y. Morishima, T. Hirose, T. Miyazawa, T. Satoh, Y. Satoh, K. Iinuma, Y. Wada and M. Tachibana, *Journal of Nuclear Science and Technology*, 2004, **41**, 880-889.
48. S. Uchida, T. Satoh, J. Sugama, N. Yamashiro, Y. Morishima, T. Hirose, T. Miyazawa, Y. Satoh, K. Iinuma, Y. Wada and M. Tachibana, *Journal of Nuclear Science and Technology*, 2005, **42**, 66-74.
49. T. Miyazawa, T. Terachi, S. Uchida, T. Satoh, T. Tsukada, Y. Satoh, Y. Wada and H. Hosokawa, *Journal of Nuclear Science and Technology*, 2006, **43**, 884-895.
50. M. Behazin, M. C. Biesinger, J. J. Noël and J. C. Wren, *Corrosion Science*, 2012, **63**, 40-50.
51. M. Behazin, J. J. Noël and J. C. Wren, *Electrochimica Acta*, 2014, **134**, 399-410.
52. K. Daub, X. Zhang, J. J. Noël and J. C. Wren, *Corrosion Science*, 2011, **53**, 11-16.
53. K. Daub, X. Zhang, J. J. Noël and J. C. Wren, *Electrochimica Acta*, 2010, **55**, 2767-2776.
54. K. Daub, X. Zhang, L. Wang, Z. Qin, J. J. Noël and J. C. Wren, *Electrochimica Acta*, 2011, **56**, 6661-6672.
55. Q. W. Knapp and J. C. Wren, *Electrochimica Acta*, 2012, **80**, 90-99.
56. A. Y. Musa, M. Behazin and J. C. Wren, *Electrochimica Acta*, 2015, **162**, 185-197.
57. A. Y. Musa and J. C. Wren, *Corrosion Science*, 2016, **109**, 1-12.
58. X. Zhang, W. Xu, D. W. Shoesmith and J. C. Wren, *Corrosion Science*, 2007, **49**, 4553-4567.
59. M. Momeni and J. C. Wren, *Faraday Discussions*, 2015, **180**, 113-135.
60. S. S. Raiman and G. S. Was, *Journal of Nuclear Materials*, 2017, **493**, 207-218.
61. S. S. Raiman, A. Flick, O. Toader, P. Wang, N. A. Samad, Z. Jiao and G. S. Was, *Journal of Nuclear Materials*, 2014, **451**, 40-47.
62. S. S. Raiman, D. M. Bartels and G. S. Was, *Journal of Nuclear Materials*, 2017, **493**, 40-52.
63. S. Lapuerta, N. Moncoffre, N. Millard-Pinard, E. Mendes, C. Corbel and D. Crusset, *Nuclear Instruments and Methods in Physics Research Section B: Beam Interactions with Materials and Atoms*, 2005, **240**, 288-292.

64. B. Muzeau, S. Perrin, C. Corbel, D. Simon and D. Feron, *Journal of Nuclear Materials*, 2011, **419**, 241-247.
65. M. Wang, S. Perrin, C. Corbel and D. Féron, *Journal of Electroanalytical Chemistry*, 2015, **737**, 141-149.
66. Y.-J. Kim, *CORROSION*, 1995, **51**, 849-860.
67. L. Dong, Q. Peng, Z. Zhang, T. Shoji, E.-H. Han, W. Ke and L. Wang, *Nuclear Engineering and Design*, 2015, **295**, 403-414.
68. G. Han, Z. Lu, X. Ru, J. Chen, J. Zhang and T. Shoji, *Corrosion Science*, 2016, **106**, 157-171.
69. G. Han, Z. Lu, X. Ru, J. Chen, Q. Xiao and Y. Tian, *Journal of Nuclear Materials*, 2015, **467**, 194-204.
70. J. Chen, Q. Xiao, Z. Lu, X. Ru, H. Peng, Q. Xiong and H. Li, *Journal of Nuclear Materials*, 2017, **489**, 137-149.
71. Z. Duan, F. Arjmand, L. Zhang and H. Abe, *Journal of Nuclear Science and Technology*, 2016, **53**, 1435-1446.
72. D. P. Butt, G. S. Kanner and R. S. Lillard, *Corrosion of target and structural materials in water irradiated by an 800 MeV proton beam*, Los Alamos National Lab., NM (United States), 1996.
73. D. K. Ford, 1996.
74. R. S. Lillard, D. L. Pile and D. P. Butt, *Journal of Nuclear Materials*, 2000, **278**, 277-289.
75. M. Urquidi-Macdonald, J. Pitt and D. D. Macdonald, *Journal of Nuclear Materials*, 2007, **362**, 1-13.
76. B. W.A, presented in part at the International Conference of Nuclear Engineering Xi'an China

2010.
77. J. Kysela, V. Švarc, K. Androva and M. Růžičková, *Crud Deposition on Fuel in VVER Reactors*, 2011.
78. M. Sterniczuk, P. A. Yakabuskie, J. C. Wren, J. A. Jacob and D. M. Bartels, *Radiation Physics and Chemistry*, 2016, **121**, 35-42.
79. A. Elliot and D. Bartels, *The reaction set, rate constants and g-values for the simulation of the radiolysis of light water over the range 20 deg to 350 deg C based on information available in 2008*, Atomic Energy of Canada Limited, 2009.
80. P. Clifford, N. J. B. Green, M. J. Pilling, S. M. Pimblott and W. G. Burns, *International Journal of Radiation Applications and Instrumentation. Part C. Radiation Physics and Chemistry*, 1987, **30**, 125-132.
81. J. M. Joseph, B. Seon Choi, P. Yakabuskie and J. Clara Wren, *Radiation Physics and Chemistry*, 2008, **77**, 1009-1020.

4.8 The interactions of corrosion and radiolysis products

This chapter outlines the literature used to inform the development of an interactions study, probing the interactions between corrosion and radiolysis products. This review paper was presented at the NPC conference (Brighton 2016) giving a brief overview of the effects of radiation on nuclear materials, and then the approaches used to investigate the interactions between corrosion products with species generated during water radiolysis.

Interactions of Corrosion Products with Radiolytic Species in PWR Primary Coolant

Paper Number 90

Elizabeth Parker-Quaife[1,2], Fabio Scenini[3], Andrew Banks[4], Andrew Powell[4], Lara-Jane Pegg[4] and Simon M. Pimblott[1,2]

[1] Dalton Cumbrian Facility, The University of Manchester, Moor Row, Cumbria, UK
[2] School of Chemistry, The University of Manchester, Manchester, UK
[3] School of Materials, The University of Manchester, Manchester, UK
[4] Rolls-Royce plc, UK

Abstract

Resolving the issues of material degradation is a major challenge in the continued safe and efficient operation of nuclear power plants. One major challenge is the corrosion and dissolution of structural materials leading to the deposition and build-up of corrosion products (CRUD). Issues arising from CRUD include increased out of core radiation fields, axial offset anomaly and reduced reactor performance. Clearly, understanding and mitigating corrosion related phenomena in nuclear environments is crucial to the best-practice management of water-cooled reactors.

This study is part of an ongoing investigation into the effects of corrosion products on the radiation induced chemistry of simulated PWR coolant systems. It aims to understand how redox processes within the primary circuit of a water-cooled reactor are affected by the operating nuclear environment by determining the relationship between corrosion mechanisms and the aqueous system in simulated PWR operating condition.

Initial experiments have focused on aqueous slurries containing corrosion product simulants irradiated using a self-shielded ^{60}Co gamma source. Concentrations of hydrogen peroxide and dissolved metal ions (released from the particulate oxides) are determined; [H_2O_2] is measured using the Ghormley tri-iodide method and the dissolved ion concentration via ICP-MS. The effects of total applied dose, dose rate, oxygen presence, as well as pre-irradiation sample treatment have been investigated. The data obtain from the irradiated samples are compared to control experiments containing known quantities of aqueous hydrogen peroxide (relating to [H_2O_2] predicted in water radiolysis) in an attempt understand the observed behaviour.

Acknowledgements

This study is supported by the Dalton Cumbrian Facility project, a joint initiative of The University of Manchester and the Nuclear Decommissioning Authority. EPQ is supported by the Nuclear Engineering Doctoral Centre studentship from the EPSRC.

Introduction

The ability to predict corrosion and CRUD behaviour within primary coolant would enable tailoring and design of reactor operations and processes to help mitigate the negative consequences of the corrosion phenomena. This research project aims to investigating the interactions between the radiation environment and the corrosion products generated by the degradation of nuclear materials; documenting any changes in the aqueous environment in the presence of ionising radiation, CRUD simulants and coolant additives. The investigation attempts to link changes in the corrosion mechanisms with the radiolytically driven chemical processes that occur within the primary coolant circuit. This paper is a review of the literature that has informed this investigation of corrosion products and radiolytic species under simulant PWR Primary coolant condition.

Corrosion, CRUD and the PWR Environment

The corrosion of materials used in Pressurised Water Reactors (PWRs) can cause both operational and safety issues, and the most of current selection of materials used in the reactor have experienced corrosion in one form or another.[1] Corrosion experienced by primary coolant systems of PWRs are usually divided into various categorised; generalised corrosion, flow accelerated corrosion, Stress Corrosion Cracking (SSC) and even radiation induced corrosion.[1] General corrosion is linked to an increased in out of core activity caused by the transport, deposition and activation of corrosion products. [1, 2]The name given to the deposition and build-up of corrosion products is CRUD. This name has origins associated with corrosion product build investigated in early reactors including those at Chalk River during the mid-1950s and was defined as Chalk River Unidentified Deposit (CRUD) during the late 1950s and has been widely referred as such since.[3-5]

In the years since its first documentation, investigations into CRUD have attempted to understand its complex nature without complete success. Processes that lead to the formation of CRUD can be summarised in seven steps: [5, 6]

1) Generation (of corrosion products, oxidation of alloys)

2) Release (of corrosion products - dissolution, erosion or scaling can cause this)
3) Transport (by the coolant)
4) Deposition on the fuel elements (where activation of corrosion products may occur)
5) Release from the fuel element
6) Transport by the coolant
7) Deposition on, and incorporation in, primary coolant surface or removal from the primary coolant systems by water treatment

To develop a comprehensive understanding of CRUD all these steps need to be understood: it is important to investigating how each step links with the others, and if mitigation of one step will prevent the others from continuing/occurring. When examining the various mechanisms in each stage, the environment and conditions must be considered. PWR operating conditions varying depending on the reactor type, and vary throughout the plant: system pH can vary; temperatures are between 280 and 330 °C; system pressures can reach 200 bar and the coolant circuit is subject to mixed radiation fields.[1]

It is important to consider the effects of radiation on CRUD processes: radiation can cause material damage as well as alter the behaviour of the coolant. Water decomposes in the presence of ionising radiation (e.g. α, β and γ- radiation) generating chemically reactive species. This is known as water radiolysis and may be summarised as: [7, 8]

$$H_2O \longrightarrow HO^{\bullet}, e_{aq}^{-}, H^{\bullet}, HO_2^{\bullet}, H_2O_2, H_2, H^{+}$$

These primary radiolysis products recombine rapidly, but low steady state concentrations are achievable which may go on to interact with any dissolved impurities and/or surfaces. The radiolysis process produces both oxidising (H_2O_2, •OH and HO_2•) and reducing species (e^-_{aq}, H• and H_2) that alter the redox behaviour of the coolant water.[9-11] When the radiation and chemical environment is constant the radiolysis products reach a steady state and, therefore, this equilibrium determines the redox behaviour of the system as well as contributing to the control of corrosion processes within the system.[9-12] A shift from this steady state value can occur as the radiolysis species are chemically active and can interact with dissolved species and each other, and concentrations are affected by system pH and temperature.[9, 12]

The ability for the corroding surface and corrosion products to interact with radiolysis products can alter the redox chemistry further, as will the type and concentrations of radiolysis species produced. Understanding the interactions between the radiolysis and corrosion processes is crucial for the prediction of corrosion and CRUD behaviour.

To add to the complexity of the CRUD challenge, there are several materials used in the primary circuits of PWRs including; carbon steel, stainless steel, Inconel 600 and zircaloy alloys (fuel cladding).[5] These materials have different compositions and mechanisms for corrosion will vary as will the dissolution and transport of their corrosion products, leading to the complex composition seen in accumulated CRUD within a reactor.

Experimental laboratory investigations have observed changes in materials, surface effects, oxide film changes or monitored changes in the aqueous environment, for example investigating dissolved metal ion and radiolysis product concentrations. The core of a reactor experiences a mixed radiation field. Due to this added complexity, studies focus on high LET radiation (heavy ions, neutrons α particles) or low LET radiation (γ-radiation). For simplicity and ease most studies probe either the high temperature aspects or the radiation effects on the corrosion and CRUD mechanisms. As the radiolysis generates many active species, with varying lifetimes and detectability studies tend to focus on tracking concentrations of stable gaseous products (H_2, O_2 etc.) or stable and transient aqueous products (H_2O_2, e^-_{aq} etc.). Hydrogen and hydrogen peroxide (stable species generated by water radiolysis) both affect the corrosion mechanism of nuclear materials, so are often investigated to give an indication of the radiolysis process. The studies described in this review focus primarily on the effects of γ-radiation.

Investigating Effects of Radiation on Corrosion

Hydrogen peroxide is a highly oxidising molecular species, which, although stable in isolation, readily undergoes decomposition in presence of various surfaces, shifting the balance of radiolysis products from the expected steady state values.[13-20] Hydrogen peroxide decomposes to water and oxygen, possibly via a hydroxyl radical intermediate. The decomposition process is not understood, but will depend of material composition, structure and presence of oxides (generated in corrosion).[21] The decomposition products can go on to interact with surfaces, corrosion films, radiolysis products and any solubilised corrosion products in the coolant. As hydrogen peroxide is a highly oxidising

species, its presence affects both the redox behaviour of the system as well as the stability of corrosion products formed.[21] Due to the similarities between the systems (presence of water and radiation fields) advances understanding the interactions between corrosion products and radiolysis products have also come about from the investigations of nuclear waste systems.[17, 18, 20, 22] This review will document the approaches used to probe the 'synergistic interactions' between corrosion processes and radiolysis products.[9]

The research reviewed here focuses either on the irradiation induced changed in alloy coupons or the radiation induced changes on CRUD simulant powders and their interactions with the water radiolysis process. Notable works have been summarised, drawing out key experimental results and discussion points. For instance:

- Wren and co-workers have looked into the electrochemical changes induced by irradiation of nuclear materials irradiated in aqueous environment, attempting to determine the effects of temperature and pH on electrochemical behaviour as well as water radiolysis. These studies have aimed to link the effects of water radiolysis on the mechanism and behaviour of corrosion.
- There have been only limited investigations of the effects of radiation on corrosion at elevated temperatures, performed predominantly by Ishigure and co-workers.[23-25].
- LaVerne *et al.* have studied the effects of surfaces on hydrogen peroxide concentrations in radiation environments as well as the chemical changes of CRUD simulants (Iron oxides).
- Jonsson led a series of investigations into understanding the effects of γ-radiation and hydrogen peroxide on a variety of oxides and materials; looking at CRUD systems as well as systems used for fuel disposal.

Electrochemical Changes Induced by Irradiation of Nuclear Materials

The studies led by Wren aim to provide kinetic details towards the mechanism of corrosion and corrosion product release; stating the investigation aims were 'to develop a fundamental understanding of how water radiolysis can influence the corrosion of steel alloys in high radiation field environments, a comprehensive program of radiation-induced reactions is being carried out'.[26] The corrosion studies investigated the effects of pH, chemical additives, applied potential and the effects of γ-radiation on carbon steels,

stainless steels moving onto cobalt and nickel based alloys.[9, 12, 26-31] Wren highlighted the importance of the link between radiolysis and corrosion that is often be ignored, investigating the γ-radiolysis process independent of corrosion surfaces so comparisons can be drawn between corrosion and radiolysis. Further studies focused on how system parameters affect the radiolysis process investigating pH, dissolved oxygen concentration, temperature, and pressure constraints.[11, 32, 33] The importance of relatively stable radiolytically generated species, such as hydrogen and hydrogen peroxide, was investigated aiming for an understanding that might lead to the mitigation of radiation-enhanced corrosion.[32] Wren deployed a combination of both experimental and simulation approaches to investigate these complex radiolysis systems. Experimental investigations used electrochemical, spectroscopy and microscope techniques to qualify the effects of environment on the corrosion.

Water radiolysis experiments showed that pH and dissolved oxygen concentration have an effect on the concentration of radiolysis products. For example an increase in oxygen concentration leads to the increase in [H_2O_2], [H_2] and [$^{\bullet}O_2^-$] and a fall in [$^{\bullet}OH$] and [$^{\bullet}e_{aq}$].[11] If the pH of the water is increased from 6.0 to 10.6 the concentrations of H_2 and H_2O_2 increase by more than two orders of magnitude.[11, 32] These studies used experimental results to inform a kinetic model to identify key reactions that determine the systems chemistry during radiolysis, which can inform the empirical steady state equations describing yields of reactive species. Once the systems kinetics and reactive species concentration are known it may be possible to develop methods, using additives, to control the corrosion of the nuclear systems.[11, 33]

The studies on carbon steels started with understanding the corrosion mechanism at ambient temperature and pressure at pH 10.6 (the CANDU operating pH), temperatures were then increased to 150 °C, moving on to investigate the effects of γ-radiation.[12, 26, 30, 31] The chemical mechanism was studied using electrochemical techniques and ex situ surface analysis; electrochemical techniques included cyclic voltammetry and electrochemical impedance spectroscopy (EIS), spectroscopy techniques included x-ray photoelectron spectroscopy (XPS) and Raman spectroscopy. Finally, optical microscopy and scanning electron microscopy (SEM) were used to observe the oxidation process.

Studies at pH 10.6 and ambient temperatures suggested that oxide growth and conversion on carbon steels occurs in three distinct potential regions with Fe_3O_4 growing at potentials

≤ -0.6 V vs SCE (Region I). Between -0.5 V V_{SCE} and -0.2 V V_{SCE} (Region II) Fe_3O_4 growth is converted to Fe_2O_3 near the oxide/solution interface, and at higher potentials (Region III 0.0 V V_{SCE} < E (vs SCE) <0.4 V V_{SCE}) this mixed oxide may be converted to γ-FeOOH, which leads to changes in the film structure and may even lead to fracture, enhancing transport pathways in the film.[30] The conclusion is that changes in thermodynamic conditions in the system (such as pH or radiolytically generated redox species) will effect corrosion rate.[30] The study of this process as a function of temperature between 25 and 80 ºC gave further information on the growth mechanisms, determining that temperature affects oxide growth and conversion, primarily by increasing the rate of dissolution/precipitation and phase transformation, with oxidation processes being dictated by the potential at the oxide/water interface.[31] The mechanism of dissolution is suggested to be driven by the hydration of Fe^{II} at the oxide/water interface and then diffusion of this species into the bulk aqueous system and this dissolution rate increases with temperature. Oxidation of Fe^{II} to Fe^{III} will supress the dissolution by creating an insulating oxide.[31] This oxidation occurs in region II when Fe_3O_4 is converted to Fe_2O_3 at the oxide/water interface, limiting the growth of magnetite and preventing thickening of the oxide. In potential region III, the conversion of Fe_3O_4/γ-Fe_2O_3 to γ-FeOOH occurs leading to the possibility of fracture and re-passivation by an alternative oxide growth process giving a defective and possibly porous film.[31] With a clear idea of the oxide growth mechanism and how dissolution occurs, investigations have gone on to investigate the effects of γ-radiation.

Corrosion and water radiolysis processes are highly dependent on pH and redox potential of the system. It is important to have a clear idea of both processes to clarify the net effects of radiolysis on corrosion of metal and corrosion product transport.[11, 12, 33] Further experimental work by the Wren group investigated both ambient and elevated temperatures, with ambient experiments comparing γ-radiation to the addition of H_2O_2. The studies employed electrochemical techniques to determine the effect of radiolysis on the corrosion: at ambient temperature, the corrosion potential (E_{corr}) and R_p behaviour under γ-radiation could be mimicked using solutions of hydrogen peroxide at concentrations equivalent to those expected to be generated by water radiolysis.[12] This result suggests that H_2O_2 is the key radiolysis product that alters the corrosion behaviour in these irradiated systems. It, therefore, may be possible to predict rate of corrosion if [H_2O_2] can be measured as the electrochemical behaviour seems to be (at least partially)

dependent on [H_2O_2].[12] The presence of γ-radiation also impacts corrosion behaviour. An increase the E_{corr} is observed dictating the type of oxide that is formed. For carbon steel systems, γ-radiation increases the E_{corr} value from -0.65 ± 0.05 V_{SCE} to 0.0 ± 0.1V_{SCE}.[12] [26] When the system temperature was investigated, there was no significant change in the oxide composition due to the temperature increase, but, in the presence of γ-radiation, at mildly basic conditions the formation of the passive oxides Fe_3O_4 and γ-Fe_2O_3 is favoured.[26]

The effects of γ-radiation on the corrosion of Stainless Steel 316 (SS 316) were investigated by determining the effects of ionising radiation on the electrochemical corrosion potential of the system. The study was carried out at ambient temperature and at a pH of 10.6. Like carbon steel, SS 316 has the ability to form several oxides and the oxide form is dependent on the potential of the system. There are four oxidation regions for corrosion processes in SS 316, with various oxidation paths being available in each region. This gives competing corrosion kinetics and unique oxide properties.[27] In the region Ox I (<0.5 V_{SCE}), surface Cr_2O_3 is converted to an iron chromite ($FeCr_2O_4$) and an outer layer of magnetite may form. Once the duplex layer of this oxide system is formed dissolution from chromite and magnetite layers may occur. In the Ox II region (-0.5 V_{SCE} to 0 V_{SCE}) oxidation of magnetite occurs forming γ-Fe_2O_3 with oxidation of hydrated Fe^{II} species to γ-FeOOH; which is a thin protective layer. Dissolution in this region is limited to the hydration of Fe^{III} at the surface and is slow (as this process is not favourable). Region Ox III occurs between 0.0 V_{SC} < E < 0.3 V_{SCE} here magnetite / maghemite and γ-FeOOH layers grow rapidly due to the facture and re-passivation of the oxides film. The rate of dissolution is higher in this potential region than Ox II. Finally region Ox IV occurs at potentials above 0.3 V_{SCE}, where dissolution of chromium occurs accompanied by the growth of a mixed oxide.[27] The effect of ionising radiation on SS 316 can be defined by a rise in the E_{corr}. Without irradiation, E_{corr} for SS 316 is ~ -0.45 V_{SCE} and under γ-radiation this value rises to 0.05 V_{SCE}. The potential -0.45 V_{SCE} is boundary between regions I and II and the value 0.05 V_{SCE} lies between II and III; this rise in corrosion potential indicates a change in corrosion mechanism and a change in preferred oxide composition.[27]

The studies by Wren provide the beginning of a mechanistic understanding of nuclear material corrosion and may be used to help predict corrosion behaviour under nuclear conditions, as well as provide some insight into the release metal cation mechanism,

suggesting that dissolution of chromium and iron occurs by hydration of metal ions at the oxide/solution and then diffusion into the bulk.[12, 26, 27, 30, 31]

The corrosion of carbon and stainless steels generates mixed oxide systems that consist of Fe_2O_3, Fe_3O_4, γ-FeOOH, Cr_2O_3 and $FeCr_2O_4$ as well as nickel ferrites, enabling the potential release of Fe^{2+}, Fe^{3+}, Ni^{2+} and Cr^{3+} ions. To relate this information on corrosion and release to the formation of CRUD, it is important to understand the release mechanisms and determine the nature of interactions of released species with water radiolysis products.[1]

Effects of Radiation on Corrosion at Elevated Temperatures

Studies led by Ishigure have considered the effects of γ-radiation and hydrogen peroxide on release of corrosion products in reactor conditions, investigating high temperature systems as well as the effects of oxygen and alloy type.[23-25] Studies of stainless steel 304 (SS 304) and carbon steels showed γ-radiation leads to an increase in the release of insoluble corrosion products (predominantly iron), but the release of soluble corrosion products is not enhanced by γ-radiation.[23-25] The effect of γ-radiation was compared to the addition of H_2O_2, with the addition of H_2O_2 leading to an increased rate of release.[24] This highlights the importance of hydrogen peroxide in the corrosion processes in nuclear environments. The suggested explanation for CRUD formation given by Ishigure is that the release of Fe^{2+} ions from the oxide/solution interface is followed by the oxidation to Fe^{3+} ions by either oxygen or radiolysis products in the bulk.[24]

A study by Cuba *et al.* investigated the formation of Fe^{II} and Fe^{III} ions from carbon steel during γ irradiation under deaerated conditions, investigating the effects of dose and temperature.[36] The study observed a decrease in pH with increased absorbed dose, which could be due to the hydrolysis of Fe ions. The concentration of Fe^{II} and Fe^{III} ions were monitored with total concentrations determined (the sum of both solid and liquid phase contributions). The results showed an increase in total Fe^{II} and Fe^{III} with increasing dose and temperature, with a clear contribution from a rise in temperature. The concentration

[1] Investigations led by Wren and co-workers into nickel and cobalt alloys are not discussed in detail here, as the current focus of this research project is stainless steel derivatives. It should be noted that under γ-radiation corrosion potentials of these materials rise and the dissolution of metal ions is dependent on both the presence of ionising radiation and system pH. 28. M. Behazin, M. C. Biesinger, J. J. Noël and J. C. Wren, *Corrosion Science*, 2012, **63**, 40-50. 34. A. Y. Musa, M. Behazin and J. C. Wren, *Electrochimica Acta*, 2015, **162**, 185-197. (35. A. Y. Musa and J. C. Wren, *Corrosion Science*, DOI: http://dx.doi.org/10.1016/j.corsci.2016.03.015.

of Fe^{II} is higher in aerated samples than in deaerated systems; however, unfortunately, a comparison of Fe^{III} under different reaction conditions was not carried out. Although a direct comparison to the studies by Ishigure cannot be made as these studies measured only the Fe^{2+} concentration of liquid phase of the system, the same trend is exhibited; the presence of oxygen enhances the release of Fe^{II} ions.[25, 36] It is clear that oxidative radiation processes are more significant in the presence of radiation.

It is important to note that the concentration of released Fe^{II} ions will quite possibly alter the corrosion processes, linking the presence of corrosion products and CRUD on the ongoing corrosion of nuclear materials. Wang *et al.* showed that corrosion processes are susceptible to change due dissolved Fe^{II} species present in solution and that the outcome is dependent on the interaction between the aqueous system and the oxide bulk and interface.[37] The study investigated the effects on carbon steel at pH 8.4 (as the solubility of Fe^{II} is favourable at this pH) and as a function of potential. At potentials less than -0.4 V_{SCE} iron is oxidised to Fe^{II} and further partially oxidised at the oxide/surface interface to $Fe^{II/III}$ forming a Fe_3O_4 layer. At the magnetite/water interface Fe^{II} hydroxide may hydrate and oxidise further towards γ-FeOOH. The presence of Fe^{II} in the solution bulk supressed the hydration and release of Fe^{II} from the oxide reducing the 'net rate of anodic oxidation.'[37] At potentials above −0.4 V_{SCE}, the system favoured the formation of γ-Fe_2O_3 via the oxidation of the magnetite and the presence of aqueous Fe^{II} encouraged the formation of γ-FeOOH crystals on the oxide surface.

The studies summarised so far have highlighted the complex nature of the systems, trying to clarify which processes and interactions drive changes in corrosion and ion release behaviour. Changes in ion release rate are determined by the corrosion processes as well as the solution conditions; γ-radiation affects both of these parameters altering the E_{corr} of the system as well as introducing radiolytically generated species. These laboratory studies above used coupons of the alloy materials. The metallic alloys have a complex composition and the mechanism for corrosion and release is corresponding complex due to this composition and the ability to form duplex layers of oxides, with mixed oxidation states. The use of simple oxide powders to simulate components of in-reactor corrosion oxides offers one way of simplifying the challenge to allow for some clarification as to which oxides contribute to the observed corrosion and CRUD behaviour and will facilitate conclusions on the behaviour of CRUD and the interactions of radiolysis

products with the corrosion products. To relate data for the oxide powders to coupon behaviour, composition and surface area corrections are necessary.

Enhanced Radiolytic Decomposition of Water at Solid Oxide Surfaces

Studies by LaVerne and co-workers have shown enhanced radiation induced decomposition of water when solid oxides are present. The initial focus was on ZrO_2, CeO_2 and UO_2, attempting to understand the effects of radiation fields on surface interactions in nuclear reactors and wet nuclear waste.[13, 38-40] Formation of molecular hydrogen can be used as an indicator of the radiolytic decomposition of water and is easily monitored due to its molecular and stable nature. Its yield in radiolysis processes has been shown to alter in the presence of surfaces.[41-43] Studies of various oxides showed that hydrogen yields increase with the presence of oxide surfaces, with a greater hydrogen yield with the decreasing number of water layers. The presence of a UO_2 surface leads to a 10 fold increase in the hydrogen yield per 100 eV absorbed in the water compared to liquid water, with a comparable increase is measure for CeO_2 and ZrO_2.[42] LaVerne suggested that the increased radiolytic yield of H_2 could be due to an energy transfer from oxide to water interface.[41-43]

To enhance the understanding of how radiation affects iron oxides on the molecular level, LaVerne examined the chemical changes of oxide surfaces irradiated using both 5 MeV ^4He ions and γ- rays.[41] Aqueous slurries of FeO, Fe_3O_4 and Fe_2O_3 were irradiation with respect to the fraction of water present, determining hydrogen productions and chemical changes to the oxide using Raman spectroscopy, XPS, X-ray diffraction and SEM.[41] Water absorption studies showed that in damp atmospheres there is little or no physical water absorption onto FeO and Fe_3O_4 leading to low observed yields of hydrogen in studies of these systems under irradiation. Fe_2O_3 systems showed absorption of water and a hydrogen yield that is s few orders of magnitude higher than that of bulk water.[41] When aqueous slurries were investigated, any enhancement of hydrogen yields was negligible until the amount of water was low, suggesting that the enhanced hydrogen production occurs close to the surface and involves only a few layers of water. No macroscopic change in the crystal structure of the material was observed, however, Raman microscopy showed islands of Fe_2O_3 in both the FeO and Fe_3O_4 samples. This appearance suggests the interactions between water and iron oxides may lead to oxidation processes and the transfer of electrons between the oxide and the water. XPS results indicated the formation

of oxygen species after radiolysis, but there nature of the environments producing these species was not conclusive.[41]

Effects of γ-Radiation and Hydrogen Peroxide on a Variety of Oxides

The Jonsson group have investigated the reactivity of hydrogen peroxide with transition metals and lanthanide compounds, as well as the effects of γ-radiation on corrosion and dissolution of materials important to waste disposal.[14-18, 20, 22, 44, 45] Their studies on hydrogen peroxide reactivity towards CRUD simulants aim to underpin reactor chemistry by elucidating the mechanism of CRUD formation and determining its stability.[18] Jonsson investigated aqueous suspensions of Fe_3O_4, Fe_2CoO_4 and Fe_2NiO_4. The powders were added to purged hydrogen peroxide solutions and left at varying temperatures (20-95 ºC) for extended time periods and the activation energies for the reaction hydrogen peroxide with the CRUD simulants were determined. Hydrogen peroxide concentration was monitored as well as the metal ion concentration. Samples were pre-treated with EDTA and/or de-ionised water to allow just the effects of hydrogen peroxide on metal ion release to be determined. At room temperature, hydrogen peroxide only reacts with Fe_3O_4 and Fe_2CoO_4. At elevated temperatures, the reactivity series was $Fe_2CoO_4 > Fe_3O_4 > Fe_2NiO_4$, however, further studies should be undertaken to distinguish the effects of particle size. The concentration of metal ions is higher with exposure to hydrogen peroxide for all cases, suggesting the final solid product is Fe_2O_3. The formation of Fe_2O_3 is consistent with the results obtained by LaVerne *et al.* that show Fe_2O_3 is formed when FeO and Fe_3O_4 are irradiated in the presence of water.[41] The presence of Fe_2O_3 indicates that hydrogen peroxide induces oxidation of Fe^{II} to Fe^{III}, and from this it can be assumed that radiolytically produced H_2O_2 and other oxidising radiolysis products can cause oxidation of Fe_2MO_4 type CRUD to Fe_2O_3 type CRUD.

Jonsson also investigated the reaction of H_2O_2 with transition metals and lanthanide oxides; specifically Fe_2O_3, CuO, HfO_2, CeO_2 and Gd_2O_3, aiming to determine if interactions occur via redox reactions or catalytic decomposition.[17] 'The main goal of this experimental work is to systematically study the reactivity of H_2O_2 towards a diversity of oxides.' The proposed interactions for oxides with hydrogen peroxide are:

$$H_2O_2 + M \rightarrow 2HO^{\bullet} + M \qquad \textbf{(4.8-1)}$$

$$HO^{\bullet} + H_2O_2 \rightarrow HO_2^{\bullet} + H_2O \qquad \textbf{(4.8-2)}$$

$$2HO_2^{\bullet} \rightarrow H_2O_2 + O_2 \qquad \textbf{(4.8-3)}$$

where M is a site on the oxide surface.[13-16] The radicals formed may bind to an oxide surface increasing their lifetimes. Alternatively, they may react with surfaces and change the system chemistry.[16] The interactions of hydrogen peroxide with the oxides were studied systematically, examining the kinetics and the mechanisms of the interactions. Kinetic studies involved oxides suspended in aqueous solutions of H_2O_2 (0.5 mM) at varying temperatures and time periods with [H_2O_2] being measured at time intervals up to 500 minutes. Mechanistic studies aimed to quantify the number of hydroxyl radicals produced via catalytic decomposition at the oxide surface using a scavenger to remove HO• from the system, specifically Tris (hydroxymethyl) aminomethane (Tris) reacting with HO• to produce formaldehyde (CH_2O).[13, 15] Activation energies and rate constants for the decomposition process were measured and compared; however, there was no (apparent) link between material stoichiometry and activation energy. The order of activation energy measured was CeO_2 < Fe_2O_3 < HfO_2 < Gd_2O_3 < CuO. Jonsson suggested that the activation energy is dictated by the microstructural properties such as type, coordination, and number of metal catalytic sites available and their degree of hydroxylation. Ultimately, the study concluded that the reactivity of hydrogen peroxide is very different for the materials examined despite their apparent similarities, suggesting decomposition is catalytically driven. Both of these studies by Jonsson added quantities of hydrogen peroxide to simulate the radiolysis process. Further studies should monitor hydrogen peroxide and metal ion concentrations under irradiation, comparing blank water samples with aqueous systems of CRUD simulants.

The radiation induced corrosion of copper has also been investigated by the Jonsson group, monitoring the dissolved copper ion concentration in respect to applied dose, at different dose rates and comparing these studies to control experiments performed with known quantities of added hydrogen peroxide.[20] The study showed a dependence of copper dissolution on total absorbed dose with a slight dependence on dose rate. For a total dose of 37 kGy at 80 Gy h^{-1} the measured copper ion concentration was 85 µM, but a dose rate of 770 Gy h^{-1} gave a copper ion concentration of 55 µM at the same total dose. The experiments gave higher concentrations of copper than predicted numerical modelling. The reference experiments (H_2O_2 containing samples that were not irradiated) did not release copper after consumption of the H_2O_2. The combination of these effects suggests that, in addition to water radiolysis, there are other contributing factors driven

by radiation that affect dissolution. These may be electrochemical in nature.[20] Radiation induced chemistry can be probed by the use of chemical scavengers, which remove radiolysis products from the system, in an attempt to separate the behaviour due radiation and that due to surface interactions/processes.

The radiolysis of water in the vicinity of a passive surface was recently studied by Renault and co-workers, who observed the fate of radiolytic radicals in the vicinity of SS 316 and the nickel-based alloy Hastelloy surfaces.[46] The production and reaction of the HO• and the solvated electron (e^-_{aq}) were monitored using scavengers, specifically the hydroxyl radical by benzoate:

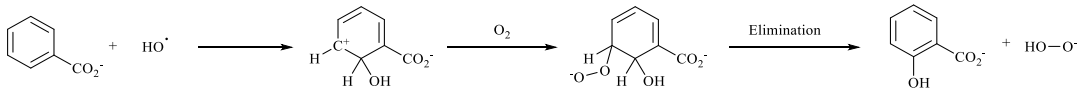

and the e^-_{aq} via glycylglycine.[46]

$$e^-_{aq} + NH_3^+CH_2CONHCH_2CO_2^- \longrightarrow NH_3 + CH_2CONHCH_2CO_2^-$$

The hydroxyl radical yield at short scavenging times was higher for Hastelloy and SS 316 than for previous studies with porous gold. In all cases over long scavenging times the HO• yield decreased.[47] [47] Renault suggested that the production and consumption mechanism of hydroxyl radical is different for SS 316 and Hastelloy with a contribution from the surface chemistry and hydrogen peroxide decomposition.[46]

The scavenging of e^-_{aq} was investigated for SS 316 systems with glycylglycine as the chosen scavenger as it does not interact with the metal. At short scavenging times, the solvated electron yield is low when comparison to the hydroxyl radical implying that radiolytically generated electrons are captured by the metal.[46] Following Grand *et al.*, Renault proposes a mechanism in which the Fermi level of metals is lower than the conductance band of water, allowing for electron scavenging by the metal before the electrons are solvated.[46-48] In this model, the metal can then hold onto the excess electron before ultimate release at a later time; the increase in yield of solvated e^-_{aq} as experiment time increased suggest that the electrons are released via processes such as hydrogen production, fitting the hypothesis that metals capture and then release electrons.[46, 49] There is insufficient data to make definite conclusions on the behaviour of radiolytically produced electrons with surfaces, but it is clear that a stainless-steel surface is able to capture low energy electrons before solvation. One might postulate that this capture of e^-

$_{aq}$ might contribute to the change of E_{corr} associated with the irradiation of nuclear materials.

Conclusion

This review has summarised aspects of the literature investigating the corrosion of, and release ions from, nuclear materials by electrochemical studies, microscopy, and solution chemistry as well spectroscopic techniques. The research outlined here shows that radiolysis processes affect the corrosion and release of materials, and it is driven by oxidative processes. Hydrogen peroxide has been shown to be a contributing factor to these oxidative processes but is not the only contributor. Furthermore, it is clear that hydrogen peroxide decomposition is driven by the catalytic nature of the surfaces present in the systems. There is significant evidence that electrochemical behaviour is altered by the presence of γ-radiation with corrosion potentials increasing markedly.[12, 26, 27] These changes are not just due to water radiolysis and other radiation processes may be at work.[20] There is also some evidence that oxidative processes can occur in the solution bulk of aqueous systems following the release and diffusion of metal ions from an oxide/solution interface which may be driven by radiation induced processes.[25] Material type and its associated surface chemistry has an effect on the observed radiolysis behaviour and altering the corrosion behaviour. It is clear that the mechanism and nature of these interactions is complicated and requires further investigation. The water radiolysis process is not the only contribution to enhanced corrosion and release of metal ions. This fact reinforces the importance of studying both the corrosion and release mechanisms using a variety of methods. Although progress has been made; it is clear that further work is needed to try and understand the interactions between corrosion products and radiolysis products. The aim should be to gain a clearer picture of the other radiation driven processes that occur in complex corrosion systems, and how they affect the corrosion and CRUD formation processes. The project underway aims to probe these interactions further; focusing on understanding the effects of γ-radiation on CRUD simulants and corrosion surfaces. The study will monitor and document dissolved metal ion and hydrogen peroxide concentrations tailoring experiments to understand the effects of chemical additives and radiolysis products on these concentrations.

References

1. M. Le Calvar and I. De Curières, in *Nuclear Corrosion Science and Engineering*, Woodhead Publishing, 2012, DOI: https://doi.org/10.1533/9780857095343.5.473, pp. 473-547.
2. F. H. Sweeton and C. F. Baes, *The Journal of Chemical Thermodynamics*, 1970, **2**, 479-500.
3. P. Cohen, A. Research, T. C. o. Water and S. i. T. P. Systems, *The ASME Handbook on Water Technology for Thermal Power Systems*, American Society of Mechanical Engineers, 1989.
4. R. A. Castelli, *Nuclear Corrosion Modelling*, Butterworth-Heinemann, Elsevier, Oxford, United Kingdom, 2009.
5. P. Rudling, A. Strasser, B. Cox, F. Garzarolli, S. Odar and R. Adamson, LCC 9, Bilboa, Spain, 2014.
6. W. E. Berry, R. B. Diegle, I. Battelle Memorial, L. Columbus and I. Electric Power Research, *Survey of corrosion product generation, transport, and deposition in light water nuclear reactors*, Electric Power Research Institute, Palo Alto, Calif., 1979.
7. J. W. T. Spinks and R. J. Woods, *An Introduction to Radiation Chemistry*, John Wiley & Sons, United States of America, 3 edn., 1990.
8. A. Vertes, S. Nagy, Z. Klencsar, R. G. Lovas and F. Rosch, *Handbook of Nuclear Chemistry*, Springer, London, 2 edn., 2011.
9. X. Zhang, W. Xu, D. W. Shoesmith and J. C. Wren, *Corrosion Science*, 2007, **49**, 4553-4567.
10. K. Ishigure, T. Nukii and S. Ono, *Journal of Nuclear Materials*, 2006, **350**, 56-65.
11. J. M. Joseph, B. Seon Choi, P. Yakabuskie and J. Clara Wren, *Radiation Physics and Chemistry*, 2008, **77**, 1009-1020.
12. K. Daub, X. Zhang, J. J. Noël and J. C. Wren, *Electrochimica Acta*, 2010, **55**, 2767-2776.
13. A. Hiroki and J. A. LaVerne, *The Journal of Physical Chemistry B*, 2005, **109**, 3364-3370.
14. C. M. Lousada, T. Brinck and M. Jonsson, *Computational and Theoretical Chemistry*, 2015, **1070**, 108-116.
15. C. M. Lousada and M. Jonsson, *The Journal of Physical Chemistry C*, 2010, **114**, 11202-11208.
16. C. M. Lousada, M. Trummer and M. Jonsson, *Journal of Nuclear Materials*, 2013, **434**, 434-439.
17. C. M. Lousada, M. Yang, K. Nilsson and M. Jonsson, *Journal of Molecular Catalysis A: Chemical*, 2013, **379**, 178-184.
18. M. A. Nejad and M. Jonsson, *Journal of Nuclear Materials*, 2004, **334**, 28-34.
19. M. Yang and M. Jonsson, *Journal of Molecular Catalysis A: Chemical*, 2015, **400**, 49-55.
20. Å. Björkbacka, S. Hosseinpour, M. Johnson, C. Leygraf and M. Jonsson, *Radiation Physics and Chemistry*, 2013, **92**, 80-86.
21. D. Fu, X. Zhang, P. G. Keech, D. W. Shoesmith and J. C. Wren, *Electrochimica Acta*, 2010, **55**, 3787-3796.
22. M. Amme, R. Pehrman, R. Deutsch, O. Roth and M. Jonsson, *Journal of Nuclear Materials*, 2012, **430**, 1-5.

23. Kenkichi Ishigure, Norihiko Fujita, Takaaki Tamura and K. Oshima, *Nuclear Technology* 1980, **50**, 169-177.
24. M. Kawaguchi, K. Ishigure, N. Fujita and K. Oshima, *Radiation Physics and Chemistry (1977)*, 1981, **18**, 733-740.
25. K. Ishigure, H. Iksie, K. Oshmia, N. Fujita and S. Ono, *Radiation Physics and Chemistry*, 1983, **21**, 281-287.
26. K. Daub, X. Zhang, J. J. Noël and J. C. Wren, *Corrosion Science*, 2011, **53**, 11-16.
27. Q. W. Knapp and J. C. Wren, *Electrochimica Acta*, 2012, **80**, 90-99.
28. M. Behazin, M. C. Biesinger, J. J. Noël and J. C. Wren, *Corrosion Science*, 2012, **63**, 40-50.
29. M. Behazin, J. J. Noël and J. C. Wren, *Electrochimica Acta*, 2014, **134**, 399-410.
30. W. Xu, K. Daub, X. Zhang, J. J. Noel, D. W. Shoesmith and J. C. Wren, *Electrochimica Acta*, 2009, **54**, 5727-5738.
31. K. Daub, X. Zhang, L. Wang, Z. Qin, J. J. Noël and J. C. Wren, *Electrochimica Acta*, 2011, **56**, 6661-6672.
32. P. A. Yakabuskie, J. M. Joseph and J. Clara Wren, *Radiation Physics and Chemistry*, 2010, **79**, 777-785.
33. M. Sterniczuk, P. A. Yakabuskie, J. C. Wren, J. A. Jacob and D. M. Bartels, *Radiation Physics and Chemistry*, 2016, **121**, 35-42.
34. A. Y. Musa, M. Behazin and J. C. Wren, *Electrochimica Acta*, 2015, **162**, 185-197.
35. A. Y. Musa and J. C. Wren, *Corrosion Science,* DOI: http://dx.doi.org/10.1016/j.corsci.2016.03.015.
36. V. Čuba, R. Silber, V. Múčka, M. Pospíšil, S. Neufuss, J. Bárta and A. Vokál, *Radiation Physics and Chemistry*, 2011, **80**, 440-445.
37. L. Wang, K. Daub, Z. Qin and J. C. Wren, *Electrochimica Acta*, 2012, **76**, 208-217.
38. J. A. LaVerne and L. Tandon, *The Journal of Physical Chemistry B*, 2002, **106**, 380-386.
39. J. A. LaVerne, *The Journal of Physical Chemistry B*, 2005, **109**, 5395-5397.
40. I. Štefanić and J. A. LaVerne, *The Journal of Physical Chemistry A*, 2002, **106**, 447-452.
41. S. C. Reiff and J. A. LaVerne, *The Journal of Physical Chemistry B*, 2015, **119**, 7358-7365.
42. J. A. LaVerne and L. Tandon, *The Journal of Physical Chemistry B*, 2003, **107**, 13623-13628.
43. N. G. Petrik, A. B. Alexandrov and A. I. Vall, *The Journal of Physical Chemistry B*, 2001, **105**, 5935-5944.
44. R. Pehrman, M. Amme, O. Roth, E. Ekeroth and M. Jonsson, *Journal of Nuclear Materials*, 2010, **397**, 128-131.
45. E. Ekeroth, O. Roth and M. Jonsson, *Journal of Nuclear Materials*, 2006, **355**, 38-46.
46. S. Moreau, M. Fenart and J. P. Renault, *Corrosion Science*, 2014, **83**, 255-260.
47. R. Musat, S. Moreau, F. Poidevin, M. H. Mathon, S. Pommeret and J. P. Renault, *Physical Chemistry Chemical Physics*, 2010, **12**, 12868-12874.
48. D. Grand, A. Bernas and E. Amouyal, *Chemical Physics*, 1979, **44**, 73-79.

49. A. Henglein and J. Lilie, *Journal of the American Chemical Society*, 1981, **103**, 1059-1066.

Chapter 5: Analytical techniques

5.1 Key experimental techniques used

The techniques implemented in this project were chosen to give characterisation of the materials exposure to radiation and to probe any changes induced during experiments. The techniques used are discussed in this chapter.

Raman Spectroscopy

Raman spectroscopy measurements were taken using a Bruker RamanScope III with varying laser power and resolution dependant on material examined. Raman spectroscopy utilises monochromatic radiation, in which its frequency is higher than the vibrational frequencies of the material and lower than the electronic frequencies, its frequency is υ_o.[1] The radiation is then scattered by the electrons in the material being examined and this scattering is analysed by the spectrometer measuring the change in frequency and energy of the incident photon. Photons will interact with the electrons around the molecular bond causing electrons to gain energy and enter 'virtual states.' The demotion of electrons from these higher states may occur in any direction and is referred to as scattering, either by Rayleigh, Raman or anti-Stokes Raman Scattering. The new frequency of the photon is equal to the incident frequency minus the vibrational frequency of the molecule υ_i, (υ_o -υ_i). Rayleigh scattering occurs via an elastic collision, the excitation in the molecule leads to no change in rational or vibrational energies, incident and scattered electrons have the same wavelength. Raman scatter is inelastic, the incident photon energy changes during the collision with either an increase or decrease in wavelength related to this energy change. If the molecule is promoted from ground to a virtual state and drops to a higher energy vibrational state (i.e. a longer wavelength) it is known as Stokes scattering. If the energy is in a higher vibrational state initially and after collision and scattering it returns to the ground state the scattered photon will gain energy and have a shorter wavelength, this is anti-Stokes scattering.[1, 2] This is represented graphically in **Figure 5.1-1.**

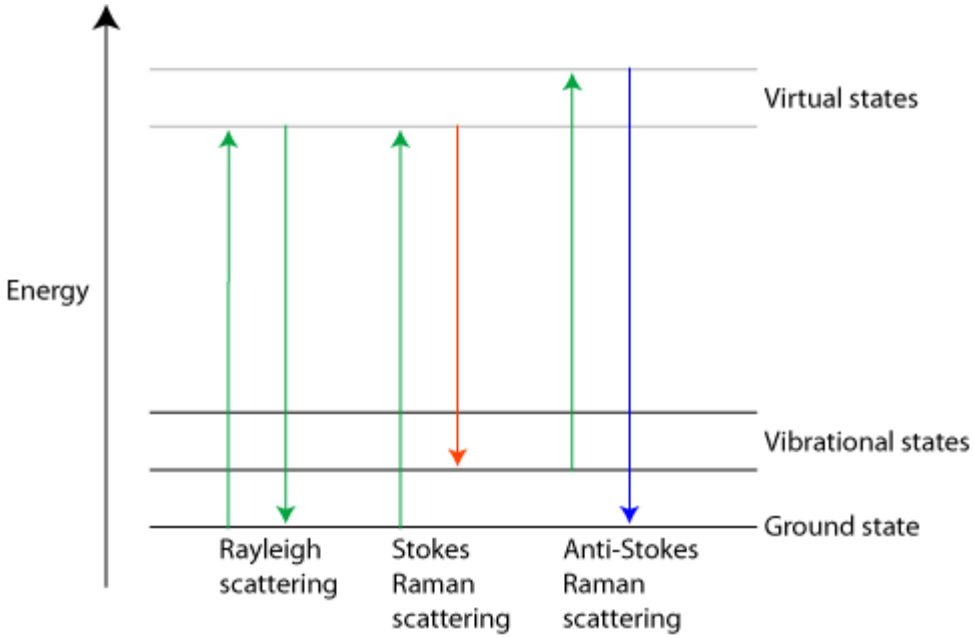

Figure 5.1-1. A pictorial representation of the scattering that may occur during Raman spectroscopy

The changes seen in these vibrational energy levels is the basis of Raman spectroscopy and each type of bond will have changes that are indicative of the type of bond and its constituent elements meaning it can be used to characterise materials**.**

Brunauer–Emmett–Teller, BET

Tri-Star II surface area and porosity analyser (Micrometrics) was used, with N_2 used as the adsorbate gas throughout. BET can give information on the specific surface area of a powder, pore size and distribution, this is done by adsorbing gas onto the surface and measuring the volume of absorbed gas at nitrogen boiling point (-196 °C). The amount of gas absorbed correlates to the total surface area of particles and their pore type. BET theory allows for concept of multimolecular layer adsorption and assumes the forces active in the condensation of the gases are responsible for the binding energies seem in multimolecular adsorption. The rate of condensation onto a surface with adsorbed gas molecules is equal to rate of evaporation from that layer and summed for infinite number of layers gives the following equation (in linear form)[3, 4].

$$\frac{1}{V_a\left(\frac{P_0}{P}-1\right)} = \frac{C-1}{V_m C} \times \frac{P}{P_0} + \frac{1}{V_m C} \qquad \textbf{(5.1-1)}$$

P	=	partial vapour pressure of adsorbate gas in equilibrium with the surface at 77.4 K (b.p. of liquid nitrogen), in pascals,
P_o	=	saturated pressure of adsorbate gas, in pascals,
V_a	=	volume of gas adsorbed at standard temperature and pressure (STP) [273.15 K and atmospheric pressure (1.013×10^5 Pa)], in millilitres,
V_m	=	volume of gas adsorbed at STP to produce an apparent monolayer on the sample surface, in millilitres,
C	=	dimensionless constant that is related to the enthalpy of adsorption of the adsorbate gas on the powder sample.

The BET Value $\frac{1}{V_a\left(\frac{P_0}{P}-1\right)}$ is plotted against $\frac{P}{P_0}$ and gradient and intercept can be used to find Vm which in turn is used to calculate surface area by:

$$S_{total} = \frac{V_m N s}{V} \quad \textbf{(5.1-2)}$$

$$S_{BET} = \frac{S_{total}}{a} \quad \textbf{(5.1-3)}$$

N	=	Avogadro constant (6.022×10^{23} mol^{-1}),
a	=	The mass of the solid sample
V	=	the molar volume of the adsorbate gas
V_m		volume of gas adsorbed at STP to produce an apparent monolayer on the sample surface, in millilitres,

These equations are used to calculate the specific surface area of the examined material and knowing this can give an indication of expected behaviour and reaction rates. The shape of the curve and the presence or lack of hysteresis loops can give information relating to the porosity of the examined material.

Scanning Electron Microscopy (SEM) with EDS Energy Dispersive Spectroscopy

A FEI Quanta FEG 250 microscope was used for all samples with energy dispersive spectroscopy when elemental composition was required. SEMs are microscopes that use electrons to form images, microscopes typically consist of a source of electrons, lenses for focus, something to raster the electrons, detection arrangements and then a way to display the image. Electrons detected can be second electrons (SE) that give information on topographical features, backscattered electrons (BSE) giving information on compositional differences, and x-ray spectrometers can be used to map elements giving both qualitative information and quantification.[5] A schematic of the typical set up for an SEM is seen in **Figure 5.1-2** and describes the process of image acquisition.[6]

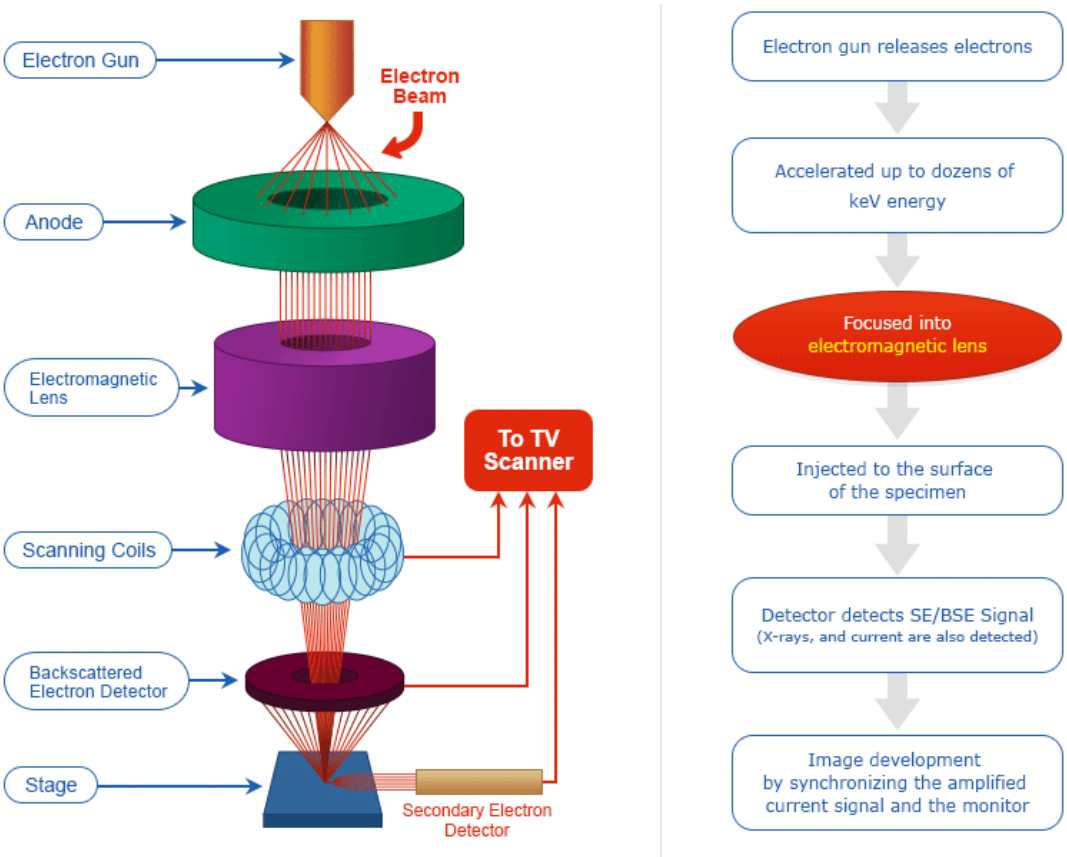

Figure 5.1-2. Schematic of a typical SEM configuration

A sample is bombarded by electrons, that have been focused using electromagnetic lenses, a condenser lens focuses the beam spot size, a further objective lens focusses the beam onto the surface which will scan across the specimen's surface. The incident electrons interact with electrons residing in the sample and cause excitation of these, which can result in electrons being ejected by the material. The ejected electrons are called secondary electrons. The incident electrons interact with the material and result in a change of energy, these electrons are either ejected or deflected and are known as BSE. Elements can be identified by the X-rays that are emitting during the electron transition. Emitted X-rays have characteristic energies representative of the orbitals in which electrons are bound within their parent atoms, governed by the principle quantum number n. As distance increases from the nucleus increases the energy decreases, with K the inner most orbit followed by the L and M, the energies of the X-rays/ photons emitted have an energy equal to the difference between the initial and final levels. These energies are used to characteristic of the material, and these transitions are used to identify the elements in the specimen. The different transition energies K_α, K_β, L_α, L_β, are examples of transitions used. Graphical representation of these orbitals and transitions are depicted in **Figure 5.1-3**. For EDS these energy and wavelength of these K_α, L_α, M_α transitions are plotted against atomic number for energies up to 10 keV, the K_α line is used elements with atomic numbers up to 30, L_α above this and M_α reserved for the heaviest elements, other lines may interfere with these so must be considered when wanting to accurately identify elements.

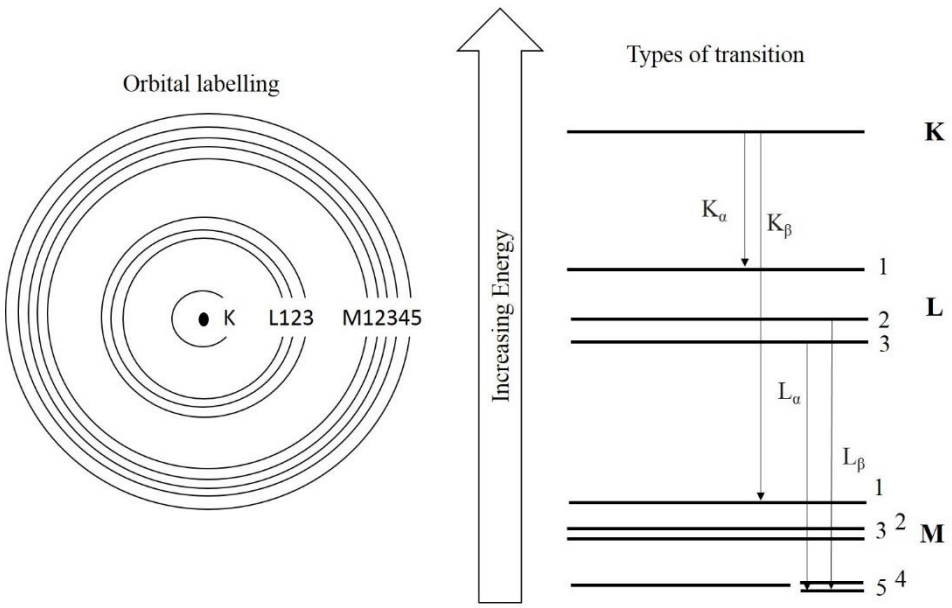

Figure 5.1-3. Representation of the transitions that may occur in SEM-EDS

The use of imaging techniques along with EDS information gives insight to material morphology, structure and composition. Cross sectional SEM was used to measure the grown oxide thickness in samples oxidised during these tests.

X-ray Photoelectron Spectroscopy (XPS)

XPS is a surface sensitive technique that looks the top 10 nm of a sample, and utilises the photoelectric effect, the emission of electrons due to stimulation by light and/or electromagnetic radiation. In XPS, specimens are exposed to X-rays that interact with electrons of elements in the materials, causing excitation and ejection. Spectra are obtained by measuring the number of emitted electrons and their kinetic energies. The total energy alongside the kinetic energy of electrons emitted are characteristic of the elements within the specimen. As the photon energy is known and related to the source of X-rays, in these studies a Kratos axis ultra-Hybrid X-ray photo spectrometer that utilises a Al Kα monochromatic source, with a photon energy of 1486.6 eV.[7] The kinetic energy is measured by the X-ray detectors this allows for the binding energy to be calculated:

$$E_{binding} = E_{photon} - (E_{kinetic} + \emptyset) \quad \textbf{(5.1-4)}$$

where Φ is a work function term related to the instrument, accounting for the energy absorbed by the instrument's detector. The binding energy is related to the atomic number of the elements and which orbital the electrons are residing in, so the binding energy can be used to identify the elements in the sample. As in SEM-EDS the peaks in the spectrum depend on initial and final states of the electrons in the absorbing atom. In XPS a survey scan will be taken to identify any obvious peaks present, then these will be the input parameters and energies for longer scans that give further information. Quantification of elements can be undertaken by fitting the peaks from the spectrum, but careful consideration should be made when using XPS for quantification as over processing of the data leads to errors. Fitting software can be used to identify the elements and for peak fitting, this work used a software called CASA XPS.[8]

X-ray Diffraction (XRD) and Grazing Incidence XRD (GI-XRD)

X-ray diffraction gives information on a materials atomic and molecular structure, giving an idea of bulk properties. XRD utilises the principles of wave particle duality, treating the incident X-rays as waves of electromagnetic radiation. Electrons in the specimen interfere with these waves, scattering them producing an array of spherical waves, with

most directions being cancelled out by destructive interference others can be added constructively using Bragg's law: [9]

$$2d\sin\theta = \eta\lambda \qquad \textbf{(5.1-5)}$$

where d is the spacing being the diffracting planes, θ the incident angle of the x-rays, n is integer when constructive interference occurs and λ is the wavelength of the incident beam. A visual representation of this can be seen in **Figure 5.1-4.**

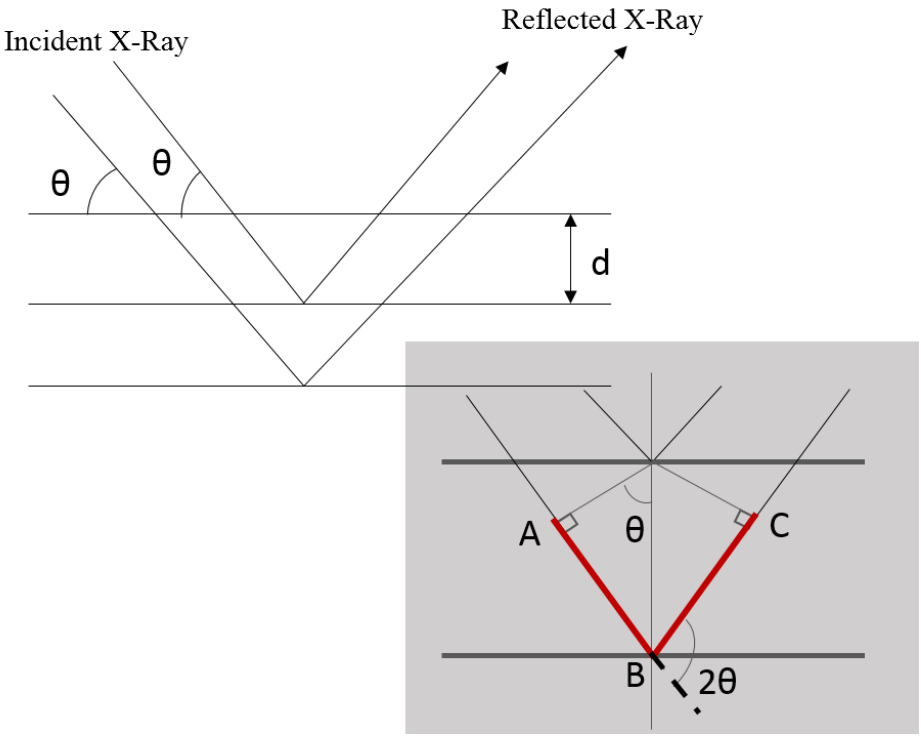

Figure 5.1-4. Representation of the possible diffraction used to derive Bragg's law

When considering Braggs' law the planes of atoms in a unit cell (lattice plane) act as reflecting points, and families of planes will produce diffraction peaks only at specific incident angles θ.[10] Peak intensity is determined by the types of atoms in the diffracting plane, and the d spacing between planes determines the peak position. Incident angle is defined between incident x-rays and the sample and the diffracted angle, 2θ, is the angle of the incident beam in relation to the detector. 2θ values are reported against relative intensities, and these are characteristic of the unit cell and its constituents, databases are the used to match these lattice parameters and identify the materials. In GI-XRD a fixed angel of incidence with only the detector arm being moved, the incident angle can be varied with iterative scans to give information about the specimen at different depths while minimising the contribution from the bulk alloy. Specimens has characteristic d spacing related to their unit cells, as such X-ray diffraction can be used to identify

materials but their diffraction pattern which is compared to a database of standards and previously examined materials.

Thermal Programmed Desorption (TPD)

Thermal programmed desorption was used to probe the interactions of water at the surface of the iron oxides before irradiation. TPD can be described as 'the measurement of the rate of desorption of adsorbed molecules as a function of temperature'[11] and can be used to extract information about these processes. The application in this case can allows for the probing of bound molecules on the surface such as water to extract information about the binding energies, which will give information regarding the binding modes. TPD measurements were undertaken at The University of Notre Dame where a custom cell holding between 50-100 mg of powder in a crucible was heated from room temperature to 500 °C at a rate of 5 °Cmin^{-1} where the sample chamber pressure was 12^{-10} bar prior to heating. The cell holder is heated at this rate, and the desorption of bound molecules was detected using a Pfeiffer Prisma quadrupole mass spectrometer and mass to charge ratios of 14, 15, 16, 18, 28, 32, 40 and 44 were monitored throughout. Kinetic parameters can be calculated from the outputted data, activation energy correlating to desorption energies will increase as peak temperature increases. Peak temperature is not dependant on the sample initial coverage by an adsorbate. Peaks are be found by plotting temperature against relative pressure, Redhead's analysis can then be applied to calculate the binding energies of the peak maxima.[12, 13]

$$E_d = RT_p[\ln\left(\left(\frac{AT_p}{B_H}\right) - 3.64\right) \qquad \textbf{(5.1-6)}$$

R	=	Gas constant
A	=	1.00E+14
T_p	=	Peak temperature
B_H	=	Rate of heating in kelvin
E_d	=	Energy of desorption

Binding energies are indicative of the molecules/ atoms bound and their binding modes, it is possible to determine if a molecule is absorbed by chemisorption or physisorption.

UV-VIS spectroscopy

Hydrogen peroxide concentrations were determined using UV-Vis spectroscopy, utilising either a Thermo Scientific UV-Vis spectrophotometer (Notre Dame experiments) or an Agilent Technologies Cary Series UV-Vis-NIR spectrophotometer (DCF experiments).

UV-Vis spectroscopy utilises the absorption or reflectance of electromagnetic radiation in the visible and ultraviolet ranges, molecules or atoms in the target molecules undergo electronic transitions when exposed to UV or visible light. The apparent colour of a material is the light reflected by it, which is the complement of the incident light absorbed.[14] The amount of light absorbed by a chemical species is an intrinsic property related to species type as photons interact with the electrons in the matter. Materials have a characteristic absorption capacity, how strongly a substance absorbs light at a wavelength is known as the extinction coefficient. Calibrations can be used to calculate the extinction coefficient, ε, of a detection solution by using known concentration of solutions and measuring their absorbance. The value of ε can be calculated using beer lambert law:

$$A = \varepsilon Cl \qquad \textbf{(5.1-7)}$$

A	=	Absorbance
ε	=	Extinction coefficient $M^{-1}cm^{-1}$
C	=	Concentration of adsorbate M
l	=	Pathlength = 1

After calibration and calculation of ε, UV-VIS spectroscopy can be used to calculate concentrations of solutions of unknown values.

Source of Radiation and Dosimetry

This project utilised two γ-generating sources a cobalt-60 (Co^{60}), a self-contained Shepard cobalt-60 (Co^{60}) source at the University of Notre Dame. The second at the University of Manchester Dalton Cumbrian facility (DCF) which is a self-shielded Foss therapy source. ^{60}Co is synthetically produced by the neutron activation of Co-59, which then undergoes β-decay to form Ni-60 emitting gamma radiation in the process, this decay pathway is summarised in **Equation (**5.1-8**).**[15] The overall decay scheme can be seen in **Figure 5.1-5.** The γ-radiation emitted in this process is utilised in these radiation chemistry studies.

$$^{59}_{27}Co + {}^{1}_{n}n \rightarrow {}^{60}_{27}Co \rightarrow {}^{60}_{28}Ni + {}^{0}_{-1}\beta + 2{}^{0}_{0}\gamma \qquad \textbf{(5.1-8)}$$

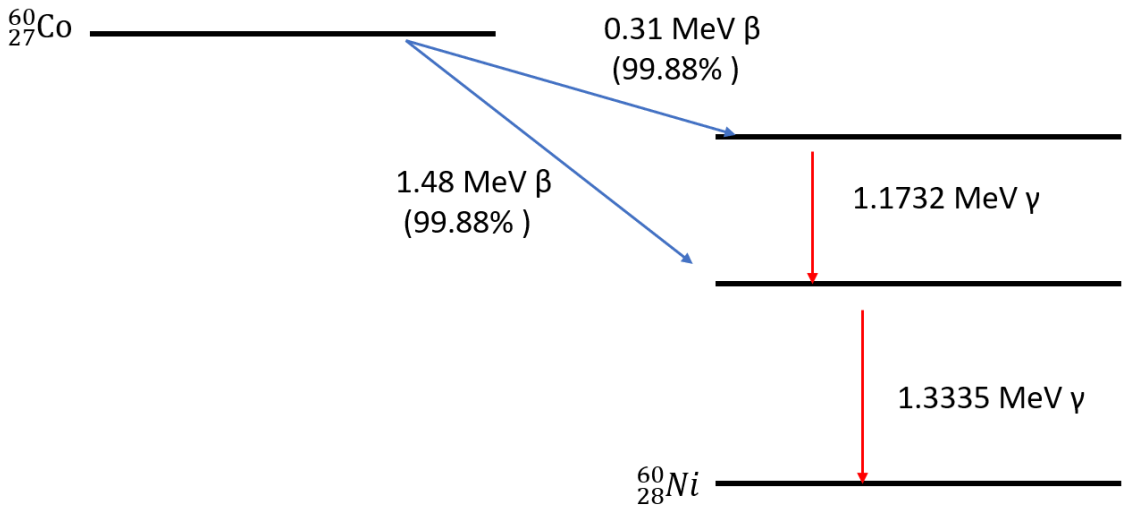

Figure 5.1-5. Schematic to show the radioactive decay that Co-60 undergoes producing gamma-rays that are utilised in many ways include use in radiation chemistry studies.

The systems used throughout this project use ^{60}Co rods that are self-shielded by various materials such as lead, during the irradiation period samples are either lowered into the radiation filed (the Shepard model) or the ^{60}Co are lifted from their housing into the experimental chamber (the Foss Therapy model). The Foss Therapy model at the University of Manchester was the most utilised throughout this study, with the HTHP recirculation facility being built to fit within this irradiators sample chamber. It is a bespoke build for the University of Manchester and allows for varied dose rates based on the position of samples in the chamber with respect to the source and the number of source rods used at a given time. The Foss therapy model is shown in **Figure 5.1-7** and sample chambers configuration showing dimensions and access ports **Figure 5.1-6.**

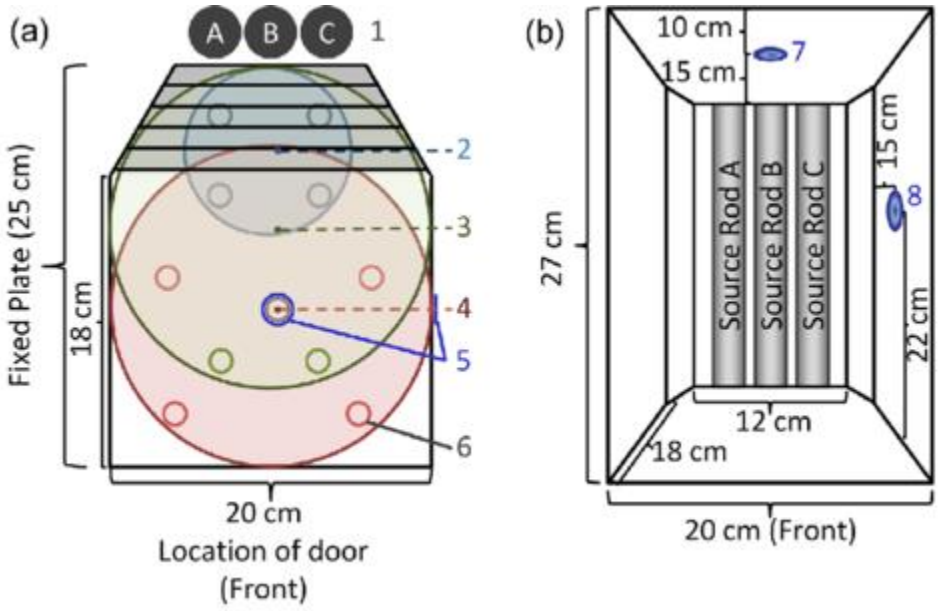

Figure 5.1-6. A schematic of the irradiation chamber showing its dimensions and access port configurations that were utilised during HTHP facility design and deployment.

Figure 5.1-7. The image on the right shows the inside of the Foss therapy irradiator, with the labelled components showing the position of the three guided rods that contain the ^{60}Co source that are utilised during irradiations

As described previously the determination of dose and dose rates can be by various dosimetry methods. Fricke dosimetry is a well-understood chemical dosimetry and was used in these studies to determine dose rates in both interaction and HTHP experimental studies. Standard Fricke solution has a concentration of 1 mol m^{-3} of ferrous sulphate in an acidified solution (0.4 mol dm^{-3} H_2SO_4). The concentration of ferric ions is monitored, these are produced via the interaction of Fe^{2+} with radiolysis radicals, hydroxyl groups and peroxides. The suggested routes to the Fe^{3+} is as follows:

$e_{aq}^- + H_3O^+ \rightarrow H + H_2O$ **(5.1-9)**

$H + O_2 \rightarrow HO_2\bullet$ **(5.1-10)**

$OH + Fe^{2+} \rightarrow Fe^{3+} + OH^-$ **(5.1-11)**

$Fe^{2+} + HO_2\bullet \rightarrow Fe^{3+} + HO_2^-$ **(5.1-12)**

$Fe^{2+} + H_2O_2 \rightarrow Fe^{3+} + OH^- + OH$ **(5.1-13)**

The response of the solution due to irradiation is assessed using UV spectroscopy, the solution absorbance is measured before and after irradiation. The absorbed dose is calculated, using the maximum value taken at ~304 nm.

The absorbed dose for chemical dosimeter is calculated by yield of radiation-induced products over the radiation chemical yield.[16]

$$\textbf{Absorbed dose } \mathbf{D(Gy)} = \frac{\textbf{yeild of radiation-induced product}}{\textbf{radiation-chemical yield}} \quad \frac{\textbf{mol kg}^{-1}}{\textbf{mol J}^{-1}}$$

(5.1-14)

When absorption spectroscopy is used to monitor dosimeter response Beer's law is assumed:

$$\text{moles product formed per m}^3 = \frac{\Delta A}{\Delta \varepsilon l} \text{ Gy} \qquad \textbf{(5.1-15)}$$

Substitution to calculate absorbed dose gives: [16, 17]

$$\textbf{Absorbed dose } \mathbf{D(Gy)} = \frac{\mathbf{(A_i - A_u)}}{\mathbf{G\varepsilon_m l \rho}} \qquad \textbf{(5.1-16)}$$

For the Fricke system the following is assumed:

$G(Fe^{3+})\varepsilon_{304} = 352 \times 10^{-6}$ $m^2\,kg^{-1}\,Gy^{-1}$ (25°C) and $\rho = 1024$ kg m^{-3} (for ^{60}Co γ rays).[16]

Which simplifies to:

$$\textbf{Absorbed dose D (Gy)} = \frac{\mathbf{280 \times (A_i - A_u)}}{\mathbf{L}} \qquad \textbf{(5.1-17)}$$

L = path length in cm

A_i = Absorbance of irradiated sample

A_u = Absorbance of unirradiated sample

Fricke dosimetry is only a reliable dosimeter when used for *absorbed doses* of less than 400 Gy, with conventional Fricke being used to determine doses of 40-400 Gy.[17, 18] For the HTHP pressure irradiation cells solid state dosimetry was also undertaken due to its higher radiation tolerance. These dosimeters work on the same principle, assessing the radio-chemical response in the selected material, assessed using UV-Vis spectroscopy. An example of this is radiation sensitive poly-methyl methacrylate (PMMA) which is optically transparent until it is irradiated and once irradiated it darkens with respect to the dose absorbed. The functional dose rate varies with the respective dosimeter type, with commercially available products having dose sensitivity from 0.1 kGy to 50 kGy dependant on colour selected.[19] The material darkening is observed using UV-Vis spectroscopy and the dose is then determined. The dosimetry procedure for the HTHP facility is described in further detail in **Chapter 6, Section 6.2.** The interaction studies utilised various dose rates which were determined by the position of samples within the irradiation chamber where a bespoke sample rack with predetermined dose rates that utilised Fricke dosimetry and updated based on the decay kinetics of the cobalt source. Possible sample positions are shown in **Figure 5.1-8** and the dose rate per position on 02.01.2017 and are labelled in $Gymin^{-1}$.

Dose rate in Gy min-1 for different states of attenuation

A	C

Table 1

192.90	245.64	238.00	209.55
125.59	144.33	151.27	136.70
84.65	92.98	96.45	87.43
61.06	64.53	65.92	63.14
45.80	47.18	47.88	46.49
33.31	34.69	35.39	33.31
27.06	27.76	27.76	27.06
20.12	22.20	22.20	22.20

Figure 5.1-8. Schematic of the positions available in the sample rack utilised for the interaction studies and the dose rate at each position as calculated for the date 02.01.2017.

References

1. N. B. Colthup, L. H. Daly and S. E. Wiberley, in *Introduction to Infrared and Raman Spectroscopy (Third Edition)*, eds. N. B. Colthup, L. H. Daly and S. E. Wiberley, Academic Press, San Diego, 1990, DOI: https://doi.org/10.1016/B978-0-08-091740-5.50004-1, pp. 1-73.
2. P. Coombe, K. Sandeman, C. Best and D. Brook, Raman, https://www.doitpoms.ac.uk/tlplib/raman/, 2018).
3. P. Analytical, Introduction to BET (Brunauer, Emmett and Teller), http://particle.dk/methods-analytical-laboratory/surface-area-bet-2/, 2018).
4. P. A. Webb, C. Orr and M. I. Corporation, *Analytical methods in fine particle technology*, Micromeritics Instrument Corporation, 1997.
5. S. J. B. Reed, *Electron Microprobe Analysis and Scanning Electron Microscopy in Geology*, Cambridge University Press, Cambridge, 2 edn., 2005.
6. NANOIMAGES, SEM Technology Overview – Scanning Electron Microscopy, http://www.nanoimages.com/sem-technology-overview/, 2018).
7. A. Walton, B. Spencer and A. Thomas, unpublished work.
8. Casa-Software-Ltd, CasaXPS: Processing Software for XPS, AES, SIMS and More, http://www.casaxps.com/, 2018).
9. P. Atkins and J. de Paula, *Atkins' Physical Chemistry*, OUP Oxford, 2010.
10. S. Speakman, Basics of X-ray Diffraction, http://prism.mit.edu/xray, 2018).
11. V. Rakić and L. Damjanović, in *Calorimetry and Thermal Methods in Catalysis*, ed. A. Auroux, Springer Berlin Heidelberg, Berlin, Heidelberg, 2013, DOI: 10.1007/978-3-642-11954-5_4, pp. 131-174.
12. P. A. Redhead, *Vacuum*, 1962, **12**, 203-211.
13. P. A. Redhead, *Vacuum*, 1963, **13**, 253-258.
14. B. J Clark, T. Frost and M. A Russel, *UV Spectroscopy techniques, instrumentation, data handling : UV spectrometry group / edited by B. J. Clark, T. Frost and M. A. Russell*, 2018.
15. B. Campus, *Journal*, 2019.
16. J. W. T. Spinks and R. J. Woods, *An Introduction to Radiation Chemistry* John Wiley & Sons United States of America 3edn., 1990.
17. A. Vertes, S. Nagy, Z. Klencsar, R. G. Lovas and F. Rosch, *Handbook of Nuclear Chemistry*, Springer, London, 2 edn., 2011.
18. A. Mozumder, *Fundamentals of Radiation Chemistry*, Academic Press, USA, 1999.
19. H. Dosimters, Perspex Dosimeters, http://www.harwell-dosimeters.co.uk/perspex/, (accessed 23.11.2015, 2015).

Chapter 6: The design and implementation of an experimental facility for radiolysis and corrosion studies under light water reactor conditions

6.1 Overview of the design and commissioning process

The design and commissioning of a HTHP recirculation loop, along with the development of an experimental program that include preliminary testing, is outlined in **Section 6.2.** The utilisation of the loop in an investigation on the effects of γ-radiation on the corrosion of Stainless-Steel 316 is described in **Section 6.3.** This facility was designed to be multifunctional, and the design process was an integral part of this EngD project. The early stages of this program were spent researching the equipment utilised in studying radiation at high temperature, and the methods and equipment using in corrosion testing and its monitoring. The design process involved collaborative work between expected users outlining the work that was to be undertaken. Initially focusing on the effects of radiation on corrosion and the transport of corrosion products and the effects of radiation on zinc acetate. Possible suppliers of corrosion testing equipment were shortlisted during this process with Cormet Testing systems being chosen having previously provided bespoke equipment to The University of Manchester. They were also able to provide the multifunctionality needed including several irradiation cells for the use in conjunction with the Dalton Cumbrian Facility's self-contained cobalt-60 gamma irradiator unit, and its 5 MV tandem pelletron heavy ion accelerator (DAFNE). It was decided to design a recirculation loop with four detachable irradiation cells, two for use with ɣ-radiation with separate cells for radiation chemistry and corrosion studies. And two more cells for the use with heavy ion radiation, again one cell for radiation chemistry and another for corrosion studies. The design paper in chapter outlines some of the considerations taken when designing a multifunctional piece of equipment and goes on to outline the results of the preliminary tests. Important design considerations included material selection and the effects of radiation on this and monitoring techniques for both system parameters and dependant variables. Design considerations included monitoring techniques such as in-situ electrochemistry, where material choice was essential so that it did not contribute to corrosion build up in examined samples. The focus of the work presented in this thesis was the design of this equipment and its utilisation in corrosion studies. The initial commissioning of the equipment was undertaken in

collaboration with Cormet testing systems. Preliminary testing allowed for an understanding of how the equipment works, the effects of ɣ-radiation on the system with no added chemical additives or metal alloys for testing, as well as dosimetry inside the larger ɣ-testing cell. These preliminary tests were carried out by Elizabeth Parker-Quaife with support from Aliaksandr Baidak, Jonathan Duff and Choen May Chan. Proton experiments outlined in **Section 6.2** were carried out by Gemma L. Draper. During these preliminary tests and subsequent work, it was decided not to continue using electrochemical methods for the corrosion tests outlined in this work, as the equipment had to remain available for multiple projects.

It was decided to corrode samples using a jig that hung from the autoclave lid and examine the effects of ɣ-radiation on the oxide film ex-situ using various surface characterisation and cross-sectional analysis. Design for this corrosion jig was supported by Samuel Holdsworth.

Modifications that arose during these early tests included the replacement of the pulsation dampener on the pressure pumps (due to possible oil leaks). The change of the cation exchange column was undertaken, switching to a smaller volume column allowing for the use of two cation exchange columns (one for lithiated conditions and one for pure water conditions). Unfortunately, the use of the recirculation loop with heavy ion irradiation cells was not undertaken during this work. The irradiation cell designed for corrosion study needs modification enable the use under vacuum at the end of the accelerator beam line. This decision was made after Stopping Range of Ions in Matter (SRIM) calculations showed that ensuring penetration through the sample would need a higher than desired beam voltage, increasing the likelihood of sample activation.

This HTHP equipment has been presented by Elizabeth Parker-Quaife in poster format at Faraday Discussion 2015,[1] with a presentation at the Rolls Royce Engineering Doctorate Conference 2015,[2] and at the International Nuclear PhD workshop run by the CEA in 2017.[3] The facility was also presented by Aliaksandr Baidak at the Nuclear Plant Chemistry conference in 2016.[4] The HTHP facility was used in the work outlined in **Section 6.3** where the effects of radiation of SS 316 corrosion was investigated. This work was carried out by Elizabeth Parker-Quaife with support from Jonathan Duff and Choen May Chan. Other projects that have utilised this recirculation facility include studies into the fundamentals of water radiolysis at high temperature[5] and the

effects of radiation on zircalloy, utilising electrochemical techniques including impedance measurements.

References

1. E. Parker-Quaife, A. Baidak, J. Duff, F. Scenini and S. Pimblott, London, 2015.
2. E. Parker-Quaife, S. Pimblott and F. Scenini, unpublished work.
3. E. Parker-Quaife, S. Pimblott and F. Scenini, Cadarache, 2017.
4. A. Baidak, J. Duff, H. Sims, E. Parker-Quaife and S. Pimblott, Brighton, 2016.
5. G. L. Draper, unpublished work.

6.2 Method development

Design and Implementation of a High Temperature High Pressure System for Investigating Radiation Induced Processes Under Simulated Light Water Reactor Conditions

Elizabeth Parker-Quaife,[1,2,*] Jonathan Duff[2], Alex Biadak,[1,2] Gemma L. Draper,[1,2] and Simon M. Pimblott[3]

[1]*The School of Chemistry, The University of Manchester, Manchester, UK*
[2] *Dalton Cumbrian Facility, The University of Manchester, Moor Row, Cumbria, UK*
[3]*Idaho National Laboratory, 1955 N. Fremont Ave., Idaho Falls, Idaho 83415, United States*

*Corresponding author: Elizabeth Parker-Quaife.

Email address: elizabethparkerquaife@gmail.com

Abstract

When considering new build Nuclear Power Plants (NPPs) and existing plant life extension, mitigation and minimisation of material degradation is crucial. Here we present the design and implementation of a system for investigating the effects of radiation on corrosion and corrosion related processes under Light Water Reactor (LWRs) conditions. Consideration has been taken to enable studies into the effects of radiation and system conditions on the radiolysis of water. The system was tested and used in conjunction with a self-contained cobalt-60 gamma irradiator unit, and its 5 MeV tandem pelletron heavy ion accelerator. Preliminary investigations probed the sensitivity of measurements for dissolved molecular hydrogen and oxygen, alongside changes in electrical conductivity when exposed to either gamma or proton irradiation at varied temperatures and flow rates. An unexpectedly high dissolved molecular hydrogen concentration was observed with exposure to gamma radiation along with an increase in conductivity possibly due to the use of commercial high-pressure pumps and cation exchange columns.

Keywords

High temperature water, simulated LWR coolant conditions, gamma irradiation, proton irradiation.

Abbreviations

HT – high temperature, HP – high pressure, LWR – light water reactor, NPP - uclear power plant, CRUD- corrosion related unidentified deposit, SRIM – stopping and range of ions in Matter, $[H_2]_{D,}$ dissolved hydrogen concentration, $[O_2]_D$ – dissolved oxygen concentration, EC- electrical conductivity.

Introduction

In the current energy arena, nuclear new build and reactor lifetime extension is a key part of maintaining a diverse energy portfolio and meeting projected increases in energy demand. Important considerations effecting the issues in Light Water Reactor (LWR) systems include material selection with an aim of minimising material degradation over reactor lifetime, and the radiation induced chemistry of the aqueous coolant. Chemical degradation of fuel cladding, core and structural materials presents a significant challenge. The corrosion and dissolution of structural materials leads to the accumulation of corrosion products (CRUD) throughout the primary circuit of the reactor. CRUD related phenomena have presented a number of safety and process efficiency implications, for example: enhanced out of core activity, axial offset anomalies, and reduced reactor performance.[1-5] The ability to predict material integrity, corrosion and CRUD behaviour (within a primary coolant system under LWR conditions) will facilitate more effective reactor design and operations to allow for the mitigation of corrosion processes, thereby safely extending current and future reactor lifetimes.

Direct examination of chemical and corrosion related processes under the extreme conditions of LWR conditions is difficult due to the presence of mixed radiation fields, high temperatures (HT), and pressures (HP), not to mention the complex chemistry of the aqueous coolant. Consequently, representative experimental data on the mechanisms of corrosion under LWR coolant conditions is limited.[6-17]

The design, development and commissioning of a research capability outlined attempts to circumvent some of these challenges by enabling the study of corrosion at high temperature and pressure (HTHP) under irradiation conditions. This capability comprises a HTHP recirculation system that can study either gamma or proton beam irradiations, while maintaining system parameters inside of an irradiation cell (autoclave); under temperature, pressure and water chemistry conditions comparable to LWR conditions. As far as the authors are aware, there are currently no other

multifunctional HTHP recirculation facilities that allow for the study of corrosion in-situ under gamma-irradiation conditions as well as the functionality for such ion beam studies. This HTHP recirculation systems utilised the university of Manchester's Dalton Cumbrian Facility's state of the art irradiation capabilities: a Foss Therapy Services Model 812 self-contained Curie cobalt-60 gamma irradiator, and a 5 MV NEC tandem pelletron ion accelerator, DAFNE. The commissioning and utilisation of these irradiation facilities has been outlined previously.[18, 19] This paper outlines the considerations taken in designing this HTHP recirculation research capability, the implementation of these considerations and the initial commissioning process with respect to chemical and corrosion investigations. The in-situ study of corrosion processes under LWR coolant conditions is complex, requiring;

- LWR conditions, system temperature and pressure;
- Variable 'coolant' flow rates with the ability to run the HTHP recirculation system under 'static' conditions;
- Dissolved gas concentration control and monitoring;
- Inlet and outlet monitoring of the 'coolant' to highlight radiolytic effects;
- Conductance measurements as an indication of corrosion behaviour;
- Electrochemical monitoring of corrosion samples;
- Use within the confined space of a gamma irradiation chamber;
- Multifunctionality, use with gamma irradiation or at the end of a DAFNE beam line and thus transportability;
- Materials selection of components due the implications of function and type of radiation exposure.

Method Development

Figure 6.2-1 give schematics of the system, showing the outline and possible flow pathways in the recirculation loop. **Figure 6.2-7** the supplementary information shows the complete loop schematic labelling the core components, alongside their descriptions in **Table 6.2-7**, information is taken from the manuals supplied by Cormet Testing Systems.[20]

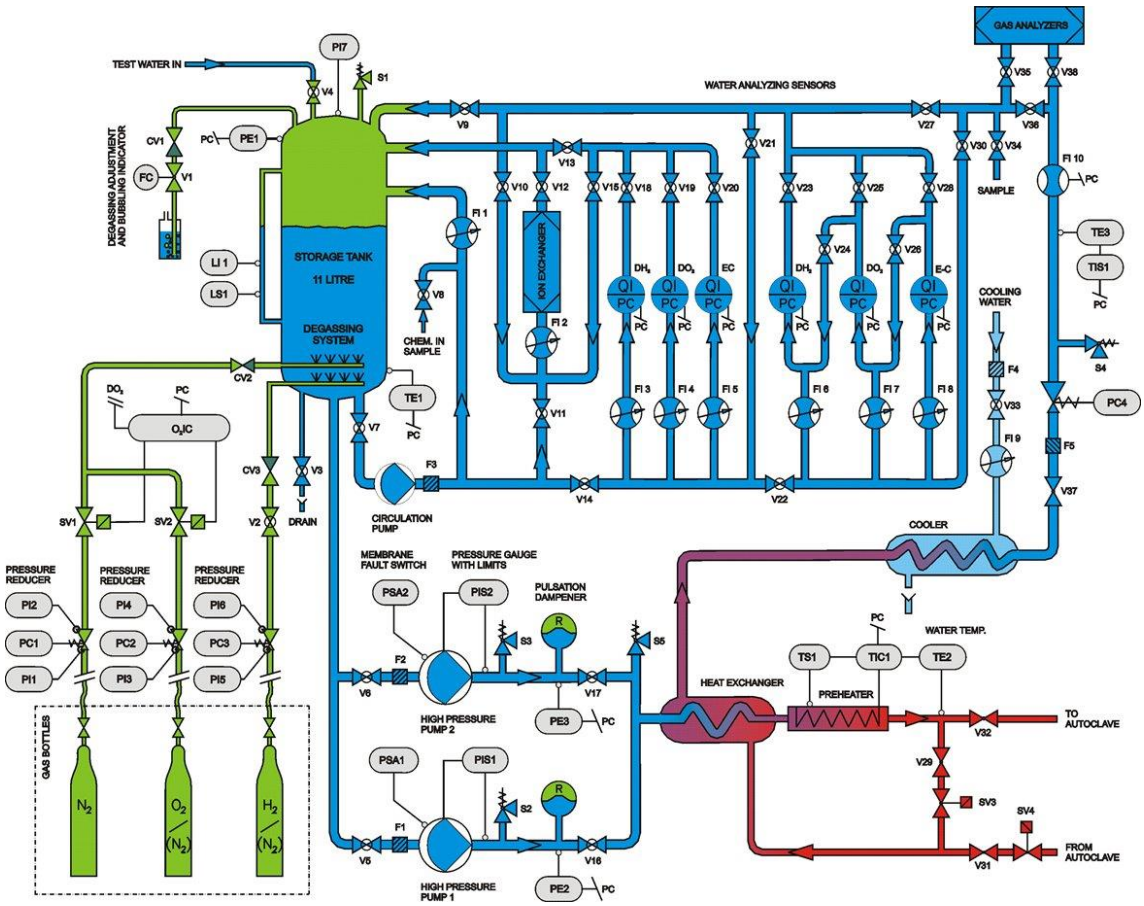

Figure 6.2-1. Schematic of the HTHP recirculation loop, showing the possible flow paths of the water to be heated and pressurised, and the monitoring systems present. (A blow up of this schematic can be viewed in the supplementary material)

Material selection

The biggest challenge in the design of the in-situ corrosion monitoring and autoclave systems is the material selection; as radiation affects both the irradiation cell parameters as well as possible the corrosion monitoring techniques. The desired experimental parameters require the simulation of LWR conditions with HTHP conditions with the addition of chemical additives that control coolant chemistry. Unfortunately, the extreme conditions and the additives used to help mitigate these enhance the corrosion of standard structural materials used in conventional autoclave systems. Simulating LWR conditions require system parameters of up to 350 °C and 220 bar of pressure but monitoring techniques require near ambient conditions consequently the loop was designed to have both hot and cold ‘legs.’

For sections of the HTHP recirculation system that are to be subjected to high and temperatures as well as exposure to ionising radiation, the most inert materials are necessary for autoclave body fabrication to reduce the possibility of autoclave corrosion product incorporation into a sample's oxide film. Consequently, Hastelloy C276 was chosen for hot parts of the loop as it possesses excellent universal corrosion resistance, with pitting and stress corrosion resistance exceeding that of stainless steel (SS) alloys.[21] The cold legs of the system were manufactured from AISI SS 316L as the corrosion resistance of this material is more than adequate under these less extreme conditions in this section of the system. The typical composition of these materials is outlined in **Table 6.2-1**.[20, 22]

Table 6.2-1. Composition of alloys used within HTHP recirculation system.

Grade	**Composition elements**								**Other**	
	Fe	Cr	Ni	C	Mn	Si	P	S	Mo	W	
316	Balance	16-18	10-14	0.08	2	1	0.045	0.003	2.0 - 3.0	n/a	n/a
316 L	Balance	16-18	10-14	0.03	2	1	0.045	0.003	2.0-3.0	n/a	n/a
C276	5	16	57	0.01	1	0.08	n/a	n/a	16	4	V 0.35, Cu 0.5

Table 6.2-2. Opeating pressures and temperature as well as material selection for HTHP recirulation system.

Low Pressure Side	
Max design / operation pressure	0.6 MPa / ~0.1 - 0.2 MPa
Max design / operation temperature	60 °C / 25 – 40 °C)
Material	AISI 316L, polymers
High Pressure Side	
Max design / operation pressure	20 MPa / 20 MPa
Max design / operation temperature	350 °C / 350 °C
Material	C-276 (hot parts), AISI 316L

Autoclave systems must also hold pressure and be leak proof. These requirements are commonly met through use of gaskets, typically composed of either Polytetrafluoroethylene (PTFE), Grafoil, or metal alloys. PTFE is as degrades under irradiation producing hydrofluoric acid (HF), which is incredibly corrosive and toxic. Thus, all PTFE components cannot be used and were replaced with more suitable alternatives - the radiation resistance of potential plastics is outlined in **Table 6.2-3.** None of the alternatives fulfilled both temperature and radiation resistance requirements necessary for the HTHP recirculation system. Grafoil (a graphite-based material) exhibits greater radiation resistance than PTFE and the other plastic formulations, but the lifetime of gaskets made from Grafoil under more extreme radiation are unknown. Consequently, nickel based metallic gaskets were used, as they provide the radiation stability and structural integrity needed as well as the pressure and leak seal requirements. Another important consideration for material selection in this system is the material to be used in the ^{60}Co irradiation autoclave for electrochemistry experiments. For HTHP work it is an industry standard to use PTFE components for electrical connections, insulation and for any electrochemistry components due to its temperature and chemical tolerance and its properties as an insulator. Wires are insulated with carbon fibre and other components are made from ceramic, both of which have good radiation tolerance compared to PTFE. Another investigation path for this is too use PEEK but its limited tolerance to high temperature an external reference electrode system was required. The electrochemical components for this work are in the supplementary material, discussing the considerations taken to overcome the outlined challenges associated with high temperature and pressure electrochemistry under irradiation conditions.

Table 6.2-3. Outline of selective plastic tolerances to temperature and radiation and thermal conductivity and surface resistance for electrochemical considerations.

Plastic	**Radiation Tolerance (**kGy**)**	**Temperature Tolerance**	**Comments**
Polytetrafluoroethylene (PTFE)	5	MP 327 °C Upper service temperature 260	Evolves HF Thermal conductivity 0.2 Surface resistance 10^{16} Ω
Ethylene-Tetrafluoroethylene (ETFE)	1,000	MP 267 °C Service temp 150°C	Surface resistance 10^{14} Ω $>10^{14}$
Aromatic polyamide	10,000		
Polyimide	10,000	Non-specific MP but can withstand high temperature. Tg assumed to be 360-410 °C	
Polystyrene	10,000	240 °C but decomposes at lower temp	Discolouration at lower doses
Polyesters, *PETE*	100,000	Upper working temperature 115 – 170 °C	Surface resistance 10^{14} Ω 0.13-0.15
Polyether ether ketone, PEEK	10,000	Thermal distortion at 162 C, TG 150 °C, MP 350 °C	Thermal conductivity 0.25 W/m.K Surface resistance 10^{14} Ω

Irradiation Cells

The HTHP recirculation system has been designed to have interchangeable irradiation cells (four autoclaves), each designed with a specific application in mind. The intended purpose and specification of the cells are outlined in **Table 6.2-4** and each cell is shown in the photographs in **Figure 6.2-2. Table 6.2-4** summarises speculative experimental scenarios and the features that make each irradiation cell suitable.

Table 6.2-4. HTHP recirculation system irradiation cell types, design specification, and intended application.

Irradiation Cell	Design specification Pressure/Temp / Volume	Material	Intended Use	Specific design features
Gamma cell 1 (**Figure 6.2-2 A**)	220 bar / 200 MPa 350 °C 50 mL	Alloy C-276-wetted parts AISI 316	Gamma radiolysis behaviour of LWR coolant	Smaller volume allowing for higher dose rate control
Gamma cell 2 (**Figure 6.2-2 B**)	220 bar / 200 MPa 350 °C 250 mL	Alloy C-276-wetted parts AISI 316	Corrosion tests/ electrochemical studies	3 feedthroughs that allow for electrodes or probes. Including 2 removal ceramic feedthroughs allowing high temperature electrochemical studies Internal volume and fixture ports to allow for attachment of corrosion jigs
Proton beam cell 1 (**Figure 6.2-2 C**)	220 bar / 200 MPa 350 °C 3 mL	Alloy C-276-wetted parts AISI 316	Proton radiolysis behaviour of LWR coolant	Smaller volume for less contact area and greater dose control.
Proton beam cell 2 (**Figure 6.2-2 D**)	220 bar / 200 MPa 350 °C 5 mL	Alloy C-276-wetted parts AISI 316	Corrosion test, Electrochemical studies	Internal platinum counter electrode and separate reference electrode. The irradiation window can be both a corrosion sample and a working electrode which is electrochemically isolated from the rest of the cell.

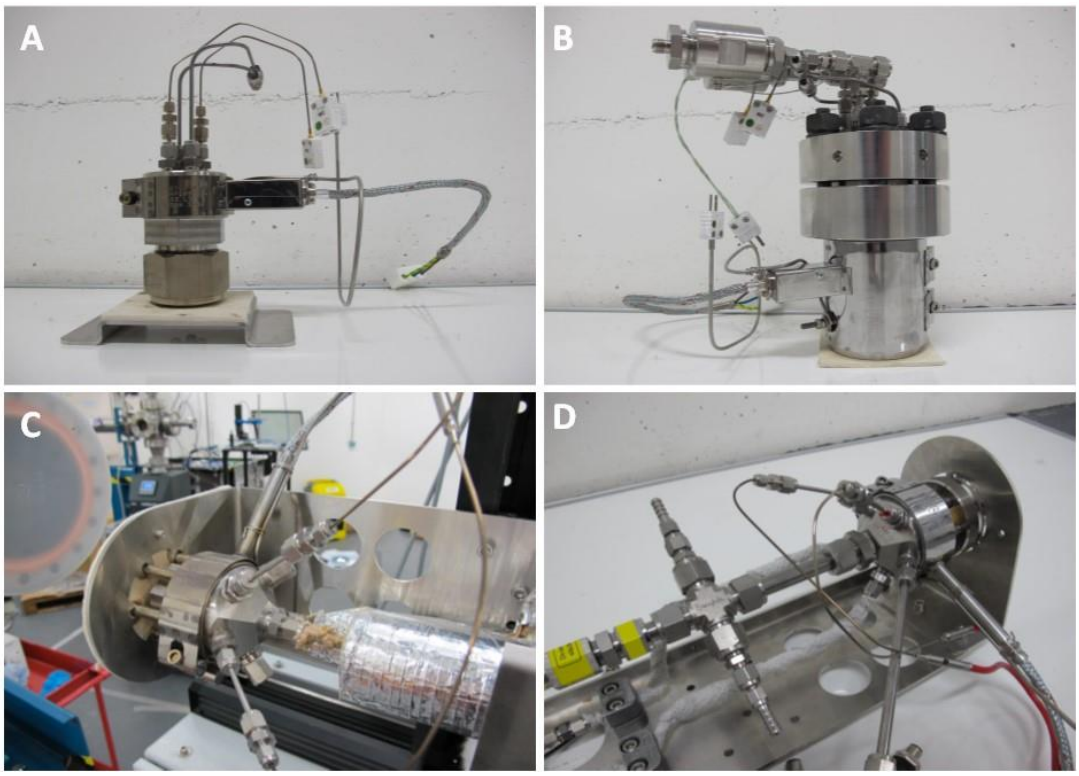

Figure 6.2-2. HTHP recirculation system irradiation cell designs: (A) small gamma autoclave; (B) large gamma autoclave; (C) water radiolysis heavy ion autoclave; (D) electrochemical heavy ion autoclave.

Experimental discussion

Preliminary experiments were undertaken for system commissioning and proof of concept. These experiments included establishing irradiation cell dosimetry, sensor response tests and corrosion robustness of the systems for both gamma and proton irradiation scenarios. The results presented demonstrate that the HTHP recirculation system can maintain and monitor a variety of conditions not limited to that of simulated LWR coolant.

Large Gamma Autoclave Experiments

Dosimetry

The estimated dose received by samples in the autoclave shown in **Figure 6.2-2 B** was measuring using both solid state and chemical dosimetry. Solid state dosimetry was performed by using two kinds of Harwell Perspex dosimeters composed of slightly different amber and red poly-methyl methacrylate (PMMA) respectively. Positioning of the solid-state dosimeters in the autoclave lead to slightly different received doses, giving an average approximate centreline dose rate of 36.98 Gy/min. The absorbance

values are determined using UV-Vis spectroscopy, Absorbance measurements are taken post irradiation as well as measurements on dosimeter thickness, the maximum absorbance is divided by thickens. This value allowed the dose to be found using the provided look-up table. The absorbance values were taken at 640 nm for the red dosimeter and at 651 nm and 603 nm for the amber dosimeter types.[23] Positions for the dosimeters are shown in the supplementary information. Fricke dosimetry was also undertaken by using sample vials containing the Fricke solutioned positioned centrally inside the autoclave. Fricke dosimetry utilises the oxidation of ferrous ions to ferric ions by the products of radiolysis. The absorbance of the solution is then taken and absorbed dose calculated using **Equation (6.2-1).**[24] The Fricke dosimetry yielded dose rates of 21.6 Gy/min and 35.23 Gy/min, dependent on when the values were taken as during these preliminary the self-contained Curie cobalt-60 gamma irradiator was refuelled. The absorbed dose from Fricke is calculated using the below formula:

$$\text{Absorbed dose D (Gy)} = \frac{280 \times (A_i - A_u)}{L} \qquad \textbf{(6.2-1)}$$

Response to Gamma Irradiation

To evaluate the performance monitoring sensors, deaerated deionised water was recirculated at varying flow rates and temperatures. Electrochemical conductivity was monitored alongside dissolved oxygen and hydrogen concentrations. For these experiments and subsequent corrosion tests, electrochemical feedthroughs were removed as they were not being used and may have added to experimental uncertainties. The experimental conditions used are outlined in **Table 6.2-5.**

Once $[O_2]_D$, $[H_2]_D$ and EC reached a stable value, ɣ-radiation was applied for an hour at ~36 Gy/ min (2.16 kGy total dose). After irradiation the monitoring parameters were left to re-stabilise, the flow rate was then changed, and the experiment repeated. This procedure was repeated for ambient, 50, 100 and 200 °C temperatures with flow rate of 3.2 kg/hr and 0.65 kg/hr. The results are reported in **Figure 6.2-3** with measured quantities plotted against the time elapsed. At the flow rate of 0.65 kg/ hr the 200 °C experiment was terminated early as the flow and monitored parameters did not stabilise. At lower flow rates the sensors appear to report less accurate results due to the limited flow, which was below the sensors preferred minimum flow rate.

Table 6.2-5. Outline of preliminary experiment conditions

Test number	Flow (kg/hr)	Temperature (°C)	Gas conditions
1, 3, 5, 7	3.2	25, 50, 100, 200	Deaerated
2, 4, 6	0.65	25, 50, 100	Deaerated

Figure 6.2-3 gives the parameters monitored throughout the gamma irradiation tests, with electrochemical conductance and dissolved molecular hydrogen and oxygen, of the water into and out of the irradiated cell reported. The shaded areas indicate the hour long ɣ-irradiations, this is an overview of the experiment showing the trends associated with the exposure to ɣ-radiation (larger reproduction in the supplementary material). **Figure 6.2-4** is a focused view of the system at 50 °C and gives the focused view of the trends observed in the systems during these investigations.

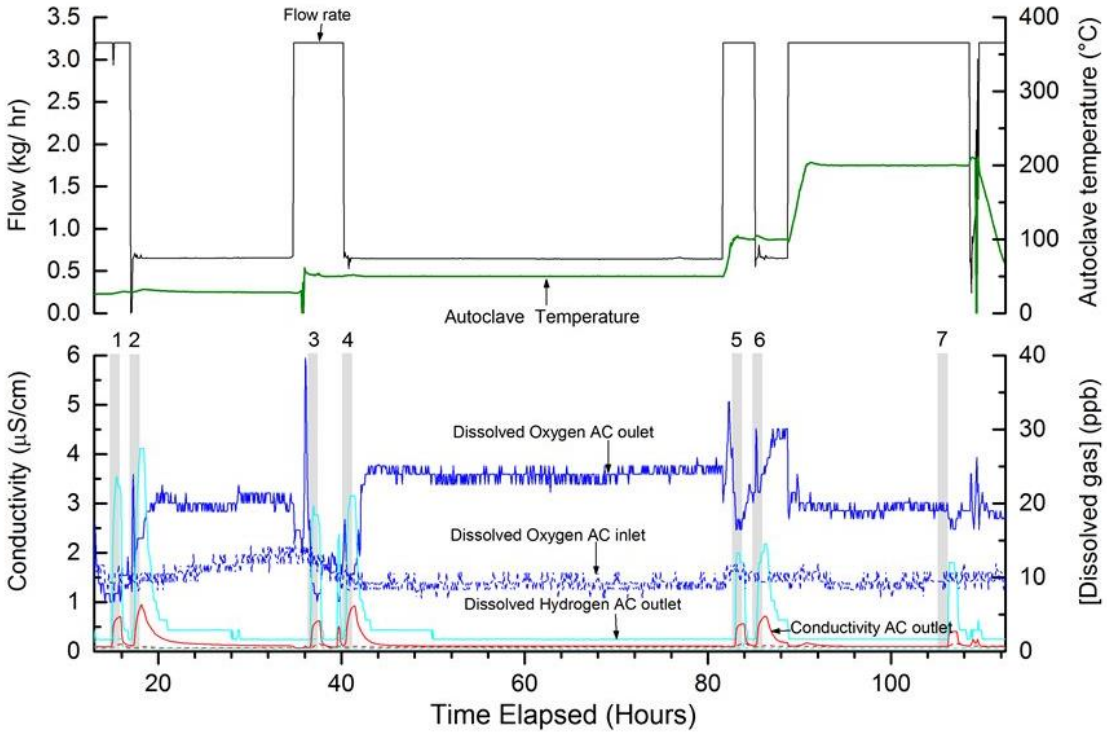

Figure 6.2-3. Outline of the full commissioning investigation, it reports the dissolved [H_2] (cyan), [O_2] (blue), electrical conductivity (red for autoclave inlet and outlet), flow rate (black) and autoclave temperature (green). Data has been decimated to removed noise created by the digitalisation of sensor data, shaded areas indicate the hour long ɣ-exposure times.

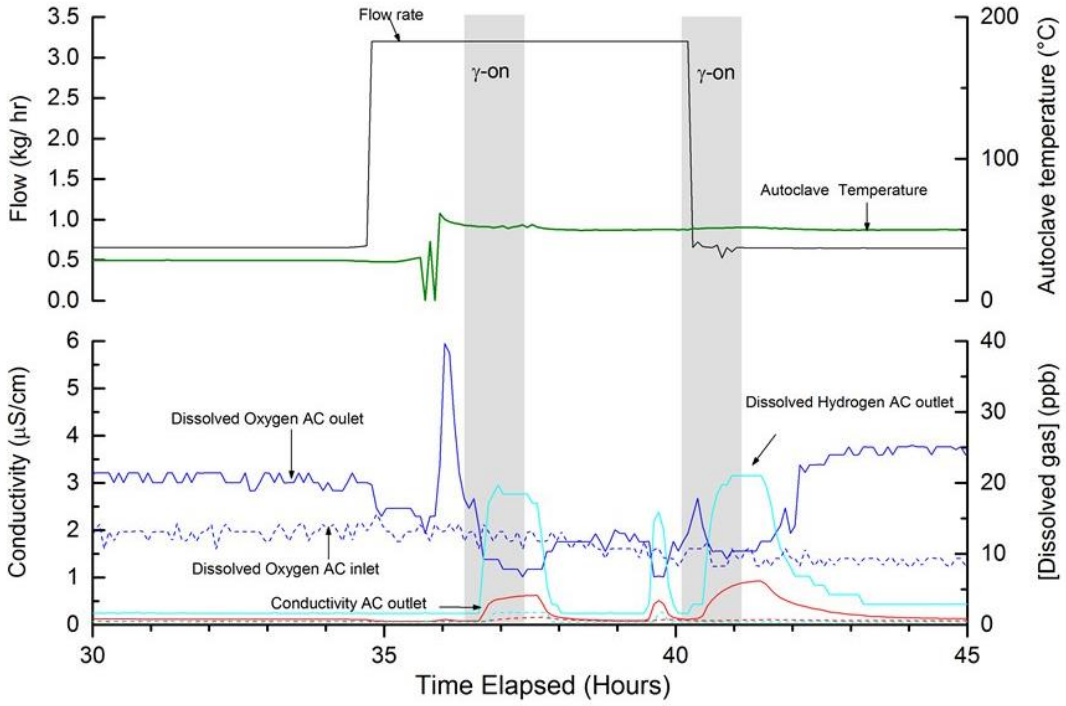

Figure 6.2-4. An example of the system parameters at 50 °C to give a clearer indication of the system changes due to ɣ-irradiation. Shaded areas indicate the ɣ-radiations.

Key observations:

- Increase in $[H_2]_D$ with onset of ɣ-radiation, which continues for a short period after radiation is terminated before returning to a low background concentration;
- Increase in electrical conductivity associated with onset of ɣ-radiation and follows a similar trend to that of the hydrogen concentration changes
- Increasing in $[O_2]_D$ associated with decreased flow rate and increased temperature;
- Decrease in $[O_2]_D$ associated with increase in hydrogen concentration.

The increase in dissolved oxygen associated with the change in flow and temperature is associated with sensor response and its adjustment for these change in parameters. The oxygen sensors used are orbisphere G1110 sensors that work on luminescence principles, a fluorescence spot is excited by blue light and a red luminescent light is detected. The presence of oxygen changes the decay of the detection light; using a calibration curve this is transformed into oxygen partial pressure.[25] The changes in oxygen concentration related to the reduction in flow rate may be due to sensor

response, the response time is up to 30 seconds with preferred flows rates between 20 to 200 mL/min.[25] The lower flow rate of 0.65 L/hr gives a value of 10.83 mL/min which may explain the higher recorded oxygen concentrations without an increased oxygen over pressure. The increase in oxygen seen with increased autoclave temperature as the sensors depend on temperature, once temperature is reached and plateaus sensors adjusts for the change in temperature of the sampled water.[26]

Discussion of hydrogen concentration

Arguably, the most interesting outcome of these experiments is the increase in hydrogen with ɣ-irradiation and the associated electrochemical conductivity increase. An increase in hydrogen is expected in these types of systems as an outcome of water radiolysis, but as the systems were un-scavenged a lower yield is expected. The substantial increase in electrical conductivity (EC) was not expected as in non-irradiated systems this increase is not observed. The increase in electroconductivity is unexpected as water radiolysis products do not account for this. The yield for radiolysis is generally reported as a G-value which is defined as the number of molecules generated per 100 eV of absorbed energy (1 *G* unit is 1.0364×10^{-7} mol of material changed per joule of energy).[24] The product yield ($G(H_2)$) for pure water exposed to ɣ-radiation is well documented and has a value of approximately 0.45 in traditional units.[24, 27] The product yield $G(H_2)$ refers to the experimental values determined form measured hydrogen concentrations. These systems use scavengers to promote H_2 production due to the difficulties with measuring hydrogen in un-scavenged systems, however it is expected to be negligible in the studies reported here.[28, 29] Calculating the yield using the $[H_2]_D$ from integrating the peaks for the irradiated system at ~25 ℃, and flow rate of 3.2 Kg/hr gives ($G(H_2)$) = 0.66, these calculations use the autoclave volume of 250 mL to calculate both the number of molecules and the dose received in eV. The G-values for all tests have been calculated using integrated peak values and density corrected values are reported as temperature and pressure affect the density of water. **Table 6.2-6** reports these values alongside the total dose received and test parameters. The $G(H_2)$ values reported are experimental values showing a trend of decreasing with temperature. This trend opposes the calculated data reported by Elliot and Bartels where the $g(H_2)$ (which is the homogenous yield of primary species once they have left a spur)[27] were with increasing temperature $g(H_2)$ increases from 0.44 at 25 °C to 0.76 at 350 °C, their

value at 200 °C is 0.51. The values reported by Elliot and Bartels are of the radiolysis of light water at low LET but are calculated using data from many experimental tests, very few of which used un-scavenged water which means although comparison will give so insight into behaviour a direct comparison is not possible. The values reported here also show a large difference between $G(H_2)$ for the two flow rates, with values much lower for flow rates of 0.65 kg/hr. At 0.65 kg/hr accuracy of the measurements may be affected by detector sensitivity with this flow being below the minimum required flow rate.

Table 6.2-6. $G(H_2)$ values for the preliminary irradiation tests, alongside flow rate and temperature.

Test number	Flow rate (kg/hr)	Temperature (°C)	Total dose received (Gy)	$G(H_2)$ after density correction
1	3.2	25	168.75	0.65
2	0.65	25	830.77	0.25
3	3.2	50	168.75	0.57
4	0.65	50	830.77	0.19
5	3.2	100	168.75	0.41
6	0.65	100	830.77	0.14
7	3.2	200	168.75	0.43

These values for the flow rate of 3.2 kg/hr at 25 °C is higher than the literature value which is unexpected; combined with the increase in electrochemical conductivity it could be argued that there is unexpected species present (an impurity) that is acting as a scavenger, and this is being ionised inducing an increase in EC. The routes for hydrogen formation are outlined below in **Equations (6.2-7)**, with the hydrogen radical recombination a key process. The processes preventing the build-up of hydrogen radiolysis products, scavenging species or impurities are outlined in **equations 6.5-7**. The hydroxyl radical plays an important role in removing the hydrogen radical as well as reacting with molecular hydrogen to prevent a concertation build-up. The presence of a scavenger or impurity enables removes of these hydroxyl radicals and promotes [H_2] increase by altering the mechanisms in which it may be removed.

$$H^{\bullet} + H^{\bullet} \rightarrow H_2 \quad \textbf{(6.2-2)}$$

$$H^{\bullet} + e_{aq}^{-} \rightarrow H_2 \quad \textbf{(6.2-3)}$$

$$e_{aq}^{-} + e_{aq}^{-} \rightarrow H_2 + 2OH^{-} \quad \textbf{(6.2-4)}$$

$$HO^{\bullet} + H^{\bullet} \rightarrow H_2O \quad \textbf{(6.2-5)}$$

$$HO^{\bullet} + H_2 \rightarrow H_2O + H^{\bullet} \quad \textbf{(6.2-6)}$$

$$HO^{\bullet} + RH \rightarrow H_2O + R^{\bullet} \quad \textbf{(6.2-7)}$$

The reduction of G(H_2) that occurs with temperature during these tests supports the presence of an impurity, with products thermal degradation of these interfering with spur chemistry and therefore preventing hydrogen formation. The reduction in electrochemical conductivity with temperature also supports a change in radiolysis behaviour, and possible degradation of impurities. The source of these impurities has not been identified. The water added to the system is deionised, and there are no measurable impurities. Possible sources of contamination include the use of cation exchange resins and impurity leaching from membranes / seals in pumps and sensors used within the circulation loop. The removal of these system components is not possible, and the issues is not present in non-irradiated conditions. For most of the recirculation applications this is an issue that can be accounted for in experimental procedure and analysis. Applications where the aim is to monitor water radiolysis, the use of the ion exchange column can be avoided by using a ‘once through flow path’, with the electrochemical conductivity into the autoclave being a good indicator for water purity in systems without chemical additives.

Corrosion experiments

Stainless Steel Type 316 coupons were cut 10 mm by 20 mm (W × H), and a 0.5 mm (diameter) hole drilled to allow for hanging inside of an irradiation cell, the samples were prepared to OPS finish on the front side and 800 grit on the back side. The samples were hung inside of the autoclave using a specially designed hanging jig, allowing for four samples at a time to be oxidised while preventing them from touching one another or the autoclave sides, thereby avoiding/minimising galvanic effects. Two oxidation tests were run for 95 hours at a system temperature of 288 °C and pressure of 200 bar. A flow rate of 3.2 kg/hr was used for the irradiated test and 1.5kg/hr for non-irradiated test at these low flow rates this difference will not affect the results. The dissolved molecular hydrogen and oxygen concentrations, electrical conductivity, pressure, temperature and flow rate were monitored and recorded throughout. The total dose received by the irradiated samples was ~123 kGy as determined by Fricke dosimetry.

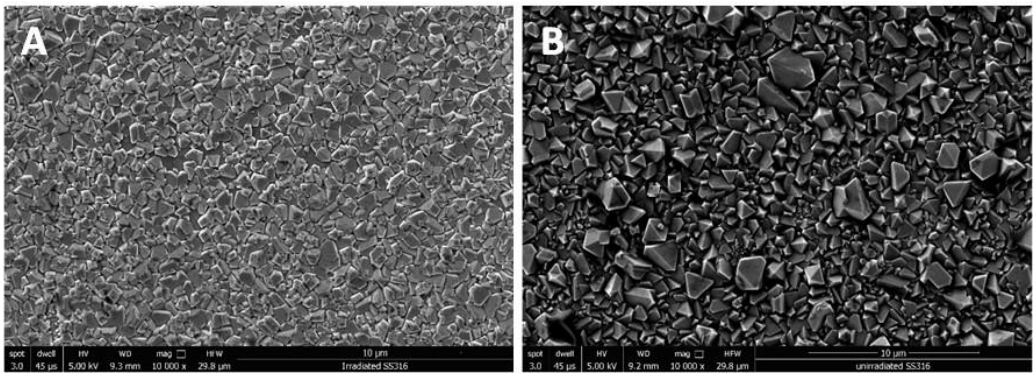

Figure 6.2-5. SEM 10K X image of SS 316L oxidised: (A) with ɣ-irradiation at 288 °C and 200 bar pressure for 95 hours; (B) at 288 °C and 200 bar pressure for 95 hours.

Typical SEM images of the coupons are shown in **Figure 6.2-5**. These were taken using a FEI Quanta FEG 250 scanning electron microscope using 5 keV electrons with secondary electron detection. The images indicate successful oxidation of both coupons supports and validates the use of the HTHP recirculation system for corrosion studies. Comparison of the two coupons (in **Figure 6.2-5**) reveals a significant difference in oxide morphology. Oxide coverage is less in the ɣ-irradiated sample, the oxide appearance is less uniform with an apparent rougher surface and crystals being visibly smaller in size. Further examination of the respective oxides is underway using

cross sectional SEM utilising EDS analysis for composition and X-ray diffraction for oxide structure.

Beam Line Experiments

(Carried out by G. L. Draper)

The HTHP recirculation system's irradiation cells were designed for investigating radiation induced water and corrosion chemistry. Heavy ion irradiations were performed using a 5 MV NEC 15SDH-4 pelletron tandem heavy ion accelerator, retrofitted with fast acting valves in case of irradiation cell failure. This proof of concept experiment used a cell designed for both accelerated proton penetration and electrochemical measurements. The cell window was composed of a Hastelloy bursting disc, allowing proton beams with energies in excess of 7.5 MeV to penetrate. Beam penetration and energy loss calculations were performed using SRIM. As the current irradiation cell design could not be used under vacuum, 7 MeV of proton energy was expected to be lost through the air gap and Hastelloy window. Consequently, for the proofing tests performed here using a 7.5 MeV proton energy with 10 nA ±10% of beam current, only 0.5 MeV was expected to be deposited into the cell's contents, i.e. water. Modifications to irradiation cell design to allow for use under vacuum would allow for lower proton energies to be used, thereby lowering chance of cell window activation, and allowing for greater amounts of energy to be deposited within the sample.

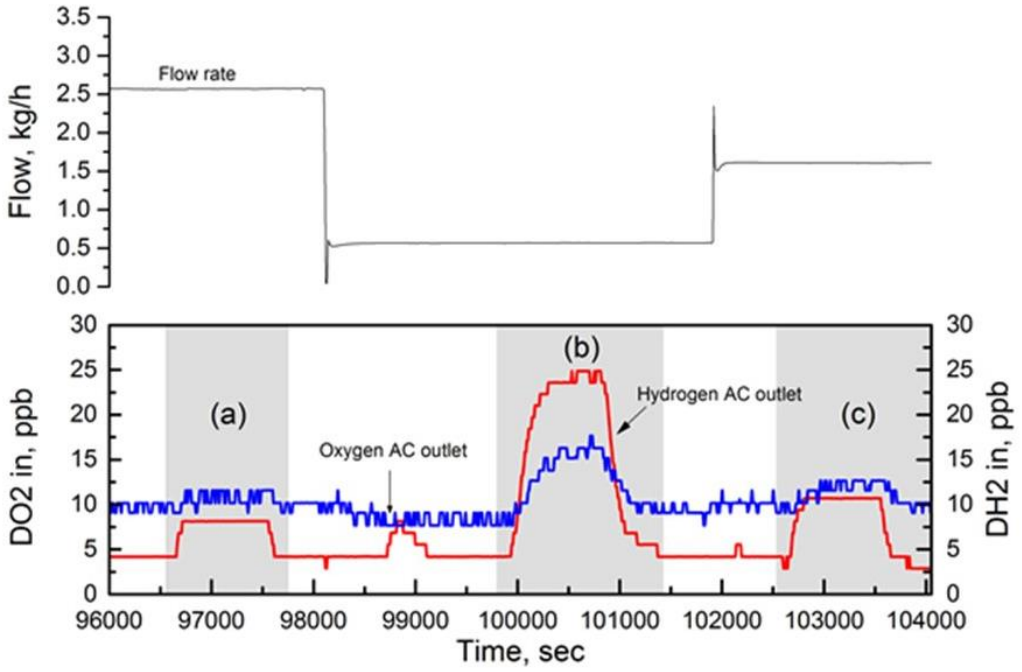

Figure 6.2-6. Dissolved [H_2], [O_2] and flow rate against time on irradiation cell outlet and varied flow rates during 7.5 MeV proton irradiation, with shaded areas showing the 15-minute irradiation period.

Preliminary beamline experiments investigated the effect of proton irradiation on aqueous solutions containing potassium bromide (1mM), sodium nitrate (1mM), and sodium formate (10 mM), the results for which are given in **Figure 6.2-6.** The purpose of these additives was to scavenge specific water radiolysis products, bromide and formate for hydroxyl radicals and nitrate for hydrated electrons and to a lesser extent hydrogen atom, thereby evaluating the sensitivity of the in-situ sensors. The HTHP recirculation system was run at room temperature and the flow varied between 0.5 and 2.5 kg/hr, bypassing the cation exchange column due to high scavenger concentrations. Proton irradiations were carried out for 15 minutes at a time, with system parameters being monitored throughout and special attention paid to dissolved molecular hydrogen and oxygen concentrations leaving the irradiation cell's outlet.

As demonstrated in **Figure 6.2-6**, a similar trend in dissolved gas concentrations can be seen in the proton irradiations as in the gamma-irradiated experiments an increase in molecular hydrogen associated with the irradiation periods. However, the concentration of dissolved molecular hydrogen is lower than that measured in the corresponding gamma experiments. This may be due to the use of a once through regime, with the water not flowing through the cation exchange column, or due to presence of the various scavengers. Caution should be exercised when considering the

two systems due to the difference in experimental set-up. The slight increase in dissolved oxygen is associated with the increased LET of proton radiation. Higher LETs favour second-order processes within the diffusion-kinetics regime of a radiation chemical track, thereby enhancing the concentration of molecular species. The presence of the scavengers may also contribute to oxygen formation. For example, the bromide scavenger reaction scheme can yield oxygen by the removal of superoxide by Br_3^- ions.[28] The increased values of both gases at lower flow rates can be attributed to a combination of longer exposure times and reduced sensor sensitivity with decreased flow rate.[25, 30] Future experiments are planned to further investigate the effects of these scavengers on the response of the HTHP recirculation systems, as well as investigating the minimum proton energy needed to produce a reproducible quantitative response in the system's sensors.

Highlights

A HTHP recirculation system was designed and commissioned at The University of Manchester's Dalton Cumbrian Facility. The commissioning process involved dosimetry calculations, monitoring system parameters in deaerated water exposed to ɣ-radiation, as well as corrosion experiments. Gamma irradiation experiments revealed unexpected increases in molecular hydrogen production relative to pure water. This has been attributed to impurities possibly originating from the cation exchange column, system membranes or seals, or the commercial high-pressure pumps. This is an important finding, as cation exchange columns are an industry standard for the removal of particulates and containments, and thus cannot be avoided. This warrants further investigation into the identity of the contaminant(s), so as to design procedures to mitigate their influence. Corrosion experiments established that the HTHP recirculation system may be used to oxidise samples under ɣ-irradiation, with dose rates up to ~36 Gy/min using a self-contained Curie cobalt-60 gamma irradiator. DAFNE beamline experiments demonstrated proof of concept, with scavenged water being exposed to 7.5 MeV protons with observable differences in dissolved oxygen and molecular hydrogen. Further work is needed to modify the current irradiation cells to allow for use with a vacuum system, thereby lower proton energies can be used for sample penetration. The successful design and commissioning of the HTHP recirculation system presents many opportunities to investigate materials

and LWR chemistry under extreme conditions of temperature, pressure and intense irradiation.

Author Information

Corresponding Author: Elizabeth Parker-Quaife

E-mail: elizabethparkerquaife@gmail.com

Acknowledgements

This work was supported by the UK Engineering and Physical Sciences Research Council **(Grant EP/G037426/**1) in conjunction with Rolls Royce PLC. The authors would like to thank the supporting staff at the Dalton Cumbrian Facility, a joint endeavour by the UK Nuclear Decommissioning Authority and The University of Manchester, and those at the Manchester Materials performance centre without whom this work would not have been possible.

References

1. M. Le Calvar and I. De Curières, in *Nuclear Corrosion Science and Engineering*, Woodhead Publishing, 2012, DOI: https://doi.org/10.1533/9780857095343.5.473, pp. 473-547.
2. C. F. Baes Jr and T. H. Handley, *Maritime Reactor Program Annual Progress Report*, Oak Ridge National Laboratory, United States of America, 1961.
3. P. B. Cohen, *Water Coolant Technology of Power Reactors*, New York : London and Breach, New York, 1969.
4. P. Rudling, A. Strasser, B. Cox, F. Garzarolli, S. Odar and R. Adamson, LCC 9, Bilboa, Spain, 2014.
5. R. A. Castelli, *Nuclear Corrosion Modelling*, Butterworth-Heinemann, Elsevier, Oxford, United Kingdom, 2009.
6. K. Daub, X. Zhang, J. J. Noël and J. C. Wren, *Corrosion Science*, 2011, **53**, 11-16.
7. K. Daub, X. Zhang, J. J. Noël and J. C. Wren, *Electrochimica Acta*, 2010, **55**, 2767-2776.
8. K. Daub, X. Zhang, L. Wang, Z. Qin, J. J. Noël and J. C. Wren, *Electrochimica Acta*, 2011, **56**, 6661-6672.
9. Q. W. Knapp and J. C. Wren, *Electrochimica Acta*, 2012, **80**, 90-99.
10. B. Muzeau, S. Perrin, C. Corbel, D. Simon and D. Feron, *Journal of Nuclear Materials*, 2011, **419**, 241-247.
11. M. Wang, S. Perrin, C. Corbel and D. Féron, *Journal of Electroanalytical Chemistry*, 2015, **737**, 141-149.
12. S. S. Raiman, A. Flick, O. Toader, P. Wang, N. A. Samad, Z. Jiao and G. S. Was, *Journal of Nuclear Materials*, 2014, **451**, 40-47.
13. S. S. Raiman, D. M. Bartels and G. S. Was, *Journal of Nuclear Materials*, 2017, **493**, 40-52.

14. S. S. Raiman and G. S. Was, *Journal of Nuclear Materials*, 2017, **493**, 207-218.
15. M. Sterniczuk, P. A. Yakabuskie, J. C. Wren, J. A. Jacob and D. M. Bartels, *Radiation Physics and Chemistry*, 2016, **121**, 35-42.
16. D. Janik, I. Janik and D. M. Bartels, *The Journal of Physical Chemistry A*, 2007, **111**, 7777-7786.
17. M. Sterniczuk and D. M. Bartels, *The Journal of Physical Chemistry A*, 2016, **120**, 200-209.
18. W. R. Bower, A. D. Smith, R. A. D. Pattrick and S. M. Pimblott, *Review of Scientific Instruments*, 2015, **86**.
19. L. Leay, W. Bower, G. Horne, P. Wady, A. Baidak, M. Pottinger, M. Nancekievill, A. D. Smith, S. Watson, P. R. Green, B. Lennox, J. A. LaVerne and S. M. Pimblott, *Nuclear Instruments and Methods in Physics Research Section B: Beam Interactions with Materials and Atoms*, 2015, **343**, 62-69.
20. Cormet, unpublished work.
21. P. Crook, *Advanced Materials & Processes*, 2007, **165**.
22. P. Cohen, A. Research, T. C. o. Water and S. i. T. P. Systems, *The ASME Handbook on Water Technology for Thermal Power Systems*, American Society of Mechanical Engineers, 1989.
23. H. Dosimters, Perspex Dosimeters, http://www.harwell-dosimeters.co.uk/perspex/, (accessed 23.11.2015, 2015).
24. J. W. T. Spinks and R. J. Woods, *An Introduction to Radiation Chemistry*, John Wiley & Sons, United States of America, 3 edn., 1990.
25. Hach, *Journal*, 2010.
26. I. YSI, *Journal*, 2009.
27. A. Elliot and D. Bartels, *The reaction set, rate constants and g-values for the simulation of the radiolysis of light water over the range 20 deg to 350 deg C based on information available in 2008*, Atomic Energy of Canada Limited, 2009.
28. J. A. LaVerne, M. R. Ryan and T. Mu, *Radiation Physics and Chemistry*, 2009, **78**, 1148-1152.
29. A. O. Allen, C. J. Hochanadel, J. A. Ghormley and T. W. Davis, *The Journal of Physical Chemistry*, 1952, **56**, 575-586.
30. Hach, *Journal*, 2016.

Supplementary material

Table 6.2-7. Describes the features labelled in the diagram in Figure 6.2-7.

	V1	Storage tank gas outlet valve	14	HP pump 1
	PC1	Nitrogen pressure reduction valve	15	Process flow schema
		Dissolved hydrogen sensor (outlet)	16	DH sensor (inlet)
		Conductivity sensor outlet	17	Conductivity sensor (inlet)
	PC2	Oxygen mixing gas pressure reduction valve	18	DO sensor (inlet)
		Dissolved oxygen sensor (outlet)	19	Controllers and displays
	LI1	Storage tank water level indicator.	20	DO measurement unit (outlet)
	PC3	Hydrogen gas pressure reduction valve	21	DO measurement unit (inlet)
	PIS1	HP pump 1 pressure gauge with limits	22	PC4 HP water back pressure valve
	PIS2	HP pump 2 pressure gauge with limits	23	FI10 HP water flow meter
		HP pump 1 pulsation dampener	24	Switches
		HP pump 2 pulsation dampener	25	DH measurement unit
		HP pump 2		

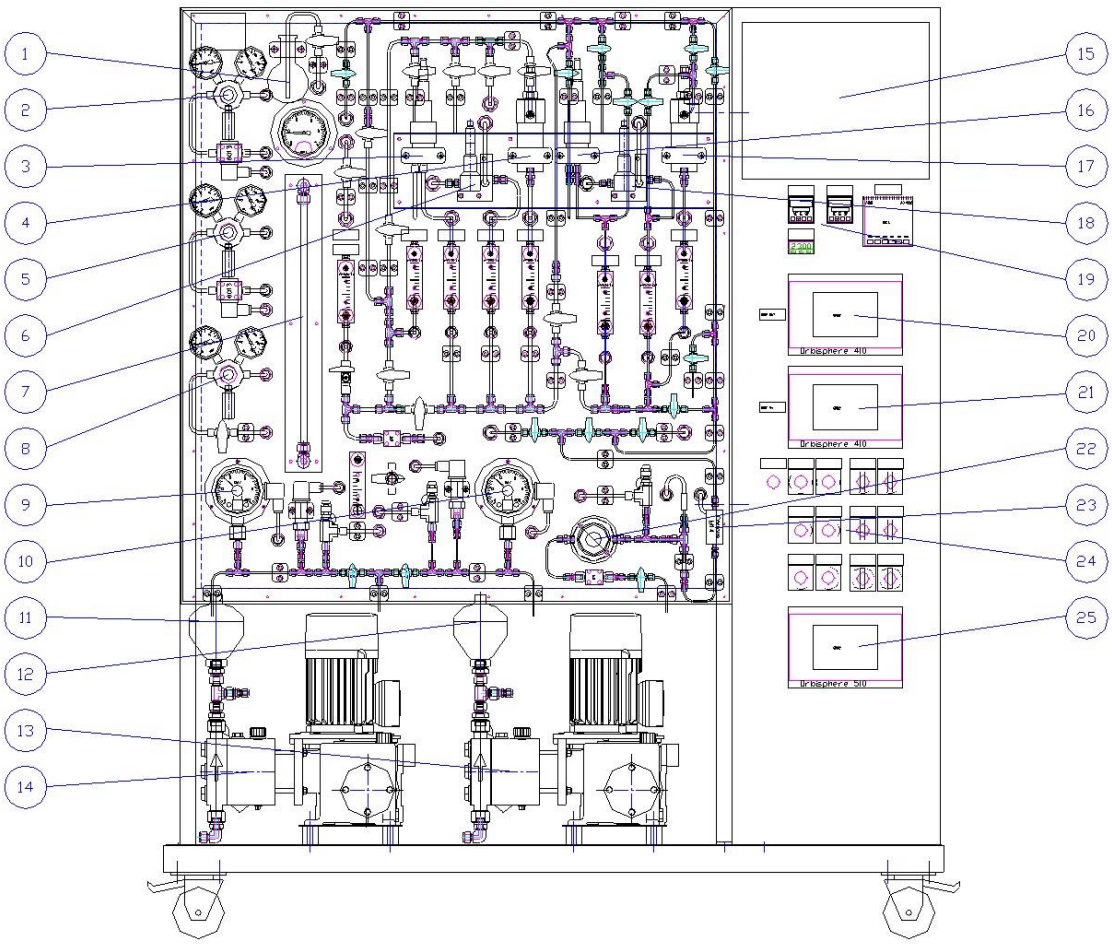

Figure 6.2-7. Labelled schematic HTHP recirculation system features, including pressure pumps, controllers, and system sensors, descriptions of features can be found in Table 6.

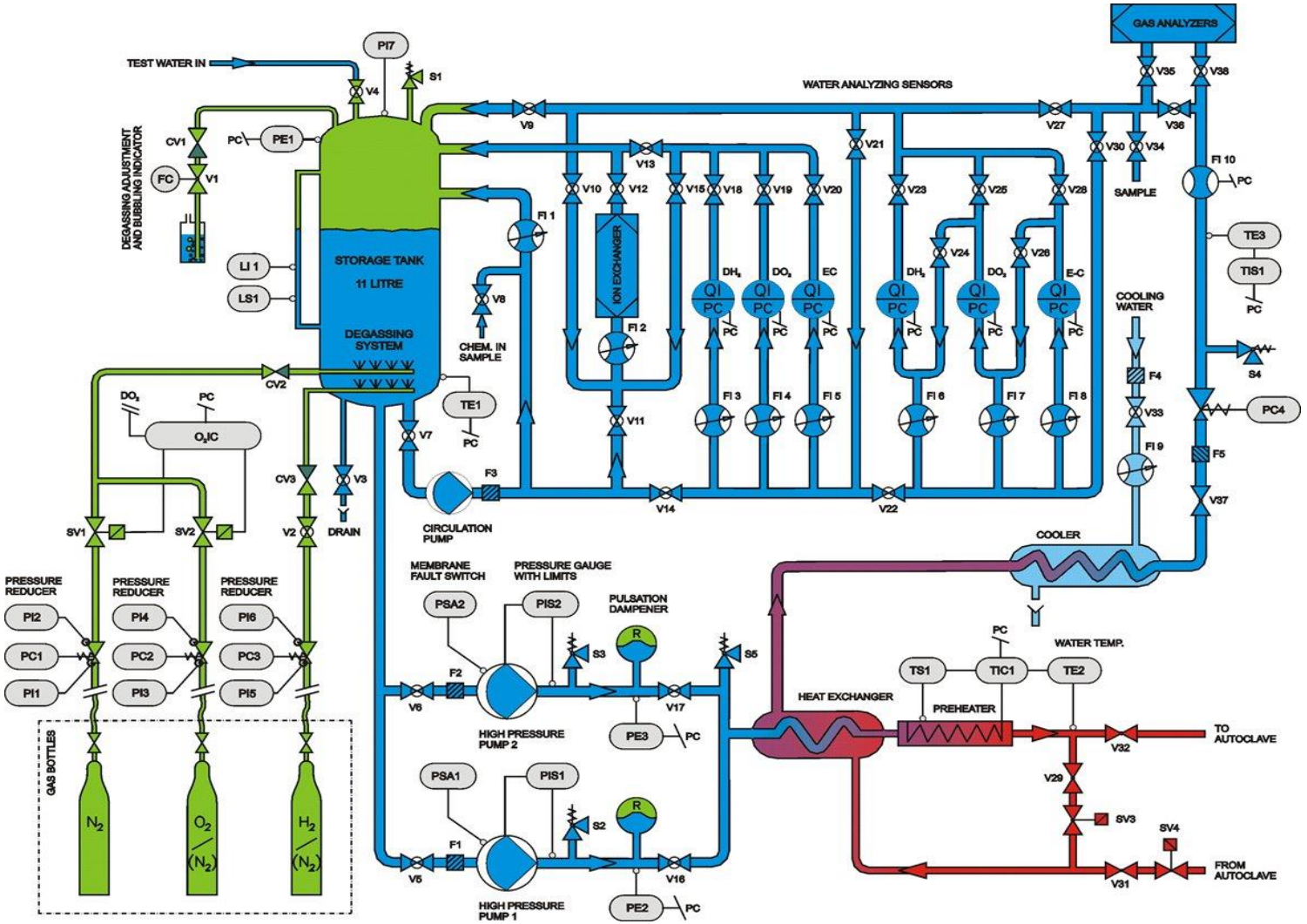

Enlargement of Figure 6.2-1. The schematic of the HTHP recirculation loop, showing the possible flow paths of the water to be heated and pressurised, and the monitoring systems present.

Discussion of electrochemical capabilities

As stated previously PTFE cannot be used in γ environments due to its degradation. To overcome this issue the electrochemical feedthroughs were designed with this in made and are made from ceramic, the feedthroughs can be seen alongside an exploded cross section of these in **Figure 6.2-8.** The feedthrough system consists of a Pt wire with a threaded end which threads a metallic fitting that acts as the connector. A metallic seal is placed onto the fitting which has a ceramic washer on either side. This is then fitted within a metallic body, along with a second metallic seal/fitting section identical to the first. The pieces fitted together are hand tightened; the holes in the body must align and are used to tighten the end pieces together further. A ceramic bushing is installed to one of the body holes and then a long M3 screw is threaded, on the other side a screw set is added, and a wire is fitted between the body, Allen bolt and its nut, allowing for electrical connections to be made. This ceramic thread through system gives an insulated connection. [20]

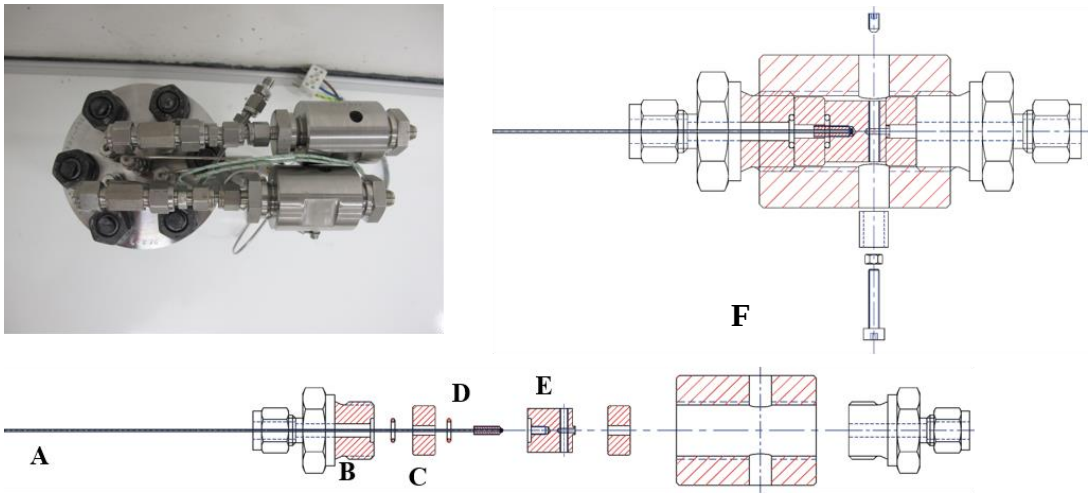

Figure 6.2-8. A photograph of the electrochemical feedthroughs of the autoclave along with a schematic of these, labelled with their description.

A. Pt wire with screw end
B. Swagelok fitting for connection
C. Metallic seal
D. Ceramic washer
E. Central piece with screw fitting
F. Body tube fitting
G. M3 bolt, with nuts and fittings

Reference electrode (RE)

The use of a ^{60}Co source means the traditional in-situ calomel reference electrodes may not be used due to their instability under irradiation and at temperature. The use of an external reference electrode allows the use of PTFE components. This issue an external RE set up was designed as shown and annotated in Figure 6.2-9. This external RE uses a luggin capillary that connects an Ag/AgCl RE to the autoclave system where the working and counter electrodes are present.

Figure 6.2-9. Photograph to show the reference electrode set up used in the recirculation loop system.

A. Reference electrode feedthrough connecting the luggin capillary to the reference electrode;
B. Valve to remove any air from the feedthrough line, and to make sure the reference electrode is in contact with the autoclave water;
C. Safety valve, to release any pressure and to prevent hot water reaching the reference electrode;
D. Luggin capillary connecting the reference electrode to the autoclave and therefore the other electrodes.

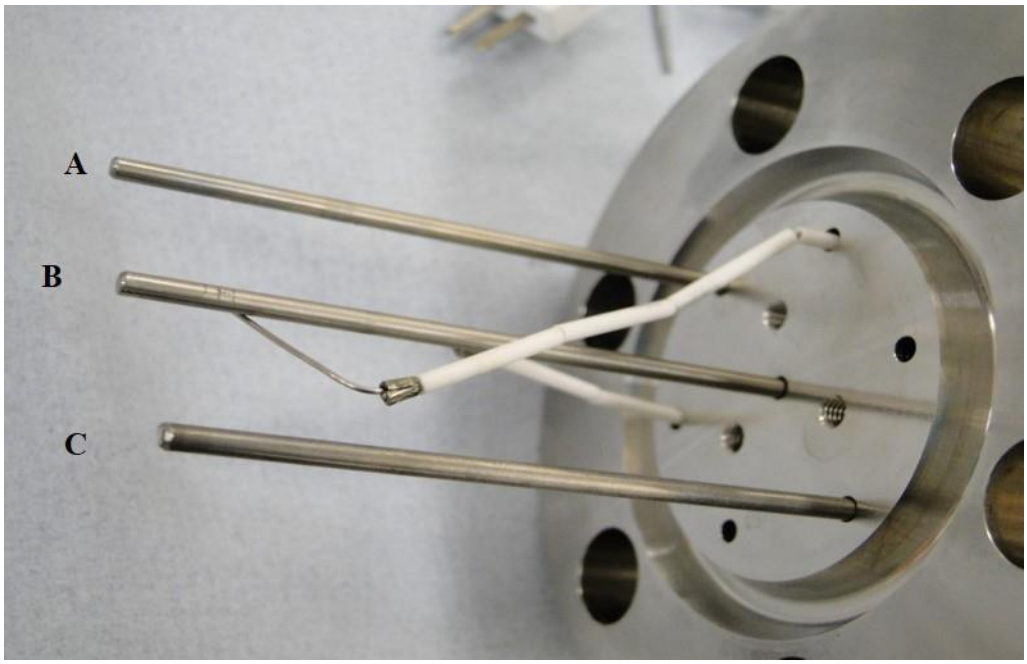

Figure 6.2-10. Photograph showing the positions of the solid-state dosimeters.

The RE is an Ag/AgCl and was first designed by Finnish R&D organisation 'VTT Manufacturing Technology'. The RE consists of a silver rod coated in AgCl, which sits in a PTFE tube with a ceramic plug along with KCl solution (0.1 M for this application). This electrode may be used at high temperature and pressures, (300 ^{o}C and 180 bar) but it cannot be used with a ^{60}Co hence the connection via a luggin system. The electrode can be tested against a calomel cell and is accurate to about +/- 5 mV and the value is a function on the internal [KCl] and temperature.

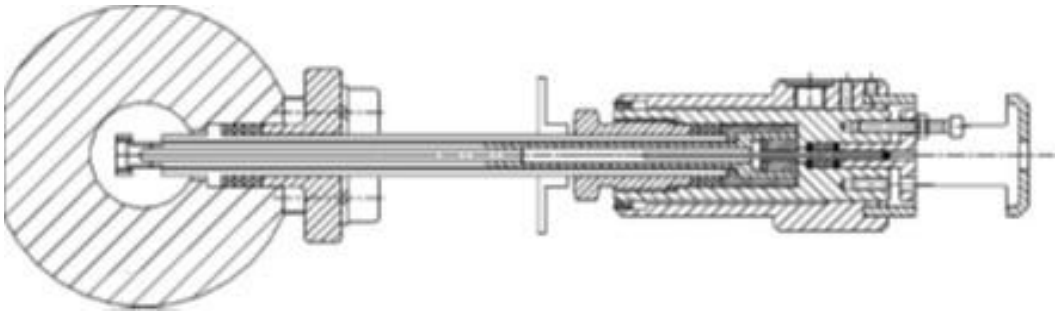

Figure 6.2-11. Schematic of the reference electrode, showing the major component

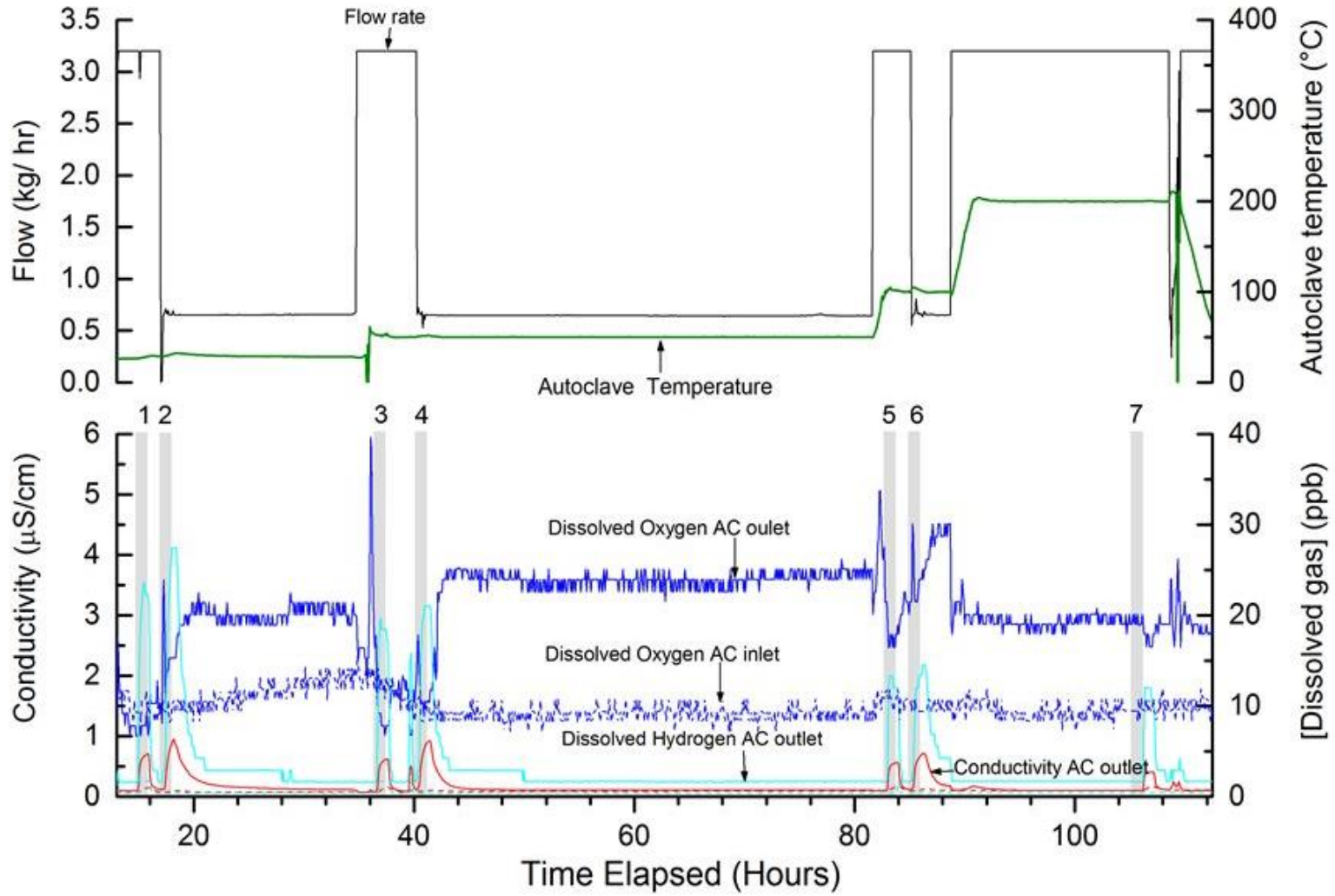

Outline of the full commissioning investigation, it reports the dissolved [H_2] (cyan), [O_2] (blue), electrical conductivity (red for autoclave inlet and outlet), flow rate (black) and autoclave temperature (green). Data has been decimated to removed noise created by the digitalisation of sensor data, shaded areas indicate the hour long ɣ-exposure times.

6.3 Investigating the effects of ɣ-radiation on corrosion

The effects of ɣ-radiation on the corrosion of stainless steel 316 under High temperature/ High Pressure conditions

Elizabeth Parker-Quaife,[1,2,*] and Simon M. Pimblott[3]

[1]*The School of Chemistry, The University of Manchester, Manchester, UK*
[2] *Dalton Cumbrian Facility, The University of Manchester, Moor Row, Cumbria, UK*
[3]*Idaho National Laboratory, 1955 N. Fremont Ave., Idaho Falls, Idaho 83415, United States*

Abstract

This work reports the successful deployment of a new experimental facility designed to simulate the conditions within a light water reactor under radiation conditions. Stainless Steel 316 samples were exposed to ɣ-radiation during oxidation at 288 °C, 200 bar of pressure and deaerated conditions for 95 hours. Unirradiated samples were also oxidised under deaerated conditions. Irradiated samples showed reduced oxide coverage with a rougher external oxide. Cross sectional examination showed both samples had a duplex oxide with irradiated samples having thinner overall oxide thickness, as well as significantly reduced inner oxide thickness. Grazing angle X-ray diffraction showed that the inner oxide in both cases was chromite, with outer oxide composition varying slightly, with spinel Fe_3O_4 and nickel chromium iron oxide in the unirradiated case and non-cubic magnetite in the irradiated sample. Raman data supported the presence of chromite and magnetite in both samples. SEM-EDS showed depleted chromium content in the inner oxide for irradiated samples suggesting chromium loss by dissolution from the chromite surface.

Key words

Stainless steel, radiation, irradiation effects, corrosion, radiolysis, Raman spectroscopy, Grazing incident XRD.

Introduction

Degradation of stainless-steel components in light water reactors may occur by corrosion and corrosion related phenomena. Irradiation accelerated corrosion, stress corrosion cracking, irradiation assisted stress corrosion cracking and CRUD related degradation are pathways that can lead to reduced reactor lifetimes and efficiencies [1-4] The effects of radiation on these corrosion related phenomena is limited, with comprehensive studies few and far between. The harsh conditions within in reactors as well as the presence of a mixed radiation field means these studies are logistically difficult. Early studies were limited to the effects of ɣ-radiation on corrosion and release, without thorough oxide characterisation being undertaken due to experimental limitations.[5, 6] Some studies have used electrochemical investigation where the effects of gamma radiolysis on reactor materials have been undertaken, but these studies do not characterise the oxide and were undertaken in static conditions at temperatures below 150 °C.[7-10] Other studies have looked at electrochemical behaviour with materials exposed to proton irradiations.[11-13] Recent work by Raiman *et al.* has investigated the effects of proton irradiation on stainless steel 316 (SS 316) with characterisation of the oxide, and proposed mechanism for growth and loss, showing reduced oxide thickness with chromium.[14-16] Deng *et al.* have characterised the oxide produced in SS 304 after exposure to simulated PWR water.[17] Other works have attempted to mimic the effects of radiation by addition of H_2O_2, oxygen or hydrogen.[9, 18-25] Works that mimic conditions with H_2O_2 or oxygen addition show depleted chromium content, some reduced oxide thickness, and outer oxide particle size is changed, often with the addition of haematite, which is not always exhibited under irradiation conditions. To continue work in this field there needs to be thorough mechanistic understanding as well as full characterisation of oxides exposed to radiation. Understanding the effects of both proton and gamma irradiation on corrosion mechanisms of nuclear materials would enable predictive models to couple these behaviours, with the aim to give lifetime prediction as well as simulate scenarios that may occur during the lifetime of a plant.

This work reports a successful implementation of a facility that is capable of in-situ corrosion studies under irradiation conditions. This facility has been designed to emulate the conditions experienced in light water conditions and was recently designed and commissioned at The University of Manchester's, Dalton Cumbrian

Facility and is equipped to study either proton or ɣ-irradiations. A design paper outlines the full utility of the equipment with information on the commissioning process.[26] The objective of the work outlined is to investigate the effects of ɣ-radiation on the corrosion of stainless steel 316, with preliminary characterisation of the oxide using Grazing Incidence X-ray Diffraction (GI-XRD), Scanning Electron Microscopy (SEM) with energy disperse spectroscopy (EDS) and Raman spectroscopy. A comparison between this work and other related work is then undertaken in order to give an idea of how these relate to one another and possible mechanisms for oxide growth and loss.

Experimental methods

A specially designed high temperature and pressure recirculation loop was designed, which allows for the irradiation of corrosion samples while maintaining high temperature and pressures. It is capable of reaching temperatures of 350 °C and up to 200 bar of pressure while being exposed to ɣ-radiation. The dose rate at the time of the experiments was ~21.6 Gy/min. The chemistry of the system is monitored via a series of inline sensors; and may be altered with gaseous or chemical additions. A corrosion jig was manufactured and used, it hung from the autoclave lid to allow several samples to undergo oxidation at once without touching one another or the corrosion cell.

Stainless Steel Type 316 coupons were cut 10 mm by 20 mm (W x H) and a 0.5 mm (diameter) hole drilled to allow for hanging inside of the irradiation cell. The samples were ground and then polished to OPS finish on the primary face and 800 grit on the back face. This is for the benefit of imaging as well as to limit any preferential corrosion. SEM and optical images were taken of samples on the OPS face before irradiations to ensure there was not any excessive scratching and that the microstructure was as expected. After imaging the samples were cleaned, then hung inside the autoclave. The autoclave was then placed inside of the chamber of the Foss therapy ^{60}Co ɣ-source for irradiation experiments and non-irradiated tests were carried out in another laboratory. The autoclave system was then attached to the recirculation loop. The tests carried out investigated the effects of ɣ-radiation only, so no chemical additives were used, with argon purging continuous and water being circulated through cation exchange column through-out the oxidation experiment. Once dissolved [O_2] and [H_2] stabilised and leak and pressure testing was carried out, the

system temperature was increased to 288 °C at a ramp rate of 50 °Chr^{-1}. The samples were exposure to 288 °C water at 200 bar pressures for 95 hours, with irradiated samples being exposed to ɣ- radiation for 95 hours. The desired oxygen concentration was <20 ppb (reported values are higher than this, but subsequent tests indicate than the calibration was incorrect). Flow rates for the system were 1.5 kg/hr for unirradiated tests and 3.2 kg/hr for ɣ-irradiated test, temperature 288 °C and pressure 200 bar. The total dose received by the irradiated sample was 123.12 kGy over 95 hours. Throughout the tests dissolved (DH_2) and oxygen (DO_2) concentrations were monitored into and out of the recirculation loop, along with electrochemical conductivity (EC). Temperature, pressure, and flow rate were also carefully monitored. A schematic of systems flow path is shown in **Figure 6.3-1**, and **Figure 6.3-2** shows a schematic of the irradiation cell that sits within the chamber of the Foss therapy ^{60}Co ɣ-source.

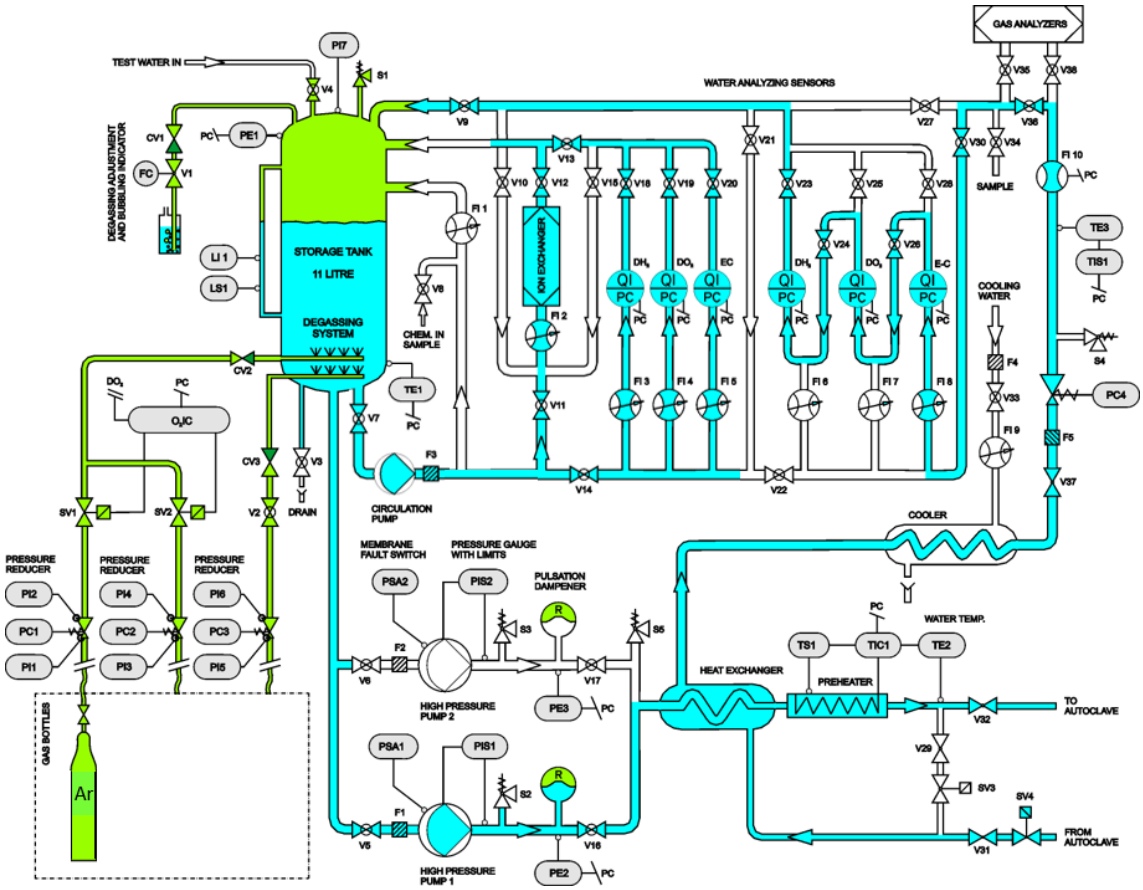

Figure 6.3-1. Recirculation flow path for tests monitoring corrosion of stainless steel 316 samples.

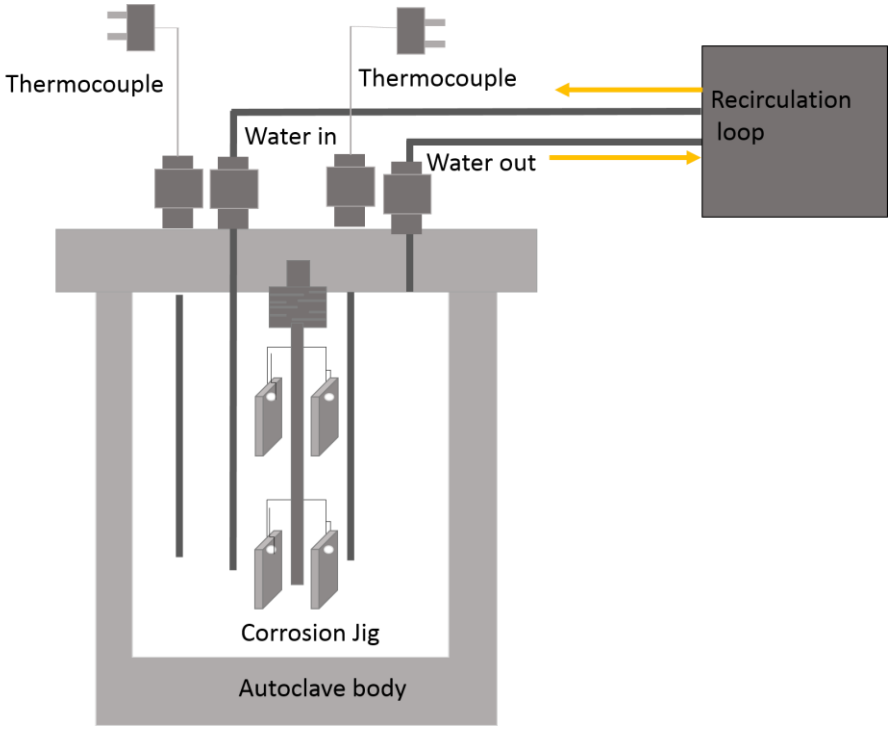

Figure 6.3-2. Schematic of the irradiation cells, showing the corrosion jig design and the autoclave configuration.

Surface characterisation was undertaken at the University of Manchester or at the Dalton Cumbrian Facility, with SEM, XRD and Raman spectroscopy being undertaken to probe any changes due to the exposure of samples to ɣ-radiation.

A FEI Quanta FEG 250 was used to image the coupons with voltages of up to 20 kV, oxford instruments AZtecLive software for SEM-EDS analysis, EDS analysis was carried out at 10 kV on mounted samples with quantification standards and deconvolution for carbon used. SEM imaging of samples after polishing and before oxidation was undertaken to ensure good surface finish and consistency between samples. Post oxidation SEM images were taken of the coupon surface and then mounted in a way which oxide cross section could be viewed. Oxide morphology was observed on the polished top surface of several samples to examine for congruence between sample. Then one of each irradiated and unirradiated samples were selected and mounted to give a cross section enabling oxide thickness to be calculated. The samples were cut and then cleaned in sonicated ethanol and water baths and mounted

in nonconductive resin, then polished to OPS finish and silver paint applied to resin mount to assist with conductivity.

Grazing Incidence X-ray diffraction was undertaken using a Philips X'Pert – MPD theta-theta diffractometer (400 mm diameter) with a PW1711 (Proportional) point detector in Bragg-Brentano geometry employing a Copper Line Focus X-ray tube with Ni kβ absorber (0.02 mm; Kβ = 1.392250 Å) Kα radiation (Kα1=1.540598 Å, Kα2=1.544426 Å, Kα ratio 0.5, Kαav=1.541874 Å). Incident beam Soller slit of 0.04 rad, incident beam mask 10 mm, programmable automated divergence slit giving a constant illuminated length of 10.0 mm, programmable anti-scatter slit observed length of 10.0 mm, receiving Soller slit of 0.04 rad, Parallel plate collimator 0.27° and diffracted beam curved graphite monochromator (002). Data was collected from 10 to 90° 2theta scans with an incidence angle in Omega of 2° (followed by 3°and 6°) at 0.05° step size of 9s/step.

Raman spectroscopy measurements were taken using a Bruker RamanScope III. Measurement were taken at several spots on the sample at a 532 nm laser power and at 10 mW energies.

Results and discussion

Figure 6.3-3 and **Figure 6.2-4** outline the system parameters throughout the oxidation tests. In both ɣ-irradiated and unirradiated tests temperature and pressure were stable. In the unirradiated tests dissolved oxygen and hydrogen concentration remained constant as did electrochemical conductivity. For ɣ-irradiated tests, conductivity and DH_2 concertation increase with the onset of irradiation. The increase in these parameters was previously seen during commissioning tests, and some increase in hydrogen is expected.[26] As irradiation continues the DH_2 concentration reduces and plateaus with conductivity showing a similar trend.

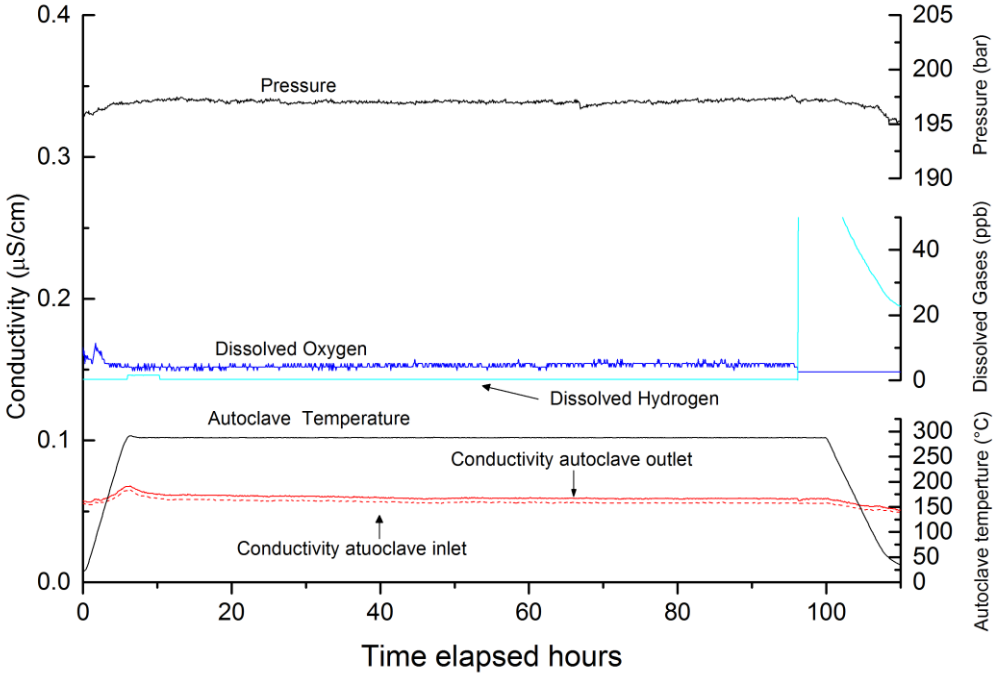

Figure 6.3-3. System parameters, conductivity, temperature, [DH_2], [DO_2] and pressure for corrosion of SS 316 without radiation exposure, oxidation period 95 hours at a flow rate of 1.5 kg/hr.

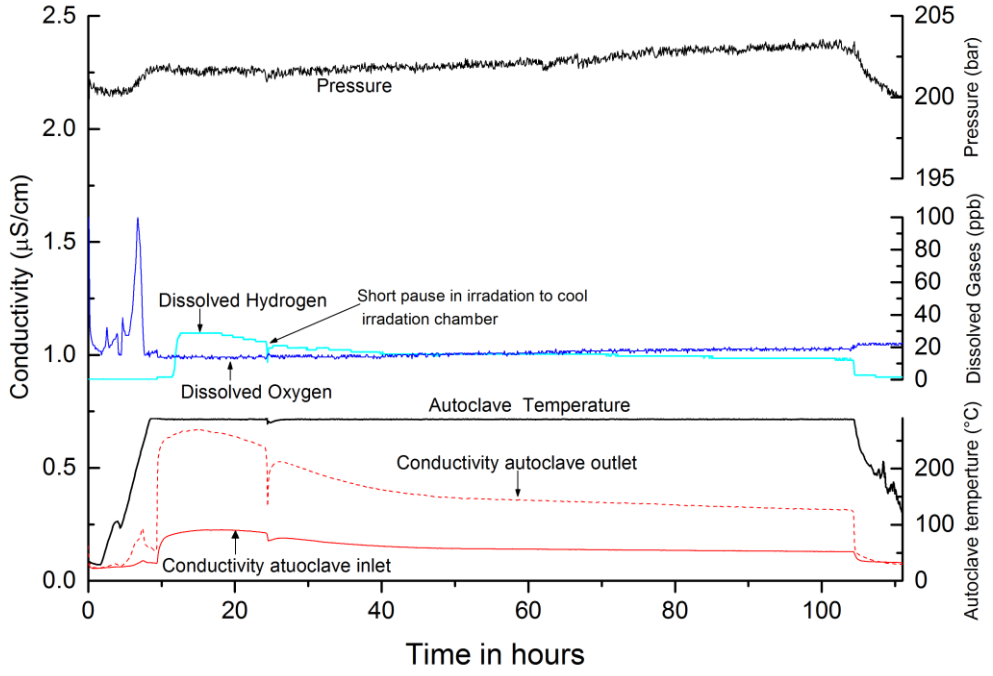

Figure 6.3-4. System parameters, conductivity, temperature, [DH_2], [DO_2] and pressure for corrosion of SS 316 with ɣ-irradiation exposure, oxidation, and ɣ-irradiation period 95 hours at a flow rate of 3.2 kg/hr.

Oxide morphology

The congruency of the oxide grown on the sample was examined using SEM imaging to give information on crystal size and coverage. **Figure 6.3-5** shows images of two non-irradiated samples oxidised at 288 °C and 200 bar pressure for 95 hours at a flow rate of 1.5 kg/hr**.** The oxide formed in the non-irradiated samples are uniform, large crystals with a high level of coverage, the crystal faces are smooth. The oxide crystals are uniform with homogenous morphology and size between samples. **Figure 6.3-6** shows SEM images of two samples oxidised under ɣ-irradiated conditions with flow of 3.2 kg/hr. The oxide is less homogenous with more varied crystal size. The crystals have rougher faucets with darker regions, the SEM examination was not able to determine if this darkening was pit formation from dissolution or deposition of released ions onto the surface. When comparing unirradiated sample 1 with ɣ-irradiated sample 1 at 20 thousand times magnification (image unirradiated 1a) and ɣ-irradiated 1a) respectively) the oxide crystals are sparser in the irradiated sample, with the larger crystals more exposed (**Figure 6.3-6**). At lower magnifications (such as those in unirradiated 2b and ɣ-irradiated 2b) the crystals in the irradiated sample are smaller (**Figure 6.3-5)**. Oxide coverage is less in the irradiated sample with smaller particles on the inner surface visible. The oxide in the unirradiated conditions have sharp edges and planer faces, the irradiated samples have blunted edges with more rounded faces. The non-irradiated samples have similar oxide morphology to previous works examining corrosion behaviour of 316 in various conditions[20, 21, 27, 28]. Work presented previously in deaerated conditions shows a duplex film structure with inner Cr rich oxide and outer iron rich spinel structures, the oxide morphology for samples oxidised under deaerated high temperature conditions show crystals with sharp edges and planar faces. The samples reported in this work have greater coverage than some of the previous work, but this difference may be explained by the addition of lithium hydroxide, boric acid, and hydrogen to emulate PWR conditions in other work. The rougher surface seen in the irradiated samples may suggest dissolution of the oxide, this rougher oxide morphology with difference in crystal packing density and size is consistent with the findings of studies that have investigated SS 304 under ɣ-irradiation[5, 6, 29], those that have simulated irradiation using H_2O_2 as a substitute[19, 22-24] and studies of the effects of radiolysis of SS 316 L induced by proton irradiation.[14-16] The oxide morphology reported in these tests is different from work undertaken by

Raiman *et al.* where the effects of proton irradiation were investigated.[14, 15] This may be due to the potential of displacement damage in proton irradiations, and the hydrogenated conditions of the tests. Work by Chen *et al.* has shown that oxide films formed under hydrogenated and deaerated conditions are similar in chemical composition but different in morphology,[21] which supports the idea that oxide morphology may be related to the hydrogenation conditions.

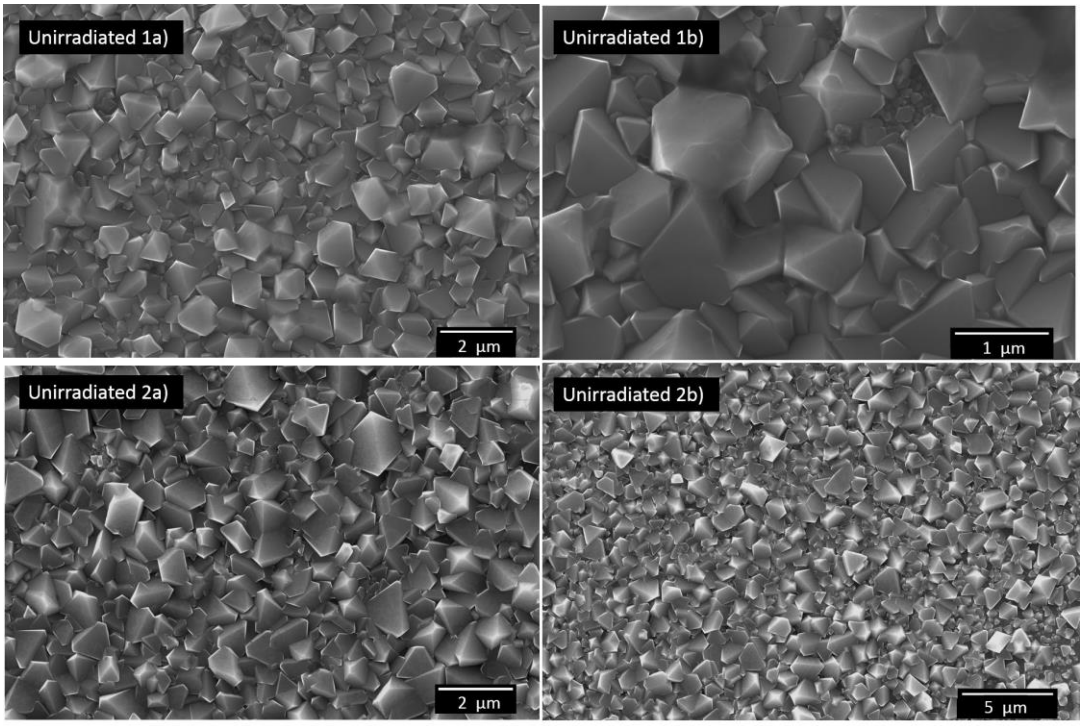

Figure 6.3-5. SEM images of the top surface of two unirradiated 316 L samples oxidised at 288 °C and 200 bar pressure for 95 hours at a flow rate of 1.5 kg/hr. 1a) Sample 1 at 20 k magnification; 1b) Sample 1 at 50 k magnification; 2a) Sample 2 at 20 k magnification; 2b) Sample 2 at 10 k magnification.

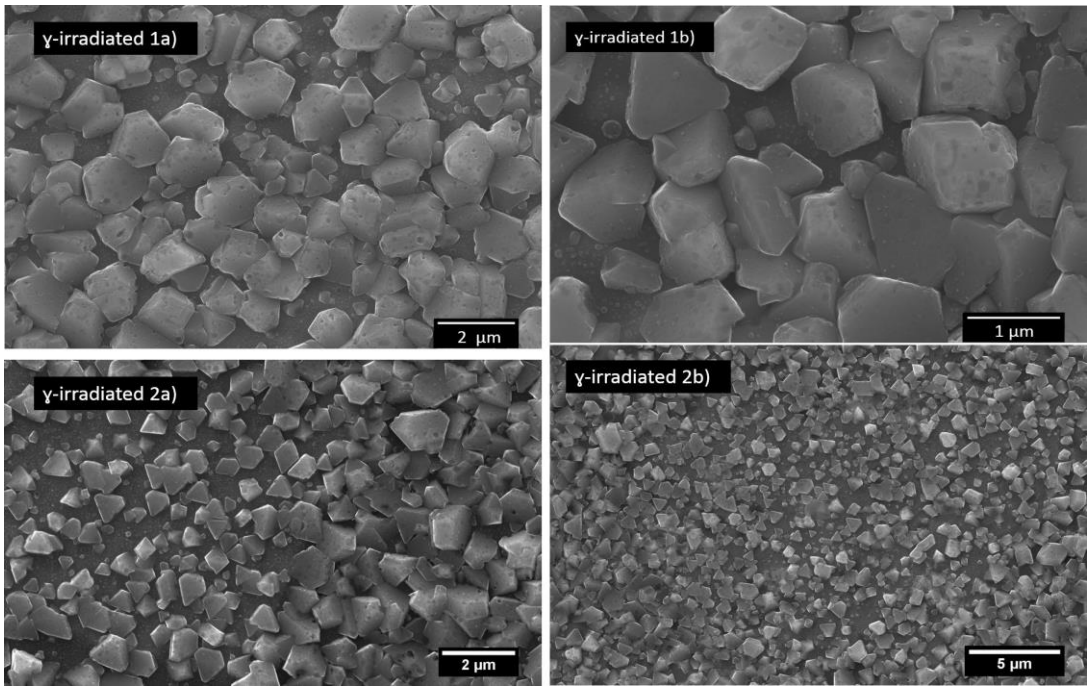

Figure 6.3-6. SEM images of the top surface of two ɣ-irradiated 316 L samples oxidised at 288 °C and 200 bar pressure for 95 hours at a flow rate of 3.2 Kg/hr. 1a) Sample 1 at 20 k magnification; 1b) Sample 1 at 50 k magnification; 2a) Sample 2 at 20 k magnification; 2b) Sample 2 at 10 k magnification.

Oxide characterisation

Mounting the samples to expose the oxides cross-section allows examination of the oxide for thickness measurements and EDS measurements which can give information on the composition of the oxide layers. Examination of the oxide continued with cross sectional SEM imaging and EDS analysis, irradiated sample 1 and unirradiated sample 1 were chosen as characterisation by this method is destructive. For each sample several images were taken at various magnifications and positions, and EDS line scans were taken at several positions also. Examples of these images can be seen in **Figure 6.3-7**. The unirradiated sample show an inner oxide with a distinguishable inner | outer oxide boundary. The inner oxide | metal substrate boundary is quite sharp with jagged edges but does not tend to be uniform in thickness. The outer oxide has clear sharp edges to the spinel structures. In the irradiated samples, the boundaries between layers is more diffuse with less distinguishability. The thickness of the inner oxide is more uniform in the irradiated samples but appears to be thinner throughout when compared

to the non-irradiated samples. The outer oxide is less uniform than in the unirradiated samples, with blunter more rounded edges and overlap between spinels.

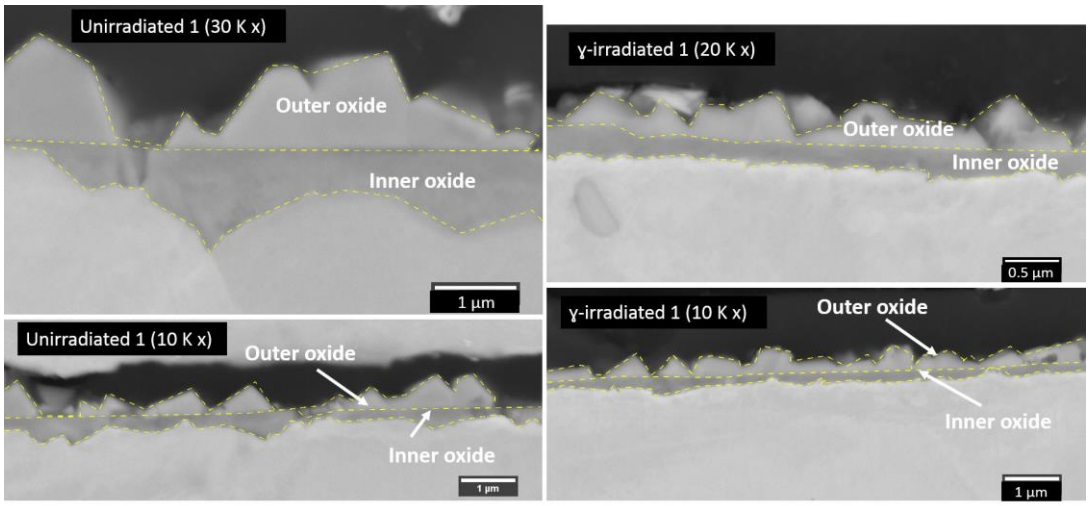

Figure 6.3-7. Comparison of the a few cross-sectional SEM micrographs for unirradiated sample 1 and gamma irradiated sample 1. These are an example of the cross-section images that were used to determine average oxide thickness.

The images were processed in image J, oxide thickness was measured on multiple images and positions within each image. These values were then averaged to give an average inner oxide thickness and overall oxide thickness. Unirradiated samples had an inner oxide thickness of 360.5 ± 98.5 ɳm and the ɣ-irradiated samples 244.5 ± 65.5 ɳm. The EDS line scan data was processed to give atomic concentration, which are plotted against distance along the path of the line scan. Measurements were also taken on these images and compared to the suggested regions given by atomic concentrations. There was good agreement with the two methods of thickness calculation. Due to the methods of thickness calculation, there is a significant error associated as each measurement is from a single position. Standard deviation is given for the average measurements attempting to account for this. Irrespective of error a clear trend can be seen. An example EDS line scan data is reported in **Figure 6.3-8a)** unirradiated sample and **Figure 6.3-8b)** for ɣ-irradiated sample. The measured values for oxide thickness and the average chromium content are given in **Table 6.3-1.**

The results reported in **Table 6.3-1** show a decrease in overall oxide thickness in ɣ-irradiated samples as well as a depletion in Cr content in the irradiated samples. Work characterising oxide formed during SS 316 corrosion under ɣ-irradiation conditions is limited but work investigating the effects of either simulated or irradiation on the

corrosion of other stainless steels shows a thinning of the inner oxide with chromium depletion.[14, 15, 17, 19-21, 25]

Table 6.3-1. Information on the measured oxide thicknesses and chromium content comparing the unirradiated and ɣ-Irradiated samples. *values determined using images from EDS scans which are of lower resolution.

Sample	Inner oxide thickness / ɳm	Overall oxide thickness / ɳm	Inner oxide thickness / ɳm (EDS *)	Overall oxide thickness / ɳm (EDS*)	Cr content inner (% atomic)
Unirradiated	360.5 ± 98.5	755.8 ± 177.7	346.7 ± 91	753.4 ±164.8	17.2 ± 2.3
ɣ-Irradiated	244.5 ± 65.5	524.4 ± 73.2	217.1 ± 66.8	571.8 ± 108.1	13.3 ± 4.7

To investigate the structure and composition of the oxide, GI-XRD was used, Raman spectroscopy was also undertaken to give information on the top surface oxide. Due to the thickness of the oxide it was not possible to use Raman spectroscopy on cross sectioned samples. The data GI-XRD reported here from incident angles of 2, 3 and 6°. XRD data was characterised by matching with standards utilising HighScorePlus software by Panalytical.

Unirradiated samples showed spinel structures of magnetite and/or Nickel Chromium Iron Oxide at incident angle of 2, presence of magnetite and nickel iron spinel in the outer oxide is consistent with previous works.[14, 15, 20, 27, 28, 30] Incident angle of 3 and 6 in the unirradiated samples give a spinel chromite (Cr_2FeO_4) with contributions from iron nickel presumably from the base metal. Chromite accounts for the chromium rich inner layer and is expected. The characterised XRD plots can be seen in **Figure 6.3-9a).**

In the irradiated sample data from incident angle of 2 matched to magnetite with a rhombohedral structure.[31] Rhombohedral structure of magnetite tends to be associated with the Verwey transition, an effect of cooling magnetite below 120 K .[31] This effect is due to ionic displacement and Fe-O change related to the ability of ions to exchange electrons, in affecting focusing iron cation centres to maintain one oxidation state. In this case the presence of rhombohedral magnetite may be due to other factors that affect length the Fe-O bonds[32], or oxidation state of the iron. Whether this is due to a chemical phenomenon such as to dissolution due to the effects of ionising radiation

and further investigations and repeats should be undertaken. Grazing angle 2 also had a contribution from chromite with incident angle 3 only having a contribution from chromite. Incident angle 6 was a series of metal-metal matches that suggest the base metal. The characterised XRD plot for ɣ-irradiated sample is presented in **Figure 6.3-9b).** The XRD data supports the EDS and line scan data, showing oxides are composed of a duplex layer of inner chromite and outer iron rich spinels.

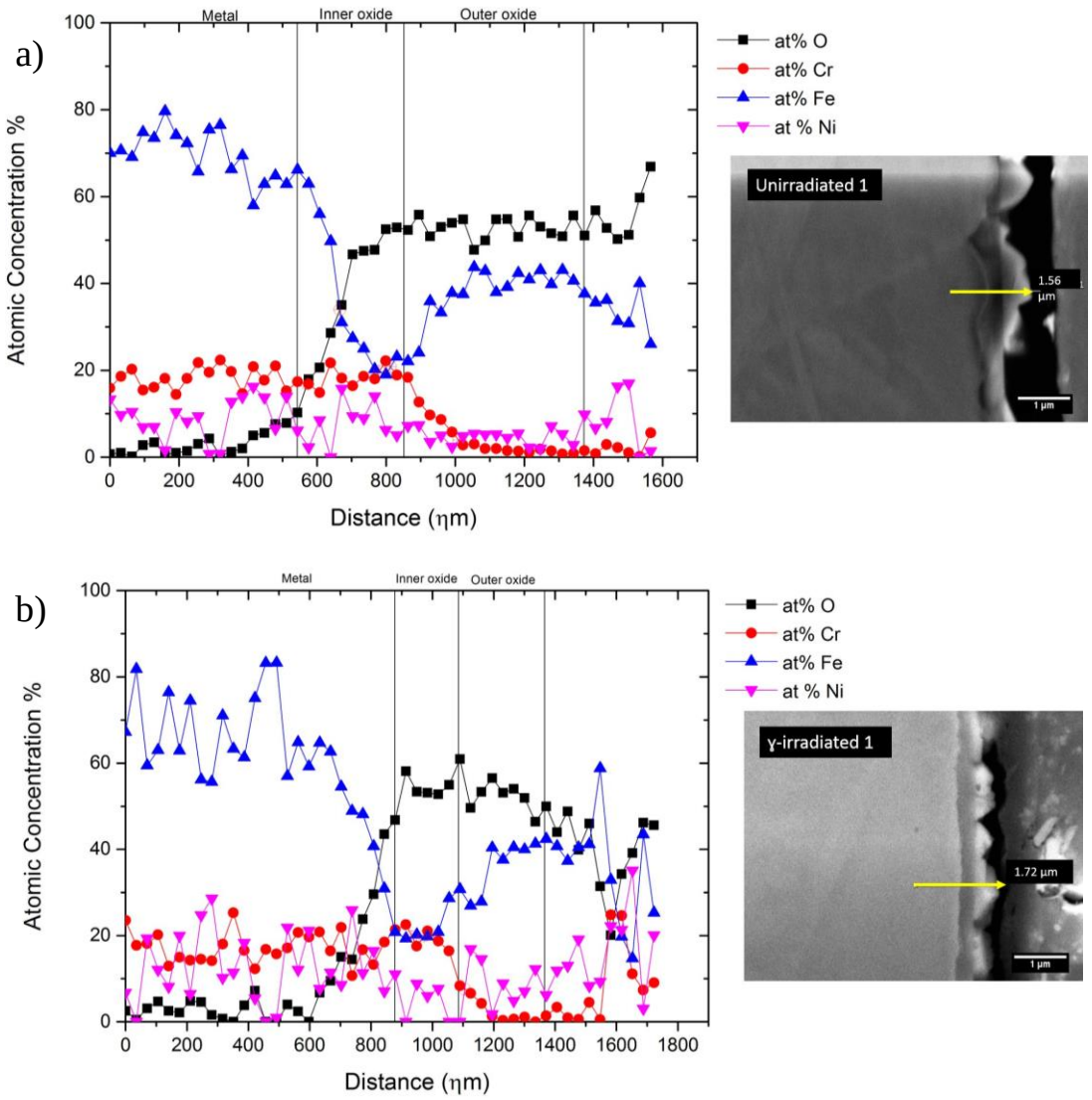

Figure 6.3-8. Example of cross-sectional SEM-EDS line scans used. The yellow line indicates the path of the scan used a) unirradiated sample; b) ɣ-irradiated sample.

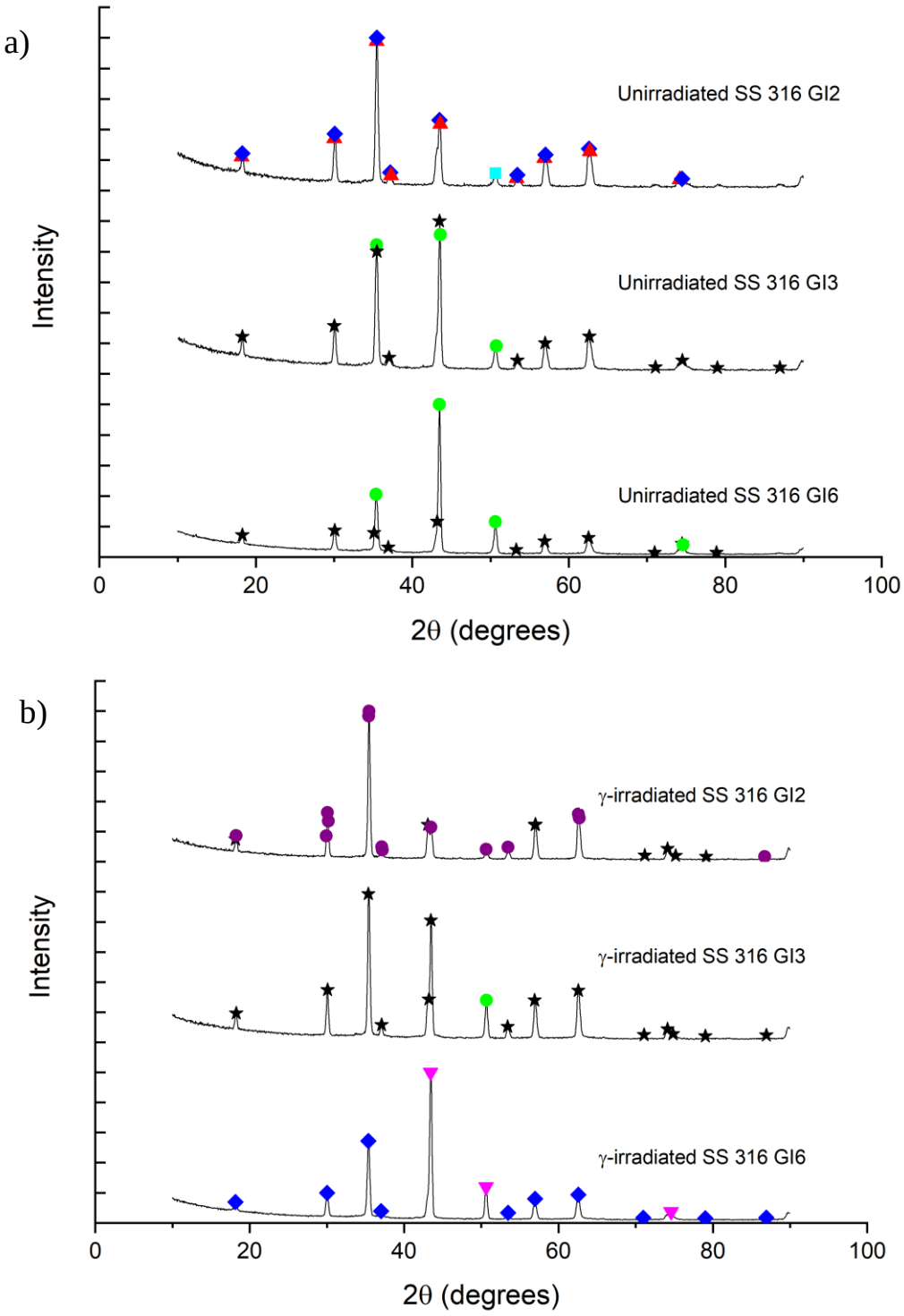

Figure 6.3-9. XRD spectra with characterised phases for grazing incident angles 2,3 and 6. a) unirradiated sample b) ɣ-irradiated sample. ▲ Magnetite (01-086-1344) ◆ Nickel Chromium Iron Oxide (04-015-0675) ★ Chromite (04-016-4072) ● Iron nickel (01-074-5839) ● Magnetite (04-012-7038) ■ Not assigned ▼ Iron Nickel (04-017-6681).

Raman spectroscopy was carried out on the top surface of the coupons, with many spectra recorded. The spectra reported in **Figure 6.3-10** and Raman shifts of the samples summarised in **Table 6.3-2,** with spectra being examples that have the least drift in the background. Raman peaks between positions on each sample show reproducibility. These spectra have been normalised to the maximum value within their measurements. Key peaks exhibited in oxide films previously characterised are labelled in **Figure 6.3-10**. The peaks at 676, 550, 420, and 320 cm^{-1} are characteristic of Fe_3O_4.[33, 34] $FeCr_2O_4$ responsible for peaks at 500 and 685 cm^{-1} and $NiCr_2O_4$ those at 512 and 686 cm^{-1}. The ɣ-irradiated samples had Raman peaks at 319 and 556 cm^{-1} along with the weak peak at 418 cm^{-1} which are due to Fe_3O_4. Peaks at 328 and 567 cm^{-1} in the unirradiated sample are likely to be Fe_3O_4. Due to the broadness and overlap at the spinel A1g peaks it is hard to distinguish what type of spinel structure it is. When the Raman data is paired with the GI-XRD data it is likely that these peaks are related to the chromite inner layer.

Table 6.3-2. Raman spectra peaks from the oxide films formed at SS 316 oxidised in deaerated conditions for 95 hours at 288 °C with and without ɣ-irradiation.

Sample	Raman shift (cm^{-1})				
Unirradiated	328.5		479.5	567	688
ɣ-Irradiated	319	418.4	481.5	556	680

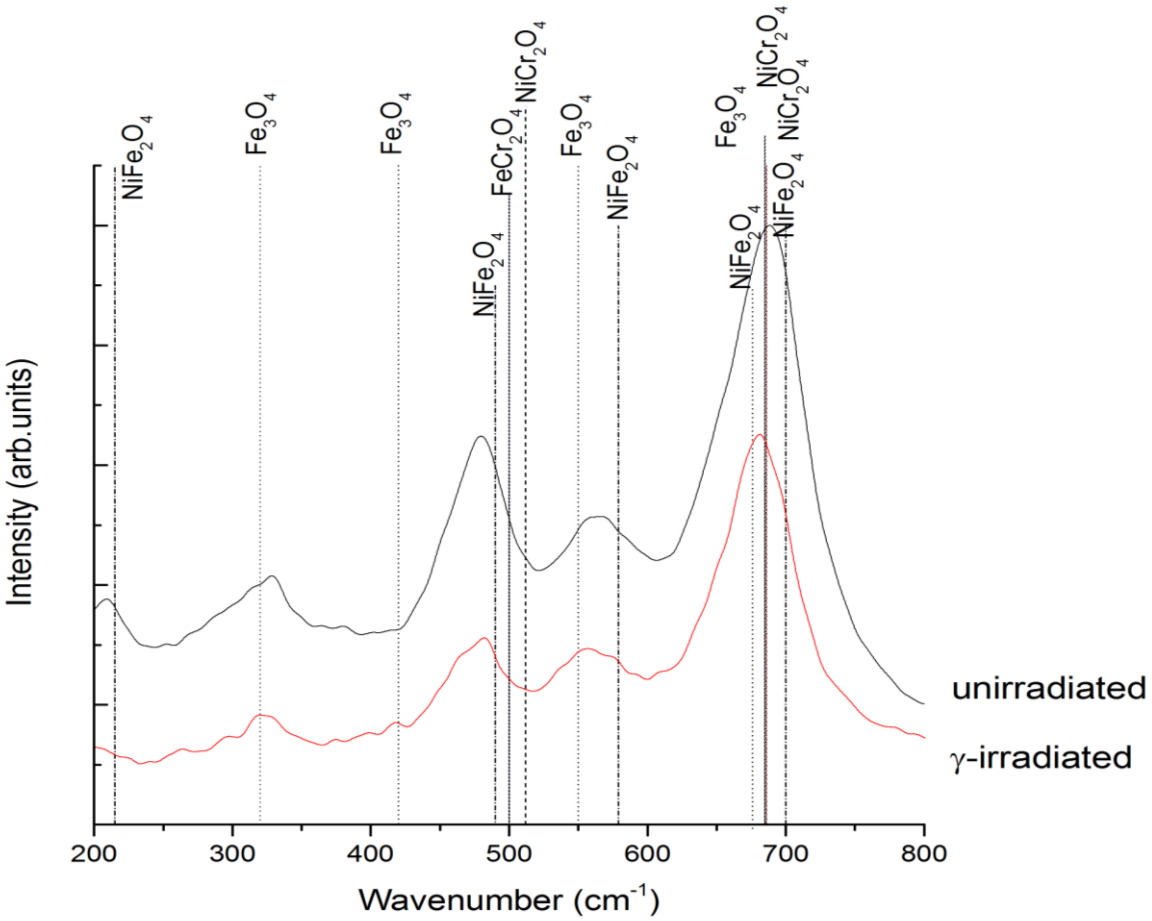

Figure 6.3-10. Raman spectra of the iron oxides formed on stainless steel 316 oxidised in deaerated conditions for 95 hours at 288 °C with and without ɣ-irradiation.

Chromium depletion and thickness reduction

In an attempt to correlate the results seen in this work with possible mechanistic detail, the results are compared to other studies in this field. Recent work by Was *et al.* has determined the effects of proton radiation on corrosion of SS 316, characterising the oxides, assessing the radiolysis driven changes.[14, 15] These works show the radiolysis produced by the proton beam increases the oxidation at the oxide | solution interface ultimately leading to the dissolution of the chromium rich spinel from the inner oxide.[14] The work suggests irradiation-induced chromium depletion, a loss of passivity and an increased dissolution rate of the oxide films. The dissolution of the outer oxide exposes the inner oxide to solution thus allowing for Cr dissolution. This study compared unirradiated samples, irradiated samples and samples that were in a non-irradiated region but exposed to long lived radiolysis products (a flow region). Samples in the flow region also exhibited heightened porosity and chromium

depletion, the authors suggested that the phenomena are due to radiolysis products and not due to displacement damage. The work presented here supports this as a thinning of the oxide which occurs alongside chromium depletion, and ɣ-radiation does not cause displacement damage. These results support the idea presented by Raiman *et al.* of oxide growth by solid state reactions at the oxide | metal interface with simultaneous loss by dissolution at the oxide | solution interface. Limitations in SEM mean that at these magnifications and resolution it is not easy to give information on oxide porosity. The work by Raiman *et al.* was undertaken in hydrogenated conditions with dissolved H_2 concentrations ([DH_2]) of 3 ppm[14, 15] previous work into the effects of DH_2 on SS 316 corrosion shows increased [DH_2] leads to decreased Cr concentrations in the inner oxide which is attributed to accelerated diffusion of the Fe ion to inner oxide layer.[30] Without a comparison to hydrogenated conditions under ɣ-radiation conditions it is not possible to draw unequivocal conclusions about the behaviour seen and if it is purely down to the radiolysis products. To give mechanistic understanding to the depletion of chromium from the oxide works have been undertaken to understand the growth and dissolution behaviour in terms of electrochemical potential needs to be considered. It has been shown that irradiation increases the corrosion potential in both the cases of ɣ-irradiation[7, 9, 10] and proton irradiation.[11, 12, 15] It has also been shown that increased potential occurs in the presence of H_2O_2 [19, 22-24] which supports the idea that radiolysis products are responsible for the changes in oxide thickness rather than radiation damage proposed by Raiman *et al.*[14, 15] Work by Knapp *et al.* propose mechanistic detail of growth by investigating the effects of ɣ-radiation on SS 316 using electrochemistry.[10] The mechanism of film growth has been investigated under potentiostatic conditions, and the corrosion potential under ɣ-conditions measured and compared. Under potentiostatic conditions there are four distinct regions: Region 1) $E < -0.5\ V_{SHE}$ chromium oxide is converted to chromite with magnetite forming as the outer layer, dissolution may occur from both chromite and magnetite. Region 2) $-0.5 < E < 0.0\ V_{SHE}$ chromite/magnetite oxide can be oxidised to maghemite, any surface Fe^{2+} may oxidise to form ɣ-FeOOH which can form a protective layer. Region 3) $0.0 < E < 0.3\ V\ V_{SHE}$ magnetite/maghemite/ɣ-FeOOH grows rapidly on the chromite inner layer, via film fracture and re-passivation, with higher rates of dissolution. Region 4) $0.3\ V_{SHE} < E$ dissolution of chromium occurs at the same time as the growth of magnetite/maghemite/ ɣ-FeOOH. Knapp *et al.* reports a value of $-0.45\ V_{SHE}$ [10] for corrosion potential under the conditions used

and Raiman *et al.* report -0.6 V_{SHE}.[15] Knapp *et al.* report a value of 0.05 V_{SHE} under ɣ-radiation conditions which would not account for the loss of chromium seen in the work reported here. Raiman *et al.* did not report an experimental value for the corrosion potential but calculated that corrosion potentials were likely to be 0.15 and 0.21 V_{SHE} based on the concentration of H_2O_2 seen during irradiation experiments. And suggest that this is close to the calculated potential of 0.29 V_{SHE} for loss of Cr by the formation of $HCrO^{-2}_4$. The proposed mechanism for chromium depletion is:

$$FeCr_2O_4 + H_2O \rightleftarrows 6H^+ + 2\,HCrO_4^- + Fe^{2+} + 6e^- \qquad E = 0.29\,V_{SHE} \quad \textbf{(6.3-1)}$$

These works give an idea of the growth and dissolution mechanisms that may be exhibited during the oxidation of SS 316 L. The presence of magnetite and chromite in both samples suggest growth may be mechanism outlined by Knapp *et al.*[10] The depletion of Cr may be explained by the reaction suggested by Raiman *et al.* that is outlined in **Equation (6.3-1).**

Unfortunately, due to the sample size, the logistical difficulties made it impossible to carry out electrochemical tests on these samples during irradiation. Further investigations should aim to address this to give clear understanding of growth and loss mechanisms.

Conclusions

This work sees the successful deployment of a new facility that enables the in-situ corrosion of samples under γ-radiation exposure simulating light water reactor conditions. The effects of ɣ-irradiation on SS 316 were investigated with post oxidation characterisation being carried out using SEM-EDS, Grazing incident-XRD and Raman spectroscopy. Work concludes:

- Outer oxide morphology is affected by ɣ-irradiation, a loss of oxide coverage is seen, and spinel crystals become rougher with less planar faces which is suggestive of enhanced dissolution and damage to the oxide film.
- Cross sectional SEM shows a duplex oxide layer, ɣ-irradiation results in decrease in overall oxide thickness, as well as a significant loss in inner oxide thickness;
- XRD gives a composition for outer oxide as a combination of magnetite and nickel chromium iron oxide in the unirradiated sample, with an inner chromite

layer. In the irradiated case outer oxide is non-cubic magnetite with an inner layer of chromite. This is support by the Raman data;

- EDS data show a depletion of chromium with in the inner oxide layer which is consistent with earlier works.

These findings support those by Raiman *et al.* that suggested the differences in oxides layer under proton irradiation conditions are likely to be caused by radiolysis products rather than any damaged caused as ɣ-radiation does not cause displacement damage in materials. Further work needs to be carried out to look at hydrogenated and oxygenation conditions to give more mechanistic understanding as well allowing more direct comparison between the works. The use of electrochemical techniques and Scanning Transmission Electron Microscopy would allow for greater understanding and mechanistic detail.

Author Information

Corresponding Author: Elizabeth Parker-Quaife

E-mail: elizabethparkerquaife@gmail.com

Acknowledgements

This work was supported by the UK Engineering and Physical Sciences Research Council **(Grant EP/G037426/**1) in conjunction with Rolls Royce PLC. The authors would like to thank the supporting staff at the Dalton Cumbrian Facility, a joint endeavour by the UK Nuclear Decommissioning Authority and The University of Manchester, and those at the Manchester Materials performance centre without whom this work would not have been possible.

References

1. P. Cohen, A. Research, T. C. o. Water and S. i. T. P. Systems, *The ASME Handbook on Water Technology for Thermal Power Systems*, American Society of Mechanical Engineers, 1989.
2. M. Le Calvar and I. De Curières, in *Nuclear Corrosion Science and Engineering*, Woodhead Publishing, 2012, DOI: https://doi.org/10.1533/9780857095343.5.473, pp. 473-547.
3. P. Rudling, A. Strasser, B. Cox, F. Garzarolli, S. Odar and R. Adamson, LCC 9, Bilboa, Spain, 2014.
4. C. F. Baes Jr and T. H. Handley, *Maritime Reactor Program Annual Progress Report*, Oak Ridge National Laboratory, United States of America, 1961.
5. M. Kawaguchi, K. Ishigure, N. Fujita and K. Oshima, *Radiation Physics and Chemistry (1977)*, 1981, **18**, 733-740.
6. K. Ishigure, H. Iksie, K. Oshmia, N. Fujita and S. Ono, *Radiation Physics and Chemistry*, 1983, **21**, 281-287.
7. K. Daub, X. Zhang, J. J. Noël and J. C. Wren, *Corrosion Science*, 2011, **53**, 11-16.
8. K. Daub, X. Zhang, L. Wang, Z. Qin, J. J. Noël and J. C. Wren, *Electrochimica Acta*, 2011, **56**, 6661-6672.
9. K. Daub, X. Zhang, J. J. Noël and J. C. Wren, *Electrochimica Acta*, 2010, **55**, 2767-2776.
10. Q. W. Knapp and J. C. Wren, *Electrochimica Acta*, 2012, **80**, 90-99.
11. M. Wang, S. Perrin, C. Corbel and D. Féron, *Journal of Electroanalytical Chemistry*, 2015, **737**, 141-149.
12. B. Muzeau, S. Perrin, C. Corbel, D. Simon and D. Feron, *Journal of Nuclear Materials*, 2011, **419**, 241-247.
13. R. Lillard, D. Pile and D. Butt, *Journal of nuclear materials*, 2000, **278**, 277-289.
14. S. S. Raiman and G. S. Was, *Journal of Nuclear Materials*, 2017, **493**, 207-218.
15. S. S. Raiman, D. M. Bartels and G. S. Was, *Journal of Nuclear Materials*, 2017, **493**, 40-52.
16. S. S. Raiman, A. Flick, O. Toader, P. Wang, N. A. Samad, Z. Jiao and G. S. Was, *Journal of Nuclear Materials*, 2014, **451**, 40-47.
17. P. Deng, Q. Peng, E.-H. Han, W. Ke, C. Sun and Z. Jiao, *Corrosion Science*, 2017, **127**, 91-100.
18. X. Zhang, W. Xu, D. W. Shoesmith and J. C. Wren, *Corrosion Science*, 2007, **49**, 4553-4567.
19. Y.-J. Kim, *CORROSION*, 1999, **55**, 81-88.
20. Y.-J. Kim, *CORROSION*, 1995, **51**, 849-860.
21. J. Chen, Q. Xiao, Z. Lu, X. Ru, H. Peng, Q. Xiong and H. Li, *Journal of Nuclear Materials*, 2017, **489**, 137-149.
22. T. Satoh, S. Uchida, J.-i. Sugama, N. Yamashiro, T. Hirose, Y. Morishima, Y. Satoh and K. Iinuma, *Journal of Nuclear Science and Technology*, 2004, **41**, 610-618.
23. J. Sugama, S. Uchida, N. Yamashiro, Y. Morishima, T. Hirose, T. Miyazawa, T. Satoh, Y. Satoh, K. Iinuma, Y. Wada and M. Tachibana, *Journal of Nuclear Science and Technology*, 2004, **41**, 880-889.

24. S. Uchida, T. Satoh, J. Sugama, N. Yamashiro, Y. Morishima, T. Hirose, T. Miyazawa, Y. Satoh, K. Iinuma, Y. Wada and M. Tachibana, *Journal of Nuclear Science and Technology*, 2005, **42**, 66-74.
25. T. Miyazawa, T. Terachi, S. Uchida, T. Satoh, T. Tsukada, Y. Satoh, Y. Wada and H. Hosokawa, *Journal of Nuclear Science and Technology*, 2006, **43**, 884-895.
26. E. Parker-Quaife and S. M. Pimblott, unpublished work.
27. G. Han, Z. Lu, X. Ru, J. Chen, J. Zhang and T. Shoji, *Corrosion Science*, 2016, **106**, 157-171.
28. G. Han, Z. Lu, X. Ru, J. Chen, Q. Xiao and Y. Tian, *Journal of Nuclear Materials*, 2015, **467**, 194-204.
29. N. F. K. Ishigure, T. Tamura, K. Oshima, , *Nuclear Technology*, 1980, **50**, 169-177.
30. L. Dong, Q. Peng, Z. Zhang, T. Shoji, E.-H. Han, W. Ke and L. Wang, *Nuclear Engineering and Design*, 2015, **295**, 403-414.
31. J. P. Wright, A. M. T. Bell and J. P. Attfield, *Solid State Sciences*, 2000, **2**, 747-753.
32. Springer, *Journal*, 2000.
33. M. da Cunha Belo, M. Walls, N. E. Hakiki, J. Corset, E. Picquenard, G. Sagon and D. Noël, *Corrosion Science*, 1998, **40**, 447-463.
34. B. D. Hosterman, Doctor of Philosophy, Univeristy of Nevada, 2011.

Supplementary information

Raman spectroscopy graphs and images to show were Raman measurements were taken.

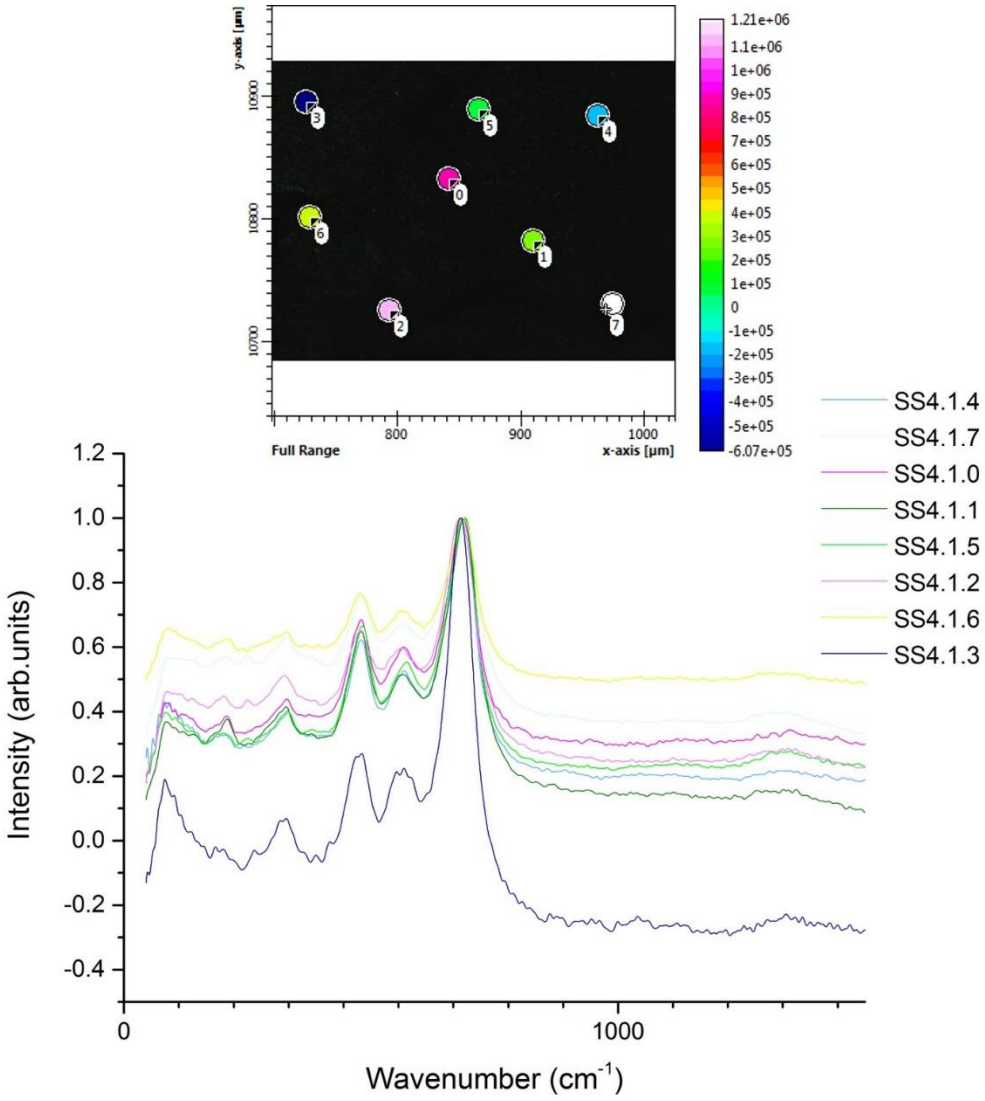

Figure 6.3-11. Raman spectra of non-irradiated SS 316 coupon showing inset shows positions on the coupon. The colours and number correspond to specific measurements. For example, SS4 1.4 is, 4 is the sample identifier, measurement 1 refers to Raman measurement run one and position 4 on the graph, light blue in both the graph and image

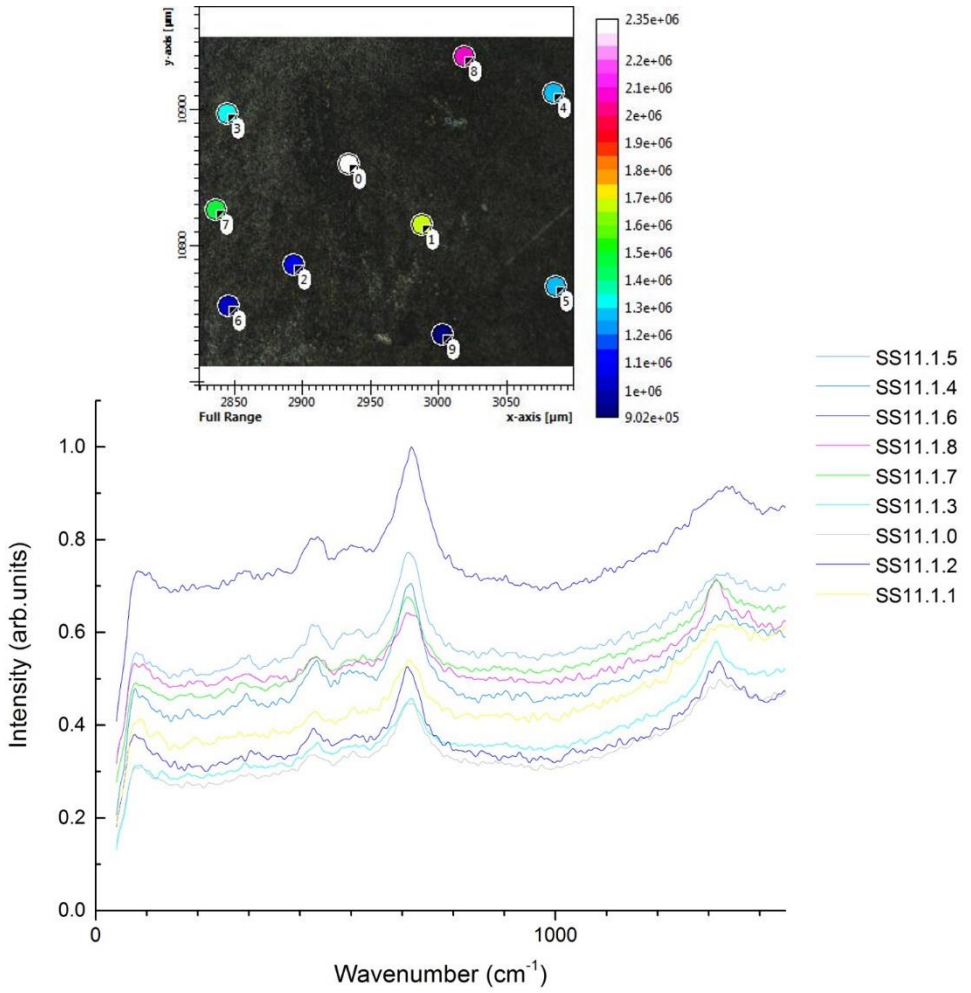

Figure 6.3-12. Raman spectra of ɣ-irradiated SS 316 coupon showing inset shows positions on the coupon. The colours and number correspond to specific measurements. For example, SS11 1.5 is, 11 is the sample identifier, measurement 1 refers to Raman measurement run one and position 5 on the image and in light blue in both the graph and image

Typical Raman values used when identifying phases in the oxides are reported in **Table 6.3-3 - Table 6.3-7.**

Table 6.3-3. Raman active peaks for Haematite (Fe_2O_3) reported in the literature

Fe_2O_3	Hosterman	Da Cuhna Belo
	226	225
	245	247
	291	293
	298	299
	410	412
	498	498
	612	613
		1320

Table 6.3-4. Raman active peaks Magnetite (Fe_3O_4) reported in the literature

Fe_3O_4	Hosterman	Da Cuhna Belo	Other literature values
	295	320	301
		420	513
	531	550	533
	667	676	662

Table 6.3-5. Raman active peaks for Chromite (Cr_2O_4) reported in the literature

Cr_2O_4	Hosterman	Da Cuhna Belo
	305	266
	353	235
	530	290
	556	352
	617	528
		547
		613
		685
		396

Table 6.3-6. Raman active peaks for Nickel chromite ($NiCr_2O_4$) reported in the literature

$NiCr_2O_4$	Hosterman	Da Cuhna Belo	Other literature values
	191	195	181
	429	480	425
	508		511
		512	580
	676	686	686

Table 6.3-7. Raman active peaks for Nickle Ferrite ($NiFe_2O_4$) reported in the literature

$NiFe_2O_4$	Hosterman	Da Cuhna Belo	Other literature values
	189	215	460
	211	339	492
	333	433	574
	456	490	595
	487	579	654
	568	655	
	590		
	663		
	704		

Chapter 7: Investigating the interactions between corrosion and radiolysis products

Once generated corrosion products have several fates, these include release, transport and redeposition. The behaviour of corrosion products with radiolysis products is an important consideration for accelerated corrosion and CRUD behaviour. To further the understanding of the interactions between corrosion and radiolysis products, a set of experiments were developed and undertaken. The experiments built on work from LaVerne *et al.* who previously studied the radiation induced chances to iron oxides,[1] as well as Jonsson *et al.* who investigated the behaviour of metallic oxides towards H_2O_2 as a ɣ-radiation substitute.[2-7] H_2O_2 has been shown to be a valid as a substitute for irradiation conditions and as one of the most oxidising species present the interactions it has with corrosion products is important.[3, 8-11] An understanding of these interactions has applications in plant operations of LWR reactors and in the storage of nuclear waste. The radiolytic production of H_2O_2 is often supressed in PWR systems by the addition of hydrogen to the coolant water, with models predicting significant suppression[12-14] but works by Laverne et al have it has been shown that H_2O_2 will reach detectable limits with LET of a high enough energy.[12] BWR systems do not employ hydrogen water chemistry therefore H_2O_2 concentrations are higher, so understanding the interactions between radiolysis and corrosion products being beneficial to these systems also.

The work presented in this chapter gives a summary of the method development followed by the results of interaction experiments where the effects of ɣ-radiation on iron oxide (as CRUD simulants) in H_2O_2 solutions. The work was carried out at the University of Manchester's Dalton Cumbrian Facility and at the Radiation Laboratory at The University of Notre Dame.

7.1 Preliminary experiments

The preliminary experiments for the interactions experiments were initially aiming to also observe any changes in dissolution behaviour, and CRUD simulants were irradiated under varying conditions using water systems with iron oxides as CRUD simulants (Fe_2O_3 and Fe_3O_4). These systems were monitored by determining the concentration of H_2O_2 and dissolved iron. H_2O_2 was monitored due to its relatively long lifetime and due to this highly oxidising nature, [H_2O_2] was determined using the

Ghormley tri-iodide method. For these preliminary results, the concentration of dissolved iron was monitored using ICP-MS. The initial results are reported and then critically analysed the experimental procedures and techniques used; highlighting sources of error and suggesting improvements that were implemented ensuring better precision during subsequent experiments.

Ghormley detection method

To determine the post irradiation concentration of H_2O_2 in the reacting system the Ghormley Tri-iodide method was used.[15] This is a spectroscopic method that utilises the colour change exhibited by the oxidation of iodide by H_2O_2. The reaction is as follows:

$$3\,I^-\,(aq) + H_2O_2(aq) + 2\,H^+(aq) \rightarrow I_3^-(aq) + 2\,H_2O\,(l) \qquad \textbf{(7.1-1)}$$

As acidic pHs stabilises tri-iodide and exhibits a yellow colour change, the intensity dependant on the concentration of H_2O_2 present. This means that UV-Vis spectroscopy can be used to determine the H_2O_2 concentration of samples by calibration with the use of the beer lambert law which can be seen in **Equation (7.1-2).**

$$A = \varepsilon c l \qquad \textbf{(7.1-2)}$$

Ghormley Method

The Ghormley method uses two detection solutions, an iodine source with a catalyst, (solution A) and a buffer to keep the pH acidic ~ pH 4.7 (Solution B).

1. Solution A – sodium hydroxide (0.5g, 0.13 mol), potassium iodide (16.5g, 0.10 mol), ammonium molybdate tetrahydrate (0.05 g, 40.5 µmol) made up volumetrically to 250 mL with deionised water;
2. Solution B – potassium hydrogen phthalate (5 g, 0.025 mol) made up volumetrically to 250 mL with deionised water.

H_2O_2 solutions of varying concentrations were used to calibrate the technique. H_2O_2 (3 mL) was added to mixture of Solution A (1.5 mL) and Solution B (1.5 mL), and then was transferred to a UV-Vis cuvette and the absorbance maximum taken. The maximum is at 350 nm with an extinction coefficient of 28122 $Lmol^{-1}cm^{-1}$ which is within a 10% error of the literature value of 24540 $Lmol^{-1}cm^{-1}$ reported by Hochanadel *et al.*[16] The absorbance graph used for calibration is reported in **Figure 7.1-1.**

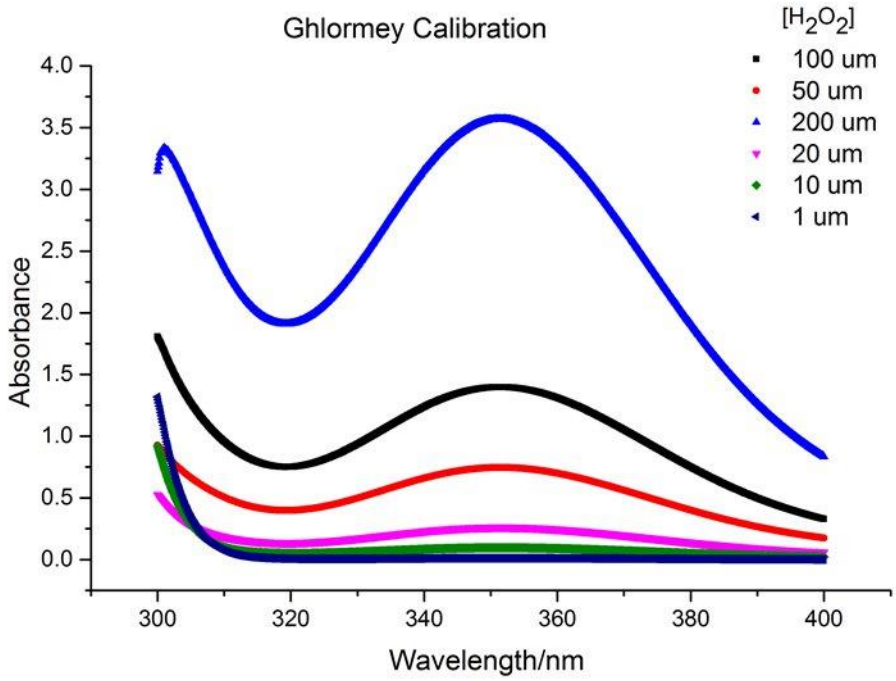

Figure 7.1-1. An example of the calibration graphs, wavelength vs Absorbance for Ghormley triiodide calibrations.

ICP-MS method

Aqueous samples (5 mL) were filtered using a 0.45 µm PVDP filter and diluted by a factor of 2. The samples were acidified using trace metal analysis grade nitric acid (200 µL). These were then analysed using ICP-MS to give dissolved iron concentration.

Irradiation experiments

CRUD simulants (0.5 g) and water (15 mL) were sealed in glass vials using polypropylene crimp camps. Half the samples were degassed with argon to remove oxygen and the other were left aerated. The samples were then irradiated for varying total doses at dose rates of ~20 Gy/min and ~100 Gy/ min. Samples were positioned inside the ^{60} Co chamber in bespoke rack where dose rates were previous determined using Fricke dosimetry, and dose is determined by the distance from the source inside the ^{60}Co chamber. Once irradiated, samples were analysed for [H_2O_2] and dissolved iron concentration; using the Ghormley tri-iodide method and ICP-MS respectively. Samples were taken from the vials using a syringe and filtered using a PVDP filter to remove any particulate material. With 3 mL retained for Ghormley detection and 5

mL for [Fe] determination. Varying dose rates were implemented as early work by Jonsson *et al.* showed that dose rate has an effect on the release rate of metal ions.[6]

Results and discussion

Initial experiments monitored the effects of CRUD simulant on radiolysis behaviour, as well as the effects of total dose and dose rates. As well as investigating the effects of oxygen presence on the accumulation of H_2O_2 as an indicator of the radiolysis behaviour of the systems. Variables monitored were concentration of H_2O_2 ($[H_2O_2]$) and dissolved iron concentration, using the Ghormley triiodide method and ICP respectively.

Figure 7.1-2 presents the results of these initial experiments, separating the experiments into deaerated and aerated systems, and system type (Fe_3O_4, Fe_2O_3 and water systems). The average results shown in **Figure 7.1-2** exhibit little difference due to the presence of the oxide in aerated static water conditions. It can be observed in **Figure 7.1-2** that the error bars on the results are large, causing an overlap between different system types. It is well documented that the presence of iron oxide and other metals alters the concentration of H_2O_2 in systems.[3 5, 17 6 18 2 1] Work by Lousada *et al.* investigated the reaction of H_2O_2 with transition metals and lanthanide oxides; aiming to 'systematically study the reactivity of H_2O_2 towards a diversity of oxides'[2] The proposed mechanism of this H_2O_2 decomposition by the oxide can be seen in **Equations (7.1-3)**,**(7.1-4**) and **(7.1-5)** where M is a site on the oxide surface.

$$H_2O_2 + M \rightarrow 2HO^{\bullet} + M \qquad \textbf{(7.1-3)}$$

$$HO^{\bullet} + H_2O_2 \rightarrow HO_2^{\bullet} + H_2O \qquad \textbf{(7.1-4)}$$

$$2HO_2^{\bullet} \rightarrow H_2O_2 + O_2 \qquad \textbf{(7.1-5)}$$

The results in **Figure 7.1-2** contradict the documented results, showing no obvious difference between systems. Further examination of the raw data shows that there is a large spread of data with some clustering of the results. **Figure 7.1-2 D)** shows Fe_3O_4 systems and there is clustering of data point around more than one 'average' is more apparent than the other systems. This may be attributed to the increased number of data points in comparison to the water **Figure 7.1-2 C**) and Fe_2O_3 systems (**Figure 7.1-2 B**). The lack of difference in the systems may be attributed to systematic and experimental errors.

Figure 7.1-3A, B, C and D consider the averaged results of deaerated systems with respect to the aerated systems. The deaerated system shows negligible or even negative [H_2O_2]. A negative concentration is not possible, so these results suggest that the concentrations of H_2O_2 in these systems is lower than the detection limit of the method. A negligible concentration of H_2O_2 in deaerated is expected at these doses as there is not a source of oxygen, which is essential for the build-up of H_2O_2 to occur. The concentration of H_2O_2 is dependent on the concentration of $\bullet e^-_{aq}$ and •OH. When systems are aerated there will be a reduction in the [$\bullet e^-_{aq}$] and [•OH], the reaction of $\bullet e^-_{aq}$ with oxygen increases the [$\bullet O_2^-$] and therefore [H_2O_2]. In these deaerated systems, pH should be neutral and therefore the [H_2O_2] is dependant the combination of two OH radicals. Without the removal of the [$\bullet e^-_{aq}$] and [•OH] radicals, the decomposition of H_2O_2 can occur via interaction with these radicals. These results suggest at neutral pHs the total doses received do not produce enough H_2O_2 to investigate the deaerated systems in this way. As PWR systems are under deaerated conditions initially it is important to understand the corrosion and dissolution behaviour of CRUD simulants in the presence of H_2O_2. Due to the high doses within the reactor and the mixed radiation field, the [H_2O_2] are not negligible. A possible route of investigation for the deaerated systems is to add a known concentration of H_2O_2 in place of water for the CRUD simulant test, observing any changes in concentration with and without gamma radiation.

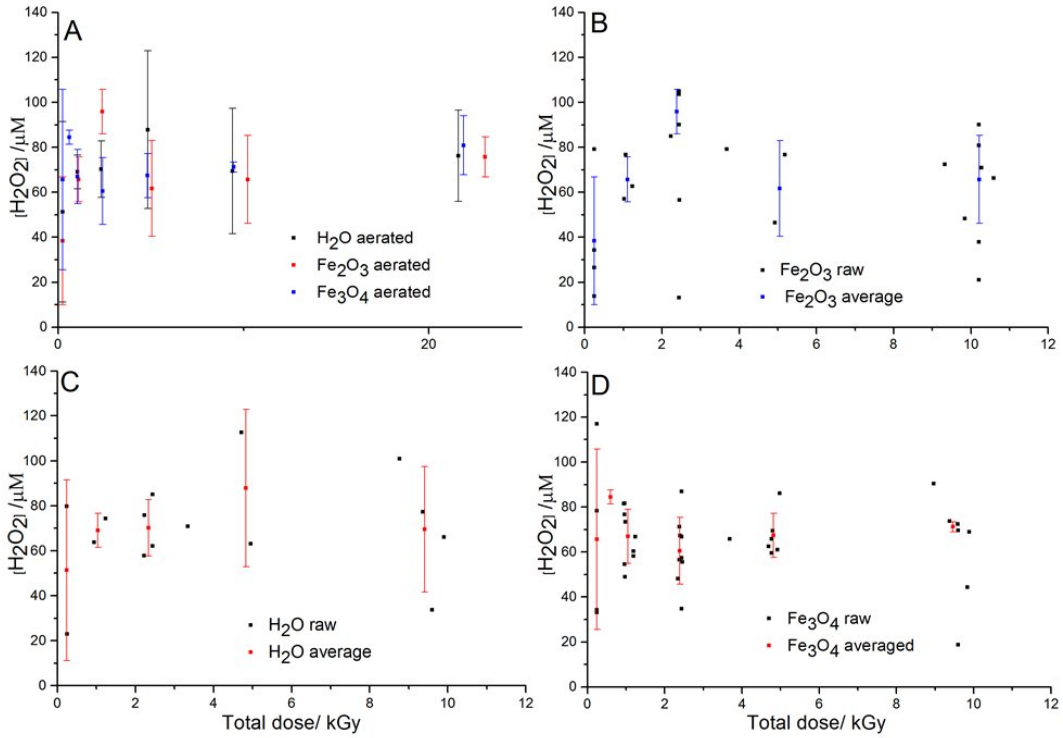

Figure 7.1-2. A) Averaged [H_2O_2] /mM vs total dose for aerated systems containing 15 mL water and 0.5 g solid unless stated; B) Fe_2O_3 systems, comparing average and raw data; C) Water systems comparing average and raw data; D) Fe_3O_4 systems comparing average to raw data.

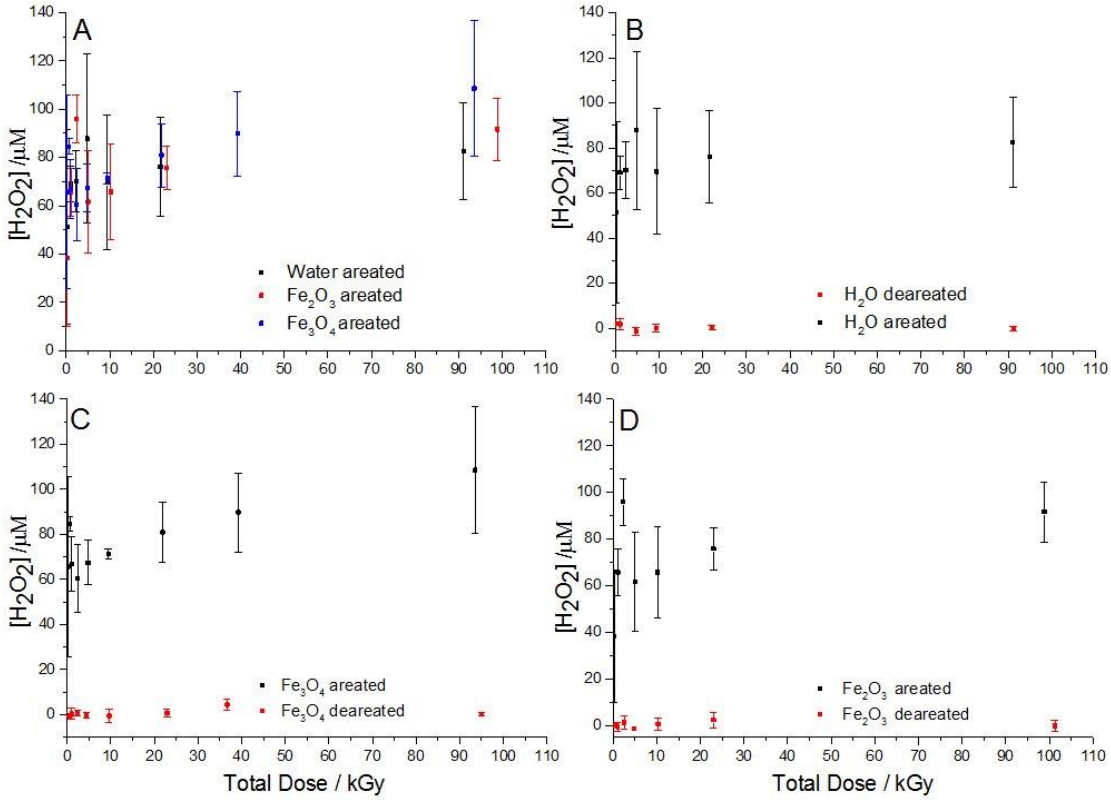

Figure 7.1-3. A) Comparison of aerated systems; B) Comparison of total dose vs average [H_2O_2] for deaerated and aerated Fe_2O_3 systems; C) Comparison of total dose vs [H_2O_2] for deaerated and aerated water systems; D) Comparison of total dose vs average [H_2O_2] for deaerated and aerated Fe_3O_4 systems.

Dissolved iron concentration results

The results of the ICP-MS studies observing the dissolved concentrations of iron after irradiation were inconclusive. **Figure 7.1-4** shows the results of ICP-MS comparing system types and dose rate. These results suggest that only Fe_3O_4 systems have a [Fe] significantly higher than that of water, this may be due to the presence of Fe^{2+} in these systems which is more soluble than the Fe^{3+} in Fe_2O_3 systems. For iron to release from hematite systems iron must be reduced to Fe^{2+} and under aerated conditions this may be less likely to occur. Results had a lot of scatter with large errors, so no conclusion can be made from these results. The errors in the results can be seen in **Figure 7.1-5.** The large error in these results may be due to the detection limit for iron is quite low, with questionable reliability of iron detection at quantities as low as ppb when using the ICP-MS technique here as the molecular weight is like that of the carrier gas used. There may also be inaccuracies in the sample preparation, contamination, or the loss of [Fe] due to pH or $[H_2O_2]$ changes over time of sample attainment. The technique also relies on a minimum volume of solute that means some samples had been diluted, potentially below the detection limit.

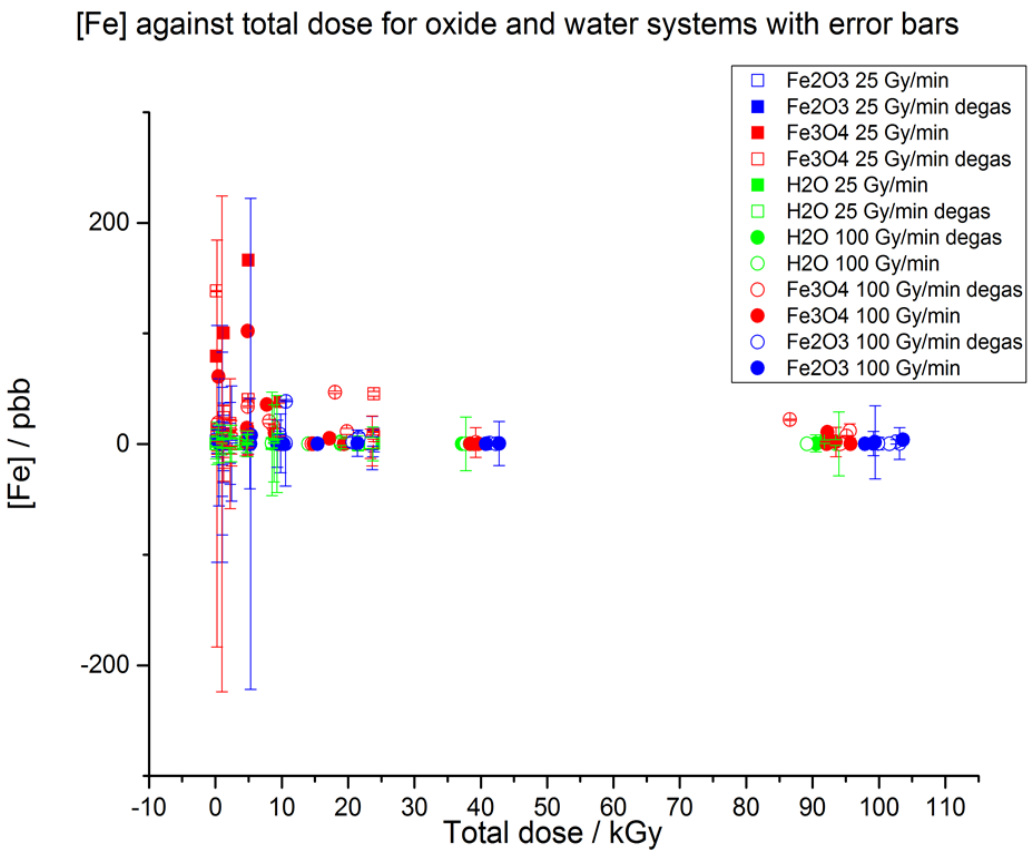

Figure 7.1-5. Total dose vs [Fe] / ppb for deaerated and aerated systems containing 15 mL water and 0.5 g of iron oxide with error bars

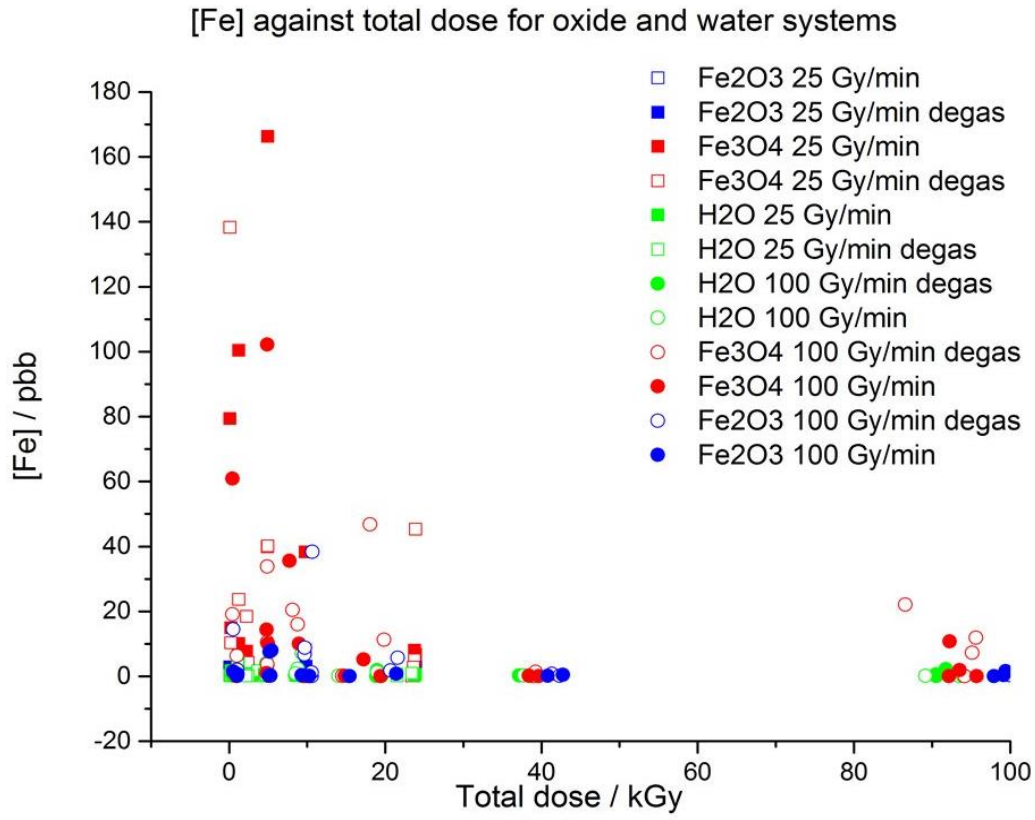

Figure 7.1-4. Total dose vs [Fe] / ppb for deaerated and aerated systems containing 15 mL water and iron oxide

Analysis of experimental procedure and possible sources of error

The following section critically analyses the experimental procedure and suggests a more thorough experimental procedure. Firstly, if the oxides are considered, these were used 'as received' under the premise that oxide size was less than 50 μm. It became clear as the experimental work continued that the oxide aggregated over time forming larger 'particles', reducing the surface area to volume ratio. Surface area to volume ratio is very important when considering reaction and absorption sites. A larger surface area to volume ratio will mean a larger number of reaction sites, thus affecting the concentration of H_2O_2. It may be hypothesised that the newer the oxide the more reactive it is in the degradation of H_2O_2, reducing the overall concentration of H_2O_2. The systems were not agitated (i.e. were static), therefore it is hypothesised that the reaction of H_2O_2 and other radiolysis products would be determined by the number of available sites on the surface and the diffusion to and from the surface. This would limit reactions to just the top 'surface' of the oxide, unless radiolysis products can penetrate the oxide powder.

Another consideration of using 'as received' oxide is that any 'free' Fe^{2+} and Fe^{3+} may interact in the bulk of the system, potentially undergoing Fenton chemistry. Fenton reactions may use both Fe^{2+} and Fe^{3+} to oxidise H_2O_2, leading to the disproportionation of the system forming hydroxyl and hydroperoxyl radicals. These reactions can be seen in **Equations (7.1-6) and (7.1-7).**[19]

$$Fe^{2+} + H_2O_2 \rightarrow Fe^{3+} + HO\bullet + OH^- \quad \textbf{(7.1-6)}$$

$$Fe^{3+} + H_2O_2 \rightarrow Fe^{2+} + HOO\bullet + H^+ \quad \textbf{(7.1-7)}$$

It is possible for there to be dissolution from the 'surface' of oxides into the bulk that would allow for these Fenton reactions to occur. The presence on 'free' iron ions provides an alternative and potentially competitive reaction between the interactions of H_2O_2 and the surface, an alternative mechanism for H_2O_2 decomposition. The decomposition of H_2O_2 by iron oxide may also provide a source of error. If the oxide is in contact with the aqueous phase for varying time, the determined H_2O_2 concentration will vary. Initial H_2O_2 concentration determination was done by removing only enough of the aqueous phase for the determination methods, meaning that there were different time intervals between experimental repeats.

Errors in results may also have arisen from [H_2O_2] determination which was carried out post irradiation. The Ghormley triiodide is a spectroscopic method where [H_2O_2] is determined by the oxidation of iodide by H_2O_2. The extinction coefficient is determine using a calibration using known [H_2O_2]. If the calibration solutions of known [H_2O_2] are incorrect the calculated extinction coefficient will also be incorrect. Due to the dependence of the method on a chemical reaction, taking measurements at different time intervals after reagent addition could lead to variance in the results. The addition of reagents and sample was not timed and controlled so some variance in [H_2O_2] will have occurred. The reaction vessel will alter the surface area and diffusion of reactants and potentially changed the reaction rate. As the experimental program proceeded, the degradation of the Ghormley reagents over time was observed and that reagent A is susceptible to light; this will have contributed to exhibited scatter in the results. In summary, there are a few clear sources of errors in the results:

- Using oxide ‘as received’ not making sure that the particle size is below a certain threshold;
- Not agitating the system, leaving reaction to depend on diffusion, as well as the absorption and desorption from the surface;
- Not removing oxide from the aqueous phase immediately;
- The Ghormley method not being well defined and not being carried out with guaranteed precision, timing is essential in the Ghormley method;
- The Ghormley reagents being stored incorrectly allowing for enhanced degradation over time.

The errors that occurred in dissolved [Fe] concentration may have arisen due to experimental inaccuracies. As the experimental program proceeded, it was highlighted that due to possible changes in oxidation states due to Fenton type reactions, dissolved iron may ‘precipitate’ out of the system or combine with other chemical species removing it from the bulk of the system. Time of contact between the aqueous system and oxide will affect this concentration of chemical and dissolved iron species, this variable was not control throughout these initial experiments. It is therefore not possible to say that the concentrations of iron measured during the ICP-MS determination are an accurate representation of the systems, a consideration for

controlling the time that the oxide is exposed to the aqueous systems will be made going forward. Another limitation of the ICP-MS measurements is that the detection limit itself causes high errors in the measurements due to its sensitivity limits. The technique is also unable to distinguish between Fe^{2+} and Fe^{3+} which is of interest to the study, as it would help determine if dissolution and H_2O_2 interactions are dependent on the oxidation state of the metal oxide. It may be possible to use a spectroscopic technique that uses a chelating agent that binds to Fe^{2+} with selectivity. In conjunction with a reduction step it may be possible to determine overall [Fe] as well as the [Fe^{2+}] and [Fe^{3+}]. Ferrozine is used widely for the detect of low concentrations of [Fe], with nanomolar concentrations being detected in biological applications.[20] [21] [22] This detection method will be investigated as an addition to the use of ICP- MS for iron detection.

The most easily rectifiable experimental error was monitoring and controlling the contact time of the aqueous phase with the oxide powder. Total contact time should be recorded, and the oxide removed from the system as soon as possible after the irradiation is finished. This was done by separating the whole system from the oxide by filtration rather than the quantity needed for [H_2O_2] and [Fe] determination. This allowed for the most accurate representation on the system. The irradiation system itself was improved upon, using flame sealed vials to grantee samples remain deaerated, as well as providing a guaranteed seal when considering sample agitation.

The Ghormley detection method can be carried out with greater accuracy with known time intervals between reagent addition and then sample addition. With both the reagents and samples being kept in the dark between addition and measurement. Work by Iwamatsu *et al.* determined that a 5-minute interval between addition of reagents A to B and then the addition of the sample is adequate. A further five minutes' interval before the absorbance measurement is taken to allow for full reaction and accuracy.[23]

During sample preparation it was shown that the iron oxides should be dried to remove any excess water. Being careful not to oxidise the sample, this may be done using a vacuum oven and keeping the temperature below the oxidation temperature. A value of 50 °C was chosen. The oxide particle size will affect the outcome, so an attempt towards uniformity was made, using a set of molecular sieves and a pestle and mortar. The particle size surface area and uniformity determined using SEM and BET

measurements. It was evaluated that for deaerated systems should be degassed for 2 minutes per mL of solute added to the oxide powder with either argon or helium.

These preliminary experiments showed that the concentration of H_2O_2 was under the detection limit in deaerated systems with a large experimental error, and the ICP-MS gave a large error in the iron concentrations. To overcome this, it has been concluded that addition of known concentration of H_2O_2 before irradiation will allow for better investigation of the interaction behaviour between corrosion and radiolysis products. The Ghormley method was also modified to enhance accuracy, controlling addition time and using an alternative buffer system for added stability. The amount of iron used was reduced from 0.5 g to 0.25 g, as this gave more reproducible results. For the experimental period reported in this section, the dissolution behaviour of iron was halted as the ICP-MS measurements did not give reproducibility. In future, it may be possible to determine these using spectroscopic or chromatographically by addition of a chelating agent such as ferrozine.

References

1. S. C. Reiff and J. A. LaVerne, *The Journal of Physical Chemistry B*, 2015, **119**, 7358-7365.
2. C. M. Lousada, M. Yang, K. Nilsson and M. Jonsson, *Journal of Molecular Catalysis A: Chemical*, 2013, **379**, 178-184.
3. M. A. Nejad and M. Jonsson, *Journal of Nuclear Materials*, 2004, **334**, 28-34.
4. M. Abili Nejad and M. Jonsson, *Journal of Nuclear Materials*, 2005, **345**, 219-224.
5. M. Yang and M. Jonsson, *Journal of Molecular Catalysis A: Chemical*, 2015, **400**, 49-55.
6. Å. Björkbacka, S. Hosseinpour, M. Johnson, C. Leygraf and M. Jonsson, *Radiation Physics and Chemistry*, 2013, **92**, 80-86.
7. C. M. Lousada, T. Brinck and M. Jonsson, *Computational and Theoretical Chemistry*, 2015, **1070**, 108-116.
8. Y. Wada, S. Uchida, M. Nakamura and K. Akamine, *Journal of nuclear science and technology*, 1999, **36**, 169-178.
9. Y.-J. Kim, *CORROSION*, 1999, **55**, 81-88.
10. Y. Hatano, Y. Katsumura and A. Mozumder, *Charged Particle and Photon Interactions with Matter: Recent Advances, Applications, and Interfaces*, CRC Press, 2010.
11. K. Daub, X. Zhang, J. J. Noël and J. C. Wren, *Electrochimica Acta*, 2010, **55**, 2767-2776.
12. B. Pastina and J. A. LaVerne, *The Journal of Physical Chemistry A*, 2001, **105**, 9316-9322.
13. D. M. Bartels, J. Henshaw and H. E. Sims, *Radiation Physics and Chemistry*, 2013, **82**, 16-24.
14. A. Elliot and D. Bartels, *The reaction set, rate constants and g-values for the simulation of the radiolysis of light water over the range 20 deg to 350 deg C based on information available in 2008*, Atomic Energy of Canada Limited, 2009.
15. A. O. Allen, C. J. Hochanadel, J. A. Ghormley and T. W. Davis, *The Journal of Physical Chemistry*, 1952, **56**, 575-586.
16. C. J. Hochanadel, *The Journal of Physical Chemistry*, 1952, **56**, 587-594.
17. R. Pehrman, M. Amme, O. Roth, E. Ekeroth and M. Jonsson, *Journal of Nuclear Materials*, 2010, **397**, 128-131.
18. X. Zhang, W. Xu, D. W. Shoesmith and J. C. Wren, *Corrosion Science*, 2007, **49**, 4553-4567.
19. H. J. H. Fenton, *Journal of the Chemical Society, Transactions*, 1894, **65**, 899-910.
20. T. M. Jeitner, *Analytical Biochemistry*, 2014, **454**, 36-37.
21. L. L. Stookey, *Analytical Chemistry*, 1970, **42**, 779-781.
22. E. Viollier, P. W. Inglett, K. Hunter, A. N. Roychoudhury and P. Van Cappellen, *Applied Geochemistry*, 2000, **15**, 785-790.
23. K. Iwamatsu, S. Sundin and J. A. LaVerne, *Radiation Physics and Chemistry*, 2017, DOI: https://doi.org/10.1016/j.radphyschem.2017.11.002.

7.2 Investigating the interactions between Corrosion products and Radiolytic species encountered in PWR primary coolant

Elizabeth Parker-Quaife,[1,2,*] Jay LaVerne,[3] and Simon M. Pimblott[4]

[1]*The School of Chemistry, The University of Manchester, Manchester, UK*

[2] *Dalton Cumbrian Facility, The University of Manchester, Moor Row, Cumbria, UK*

[3] *Radiation Laboratory and Department of Physics, University of Notre Dame, Notre Dame, Indiana 46556, United States*

[4]*Idaho National Laboratory, 1955 N. Fremont Ave., Idaho Falls, Idaho 83415, United States*

*Corresponding author Elizabeth Parker-Quaife.

Email address: elizabethparkerquaife@gmail.com

Abstract

The gamma-irradiation of iron oxides (Fe_2O_3, Fe_3O_4 and FeO as CRUD simulants) in aqueous hydrogen peroxide (H_2O_2) solutions under varying conditions were undertaken. Oxides were characterised pre-irradiation using Raman spectroscopy, temperature-programmed desorption, BET and SEM images. The decomposition of H_2O_2 on the oxides was monitored using the Ghormley tri-iodide method post-irradiation. H_2O_2 decomposition seemed to occur rapidly pre-irradiation in Fe_2O_3 systems via Fenton reactions, which generates hydroxyl species and oxygen. These species promote the radiolytic generation of H_2O_2 , that then may decompose via radiolytic or homogenous Fenton chemistry. Fe_3O_4 and FeO systems had slower initial decomposition of H_2O_2 pre-irradiation, followed by decomposition due to interaction with radiolysis products and the release of Fe^{2+} into the bulk solution allowing for homogenous Fenton reactions to occur. Longer irradiations strengthened the hypothesis of slow release of Fe^{2+} under all conditions, which was qualitive assessment as no quantification of solubilised iron was undertaken in this study. Examination of the iron oxides post-irradiation by X-ray diffraction, XPS and Raman spectroscopy showed small changes in surface and bulk morphology; with Fe_2O_3 systems having observable changes in XRD measurements which may be attributed to the reduction to Fe_3O_4 by the decomposition of H_2O_2.

Key words

Radiolysis, hydrogen peroxide, iron oxides, CRUD, Raman Spectroscopy, XPS spectroscopy.

Introduction

Understanding the interactions between radiolysis and corrosion products is essential in deconvoluting the complex corrosion behaviour observed in the nuclear industry; with enhanced understanding benefiting life time extension projects and waste storage processes. Corrosion and dissolution of reactor materials leads to the build-up of mixed corrosion products (a phenomenon termed CRUD)[1, 2] of concern for both the performance and safety of affected reactors.[2] Characterisation of corrosion related deposition products, will afford the ability to better predict such behaviour. Radiolysis of water results in the production of both oxidising and reducing species in both radical and molecule species which may be summarised as: [3, 4]

$$H_2O \longrightarrow HO^{\bullet}, e_{aq}^{-}, H^{\bullet}, HO_2^{\bullet}, H_2O_2, H_2, H^{+} \qquad \textbf{(7.2-1)}$$

These radiolysis products may recombine to form water but may also interact with dissolved impurities or any surfaces present. These interactions are of interest in the fields of radiation chemistry, material science and nuclear engineering. H_2O_2 is the most stable molecule radiolysis product and detection facile. H_2O_2 has been shown to be a suitable way to emulate the effects of ionising radiation when a source is not available.[5-9] Observing the effects of radiolysis in deaerated systems can be problematic as total dose needed for detectable concentrations of H_2O_2 by chemical methods are high. To overcome this, H_2O_2 is added to systems designed to simulate the effects of radiation. It also possible to induce irradiation using a known concentration of H_2O_2 at initiation. This study aims to further the understand the interaction between these corrosion and radiolysis production. Although it is an important oxidising species, the fundamental behaviour of H_2O_2 is currently understudied. Recent work by K. Iwamatsu *et al.* investigated the H_2O_2 kinetics in water radiolysis by addition of varying [H_2O_2] followed by either ɣ or heavy iron radiation. The effects of hydrogen addition were also investigated, the work concluded that the radiation of H_2O_2 is much more complicated than expected.[10]

Previous studies have investigated the interaction of H_2O_2 with materials used within the nuclear industry;[9-18] while others on the effects of radiation on the corrosion of

nuclear materials, including copper,[19] stainless and carbon steels,[8, 20, 21] along with corrosion products such as iron oxides.[22-24] These studies have attempted to understand the radiation inducted corrosion behaviour but there are still questions regarding the mechanisms and behaviour of these systems. Understanding these would benefit operators and designs of Pressurised Water Reactor (PWRs) and Boiling Water Reactors (BWRs) plants, as well as storage of spent fuel and nuclear waste. Parker-Quaife *et al.* have previously reviewed prominent literature used to inform the studies into the interaction between radiolysis and corrosion products.[25]

Following on from work by Laverne *et al.* where the radiation-induced chemical changes to iron oxides were investigated, this paper investigates the effects the interaction of ɣ-radiolysis products with iron oxides. A known [H_2O_2] was added to three iron oxide, FeO, Fe_2O_3, Fe_3O_4 and then exposure to ɣ-radiation to varying total doses, with [H_2O_2] determined post irradiation. The iron oxides were characterised prior to irradiation using Brunauer-Emmett Teller (BET), Temperature-Programmed Desorption (TPD), Scanning Electron Microscopy (SEM), Raman spectroscopy, X-ray Photoelectron Spectroscopy (XPS) and X-ray diffraction. Post-irradiation sample surfaces were probed using XPS, XRD and Raman spectroscopy.

Experimental methods

Sample preparation and surface analysis

Iron (II) oxide (FeO, 99.5% 10 mesh), Iron (II, III) oxide (Fe_3O_4, 95% <5 µM) and Iron (III) oxide (Fe_2O_3, 99% <5 µM) were purchased from sigma Aldrich. Samples were baked at 50 °C in a vacuum oven overnight to ensure the powder was dry then FeO was crushed and passed through a 90 µM sieve. Fe_3O_4 and Fe_2O_3 were fine enough to pass through the sieve without any crushing. The BET methodology was used to determine the surface area size of the oxide powders, with a Tri-Star II surface area and porosity analyser (Micrometrics) used, with N_2 use as the adsorbate gas throughout. SEM images were taken to give an indication of particle size and uniformity. A FEI Quanta FEG 250 was used to image the powders which were mounted on SEM stubs with carbon tape, voltages of up to 5 kV and magnification up to 40000X.

The oxide powders were analysed using temperature programmed desorption to analyse water and contaminates at the surface of the oxides. TPD measurements were

undertaken at The University of Notre Dame. A custom cell that holds between 50-100 mg of powder in a crucible and this was heated from room temperature to 500 °C at a rate of 5 °Cmin^{-1}. The chamber pressure was 12^{-10} bar prior to heating. The gases desorbed were measured using a Pfeiffer Prisma quadrupole mass spectrometer and mass to charge ratios of 14, 15, 16, 18, 28, 32, 40 and 44 were monitored throughout. A blank was taken before each measurement and this was subtracted from the oxide measurements. Redhead analysis was undertaken using the mass to charge ratio 18 which gave the binding of species on the surface. These values are used to determine the type of species and the binding type.

Raman spectroscopy measurements were taken using a Bruker RamanScope III. as FTIR measurements proved inconclusive due to high wavelengths of light causing the oxides to oxidise as well as the reflectance spectra giving little response due to the dark colour of the oxides. A 785 nm laser was used for the Fe_2O_3 powder analysis and 532 nm laser for Fe_3O_4 and FeO powders to prevent further oxidation of the powders by the laser.[23] The lowest laser power was also selected for these samples and was 1 mW for Fe_2O_3 and 2 mW for Fe_3O_4 and FeO as measurements taken at 0.2 mW were unable to give spectra.

XPS measurements were taken with a Kratos axis ultra-Hybrid X-ray photo spectrometer that utilises an Al Kα monochromated source, with a photon energy of 1486.6 eV.

Powder XRD was undertaken using a Philips X'Pert – PRO theta-theta PW3050/60 diffractometer (480 mm diameter) with PW3064 sample spinner and X'Celerator (2.122° active length) 1D-detector in Bragg-Brentano geometry employing a Copper Line Focus X-ray tube with Ni kβ absorber (0.02 mm; Kβ = 1.392250 Å) Kα radiation (Kα1=1.540598 Å, Kα2=1.544426 Å, Kα ratio 0.5, Kαav=1.541874 Å). An incident beam Soller slit of 0.04 rad, 2° fixed anti scatter slit, incident beam mask of 10 mm and programmable automated divergence slit giving a constant illuminated length of 10.0 mm and receiving Soller slit of 0.04 rad were used. Data collections from 10.2 to 89.93° coupled 2theta/theta at 0.05° step 1550.67 s/step was undertaken.

Hydrogen peroxide determination

Hydrogen peroxide standard solutions (H_2O_2, Fisher scientific or Sigma) were used as received without extra purification. Solutions were made up using ultra-pure water

(>18.2 MΩ cm) purified by UV-lamps and filters. H_2O_2 concentration were determined using the Ghormley tri-iodide method where I^- is oxidised by H_2O_2 to I_3^-, absorbance maximum is taken at 350 nm.[26] Absorbance maximum 25080 $M^{-1}cm^{-1}$ Evolution 220, Thermo Scientific (Notre Dame experiments) and average absorbance 24839 M^{-1} cm^{-1} for DCF experiments using a Agilent Technologies Cary Series UV-Vis-NIR spectrophotometer. These values are in good agreement with previous work.[18, 26-28]

Irradiations

Samples cells for ɣ-radiations were Pyrex test tube of ~ 10 mm in diameter and 10 cm in length. Short deaerated γ-irradiations were performed using a self-contained Shepard ^{60}Co source at the University of Notre Dame, Radiation Laboratory which had a dose rate of ~ 111 Gy min^{-1}. Samples containing iron oxide (0.25 g) and H_2O_2 (50 µM, 3 mL) were deaerated with high purity helium for 6 minutes, then flame sealed. (Previous studies have shown that 2 minutes per mL of solute is suffice for oxygen removal). Flame sealing was immediately followed by irradiation and [H_2O_2] determination using the Ghormley triiodide method (samples were immediately filtered from the iron oxide post irradiation to minimise H_2O_2 degradation due to surface/ redox / bulk reactions due to iron).[26, 29, 30]

Short aerated Gamma ray irradiations were performed at the University of Manchester Dalton Cumbrian facility (DCF) using a self-shielded Foss therapy ^{60}Co source utilising dose rate of ~ 158 Gy min^{-1}. Samples containing iron oxide (0.25 g) and H_2O_2 (50 µM, 3 mL) were bubbled with synthetic air for 6 minutes (to minimise experimental variance) then flame sealed, immediately followed by irradiation and [H_2O_2] determination. Longer irradiations were undertaken to compare the effects of irradiation to exposure of H_2O_2. Total doses for these experiments reached ~ 290 kGy. Other irradiations were undertaken at the DCF to determine if there were any changes in the iron oxides after shorter irradiations showed undetectable changes to surfaces using the outlined surface techniques, but changes were indicated by the H_2O_2 behaviour.

Results and discussion

Surface characterisation

Characterisation of the oxide surface was undertaken pre and post irradiation. H_2O_2 is known to reaction will react at oxide/surface interfaces, [9, 14-16, 18, 27, 31] and the pathways are thought to include both redox reaction and catalytic decomposition which may lead to change in oxide composition.[14, 18] BET measurements determined the average from multiple runs gave the surface areas to be 0.23 ± 0.002 m^2/g, 5.29 ± 0.02 m^2/g and 5.99 ± 0.02 m^2/g for FeO, Fe_2O_3 and Fe_3O_4 respectively. A representative isotherm for each oxide powder is given in **Figure 7.2-1**. The shape of the isotherms and the lack of hysteresis between the adsorption and desorption curves suggest that the particles are macroporous, or lack porosity entirely. There is a large difference between the surface areas of Fe_2O_3 and Fe_3O_4 and that of FeO.

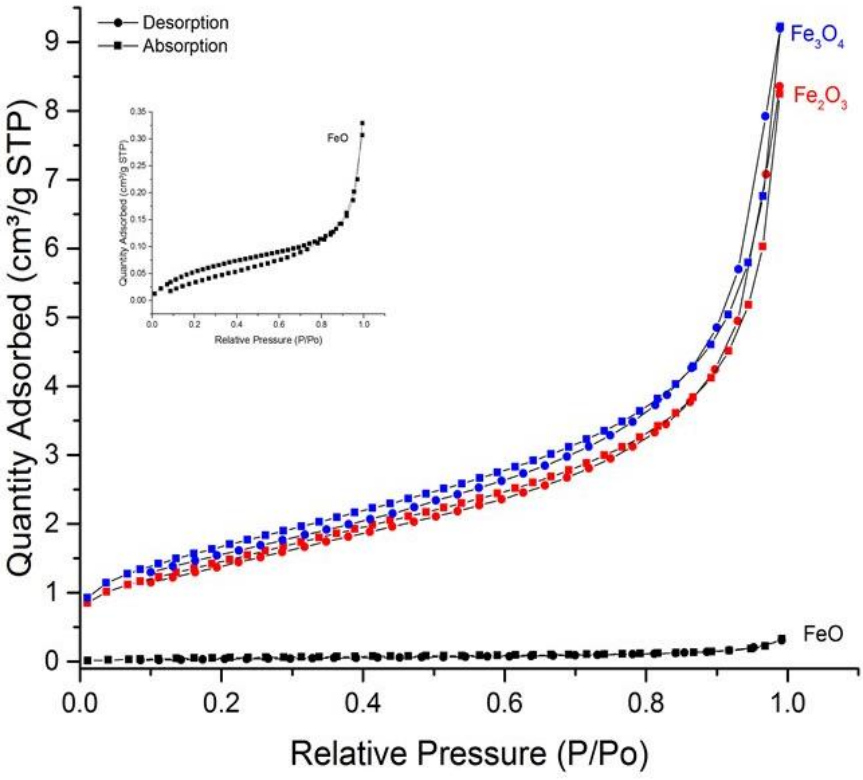

Figure 7.2-1. Isotherms obtained from N_2 absorption (■) and desorption (●) for FeO (enlarged in the inset), Fe_2O_3 and Fe_3O_4.

SEM imaging allowed for the visualisation of the particles, allowing for qualification of oxide particle shape and size, (images can be seen in **Figure 7.2-2)**. The SEM images support the BET measurements. The FeO particles are larger in size, and therefore would have a lower surface area. Both the Fe_2O_3 and Fe_3O_4 powders appear to agglomerate together giving larger structures, making a determination of particle

shape difficult. Agglomeration is less prevalent in the FeO samples, although there is evidence of this to a lesser extent. There is no clear indication of porosity in the samples from the SEM imaging.

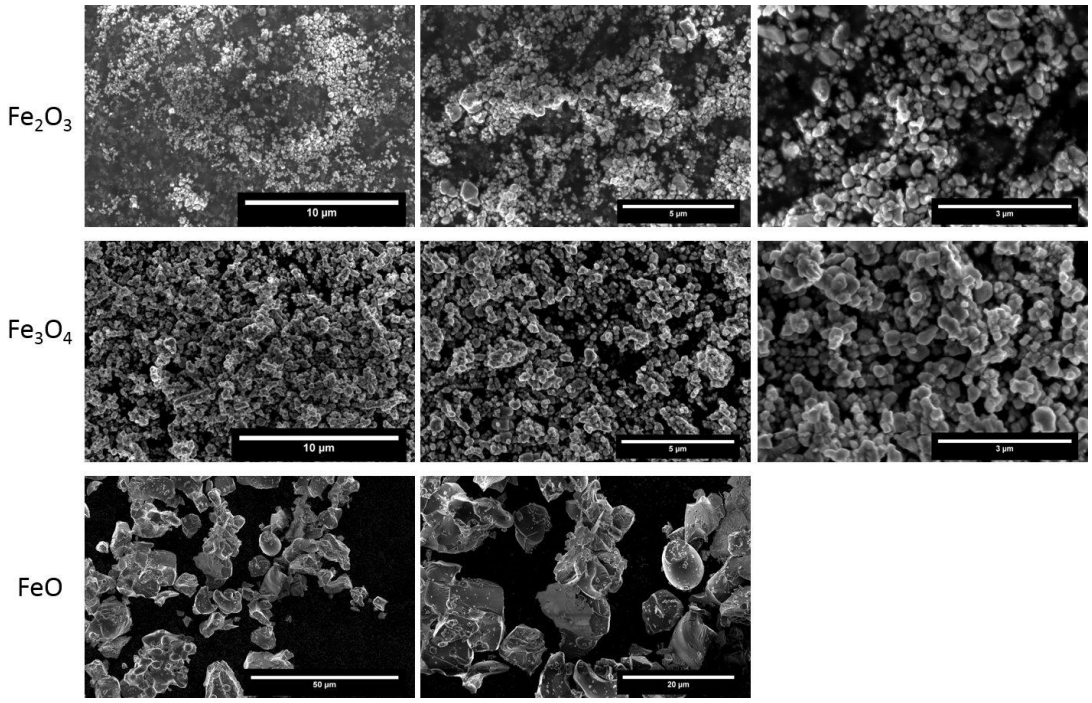

Figure 7.2-2. SEM images of Fe_2O_3 (top), Fe_3O_4 (middle) and FeO (bottom) at different magnifications.

The absorption of species such as water onto the oxide surface was probed using TPD. These measurements are shown in **Figure 7.2-3**, with at least two peaks for each oxide powder. The presence of more than one peak can be expected as powder samples will have many exposed surfaces and therefore several possible adsorption sites. The adsorption energy for each peak was calculated using Redhead's method.[32] Peak values for Fe_2O_3 corresponded to 1.2, 1.4 and 1.6 eV, with similar reported by LaVerne and Reiff. With values for Fe_3O_4 similar and FeO having values slightly higher than reported here and thus may be due to the difference in heating rate.[23] These values are higher than the reported value for physiosorbed water at 0.35 eV suggesting, multiple sites where the chemisorption of water may take place.[23, 33]

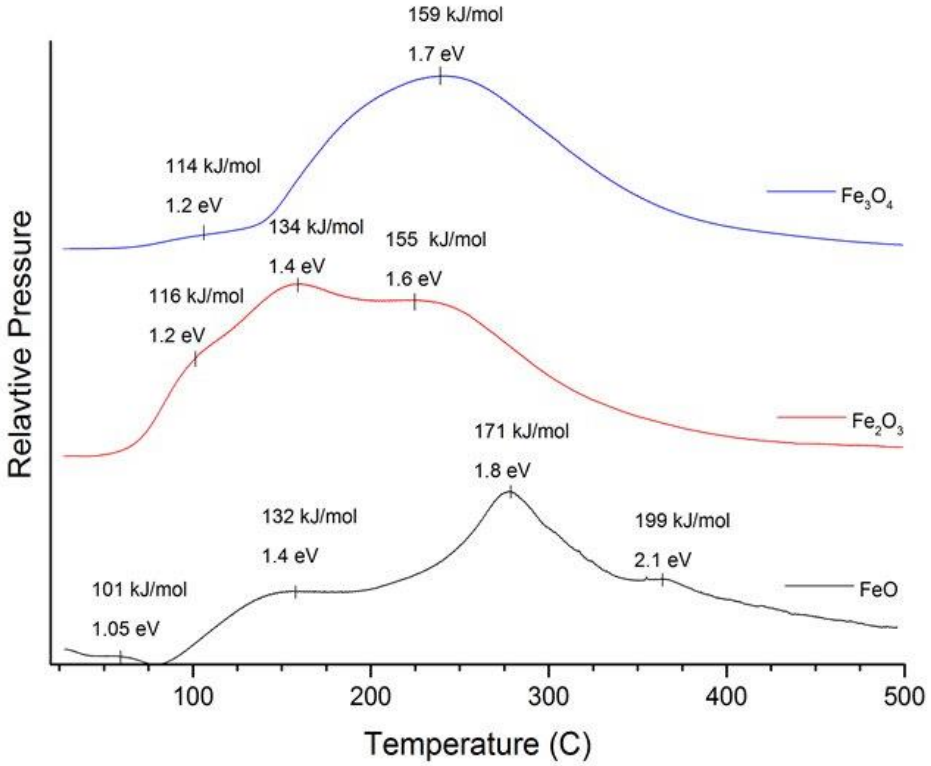

Figure 7.2-3. Temperature Desorption curves for Fe_3O_4 (top), Fe_2O_3 (middle) and FeO (bottom) take at a rate of 5 °C/min. Peaks are labelled with absorption energies calculated using Redheads method.

The effects of irradiation on hydrogen peroxide concentration

The irradiation conditions were variable, with samples being exposed to gamma-radiation to varied total doses. Samples were either degassed with helium or argon, and to investigate the effects of oxygen on the system a set of samples were purged with synthetic air. Sample degassing (or purging) helped to reduce sample variation as H_2O_2 will decompose with contact to oxides. Once purged the samples are flame sealed and irradiated or left for the experimental time (time from addition of H_2O_2 to time of quenching). The samples were filtered post irradiation to prevent further H_2O_2 decomposition on the oxide surface. The decomposition of H_2O_2 may occur in these systems via interaction with the oxide surface, bulk aqueous reactions which may involve iron or induced by radiolysis products.

H_2O_2 degradation by iron is known widely as Fenton reactions, with homogenous Fenton reactions first reported in 1894[34] with the decomposition occurring in solution, by Fe^{2+} forming Fe^{3+} that further react with H_2O_2, known as an autocatalytic reaction. Much later heterogenous Fenton reactions were proposed where reaction of H_2O_2 can occur at iron oxide surfaces, utilising both Fe^{2+} and Fe^{3+} sites.[30, 35, 36] Current work

suggests that heterogenous Fenton systems involve two stages, a slow induction period and then a quicker oxidation period. With research into this heterogenous surface reactions showed that the leaching of iron is followed by homogenous Fenton in the solution bulk.[30, 37, 38] The equations below outline the possible H_2O_2 degradation mechanisms via Fenton or radiolytic pathways.

Radiolytic pathways for hydrogen peroxide degradation

$$HO^{\bullet} + H_2O_2 \rightarrow HO_2^{\bullet} + H_2O \quad \textbf{(7.2-2)}$$

$$H_2O_2 + e_{eq}^{-} \longrightarrow HO^{\bullet} + HO^{-} \quad \textbf{(7.2-3)}$$

$$H_2O_2 + H^{\bullet} \longrightarrow HO^{\bullet} + H_2O \quad \textbf{(7.2-4)}$$

Fenton pathways for hydrogen peroxide degradation

Homogenous

$$Fe^{2+} + H_2O_2 \longrightarrow Fe^{3+} + OH^{-} + HO^{\bullet} \quad \textbf{(7.2-5)}$$

$$Fe^{2+} + HO^{\bullet} \longrightarrow Fe^{3+} + OH^{-} \quad \textbf{(7.2-6)}$$

$$Fe^{3+} + HO_2^{-} \leftrightarrow Fe^{2+} + HO_2^{\bullet} \quad \textbf{(7.2-7)}$$

$$HO^{\bullet} + H_2O_2 \longrightarrow H_2O + O_2^{\bullet -} + H^{+} \quad \textbf{(7.2-8)}$$

$$O_2^{\bullet -} + H^{+} + H_2O_2 \longrightarrow O_2 + HO^{\bullet} + H_2O \quad \textbf{(7.2-9)}$$

Heterogenous

$$Fe^{3+} + H_2O_2 \longrightarrow Fe^{2+} + HO_2^{\bullet} + H^{+} \quad \textbf{(7.2-10)}$$

$$Fe^{2+} + H_2O_2 \longrightarrow Fe^{3+} + OH^{-} + HO^{\bullet} \quad \textbf{(7.2-11)}$$

$$HO_2^{\bullet} \leftrightarrow H^{+} + O_2^{\bullet -} \quad \textbf{(7.2-12)}$$

$$Fe^{3+} + HO_2^{\bullet} \longrightarrow Fe^{2+} + H^{+} + O_2 \quad \textbf{(7.2-13)}$$

Although these irradiated systems had [H_2O_2] of 50 µM added to them initially, the reactivity of the oxides towards H_2O_2 meant that this was not the case at the start of the ɣ-radiations. To determine the loss of H_2O_2 due to the iron oxides and not due to exposure to γ-radiation samples were left for a total experimental time under non-irradiation conditions. These non-irradiated samples exhibited different end [H_2O_2]. Fe_2O_3 had the lowest concentration and FeO the highest comparative concentration after ~ 20 minute exposure time (these are reported in the plots in **Figure 7.2-4** and **Figure 7.2-5** as zero total dose). Non-irradiated systems showed a trend of reactivity towards H_2O_2: Fe_2O_3 > Fe_3O_4 > FeO. The irradiated systems behaviour cannot be

simplified to this extent, as radiolysis behaviour introduces pathways for both H_2O_2 formation and its removal. Work by Iwamatsu *et al.* investigated the H_2O_2 kinetics in water radiolysis and concluded that the steady state concentration of H_2O_2 after irradiation is proportional to the initial H_2O_2 concentration.[10] The deaerated systems exposed to ɣ-radiation reported in this work show that the concentration of H_2O_2 converges to the same minimum concentration ~5 µM, although they would have had a different initial H_2O_2 concentration at the start of irradiation. This convergence suggests that the presence of oxides complicates the mechanism for radiolytic H_2O_2 degradation, with the possibility of multiple chemical and radiolytic pathways being in competition with one another. This convergence may also suggest a change in the oxide composition and morphology towards one oxide type or suggest mechanisms that are dependent on the availability of catalytic sites on oxide the surface or release of ions into the aqueous bulk, which is investigated by physical characterisation of the oxide surface.

A notable and unexpected observation was that the deaerated Fe_2O_3 systems exposed to H_2O_2, but with no subsequent irradiation treatment showed negligible [H_2O_2]. Work by Jonsson *et al.* investigated H_2O_2 reactivity towards CRUD simulants and transition metal oxides.[9, 14] The study into Fe_2O_3 reports a higher H_2O_2/ $H_2O_{2\,0}$ ratio than in this work, but as the initial [H_2O_2] is greater at 0.5 mM and initial has been shown to affect the reactivity towards oxides and γ-exposure. The initial aqueous volumes in these studies are 50 mL containing 0.2 to 1.5 g of oxide; compared to the 3 mL with 0.25 g oxide used here. Furthermore the oxide also had a lower surface area at 4.5 m^2/g which will also have an effect on the system.[14] The mechanism proposed by Jonsson *et al.* for degradation supports the idea of a release of Fe^{2+} from the Fe_2O_3 surface allows for a homogenous Fenton type reaction to occur in the bulk aqueous solution. Release of Fe^{2+} from the surface maybe occur with the reduction of Fe^{3+} by the HO_2 radical produced in the decomposition of H_2O_2. This reduction also involves a $O_2^{\bullet-}$ radical forming O_2.[14, 39, 40]

After irradiation the hematite containing systems the [H_2O_2] increased and plateaued to a similar value of Fe_3O_4 systems. This supports the suggestion that Fe^{3+} in hematite has been reduced to Fe^{2+} during the H_2O_2 degradation process at its surface and released oxygen into aqueous system promoting radiolytic H_2O_2 formation. After further ɣ-exposure, the radiolytic degradation and possible aqueous degradation (via homogenous Fenton reactions due to released Fe^{2+}) will occur during radiation exposure which would explain the end concentration of H_2O_2 in haematite systems being like those containing magnetite. Magnetite and wustite system appear to release Fe^{2+} to the bulk solution allowing for degradation via homogenous Fenton reactions. This mechanism can be also catalytic in behaviour. The concentration of H_2O_2 at zero total dose suggests that the release of Fe^{2+} is slow, and that decomposition may be occurring via the previously described two stage heterogenous Fenton reaction. Further deaerated irradiations are needed to see where the steady state concentration occurs.

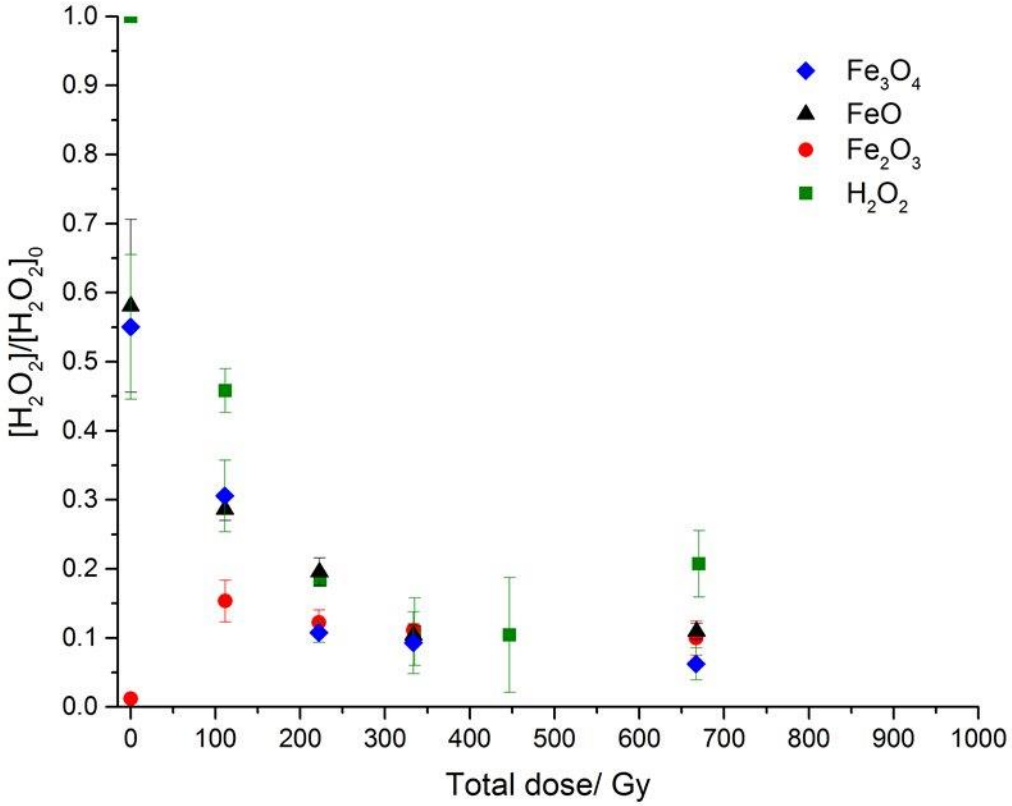

Figure 7.2-4. Normalised hydrogen peroxide concentration ([H_2O_2] post irradiation/ [H_2O_2] added to oxide) against the total dose received for deaerated systems.

To probe this release of oxygen, further experiments under aerated conditions were undertaken to see if the behaviour followed the same trend. The data from these experiments is reported in **Figure 7.2-5.** The systems with no ɣ-radiation exposure, but the same time of exposure to H_2O_2, showed the same trend of reactivity as in deaerated systems, and exposure to ɣ-radiation gave a trend of increased [H_2O_2] with total dose. These aerated systems have an end [H_2O_2] that appears to be related to the concentration at ɣ-radiation initiation. Whereas those systems exposed to H_2O_2 alone appear be reaching a plateau within these irradiations. The presence of the oxide does not seem to hinder H_2O_2 formation, as differences in [H_2O_2] may be explained by the different concentrations at irradiation initiation suggesting that pathways for formation are favoured over those of degradation. The Fe_2O_3 systems exhibit a lower post irradiation concentration, although this reaches what appears to be the state of 'H_2O_2 only' systems plateau within this set of irradiations, suggesting the promotion of H_2O_2 by the presence of oxide. This may be related to the further release of oxygen with Fenton chemistry. If the heterogenous Fenton pathways are initially slow (as proposed in the literature) and then is followed by quicker homogenous reactions this may also go some way to explaining the observed trend in these aerated tests. The systems containing oxides do not appear to be reaching a plateau concentration within these results. Further irradiations are needed to give more information of the competing mechanisms and the cause of H_2O_2 build up and loss. A possible competing pathway that would affect both Fenton and radiolytic pathways is the release of Fe^{2+} into this system which can also remove radiolysis products by reduction oxidation reactions:[41-43]

$$Fe^{2+} + HO^{\bullet} \rightarrow Fe^{3+} + OH^{-} \quad \textbf{(7.2-14)}$$

$$Fe^{3+} + e^{-}_{aq} \rightarrow Fe^{2+} \quad \textbf{(7.2-15)}$$

These reactions can prevent the build-up of H_2O_2, but also prevent the removal of it by hydroxyl radical and solvated electron mechanisms. These reduction/oxidation reactions with ferrous and ferric ions will compete with H_2O_2 degradation by both radiolytic and Fenton pathways. The rates of this equations will dictate the behaviour undertaken.

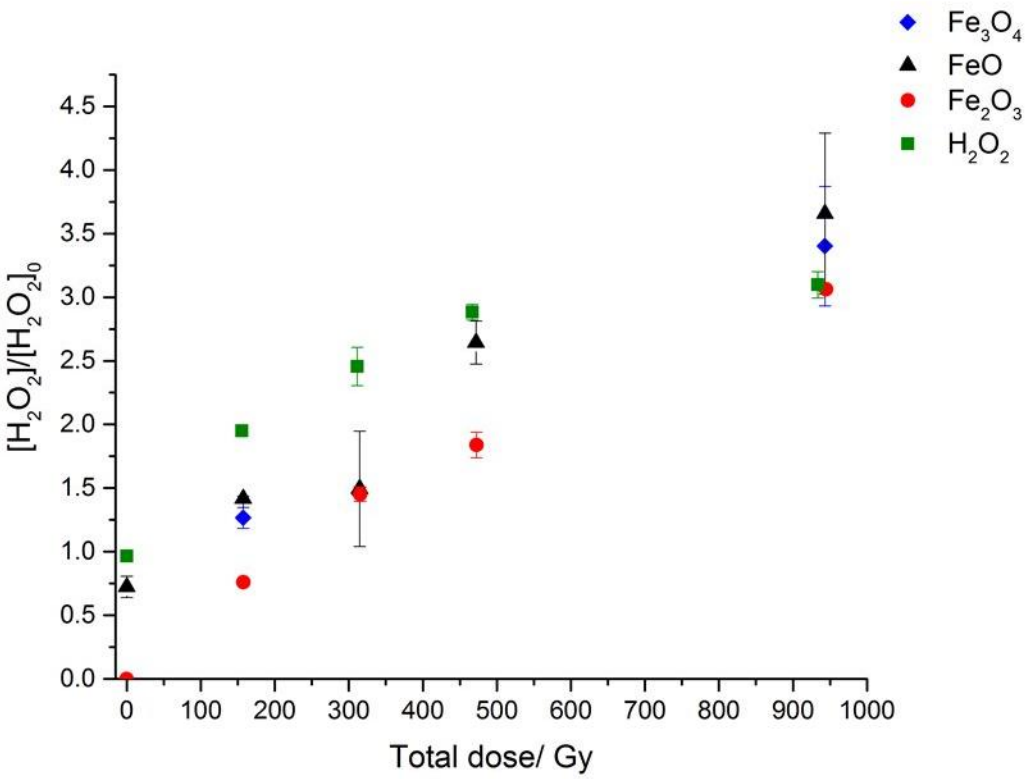

Figure 7.2-5. Normalised hydrogen peroxide concentration ([H_2O_2] post irradiation/ [H_2O_2] added to oxide) against the total dose received for aerated systems.

To investigate the likelihood of a slow Fe^{2+} release followed by homogenous Fenton chemistry or other possible pathways, longer irradiation and exposure periods were undertaken (up to 24 hours). The results (**Figure 7.2-7)**, in which control experiments were not irradiated but are exposure to H_2O_2 for up to 24 hours after deaerating. The aerated and deaerated systems were irradiated for total doses up to 290 kGy. The suggestion that the magnetite and Wustite system decompose H_2O_2 by a homogenous Fenton reaction is supported by the almost complete removal of H_2O_2 in wustite systems. Long exposure time allows for more Fe^{2+} to be released to the bulk solution. The irradiated samples also support this hypothesised release and autocatalytic behaviour as the H_2O_2 concentration does not reach as large a concentration as that seen in the Fe_2O_3 and Fe_3O_4 systems. The release of oxygen from hematite systems during H_2O_2 degradation is also further supported in these longer irradiations, with the deaerated hematite system having a larger [H_2O_2] than the other deaerated oxide systems.

The behaviour of the magnetite systems under these longer irradiations needs further investigation as end [H_2O_2] in aerated conditions is high, although it may be the radiolytic formation of H_2O_2 under these conditions is more favourable than any of the available degradation mechanisms. Several considerations that should be made for the FeO containing systems: 1) the surface area is less so the reaction is expected to be slower that the other oxides. There does not seem to be a significant difference in these irradiation experiments, and 2) is that when FeO is solubilised it generates H_2.[44] This is supported by the work by LaVerne and Reiff that show elevated production of hydrogen in systems irradiated in varying water concentrations for FeO systems, H_2 yields for Fe_2O_3 and Fe_3O_4 are only slightly larger than that reported for bulk water.[23] The kinetic study by Iwamastu *et al.* supports this also, showing that the addition of hydrogen to H_2O_2 solutions reduces the steady state [H_2O_2] due to ɣ-radiolysis.[10] Hydrogen prevents H_2O_2 formation by the reactions proposed by Allen *et al.*, H_2O_2 is reduced back to water when hydrogen is present.[29]

$$HO^{\bullet} + H_2O_2 \rightarrow H_2O + O_2H^{\bullet} \quad \textbf{(7.2-16)}$$

$$H^{\bullet} + H_2O_2 \rightarrow H_2O + HO^{\bullet} \quad \textbf{(7.2-17)}$$

At lower exposure times this hydrogen release may be less likely, but over the longer irradiation experiments it may be contributing to the low H_2O_2 concentrations seen in the irradiated Wustite systems. Due to the multiple pathways to H_2O_2 decomposition is it not possible to fully deconvolute the mechanisms in these systems. The results do indicate that there will be contributions from radiolytic processes as well as interactions with the oxides and that the reduction and oxidation involving Fe^{2+} may also be occurring in these systems. There is evidence of iron release into the solution bulk with longer exposure to iron oxides giving a lower end [H_2O_2]. This requires a further investigation to examination of the aqueous phase, and this could utilise ICP-MS, moss Bauer spectroscopy or quantification with by a chemical assay such as EDTA or ferrozine. Kinetic studies may also give further insight to the which of the proposed mechanisms is dominant.

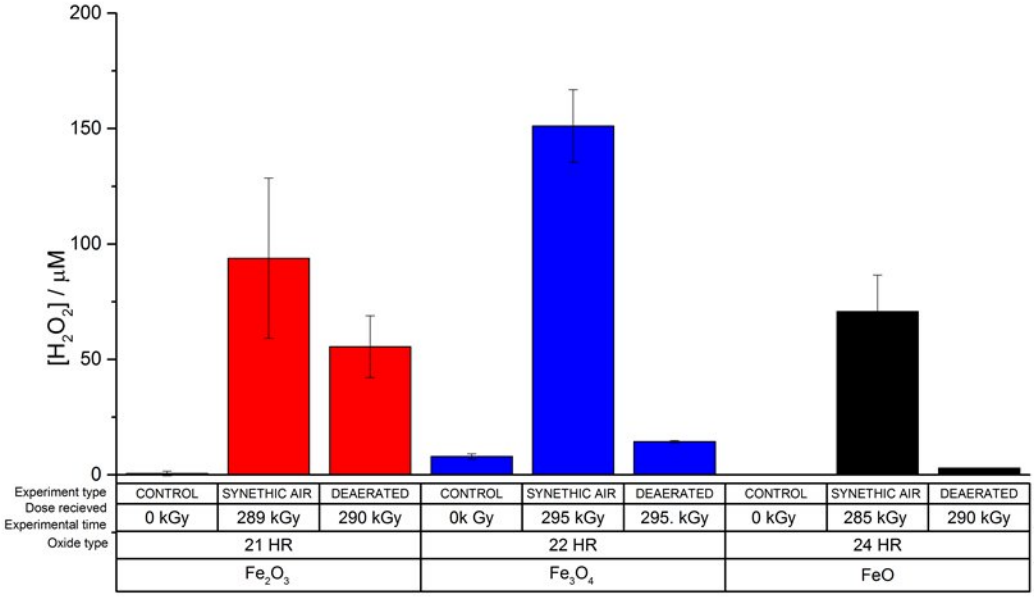

Figure 7.2-7. Hydrogen peroxide coentration histograms plotted against system parameters, ivestigation the effects of longer exposure periods on the interaction between radiolysis and corrosion products.

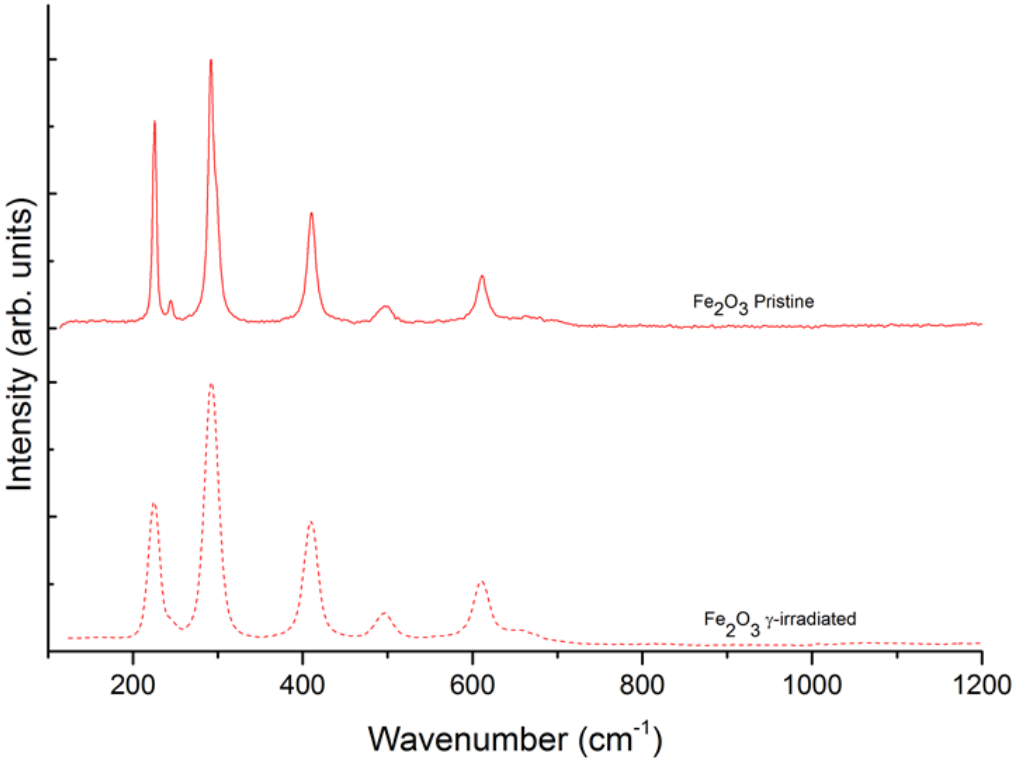

Figure 7.2-6. Raman spectra of Fe_2O_3 pristine powder and after ɣ-irradiation to ~1.7 MGy, solid line is pristine, dashed is the ɣ-irradiated powder.

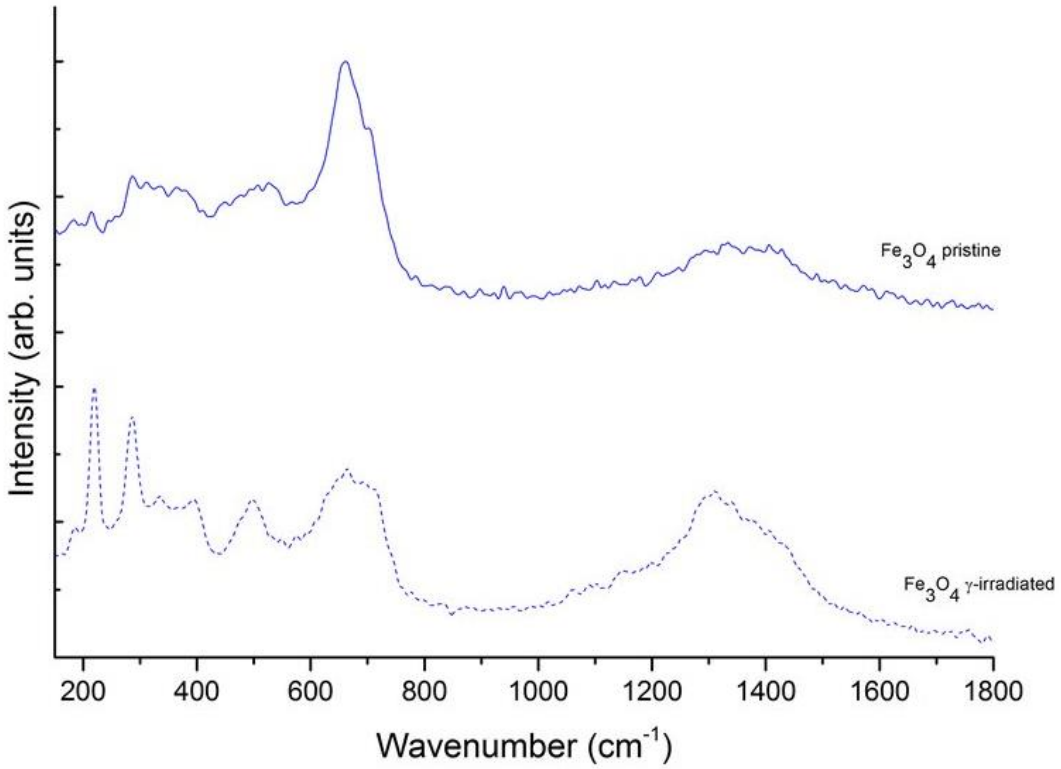

Figure 7.2-9. Raman spectra of Fe_3O_4 pristine powder and after ɣ-irradiation to ~1.7 MGy, solid line is pristine, dashed is the ɣ-irradiated powder.

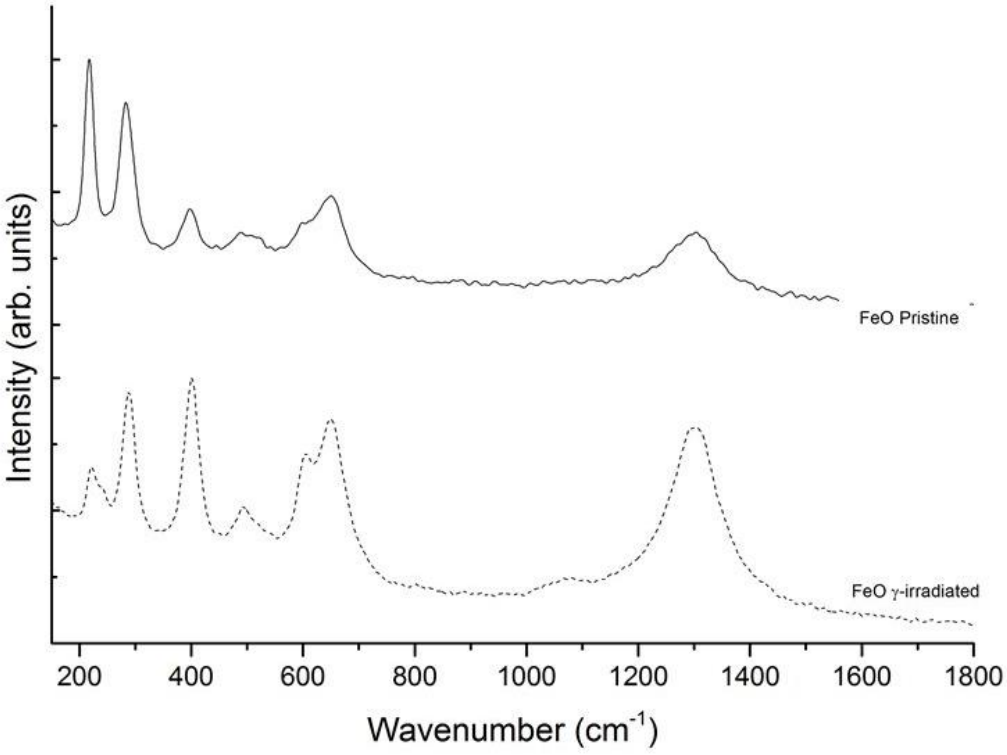

Figure 7.2-8. Raman spectra of FeO pristine powder and after ɣ-irradiation to ~1.7 MGy, solid line is pristine, dashed is the ɣ-irradiated powder.

Interaction induced changes to the oxide

To examine any induced changes to the oxides due to radiation and the presence of hydrogen peroxide samples were irradiated up to 1.7 MGy and the oxide dried post-radiation and examined using XPS, XRD and Raman spectroscopy.

Any chemical changes to the surface were examined using Raman spectroscopy, and the spectra for Fe_2O_3, Fe_3O_4 and FeO are shown in **Figure 7.2-6 to Figure 7.2-8.** The samples were irradiated in a 50 µM H_2O_2 solution to a total dose of ~1.7 MGy. This dose was chosen to give the best chance for visible changes in oxide behaviour, as a smaller dose did not give reproducible detected changes in oxide.

Figure 7.2-6 compares Fe_2O_3 pristine and the ɣ-irradiated sample. The pristine sample has peaks at 226, 245, 292, 411, 496 and 612 cm^{-1} which are the same as those reported in the literature.[45-47] ɣ-irradiation resulted in the broadening of peaks and the loss of the small peak at 245 cm^{-1}.

Figure 7.2-9 reports the Fe_3O_4 and in the pristine sample relevant peaks are at 287, 379, 527, and 662 with a small peak at 1324 cm^{-1}. Literature report peaks at 532 and 667 cm^{-1} as dominate peaks with other peaks at 298, 319, 550 676, 1322 cm^{-1}.[45-47] The peaks report here are consistent with the literature, but laser power and resolution may have effect the quality of the spectra. The irradiated Fe_3O_4 sample has peaks at 220, 287, 334, 394, 497, 664, 694 and 1312 cm^{-1}. There is a loss of the peak at 527 cm^{-1} and the peak ~1300 becomes larger. The most intense peaks present in the irradiated samples that are not in the pristine samples are 220, 286, 394, 497 and 664 cm^{-1} which are in good approximation to the values reported for δ-FeOOH.[46] But due to the broadness of the peaks it may also be possible for there to be a contribution from Fe_2O_3.

Figure 7.2-8 reports the FeO samples and a change in intensity in peaks between pristine and ɣ-irradiated samples can be seen. The spectra are consistent with those reported by Oliveira *et al.*[45] The spectra reported by Olivera *et al.* are attributed to decomposed wustite with components from α-Fe_2O_3 and Fe_3O_4. The relative ease of wustite oxidation may account for this. The changes in intensity for between the pristine and ɣ-irradiated sample may be attributed to the oxidation of FeO by H_2O_2 in during the irradiation experiments.

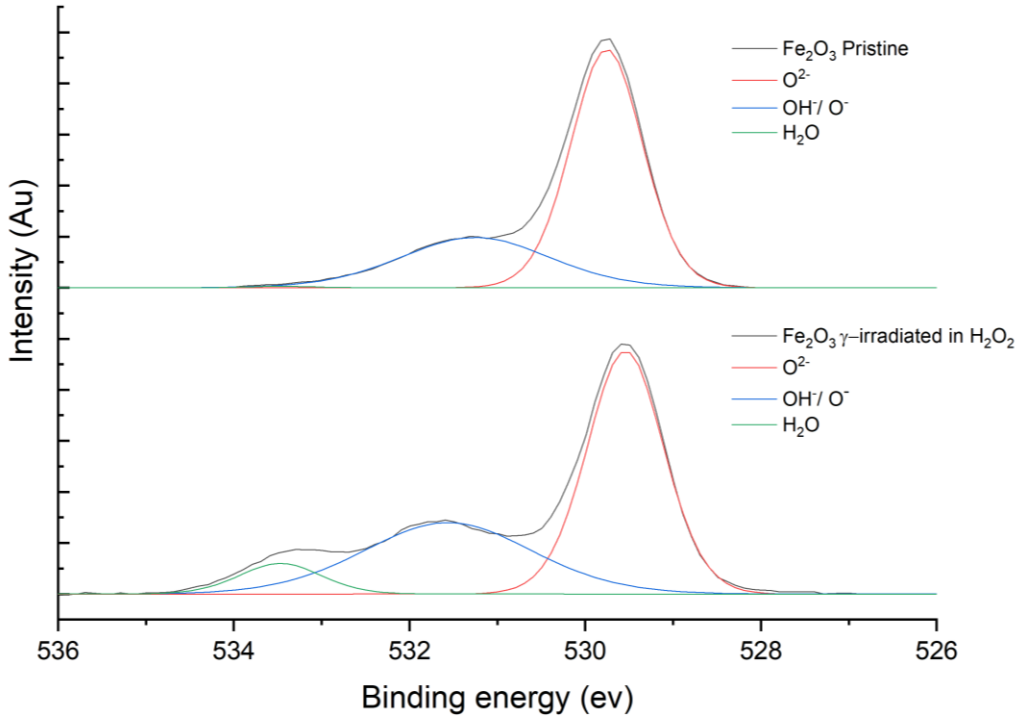

Figure 7.2-10. Normalised XPS spectra of the O 1s peak for Fe_2O_3 powders, spectra are offset for clarity. Peak analysis was undertaken using Casa XPS, spectra were chosen by evaluating the residual of the fitting.

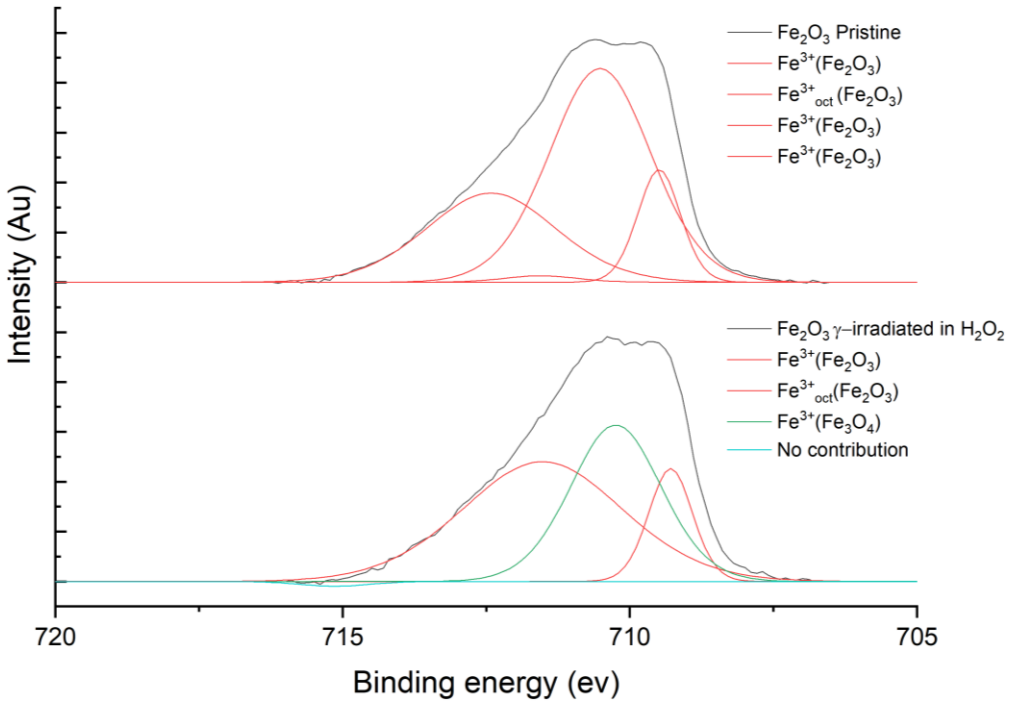

Figure 7.2-11. Normalised XPS spectra of the Fe 2p peak for Fe_2O_3 powders, spectra are offset for clarity. Peak analysis was undertaken using Casa XPS, spectra were chosen by evaluating the residual of the fitting.

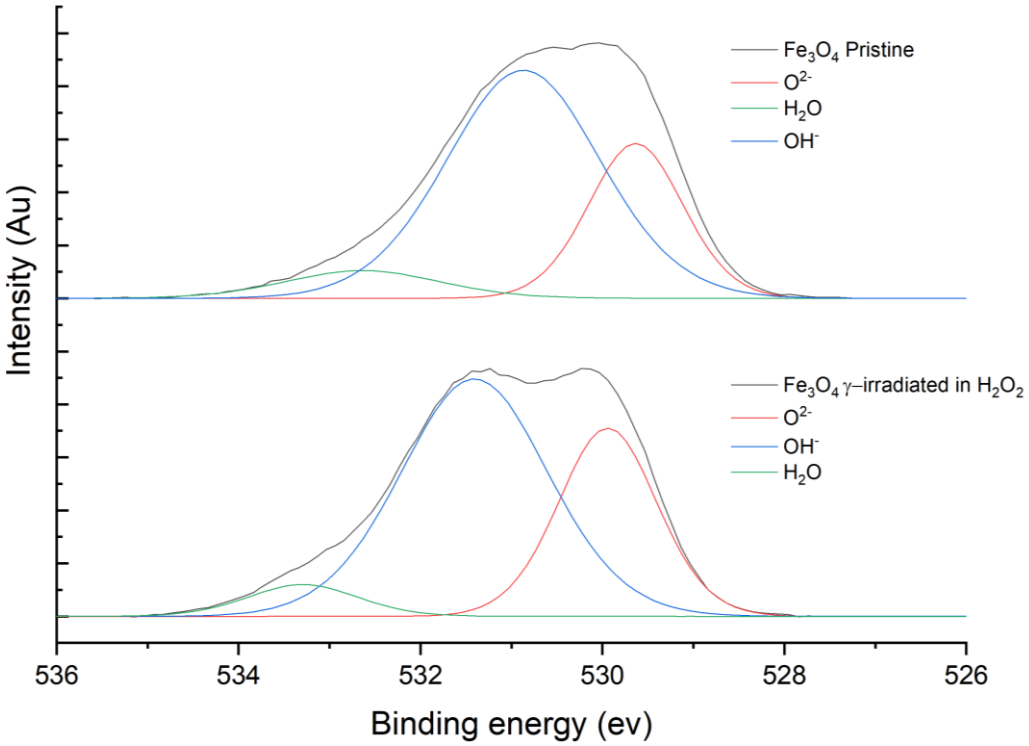

Figure 7.2-13. Normalised XPS spectra of the O 1s peak for Fe_3O_4 powders, spectra are offset for clarity. Peak analysis was undertaken using Casa XPS, spectra were chosen by evaluating the residual of the fitting.

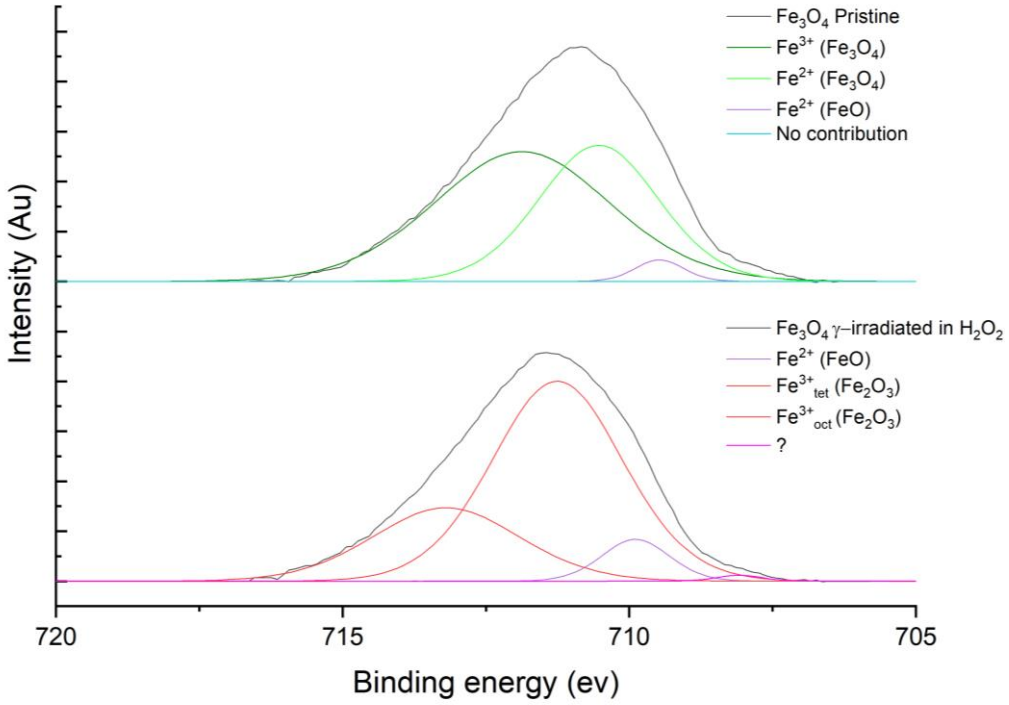

Figure 7.2-12. Normalised XPS spectra of the Fe 2p peak for Fe_3O_4 powders, spectra are offset for clarity. Peak analysis was undertaken using Casa XPS, spectra were chosen by evaluating the residual of the fitting.

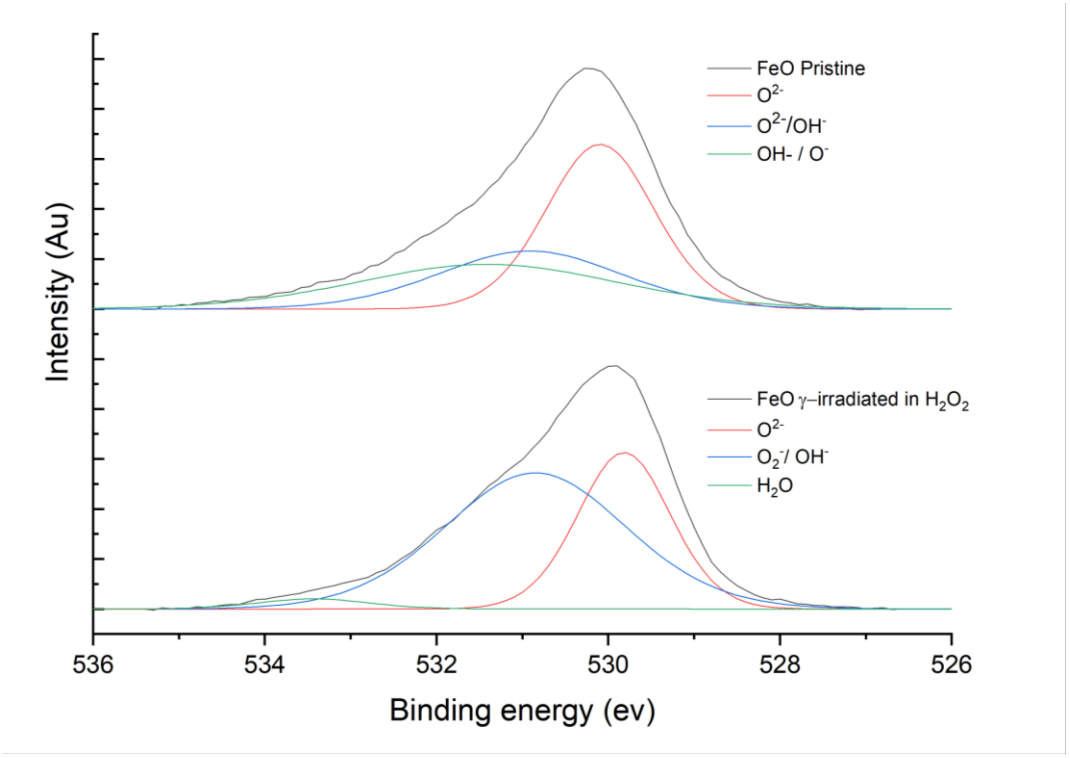

Figure 7.2-14. Normalised XPS spectra of the O 1s peak for FeO powders, spectra are offset for clarity. Peak analysis was undertaken using Casa XPS, spectra were chosen by evaluating the residual of the fitting.

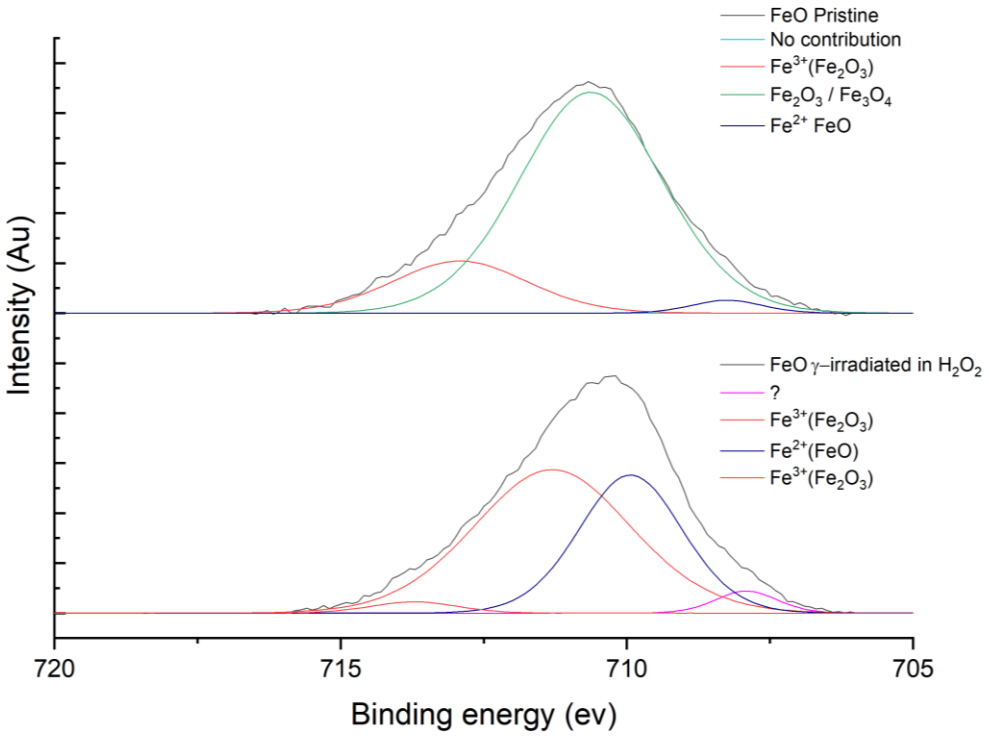

Figure 7.2-15. Normalised XPS spectra of the Fe 2p peak for FeO powders, spectra are offset for clarity. Peak analysis was undertaken using Casa XPS, spectra were chosen by evaluating the residual of the fitting.

High resolution XPS scans for the Fe 2p, O 1s, and C 1s regions were taken for each oxide for both pristine and ɣ-irradiated samples. Data analysis was done using CASA XPS, which utilises the instrument parameters. Following standard procedure spectra were calibrated to the carbon peak at 284.8 eV. The O 1s spectra are reported in **Figure 7.2-10, Figure 7.2-13, and Figure 7.2-14**. Fe 2p spectra are reported in **Figure 7.2-11, Figure 7.2-12 and Figure 7.2-15** The spectra were chosen from multiple sample measurements based on the accuracy of fitting, with samples having the lowest residual between spectra and the fitted envelope chosen.

The complicated nature of transmission metal XPS data means a cautious approach to deconvolution and peak fitting is necessary, the difficulties in obtaining reliable fitting results both in the O 1s and Fe 2p peaks has previously been reported alongside studies attempting to find a systematic approach.[48-51] Peaks were fit using literature as guidance, and peak position and contributing percentage determined. Changes in peak position and contributing peak percentages between pristine and irradiated were used to infer any chemical differences between samples. **Table 7.2-1** reports peak position, percentage contribution and chemical attribution for pristine iron oxide and ɣ-irradiated iron oxides in the presence of H_2O_2.

Typically, when reporting the O 1s peak metal-oxygen peaks are at 530 eV or below, metal carbonate and carbon-oxygen peaks from 531.5 to 532 eV, hydroxyl groups may complicate this with overlapping peaks in this region. There is the possibility of OH^- from metal hydroxides and those bound at the surface.[52] It has been reported that between 531-532 eV a contribution from O^- ions can occur; compensating any deficiencies in the subsurface of transition metal surfaces.[48, 49] These complexations lead to broad peaks around 531 eV, where the Full Width Half Maximum (FWHM) cannot be fit to unity with the water peak which is typical when fitting non transition metal O 1s peaks. Peaks at 532 eV and above are associated with weakly absorbed species and are attributed to water for the data reported here. Work by Levasseur et al probed the complexity of fitting the O 1s peak for a variety of metal oxides, hydroxides and peroxides giving the binding energy scale reproduced in **Figure 7.2-16.**[48]

For the XPS fitting of the O 1s peaks in this work there are 3 major peaks labelled. Peaks between 529 and 530.5 eV are labelled O^{2-} for lattice oxygens, from 530.5 to 532 eV peaks are labelled OH/O^-, peaks above 532 are attributed to water or weakly absorbed species and are labelled H_2O. The presence of metal carbonates and carbon oxygen is possible in peaks labelled OH/O^- as carbonation of the metal oxide can occur with exposure to air but for simplicity these peaks are assumed to be due to OH or O^-. Iron oxides may undergo redox processes during exposure to H_2O_2 and γ-irradiation iron hydroxides may form, so the OH^- contribution may consist of hydroxyl groups at the surface or any iron hydroxide present. The OH^- are broader than the in this region, where the FWHM is larger than both the lattice and water oxygens, which is supported by work reported by LaVerne *et al*, where peaks at ~ 531 eV are attributed to OH groups.[23]

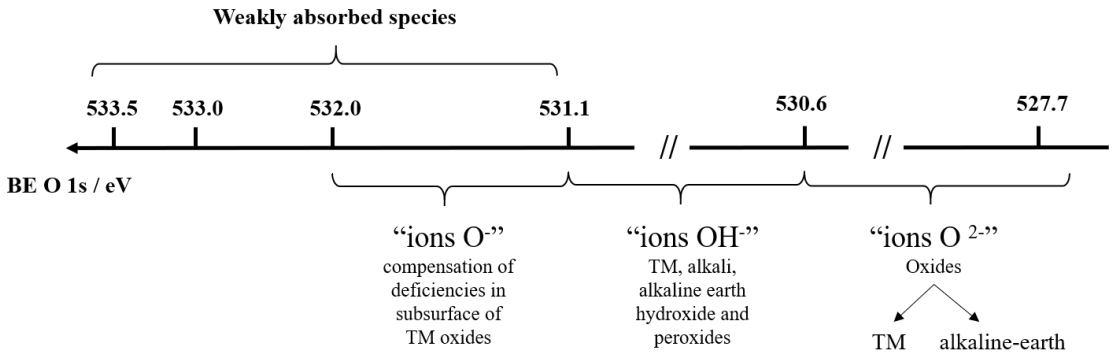

Figure 7.2-16. A binding energy scale for O1s peak, reproduced from work by Levasseur *et al*

Iron fitting is far more complex than that of oxygen or carbon 1s peaks, as is dependent on oxidation state of the iron centre, with satellites occurring due to shake effects.[53] Satellite peak position is highly sensitive and dependant on the iron oxidation state which results in the differences between spectra being somewhat more subtle and increased by instrument limitations, and quantitative deconvolution of these materials in the literature is therefore limited.[51, 54] When considering the iron oxide spectra in their entirety without deconvolution of ion centre contribution the there is a lack of distinguishable/definable difference in iron 2p spectra between oxide types has which been reported previously by LaVerne *et al.*, and suggested that there may be a layer Fe_2O_3 that contributes to the similarity in the spectra which is supported by the work of McIntyre and Zeturak.[23, 55] Previous experimental work give values of the Fe(p3/2) peak for haematite in the range of 710.6 to 711.2 eV including associated satellites.[51,

[54] Work by Yamashita *et al.* in magnetite XPS spectra deconvolution determine a Fe(2p 3/2) energy of 710.6 eV without an associated satellite and wustite having a shoulder satellite and a Fe(2p 3/2) peak energy of 709.5 eV.[51] The samples have Fe (2p 3/2) peak energies between 710.5 and 711.35 eV and presence of satellite in all samples. Several works have attempted further deconvolution the Fe (2p 3/2), suggesting it is possible to fit and assign peaks for the various oxidation states possible.[50, 51, 54, 56] For Haematite McIntyre *et al* report 4 major peaks at 709.8, 710.7, 711.4, and 712.3 eV[57] with follow up work Biesinger *et al* report adding peaks at 713.7 and 719.3 eV.[54] Other works by Hayes *et al,* and Kelber *et al,* attributing peaks at ~711.0 eV to Fe^{3+} centres. Scott *et al* labelled the peaks at ~711 eV as Fe^{3+}_{oct} and identified the peaks between 712-713 eV as Fe^{3+}_{tet} centres. Fe^{2+} peaks have been identified in magnetite and Wustite to be between 708-710 eV with both systems also having contributions from Fe^{3+} centres that may have various binding energies. Hayes *et al* give the identifying peak for Fe_3O_4 to be 710.6 eV and for FeO, 709.5 eV. McIntyre *et al* assign Fe^{2+} as 708.3, 709.3 and 710.4 eV and Fe^{3+} 710.25, 711.3, 712.4 and 713.6 eV in Fe_3O_4.[55, 57] These binding energies have informed the peak assignment reported in table due to the use of different instrumentation and calibration methods it is not unexpected to have variation between the reported literature values, and the works reported here may also vary.

Pristine Fe_2O_3 peaks were recorded are at 709.49, 711.55, 710.52, 712.4 eV agreeing well with data published by McIntyre. Samples γ-irradiated in H_2O_2 show a loss of the peak at 712.42, suggesting a loss associated with Fe^{3+}_{tet} indicating a possible reduction in number of Fe^{3+} centres. The O 1s peaks O^{2-} peak showed a reduction in contribution from 69.37% in the pristine material to 56.54% in the irradiated material, alongside an increase in OH/O^- and H_2O contributions which further a suggests a reduction of the Fe_2O_3 due to the presence of H_2O_2 and/or γ-irradiation. This may be due to the mechanism of H_2O_2 decomposition prior to irradiation with some loss of oxygen due to the reduction of Fe^{3+} to Fe^{2+} that is hypothesised earlier.

Pristine Fe_3O_4 has 3 major peaks assignment if these took into consideration the percentage of each peak to overall area and the expected atomic ratio of Fe^{2+} to Fe^{3+} (reported by Hayes et al to be around 34% Fe^{2+} and 66% Fe^{3+}).[51] A small contributing peak at 709.47 can likely be attributed to Fe^{2+}. The peak at 710.53 agrees with the identifying peak reported by Hayes and the percentage contribution is 40.63% so is

assigned to be Fe^{2+} and the one at 711.87 contributes 56.77 % and is thus labelled Fe^{3+}. Once exposed to γ-irradiation in the presence of H_2O_2 the percentage contribution for the peak at 711.25 increases from 56.77 % to 65.37 %, there is an inclusion of a peak at 713.2 eV a peak associated with Fe^{3+}_{tet} centres that suggests an oxidation of magnetite to hematite. The O 1s peak fittings shows an increase in O^{2-} percentage contribution and a reduction in OH^-/O^- contribution which further supports the oxidation of magnetite under these conditions.

The XPS for pristine FeO gives fittings for the Fe 2p at 710.64 and 712.92 eV with some contribution from a peak at 708.25 eV. The peak at 710.64 eV which could be the identifying peak for Fe_3O_4 or one of the contributing peaks of Fe^{3+} in hematite, a peak at 712.92 is indicative of Fe_2O_3 which suggests that there is a mixture of oxides present in this system, this is further supported by the O 1s peaks where there are two peaks below 531 eV suggesting two iron oxide contributions. This is not surprising giving the comparatively high reactivity to the atmosphere FeO has and this is supported but the Raman spectroscopy, that shows contributions from magnetite and haematite. The samples exposed to H_2O_2 and γ-radiation have reduced the percentage contributions of the fitting at ~ 713 eV suggesting a loss of Fe^{3+}_{tet} sites, and the peak at 710.63 eV is replaced by one at 711.3 eV which is more representative of Fe^{3+}_{oct} centres. A peak at 709.93 eV suggests Fe^{2+} centres in wustite. These changes suggest exposure causes oxidation towards a more resolved hematite system, with the O1s data continuing to show two possible O^{2-} contributions. These findings are supported by the Raman data showing broadening and intensity changes in the spectra which is suggested to be due to the oxidation of wustite towards haematite.

Table 7.2-1. Iron oxide samples ɣ-irradiation in a 50 µM hydrogen H_2O_2 solution to a total dose of ~1.7 MGy.

	Binding energy	% contribution	Assignment	Binding energy	% contribution	Assignment
FeO – pristine	708.25	2.28	Fe^{2+} (FeO)	530.09	44.59	O^{2-}
	710.63	79.97	Fe^{3+}(Fe_2O_3 / Fe_3O_4)	530.95	26.53	O^{2-}/OH^-
	712.62	17.76	Fe^{3+}(Fe_2O_3)	531.31	28.8	OH^- /O^-
FeO-H_2O_2 ɣ-irradiated	707.92	3.47		529.82	36.02	O^{2-}
	709.93	36.54	FeO	530.85	61.18	O^{2-} OH^-
	711.3	57.52	Fe^{3+} (Fe_2O_3)	533.44	2.8	H_2O
	713.73	2.48	Fe^{3+} (Fe_2O_3)			
Fe_3O_4 – pristine	709.47	2.6	Fe^{2+} (FeO)	529.63	27.4	O^{2-}
	710.53	40.63	Fe^{2+} (Fe_3O_4)	530.68	65.03	O^{2-} /OH^-
	711.87	56.77	$Fe^{3+}{}_{oct}$	532.63	7.87	H_2O
Fe_3O_4 - H_2O_2 ɣ-irradiated	708.08	0.68		529.94	32.55	O^{2-}
	709.89	7.07	Fe^{2+}(FeO)	531.41	61.33	OH^- /O^-
	711.25	65.37	$Fe^{3+}{}_{oct}$ (Fe_2O_3)	533.29	6.12	H_2O
	713.2	26.88	$Fe^{3+}{}_{tet}$ (Fe_2O_3)			
Fe_2O_3 – pristine	709.49	38.58	Fe^{3+}(Fe_2O_3)	529.75	69.380	O^{2-}
	710.52	56.33	Fe^{3+}(Fe_2O_3)	531.25	30.27	OH^-/O^-
	711.55	1.23	Fe^{3+}(Fe_2O_3)	533.44	0.35	H_2O
	712.45	29.94	$Fe^{3+}{}_{oct}$ (Fe_2O_3)			
Fe_2O_3 - H_2O_2 ɣ-irradiated	709.61	13.05	Fe^{3+} (Fe_2O_3)	529.54	56.54	O^{2-}
	710.24	37.44	Fe^{3+} (Fe_3O_4)	531.56	36.31	OH^-/O^-
	711.56	50.36	$Fe^{3+}{}_{oct}$ (Fe_2O_3)	533.47	7.53	H_2O

Surface characterisation by XPS and Raman show that ɣ-irradiation in the presence of H_2O_2 induces changes on the surface of Fe_2O_3, Fe_3O_4 and FeO systems. Post irradiated Fe_2O_3 appears to have a loss of contributing Fe^{3+} at ~713 eV suggesting a loss of tetrahedral iron centres. Supported by the loss of intensity and broadening of peaks in the Raman it is suggested that exposure to γ-irradiation and H_2O_2 leads to reduction of Fe_2O_3. XPS characterisation of post irradiated Fe_3O_4 showed an increase in oxygen concentration at the surface, the increase in oxygen is also supported by the Raman results, with the presence of a contribution from either Fe_2O_3 or FOOH, the presence of peaks at 711.26 and 713.2 eV suggest that it is likely to be oxidation toward haematite. Finally post irradiated FeO shows behaviour in both XPS and Raman that would suggest oxidation of the Wustite. The work by LaVerne *et al.* showed no conclusive change at the surface due to ɣ-irradiation in the presence of water,[23] as such it may be suggested that the changes seen here may be due to the presence of H_2O_2 and the mechanisms by which the oxide interact with it.

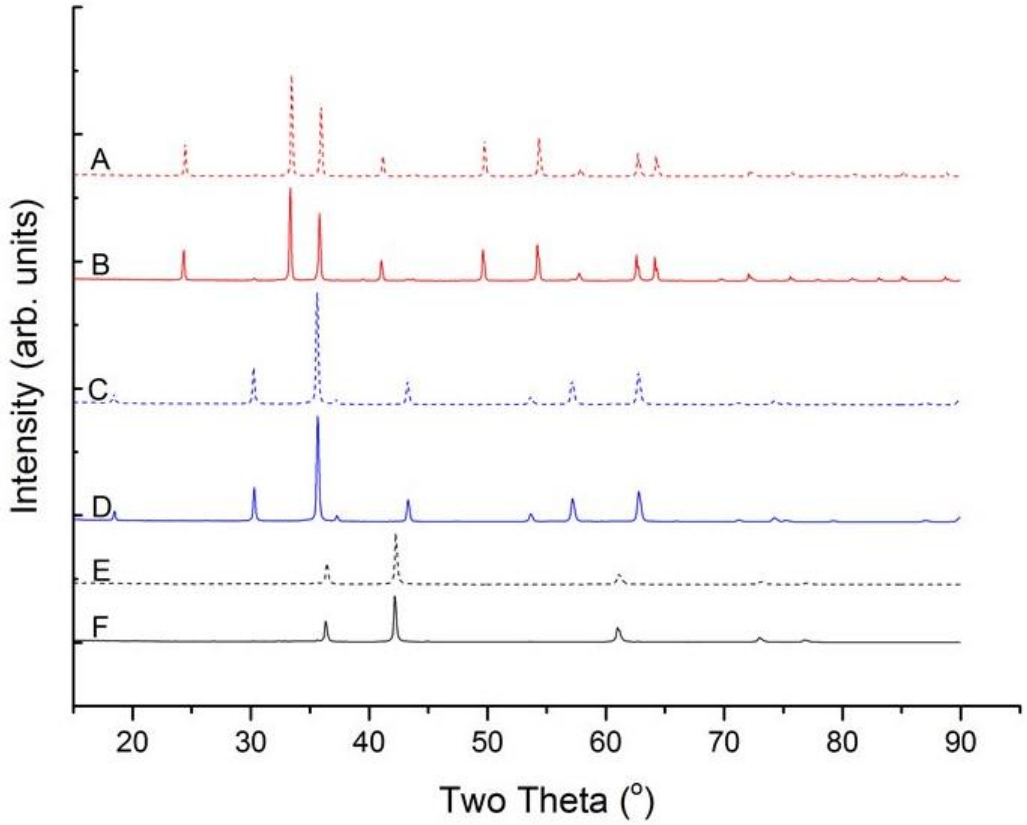

Figure 7.2-17. X-ray Diffraction pattern for (A and B) Fe_2O_3, (C and D) Fe_3O_4 and (E and F) FeO. The dashed lines (A, C, E) are the ɣ- irradiated samples that received a dose of 1.7 MGy. The solid lines (B, D, F) the pristine powders after sieving and baking. Lines are offset for clarity.

Bulk changes were probed using XRD diffraction patterns are reported in **Figure 7.2-17**. XRD data shows little change between oxide types, slight changes can be seen in the lattice parameters when probing the oxide type. The only real change to be seen is that irradiated haematite shows a deviation from the pristine Fe_2O_3 sample with the inclusion of magnetite, supporting the hypothesis that the hematite is reduced during the H_2O_2 degradation, and possible further through radiolysis induced interactions. The lack of change in XRD shows that interactions between the radiolysis products with the iron oxide occur at the oxide | solution interface or in the bulk aqueous phase following the release of iron ions.

Highlights

CRUD simulants were ɣ-irradiated in H_2O_2 solutions under either deaerated or aerated conditions to probe the interaction of corrosion and radiolysis products. The investigation was monitored by determining H_2O_2 concentration after radiation exposure, and changes to the oxide by characterisation using Raman spectroscopy, XPS and XRD .The interaction of H_2O_2 with the iron oxide appears to depend on oxide type with haematite reacting rapidly with the H_2O_2 via a heterogenous Fenton reaction that results in the release of Fe^{2+} as well as oxygen to the aqueous bulk, allowing for further homogenous Fenton chemistry to occur. In Fe_3O_4 and FeO systems initial reactivity toward H_2O_2 is less due to the slow release of Fe^{2+}, preventing the quicker homogenous Fenton chemistry from occurring. An attempt to probe the reaction further with aerated systems and longer irradiation experiments support the idea of FeO systems depending on Fe^{2+} release and suggest a release of hydrogen that hinders the build-up of H_2O_2. The longer irradiations support the hypothesis that hematite is reduced releasing oxygen that promotes the build-up of H_2O_2, and the reduction to magnetite is supported when examining the XPS and XRD data. Examination of the FeO and Fe_3O_4 give little insight to the interactions between the corrosion and radiolysis products but both exhibit some oxidation behaviour. There are no bulk changes, Raman and XPS suggest any interactions that occur do so at the oxide | solution interface, with oxidation likely reading to release and further interactions occurring in the solution bulk. Further investigation of the solution bulk would give further insight and may be undertaken using spectroscopic techniques, ICP-MS, or Moss-Bauer spectroscopy. It can be concluded that the interaction between radiolysis

and corrosion products is complicated, and more investigations should be undertaken to deconvolute this behaviour.

Acknowledgments

This work was supported by the UK Engineering and Physical Sciences Research Council (**Grant EP/G037426/**1) in conjunction with Rolls Royce PLC. The authors would like to thank the supporting staff at the Dalton Cumbrian Facility, a joint endeavour by the UK Nuclear Decommissioning Authority and The University of Manchester, without which this work would not have been possible, with a special thanks to Ruth Edge and Thomas Donoclift. The authors also are thankful to those from The University of Notre Dame Radiation Laboratory for their collaborative efforts, with special thanks to Kazuhiro Iwamatsu, Patricia Huestis and Gregory Horne for their help throughout this work.

Reference

1. P. B. Cohen, *Water Coolant Technology of Power Reactors*, New York : London and Breach, New York, 1969.
2. M. Le Calvar and I. De Curières, in *Nuclear Corrosion Science and Engineering*, Woodhead Publishing, 2012, DOI: https://doi.org/10.1533/9780857095343.5.473, pp. 473-547.
3. J. W. T. Spinks and R. J. Woods, *An Introduction to Radiation Chemistry*, John Wiley & Sons, United States of America, 3 edn., 1990.
4. A. Mozumder, *Fundamentals of Radiation Chemistry*, Academic Press, USA, 1999.
5. Y. Wada, S. Uchida, M. Nakamura and K. Akamine, *Journal of nuclear science and technology*, 1999, **36**, 169-178.
6. Y.-J. Kim, *CORROSION*, 1999, **55**, 81-88.
7. Y. Hatano, Y. Katsumura and A. Mozumder, *Charged Particle and Photon Interactions with Matter: Recent Advances, Applications, and Interfaces*, CRC Press, 2010.
8. K. Daub, X. Zhang, J. J. Noël and J. C. Wren, *Electrochimica Acta*, 2010, **55**, 2767-2776.
9. M. A. Nejad and M. Jonsson, *Journal of Nuclear Materials*, 2004, **334**, 28-34.
10. K. Iwamatsu, S. Sundin and J. A. LaVerne, *Radiation Physics and Chemistry*, 2017, DOI: https://doi.org/10.1016/j.radphyschem.2017.11.002.
11. C. M. Lousada and M. Jonsson, *The Journal of Physical Chemistry C*, 2010, **114**, 11202-11208.
12. C. M. Lousada, M. Trummer and M. Jonsson, *Journal of Nuclear Materials*, 2013, **434**, 434-439.
13. R. Pehrman, M. Amme, O. Roth, E. Ekeroth and M. Jonsson, *Journal of Nuclear Materials*, 2010, **397**, 128-131.

14. C. M. Lousada, M. Yang, K. Nilsson and M. Jonsson, *Journal of Molecular Catalysis A: Chemical*, 2013, **379**, 178-184.
15. M. Yang and M. Jonsson, *Journal of Molecular Catalysis A: Chemical*, 2015, **400**, 49-55.
16. C. M. Lousada, T. Brinck and M. Jonsson, *Computational and Theoretical Chemistry*, 2015, **1070**, 108-116.
17. M. Amme, R. Pehrman, R. Deutsch, O. Roth and M. Jonsson, *Journal of Nuclear Materials*, 2012, **430**, 1-5.
18. A. Hiroki and J. A. LaVerne, *The Journal of Physical Chemistry B*, 2005, **109**, 3364-3370.
19. Å. Björkbacka, S. Hosseinpour, M. Johnson, C. Leygraf and M. Jonsson, *Radiation Physics and Chemistry*, 2013, **92**, 80-86.
20. K. Daub, X. Zhang, J. J. Noël and J. C. Wren, *Corrosion Science*, 2011, **53**, 11-16.
21. Q. W. Knapp and J. C. Wren, *Electrochimica Acta*, 2012, **80**, 90-99.
22. V. Čuba, R. Silber, V. Múčka, M. Pospíšil, S. Neufuss, J. Bárta and A. Vokál, *Radiation Physics and Chemistry*, 2011, **80**, 440-445.
23. S. C. Reiff and J. A. LaVerne, *The Journal of Physical Chemistry B*, 2015, **119**, 7358-7365.
24. M. Dos Santos Afonso, C. D. Di Risio, A. Roitberg, R. O. Marqués and M. A. Blesa, *International Journal of Radiation Applications and Instrumentation. Part C. Radiation Physics and Chemistry*, 1990, **36**, 457-460.
25. E. Parker-Quaife, F. Scenini, A. Banks, A. Powell and S. M. Pimblott, presented in part at the 20th Nuclear Plant Chemistry (NPC) International Conference, Brighton, 2016.
26. C. J. Hochanadel, *The Journal of Physical Chemistry*, 1952, **56**, 587-594.
27. O. Roth, A. Hiroki and J. A. LaVerne, *The Journal of Physical Chemistry C*, 2011, **115**, 8144-8149.
28. B. Pastina and J. A. LaVerne, *The Journal of Physical Chemistry A*, 1999, **103**, 1592-1597.
29. A. O. Allen, C. J. Hochanadel, J. A. Ghormley and T. W. Davis, *The Journal of Physical Chemistry*, 1952, **56**, 575-586.
30. P. V. Nidheesh, R. Gandhimathi and S. T. Ramesh, *Environmental Science and Pollution Research*, 2013, **20**, 2099-2132.
31. J. A. LaVerne and L. Tandon, *The Journal of Physical Chemistry B*, 2002, **106**, 380-386.
32. P. A. Redhead, *Vacuum*, 1962, **12**, 203-211.
33. M. Dyar, C. Hibbitts and T. Orlando, *Mechanisms for incorporation of hydrogen in and on terrestrial planetary surfaces*, 2010.
34. H. J. H. Fenton, *Journal of the Chemical Society, Transactions*, 1894, **65**, 899-910.
35. J. He, X. Yang, B. Men and D. Wang, *Journal of Environmental Sciences*, 2016, **39**, 97-109.
36. J. J. Pignatello, E. Oliveros and A. MacKay, *Critical Reviews in Environmental Science and Technology*, 2006, **36**, 1-84.
37. J. He, X. Yang, B. Men and D. Wang, *Journal of Environmental Sciences*, 2016, **39**, 97-109.
38. L. Xu and J. Wang, *Journal of Hazardous Materials*, 2011, **186**, 256-264.

39. H. B. Dunford, *Coordination Chemistry Reviews*, 2002, **233-234**, 311-318.
40. H. Fischer, *Journal*, 2004, **43**, 275-276.
41. D. M. Bartels, J. Henshaw and H. E. Sims, *Radiation Physics and Chemistry*, 2013, **82**, 16-24.
42. T. I. Sutherland, C. J. Sparks, J. M. Joseph, Z. Wang, G. Whitaker, T. K. Sham and J. C. Wren, *Physical Chemistry Chemical Physics*, 2017, **19**, 695-708.
43. P. Yakabuskie, J. Joseph, P. Keech, G. Botton, D. Guzonas and J. Wren, *Physical Chemistry Chemical Physics*, 2011, **13**, 7198-7206.
44. P. Cohen, A. Research, T. C. o. Water and S. i. T. P. Systems, *The ASME Handbook on Water Technology for Thermal Power Systems*, American Society of Mechanical Engineers, 1989.
45. D. L. A. d. Faria, S. V. Silva and M. T. d. Oliveira, *Journal of Raman Spectroscopy*, 1997, **28**, 873-878.
46. S. J. Oh, D. C. Cook and H. E. Townsend, *Hyperfine Interactions*, 1998, **112**, 59-66.
47. A. M. Jubb and H. C. Allen, *ACS Applied Materials & Interfaces*, 2010, **2**, 2804-2812.
48. J.-C. Dupin, D. Gonbeau, P. Vinatier and A. Levasseur, *Physical Chemistry Chemical Physics*, 2000, **2**, 1319-1324.
49. M. C. Biesinger, Oxygen 1s for Transistion Metals http://www.xpsfitting.com/2012/01/oxygen-1s-for-transition-metals.html, (accessed 20.2.2019, 2019).
50. T.-C. Lin, G. Seshadri and J. A. Kelber, *Applied Surface Science*, 1997, **119**, 83-92.
51. T. Yamashita and P. Hayes, *Applied Surface Science*, 2008, **254**, 2441-2449.
52. T. scientific, Thermo scientific XPS, https://xpssimplified.com/elements/).
53. B. Mayer, S. Uhlenbrock and M. Neumann, *Journal of Electron Spectroscopy and Related Phenomena*, 1996, **81**, 63-67.
54. M. C. Biesinger, B. P. Payne, A. P. Grosvenor, L. W. M. Lau, A. R. Gerson and R. S. C. Smart, *Applied Surface Science*, 2011, **257**, 2717-2730.
55. N. S. McIntyre and D. G. Zetaruk, *Analytical Chemistry*, 1977, **49**, 1521-1529.
56. H. Pullin, R. Springell, S. Parry and T. Scott, *Chemical Engineering Journal*, 2017, **308**, 568-577.
57. A. P. Grosvenor, B. A. Kobe, M. C. Biesinger and N. S. McIntyre, *Surface and Interface Analysis*, 2004, **36**, 1564-1574.

Chapter 8: Thesis summary, industrial impact and further work

8.1 Summary

There have been two significant strands of work undertaken in this NengD project.

1) HTHP experimental set up and implementation
    - The design, development and implementation of a high temperature and pressure experimental facility able to investigate radiolysis and corrosion. The successful utilisation of this equipment to investigate the ɣ-effects of radiation on 316 corrosion has been outlined.
2) Interactions between corrosion and radiolysis products
    - The investigation of simulant corrosion products with radiolysis products, with ɣ-irradiation experiments of iron oxide (CRUD simulants) in aqueous hydrogen peroxide solutions.

The significant outcome can be summarised as the following:

HTHP experimental set up and implementation

- Successful design and implementation of high temperature and pressure equipment used in conjunction with ionising radiation sources;
- During preliminary work a higher than expected hydrogen concentration and electrical conductivity was observed, likely to be due to use of cation exchange column. This is an important observation as primary coolant circuits in nuclear reactor systems rely on the use of cation exchange columns to remove unwanted particulates, ionic species and contaminates;
- Oxidation of SS 316 with ɣ-radiation exposure at 288 °C in detreated conditions for 95 hours leads to a reduced overall oxide thickness with depleted chromium content. XRD suggests the outer oxide is magnetite in ɣ-irradiated conditions with a chromite inner layer. For unirradiated samples outer oxide is magnetite with a contribution from nickel chromium iron oxide and an inner chromite layer;
- Oxide morphology changes with sparser less planar outer oxide that has rougher faces;

- When compared to other works in this field, the changes in oxide thickness and morphology along with depleted chromium, it is hypothesised that these effects are due to a loss of chromium via dissolution from oxide | metal interface.

Interactions between corrosion and radiolysis products

- Iron oxide variations exhibited different interaction behaviour with haematite reacting most rapidly with H_2O_2 before irradiation via heterogenous Fenton chemistry. This reaction causes oxygen generation allowing for H_2O_2 to build up;
- Radiolytic degradation of H_2O_2 is in competition with Fenton reactions that occur in the presence of iron oxides;
- Fe^{2+} release in magnetite and wustite is slow initially, with solubilisation of Wustite leading to the lowest H_2O_2 concentration at the end of the experiment. It is hypothesised that this is due to the release of hydrogen with Fe^{2+} dissolution. This hypothesis was supported by other current works in this field;
- The release or generation of Fe^{2+} enables reduction/oxidation reactions to occur with radiolytic species;
- The interaction mechanisms do not result in any bulk changes to Fe_3O_4 and FeO suggesting interactions are at the oxide | solution interface or in the solution bulk and these hypotheses are supported by Raman and XPS results
- Both heterogenous and homogenous Fenton chemistry contribute to complex behaviour exhibited by these systems;
- There appears to be coupled behaviour between oxide | solution interface and the solution bulk that requires further investigation.

8.2 Industrial relevance and possible application to Rolls Royce

This project is sponsored by Rolls Royce and aimed to provide experimental results and data that can be utilised in computational modelling of primary coolant circuits. Models aim to provide further mechanistic insight of these complex systems with the goal to predict corrosion and CRUD behaviour. The ability to predict behaviour allows for better reactor lifetime estimates and can play a part in lifetime extension, as well as informing next generation design. Models for these systems are complex as the coupling of several individual systems is needed. The corrosion mechanism and subsequent behaviour of the structural materials, the behaviour, and fates of these corrosion products, of which dissolution, transport, precipitation and deposition are

possible. Added complications occur when coupling these systems with radiolysis models as the behaviour is interconnected and dependant. Reaction sets needed to be coupled, outlining redox behaviour of the materials, equilibrium coefficients, rate equations and constants. Experimental data gives a standard and validation method for predictive models allowing them to be tested for effectiveness.

The design and implementation of the HTHP recirculation facility gives experimental data for system parameters during irradiation. The commissioning and preliminary testing gave unexpected results in terms of hydrogen concentration and electrical conductivity, suggesting leaching from cation exchange resins. The increased hydrogen concentration and electrical conductivity alter radiolysis behaviour further, as well as changing the redox behaviour of the primary coolant circuit materials. This finding requires further investigation to validate the effects being due to cation resin or pumps, and these parameters should also be investigated, with fundamental studies on the cation resins and simulated LWR coolant. Oxidation tests give information of SS 316, a material increasingly used in reactor internals. This work has provided some information on system parameters throughout oxidation tests which may be fed into predictive models, such as dissolved hydrogen and oxygen concentration as well as electrical conductivity. These tests also gave information on the effects of ɣ-radiation on oxide morphology and composition, which gives some insight to growth and loss mechanisms. These insights need to be researched further, but this information may also be used with in predictive models. Another possible use of modelling is the validation of possible mechanistic hypothesis. The parameters from these oxidation tests can be included in a model, and the inclusion of loss mechanisms like the loss of chromium by dissolution outlined in **Equation (6.3-1)**.

The interactions study of the relationship between corrosion and radiolysis products have provided some insight to the possible reactions that occur and should be considered when modelling these systems. It is well known that iron oxides have varied oxidation states that may occur. Although the study has not resulted in a definite understanding, it has shown that there may be several competing reactions occurring within systems. Such as both hetero and homogenous Fenton chemistry, and the reaction between solubilised iron and other radiolysis products preventing H_2O_2 build up. These reactions seem to contribute to changes in radiolysis behaviour, with contributions from the oxide surface | solution interface and bulk solution. In these

CRUD type simulations, it is valid to suggest the inclusion of heterogenous and homogenous Fenton reactions with both interface reactions and bulk solution. As well as the reduction/oxidation Fe^{2+} can undergo with radiolysis products. The data produced in these interaction experiments may be used as input parameters or validation standards for the modelling of these systems.

The interactions between corrosion and radiolysis products is a contributing factor to the complex behaviour observed in PWR systems. The corrosion products are related to the corrosion of the materials, which has been shown to be altered by the presence of radiation. For these systems a realistic approach would be the development and coupling of several models, one tackling the corrosion of the materials, the bulk radiolysis of water including the interactions for the radiolysis products and released corrosion products. This should then be coupled with a model that tackles the corrosion of the material with the loss, transport, and deposition of corrosion products, including reactions occurring at the oxide | interface.

An example of a model that considers oxide growth is the mechanistic model of oxide growth and dissolution curing corrosion of Cr-Containing alloys by Momeni and Wren.[1] This model considers the electrochemical reactions that occur at metal | oxide and oxide | solution interfaces and the flux of cations from metal to the solution through the oxide. This model maintains charge and mass balance i.e. oxidation flux must equal oxide growth flux and dissolution, which can simplify the system by removing the need for more detailed charge transport modelling. This model has successfully predicted the time dependent potentiostatic corrosion of pure iron, Co-CR and Fe-Ni-Cr alloys. There are numerous examples of radiolysis models, some looking at the effects of temperature on the yield of radiolysis products, others the effects of scavengers, impurities or effects of pH.[2-5] These are examples of both ‘water only systems’ and those that simulate more realistic systems with the inclusion of additives and surfaces. One example of this is work by Bartels, Henshaw and Sims that attempt to validate the hydrogen concentrations observed at the AECL test reactor and suggest the inclusion of loop impurities is responsible for observed experimental data. With sources of impurities including the ferric ions and its oxidation/reduction and the conversion of nitrogen (from the deaeration of coolant water) to ammonia and its subsequent reactions.[4]

Corrosion product and transport models include work by Boc Lee who developed a CRUDSIM model looking at the CRUD transport and activation considering its dissolution, transport and deposition.[6] A thorough review by the IAEA reviews codes and approaches for modelling these CRUD and activity transport behaviours.[7] To summarise; it is important to provide that experimental data is used in conjunction with modelling to predict corrosion and its related behaviour. That modelling of these systems is a powerful tool for furthering understanding and prediction of system parameters. This research project has provided data and insight that is valuable for the modelling work being undertaken at Rolls Royce and has highlighted the importance of considering oxide | solution interfaces in these systems alongside the bulk material and solution behaviour.

Operational considerations related to this thesis research

The work undertaken in this thesis has highlighted the complicated nature of radiation chemistry and corrosion research, providing a strong foundation for future research into the effects of radiation on nuclear materials. The documentation of the design and deployment of this unique HTHP facility used in conjunction with a γ-irradiation source will provide a useful knowledge base for future users of this. Alongside others who wish to investigate water radiolysis behaviour and the mechanisms of corrosion under simulated LWR conditions. It has shown that LWR conditions are complex and somewhat difficult to emulate, considerations must be made in terms of material selection and degradation pathways for structural materials but for operational components. This work has shown that operational equipment such as cation exchange columns and recirculation pumps may influence the chemistry of these systems. Plant operators amongst research scientist benefit from this information and it highlights the importance of regular inspection and maintenance of pumps and columns to avoid contamination.

Although aimed at providing data for predictive modelling of PWR conditions, this work has provided work that may be applied when considering the use of BWR rectors in future. The HTHP facility will be able to emulate the conditions of a BWR and enable the study of water under these conditions. The studies undertaken using this HTHP show that without added water chemistry systems experience increased electrochemical conductivity and hydrogen production, further studies should be undertaken with incremental introductions of LWR additives to give an understanding

of when these issues are suppressed. Plant operators show be aware of these issues, and that chemistry control and monitoring is of the upmost importance.

The investigation of SS 316 L under γ-irradiation show a change in oxide morphology, thickness and composition, these tests were under carried out without added water chemistry, so these changes are a result of the radiation exposure. When taken with other work in this field it shows that the oxide composition is not only affected by the presence of radiation but of the water chemistry for example hydrogen conditions. This is important to note this as chemical additives are introduces as a means of preventing degradation of the materials but may in fact be causing undesired changes in corrosion behaviour and oxide morphology, in some cases reducing the protectiveness of these.

The interactions studies showed complex behaviour between the radiolysis and corrosion products. With changes in both the solution and surface chemistry due to these interactions, further study of the solution bulk via either spectroscopic techniques or ICP-MS may help deconvolute this behaviour further. The corrosions products interact with the radiolysis products at the solution | oxide interface and may lead to ions being released. These interactions affect the level of hydrogen peroxide that accumulates indicating a change in the radiolysis behaviour of water. This is an important consideration in that LWR operators must take into consideration, as this release of metal ions into solution may hinder the chemistry added to supress corrosion and enhance reactor performance. This is particularly important in BWR systems as hydrogen peroxide is not supressed by the addition of hydrogen, so other approaches may need to be considered to reduce the impact of CRUD on plant operations.

8.3 Further work

The effects of radiation on corrosion

This experimental program successful commissioned and implemented the use of a high temperature and pressure recirculation loop for the investigation of the effects of γ-radiation on corrosion of SS 316. Further characterisation of the samples from this would allow for better comparison to other works for further mechanistic understanding of oxide growth. For example, TEM imaging of the oxide films may illuminate further the oxide composition and morphology, with STEM-HAADF and EDS line scans giving more precise compositional information. Giving better image resolution so information on oxide porosity could be provided. Experimental

limitations meant that the electrochemical behaviour of SS 316 under these conditions was not investigated. An experimental program should be developed to utilise the equipment functionality to investigate this, as it will provide further mechanistic understanding of these corrosion processes as well as validate the behaviour seen in this work along with others in this research area. For better mechanistic understanding the effects of additives should be investigated, with hydrogen saturation and elevated oxygen concentration a good starting point. Eventually moving towards the simulation of PWR chemistry by the addition of lithium hydroxide, boric acid, and acetate.

The use and validation of the recirculation loop for corrosion studies under proton experiments should be undertaken allowing for comparison to other works in this area as well as testing the hypothesis that changes are related to the radiolysis products and their interaction with the metal than any displacement damage in material.

Interactions between corrosion and radiolysis products

The interactions experiments gave some interesting data as to nature of the interactions between radiolysis and corrosion products. The studies highlighted the importance of Fenton chemistry and both heterogenous and homogenous contributions occurring in these systems and showed that the presence of Fe^{2+} in solution bulk may lead to altered radiolysis behaviour. Further work should encourage mechanistic understanding with a kinetics experiment to determine the dominant pathways in these systems. The importance of the hydroxyl radical and solvated electron in these interactions may be investigated using scavengers in the aqueous phase. Formate and potassium bromide may be added to scavenge hydroxyl radicals and nitrate to scavenge solvated electrons. Changes in the observed H_2O_2 concentration will be indicative for the importance of these species and how they interact with corrosion products. The concentration of iron may also be monitored to give further information as to the nature of interactions. For example, whether the reactions are in the bulk solution or the oxide surface. The use of ICP-MS was unsuccessful due to detection limits, but the use of a chemical assay may allow for the determination of smaller concentrations of solvated iron. The addition chelating agent to bind with Fe^{2+} followed by concentration determination by spectroscopic techniques is a possible route. An example of this that has been applied widely in biological and geological applications is the use of ferrozine. This selectively binds to Fe^{2+} but it is possible to determine Fe^{3+} concentration is buy the introduction of a reduction step.[8-10] The would allow for quantification of both Fe^{3+} and Fe^{2+} and

would give insight to the dominate interactions. Application of this assay has recently been undertaken in a radiation related field, a kinetic study probed the effects of ferrous ion concentration on radiation induced iron-oxide nanoparticle formation and growth, which proves proof of concept for this application.[11] The application of these interactions studies would be in modelling LWR conditions, so the effects of temperature, pH and chemical additives would also be a good route of investigation and enable further mechanistic and applicational understanding. It may also be beneficial to agitate the systems with constant mixing to see if contact area effects the build-up and loss of H_2O_2. As the iron oxides in these investigations have different surfaces areas, with FeO having a much smaller surface area, these effects should be further investigated by varying the surface area of the samples. The use of other CRUD simulants would be the last recommendation as iron oxide are very simple CRUD simulants with more realistic examples including nickel oxides, Nickel ferrite ($NiFe_2O_4$) and chromium containing oxides.

Finally, these experimental data sets should be incorporated, starting with a simple model involving the iron oxide reactions with H_2O_2 coupled to a water radiolysis model. This could be carried out in FACSMILE, a program that can model kinetics of chemical systems by solving differential equations. This model would need to include the Fenton reactions, reduction, and oxidation reactions of iron by radiolysis products, the redox reactions of the iron oxides and the radiolysis reaction set. An example of the kind of equations needed for this is in **Appendix 1** work carried out by Elizabeth Parker-Quaife building on work by Donoclift and Horne *et al.*[12]

References

1. M. Momeni and J. C. Wren, *Faraday Discussions*, 2015, **180**, 113-135.
2. A. Elliot and D. Bartels, *The reaction set, rate constants and g-values for the simulation of the radiolysis of light water over the range 20 deg to 350 deg C based on information available in 2008*, Atomic Energy of Canada Limited, 2009.
3. J. M. Joseph, B. Seon Choi, P. Yakabuskie and J. Clara Wren, *Radiation Physics and Chemistry*, 2008, **77**, 1009-1020.
4. D. M. Bartels, J. Henshaw and H. E. Sims, *Radiation Physics and Chemistry*, 2013, **82**, 16-24.
5. P. A. Yakabuskie, J. M. Joseph and J. Clara Wren, *Radiation Physics and Chemistry*, 2010, **79**, 777-785.
6. C. B. Lee, Doctor of Philosophy, Massachusetts Intitute of Technology, 1990.
7. IAEA, *Modelling of Transport of Radioactive Substances in the Primary Circuit of Water Cooled Reactors*, Vienna, Austria, 2012.
8. T. M. Jeitner, *Analytical Biochemistry*, 2014, **454**, 36-37.
9. L. L. Stookey, *Analytical Chemistry*, 1970, **42**, 779-781.
10. E. Viollier, P. W. Inglett, K. Hunter, A. N. Roychoudhury and P. Van Cappellen, *Applied Geochemistry*, 2000, **15**, 785-790.
11. T. I. Sutherland, C. J. Sparks, J. M. Joseph, Z. Wang, G. Whitaker, T. K. Sham and J. C. Wren, *Physical Chemistry Chemical Physics*, 2017, **19**, 695-708.
12. G. P. Horne, T. A. Donoclift, H. E. Sims, R. M. Orr and S. M. Pimblott, *The Journal of Physical Chemistry B*, 2016, **120**, 11781-11789.

Chapter 9: Appendices

Appendix 1: FACSIMILE model of magnetite and hematite aqueous reactions

```
*------------------------LONGEST LENGTH-----------------
-------------;
EXECUTE OPEN 1 "Y:/f5/one.out";
*EXECUTE OPEN 2 "in.txt" OLD;
EXECUTE OPEN 3 "Y:/f5/two.txt";
EXECUTE OPEN 4 "Y:/f5/three.txt";
EXECUTE OPEN 11 "Y:/f5/box1.txt";
EXECUTE OPEN 12 "Y:/f5/box2.txt";
EXECUTE OPEN 13 "Y:/f5/box3.txt";
EXECUTE OPEN 14 "Y:/F5/FOUR.TXT";
PERMIT +- ;
*----------------;
integer #n 3;

*------DEFINE-VARIABLES ------;
*These variables are concentrations of
species formed and consumed for magnetite
solubilities;
*-----Define-Variables -------;

*Chemical species in Magnetite parameter;

VARIABLE <#n> H2O H+ H2 Fe3O4 Fe3+ Fe2+ OH- FeOH2 FeOH+
FeOH3-
Fe2O3 FeOH+2 FEOH2+ FeOH3 FEOH4- Fe2OH2 O2 E-;
```

```
parameter <5000> work;

parameter <#n> totfe pH 6 7 8 H2cckg cH2 10 30 60;

*chemical species in haematite parameter, some species are
previously defined


*-----REACTION-FIRE-COUNTERS-------*
VARIABLE R0 R1 R2 R3 R4 R6 R7 R8 R9 R10 R11 R12 R13 R14
R15 R16;
*----DEFINE-PARAMETERS-------------*
*These parameters are defining the initial concentrations
of
the species present in these systems;

PARAMETER
<#n> Tempc 25 100 150 TempK tf solh2;
parameter cH2O cH+ cFe3O4 cFe3+ cFe2+ cOH- cFeOH2
cFeOH+ cFeOH3- cFe2O3 cFeOH+2 cFEOH2+ cFeOH3 cFEOH4-
cFe2OH2 cE-;


*----------------------------------;
*defining the rate of back reaction
PARAMETER
k1 k2 k3 k4 k5 k6 k7 k8 k9 k10 k11 K k12 k13 k14 k15 k16;
*----------------------------------;
PARAMETER <#n> KFE4c 1 3 6 kMAG1 1e-6 1e-4 1e-3;
*----------------------------------;
*currently pk12=16 are nonsense the rate constants of
```

```
hydrolysis or solubility constants;
PARAMETER <#n>
dw kw
pk1 -12.026 -8.548 -6.958
pk2 -2.713 -1.149 -0.429
pk3 8.533 7.852 7.534
pk4 17.418 16.086 15.460
pk6 2.19 0.67 0.023
pk7 2.95 1.52 3.48
pk10 5.67 2.6 1.16
pk5 0.47 -1.163 -2.59
pk12 0.5 1.0 2.0
pk13 0.5 1.0 2.0
pk14 0.5 1.0 2.0
pk15 0.5 1.0 2.0
pk16 0.5 1.0 2.0;
*-----------------------------------------------------;
PARAMETER <#n>
kb kc kd ke kf kg kh ki kj kk kl km kn ko kp;
*-----------------------------;
*------PARAMETERS FOR TEMPERATURE DEPENDANCE----------;
* Temperature dependence follows the form
(RlnK= -A/T +B[ln(T/273.15)-1]+D)
AF-A for Fe2+, BF-B for Fe2+, DF D for Fe2+
AFOH-A for FeOH+, BFOH-B for FeOH+, DFOH D for FeOH+
AFOH2-A for FeOH2, BFOH2-B for FeOH2, DFOH2 D for FeOH2
AFOH3-A for FeOH3, BFOH3-B for FeOH3, DFOH3 D for FeOH3;
*-----------------------------------------------------;
PARAMETER
```

```
AF BF DF
AFOH BFOH DFOH
AFOH2 BFOH2 DFOH2
AFOH3 BFOH3 DFOH3;

compile equilib;

array <#n> work;
tempk = Tempc + 273.15;



* density in kg/dm3  ;
tf  = 647.25 - tempK;

dw = 1 + 0.1342489*tf@(1/3) - 3.946263e-3*tf;
dw = dw/(3.1975 - 0.3151548*tf@(1/3) - 1.203374e-3*tf
     + 7.489081e-13*tf@4);

kw = 10@(-4.098 - 3245.2/tempK + 2.2363e5/tempK**2 -
        3.9984e7/tempK**3 + (13.957 - 1262.3/tempK +
        8.5641e5/tempK**2)*log10(dw));

kw=kw*dw@2;



SOLH2    =    EXP(-104.288    +    (4804.235/tempK)    +
(14.2283*LOG(tempK))); molal bar-1

KFE4C    =        10@(22153.5/tempK    -    126.024    +
35.5792*LOG10(tempK));MULTEQ/Mag
```

```
KFE4C =  KFE4c/SOLH2/dw@4;

array end;
**;
COMPILE INITIAL;
*THIS-IS-TO-GIVE-VALUES-TO-VARIABLES at time zero;
*------INITIAL-SPECIES-CONCENTRATIONS----------------;
TSTART = 100;
H2Oi = 1;
cH+ = 1E-7;
cFe3O4 = 1E-6;
cFe3+ = 1E-6;
cFe2+ = 1E-6;
cOH- = 1E-22;
cFeOH2 = 1E-22;
cFeOH+ = 1E-22;
cFeOH3- = 1E-22;
cFe2O3 = 1E-6;
cFeOH+2 = 1E-22;
cFEOH2+ = 1E-22;
cFeOH3 = 1E-22;
cFEOH4- = 1E-22;
cFe2OH2 = 1E-22;
CE- = 1E-22;

array <#n> work;
T = TSTART;
H2O = H2Oi;
H+ = 10@( -pH);
```

```
H2 = cH2/22400;;
Fe3O4 = cFe3O4;
Fe3+ = cFe3+;
Fe2+ = cFe2+;
OH- = kw/H+;
FeOH2 = cFeOH2;
FeOH+ = cFeOH+;
cFeOH3- = cFeOH3-;
Fe2O3 =  cFe2O3;
FeOH+2 = cFeOH+2;
FEOH2+ = cFEOH2+;
FeOH3 = cFeOH3;
FEOH4- = cFEOH4-;
Fe2OH2 = cFe2OH2;
E- = CE-;

array end;



*write headings for the loops here as best work round
found;

write 1=11, "      time            pH            H2cckg
fe3o4
        totfe         fe3+         fe2+        fe2o3" ;

write 1=13, "      time            pH            H2cckg
fe3o4
        totfe         fe3+         fe2+        fe2o3" ;
```

```
write 1=12, "      time             pH             H2cckg
fe3o4
        totfe         fe3+         fe2+        fe2o3" ;



*-------K-VALUES-ARE-ARBITART-SO-HARDCODED------------;
k2 = 10E10;
k3 = 10E10;
k4 = 10E10;
k5 = 10E10;
k6 = 10E10;
k7 = 10E10;
*k8 = 10E10;
*k9 = 10E10;
k10 = 10E10;
k11 = 10E10;
k12 = 10E10;
k13 = 10E10;
k14 = 10E10;
k15 = 10E10;
k16 = 10E10;
*--------IF-USING-TEMPERATURE-DEPENDANCE---------------
--------------;
*READ 2 AF;
*READ 2 BF;
*READ 2 DF;
*READ 2 AFOH;
*READ 2 BFOH;
*READ 2 DFOH;
```

```
*READ 2 AFOH2;
*READ 2 BFOH2;
*READ 2 DFOH2;
*READ 2 AFOH3;
*READ 2 BFOH3;
*READ 2 DFOH3;
*------------K-VALUES------------------------------;
array <#n> work;

kb = 10@-(pk1 - pk2);
kc = 10@-(pk2 - pk3);
kd = 10@-(pk3 - pk4);
ke = 10@-(pk5);
kf = 10@-(pk6);
kg = 10@-(pk7);
*kh = 10@-(pk8);
*ki = 10@-(pk9);
kj = 10@-(pk10);
*kk = 10@-(pk11);
kl = 10@-(pk12);
km = 10@-(pk13);
kn = 10@-(pk14);
ko = 10@-(pk15);
kp = 10@-(pk16);

array end;

call equilib;
call iprint;
```

```
**;
compile iprint;
write 1 = 4, "INITIAL FE2OH" (E13, 3) FEOH2;
write 1 = 4,"kb kc kd" (E13, 3)  kb kc kd;
write 1 = 4,"kfe4c kmag1 dw kw" (E13, 3) kfe4c kmag1 dw
kw ;
**;
*--------------REACTIONS--------------------------;
*it is k k/ka due to the rate forms v=k[a] and v=ka[b]
laws dictating that
forward must equal back and rearrangement;

COMPILE EQUATIONS;

array <#n> work;

% kmag1/(KFE4c*H2*H+**6) :
Fe2+ + Fe2+ + Fe2+ + H2Oi + H2Oi + H2Oi + H2Oi = Fe3O4 +
H+ +
H+ + H+ + H+ + H+ + H+ + H2 ;

= kmag1*exp(-1e-14/(ramp(Fe3O4) + 1e-17)) : Fe3O4 + H+ +
H+ + H+ + H+
+ H+ + H+ + H2 = Fe2+ + Fe2+ + Fe2+ + H2Oi + H2Oi + H2Oi
+ H2Oi ;

% k2 %k2/kb :   Fe2+ + H2Oi = FeOH+ + H+ ;
% k3 %k3/kc :   FeOH+ + H2Oi = FeOH2 + H+ ;
% k4 %k4/kd :   FeOH2 + H2Oi = FeOH3- + H+ ;
% k5 %k5/ke :    Fe2O3 + H+ + H+ + H+ + H+ + H+ + H+ + H+  =
Fe3+ + Fe3+ +
```

```
H2Oi + H2Oi + H2Oi;

% k6 %k6/kf :   Fe3+ + H2Oi = FeOH+2 + H+ ;

% k7 %k7/kg :   Fe3+ + H2Oi + H2Oi = FeOH2+ + H+ + H+ ;

* % k8 %k8/kh :   Fe3+ + H2Oi + H2Oi + H2Oi = FeOH3 + H+
+ H+ + H+ + R8; not defined in asme

* % k9 %k9/ki :   Fe3+ + H2Oi + H2Oi + H2Oi + H2Oi = FeOH4-
+ H+ + H+ + H+ + H+;

% k10 %k10/kj :   Fe3+ + Fe3+ + H2Oi + H2Oi = Fe2OH2+4 +
H+ + H+;

*% k11 %k11/kk :   Fe3+ + Fe3+ + Fe3+ + Fe3+ + Fe3+ + Fe3+
+ Fe3+ + Fe3+

+ Fe3+ + Fe3+ + Fe3+ + Fe3+ + H2Oi + H2Oi + H2Oi + H2Oi +
H2Oi + H2Oi

+ H2Oi + H2Oi + H2Oi + H2Oi + H2Oi + H2Oi + H2Oi + H2Oi +
H2Oi

+ H2Oi + H2Oi + H2Oi = Fe3O4 + Fe3O4 + Fe3O4 + Fe3O4 +

H+ + H+ + H+ + H+ + H+ + H+ + H+ + H+ + H+ + H+ + H+ + H+ +

H+ + H+ + H+ + H+ + H+ + H+ + H+ + H+ + H+ + H+ + H+ + H+ +

H+ + H+ + H+ + H+ + H+ + H+ + H+ + H+ + H+ + H+ + H+ + H+
+ O2

%k12 %k12/kl : Fe3+ + E- = Fe2+;

%k13 %k13/km : Fe3+ + E- + E- + E- = Fe3+;

%k14 %k14/kn : H2O = O2 + H+ + H+ + H+ + E- + E- + E-;

%k15 %k15/ko : H+ + H+ + E- + E- = H2;

%k16 %k16/kp : H2O = OH- + H+;

array end;

**;


WHENEVER TIME= 0 + 1*59 % CALL REPORT;
```

```
**;

PARAMETER TOTFEOUT fe2+OUT feoh+OUT feoh2OUT fe3o4out
FeOH3-OUT
FE3+OUT Fe2O3OUT FeOH+2OUT FEOH2+OUT FeOH3OUT FEOH4-OUT
Fe2OH2OUT
H+OUT H2OUT H2OOUT OH-OUT E-OUT pHOUT ;

setpstream 1 3 20;
time TOTFEOUT fe2+OUT feoh+OUT feoh2OUT fe3o4out FeOH3-
OUT
FE3+OUT Fe2O3OUT FeOH+2OUT FEOH2+OUT FeOH3OUT FEOH4-OUT
Fe2OH2OUT;
**;

setpstream 2 1 20;
time TOTFEOUT feoh2OUT FeOH3-OUT fe3o4out fe2+OUT FE3+OUT
Fe2O3OUT FEOH2+OUT Fe2OH2OUT; ka kb kc k2 k3 k4 H+ H2;
**;

setpstream 3 14 20;
time H+OUT H2OUT H2OOUT OH-OUT E-OUT pHOUT FE3+OUT
fe2+OUT;
**;

*COMPILE HEAD;
*PRINT HEADINGS;
*write 1=#3, "    time     ph          H2cckg      fe3o4
    totfe      fe3+     fe2+      fe2o3";
*write 1=12,  "     time            ph            H2cckg
fe3o4
```

```
     totfe      fe3+     fe2+      fe2o3";
*write 1=13,  "      time            ph             H2cckg
fe3o4
     totfe      fe3+     fe2+      fe2o3";

*WHENEVER TIME= 0 CALL HEAD;



COMPILE REPORT;
array <#n> work;
TOTFE = (FE2+ + FeOH2 + FeOH+ + FeOH3-)*55.85*1e6;
ph=-log10(H+);
h2cckg=h2*22400;
array end;

do 10 for #1=0(1)#n - 1;

*WRITE 1, (E13,3) TOTFE<#1>;
*write 1=1, "Ra<2> Ra<2> Ra<#n>" Ra<2> Ra<2> Ra<#n>;
*write 1=1, "k2 k3 k4", k2 k3 k4;
*write 1=1, "ka kb kc", ka kb kc;
*write 1=1,"H+ H2 H2oi" H+ H2 h2oi;



label 10;
TOTFEOUT=TOTFE<0>;
fe2+OUT=FE2+<0>;
feoh+OUT=FEOH+<0>;
feoh2OUT=FEOH2<0>;
```

```
fe3o4out=Fe3O4<0>;
FeOH3-OUT=FEOH3-<0>;
fe3+OUT=FE3+<0>;
Fe2O3OUT=Fe2O3<0>;
FeOH+2OUT=FeOH+2<0>;
FEOH2+OUT=FeOH2+<0>;
FeOH3OUT=FeOH3<0>;
FEOH4-OUT=FeOH4-<0>;
Fe2OH2OUT=Fe2OH2<0>;
*ka=ka<0>;
*kb=kb<0>;
*kc=kc<0>;
*k2=k2<0);
*k3=k3<0>;
*k4=k4<0>;
*H+=H+<0>;
*H2=H2<0>;
H+OUT=H+<0>;
H2OUT=H2<0>;
H2OOUT=H2O<0>;
OH-OUT=OH-<0>;
E-OUT=E-<0>;
pHOUT=pH<0>;

do 20 for #2=0(1)2; for intg 2 from zero of increments 1
to 2
do 30 for #3= #2 +11; in this loop refer to #2 as 1 2 and
3
```

```
write 1=#3, ((e13, 3)) time  pH<#2>, H2cckg<#2> fe3o4<#2>
totfe<#2>
fe3+<#2> fe2+<#2>  fe2o3<#2> ;
label 30;
label 20;

*write 1,  "time  pH, H2cckg fe3o4 totfe fe3+ fe2+ fe2o3";
*write 1, "time  pH, H2cckg fe3o4 totfe fe3+ fe2+ fe2o3";

pstream 1;
pstream 2;

**;
BEGIN;
STOP;
```

Appendix 2: Use of electrochemistry in recirculation loop

Work is taken from second year transfer report by Elizabeth Parker-Quaife

Electrochemical test for recirculation loop

The recirculation loop was set up to allow for electrochemical measurements of samples at room temperature. A Stainless steel 304 sample was prepared to 1200 grit on all sides, this was connected to the autoclave wire feedthroughs using a 1 cm piece of stainless-steel tubing and a crimping technique. A Pt flag was also connecting to the feedthroughs; these were manipulated to face one another with a gap of ~ 5 cm. The connections were rinsed with acetone, ethanol, and distilled water to remove any contamination or residues. The autoclave was then closed and connected to the recirculation loop following the instruction in the Cormet manual (section3) along with the reference electrode system. The recirculation loop was leaked tested and deoxygenated using argon gas, the pressure was kept at around 50 bar to maintain flow in and out of the autoclave. The electrode set up can be seen below. OCP measurements were taken when [O_2] dropped below 10 ppb, potential of both working electrodes were measured using an IVUM CompStat, for 120 sec with EOC interval of 1 s. The [H_2] was then increased at measurements of the OCP were taking for 15 mins, with EOC interval of 1s.

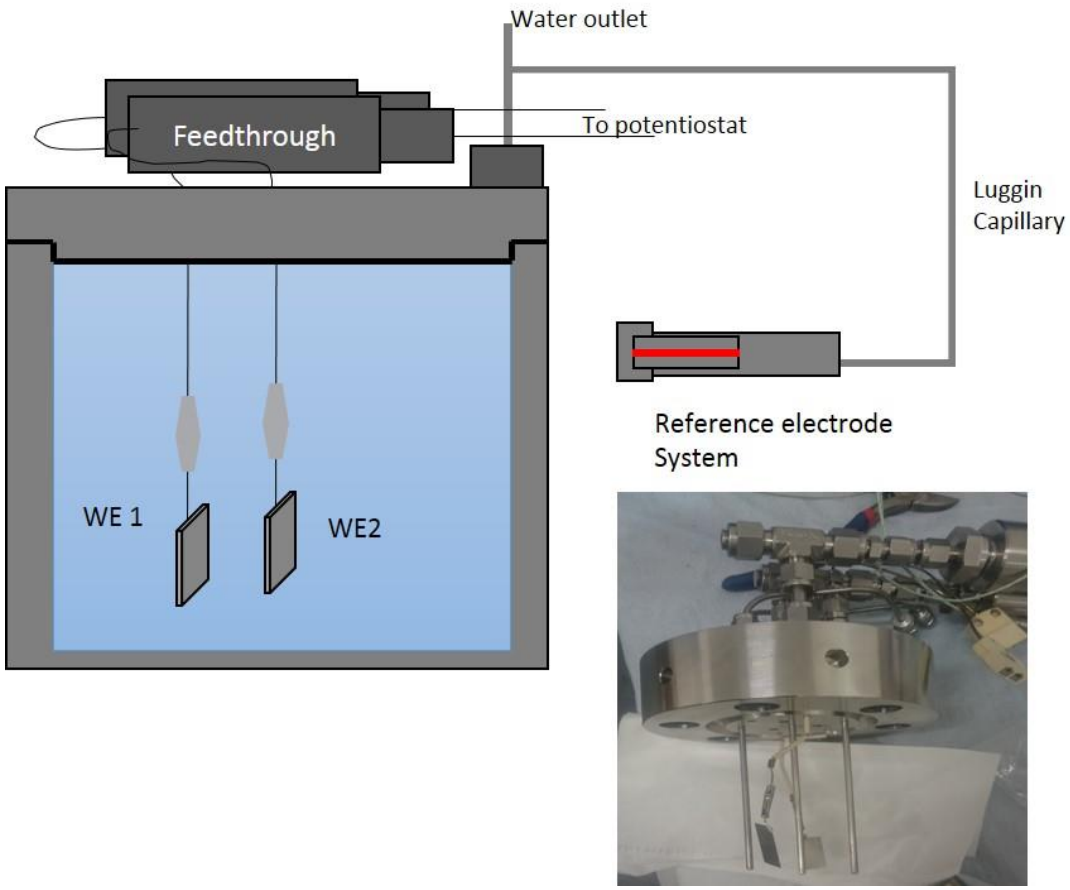

Appendix 1. Schematic to indicated electrode step up inside the autoclave. Inset a photo of the electrochemical set up before being secured.

Results of electrochemical testing

The electrochemical connections are mentioned in the experimental explanation; being stainless steel tubing, connecting spot welded WE and Pt counter to the platinum feedthroughs wires. It has been mentioned previously in **Section 4.2** that material selection was a major consideration meaning that the standard feedthroughs and connections could not be used, as these contain PFTE that will have degraded to produce HF under γ-radiation. The solution was to use the ceramic feedthroughs shown previously which introduces a platinum wire into the autoclave, which had to be connected to the sample electrodes. The platinum wire is insulated with zirconia ceramic beads. Traditional connections have samples spot welded to one length of wire, this was not possible in this system, as Pt is hard to spot weld and with geometric constraints it could not proceed. Initially it was suggested to use nickel lugs crimped to samples that could be screwed together and removed easily. This solution would have introduced a complexity that would lead to a possible galvanic couple, as the metals in the sample are dissimilar to metals in the lugs and screws. It would mean any

OCP measurements would not be true representations of the sample, but the system generated by the lug, screw, and wire. The solution was to use a piece of stainless steel tubing to connect the spot-welded samples to their feedthrough connections. For the SS sample a smaller piece of SS tube was inserted into a larger one to enable crimping between the thicker diameter Pt wire and the SS wire spot welded to the sample. The stainless-steel tubing was then crimped to the wire to provide a connection. The OCP of both working electrodes (Pt and SS) was monitored for 120 seconds for inert conditions and for 900 s for hydrogenated conditions. It is expected on a passivated surface that when hydrogen is introduced that the potential becomes more negative. This was not seen for this example, this may be due to the [H_2] not reaching equilibrium or minimum, but also for the SS WE the electrode has not been oxidised yet, so the surface is not passivated. So, it is expected to see this slight increase in OCP; this can be overcome by oxidising the sample and repeating. The increase in OCP for the Pt electrode is unexpected also, but the graph shows fluctuation in OCP under inert conditions, which may be accounted for by any electrical background noise changes, as it shows a jump and then decrease. The fact the OCP is not stable and fluctuates suggests that it may not be a true value and therefore direct comparison to the hydrogen conditions cannot be made. The lowering and drifting of the OCP under hydrogen is consistent of the hydrogen concentration increasing over time. The OCP value for SS 304 for the hydrogenated experiment does not drift much and the average is around -0.1 V and the noise is the result is consistently approx. 15 mV. In comparison to the non-hydrogenated value which was ~ -0.12 V which is more than the hydrogenated value, which is not expected, but the fact the sample is not oxidised could account for this. To improve the validity for these experiments; longer durations are required with more repetitions to gain consistent results. The hydrogen and oxygen concentrations should be monitored and plotted with the OCP values to assess their effect. Another route to investigate is to oxidise the sample, observing OCP, and impedance of the sample and then repeat the hydrogenation experiments.

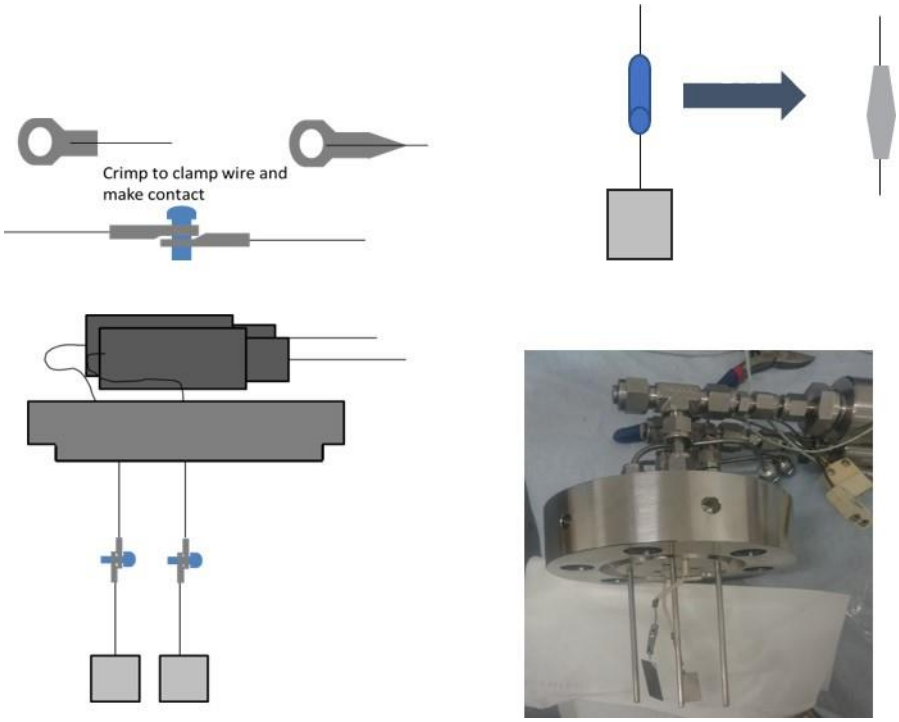

Appendix 2. Schematic showing the unsuccessful attempts of connection and the solution used. Inset photograph of the set up used.

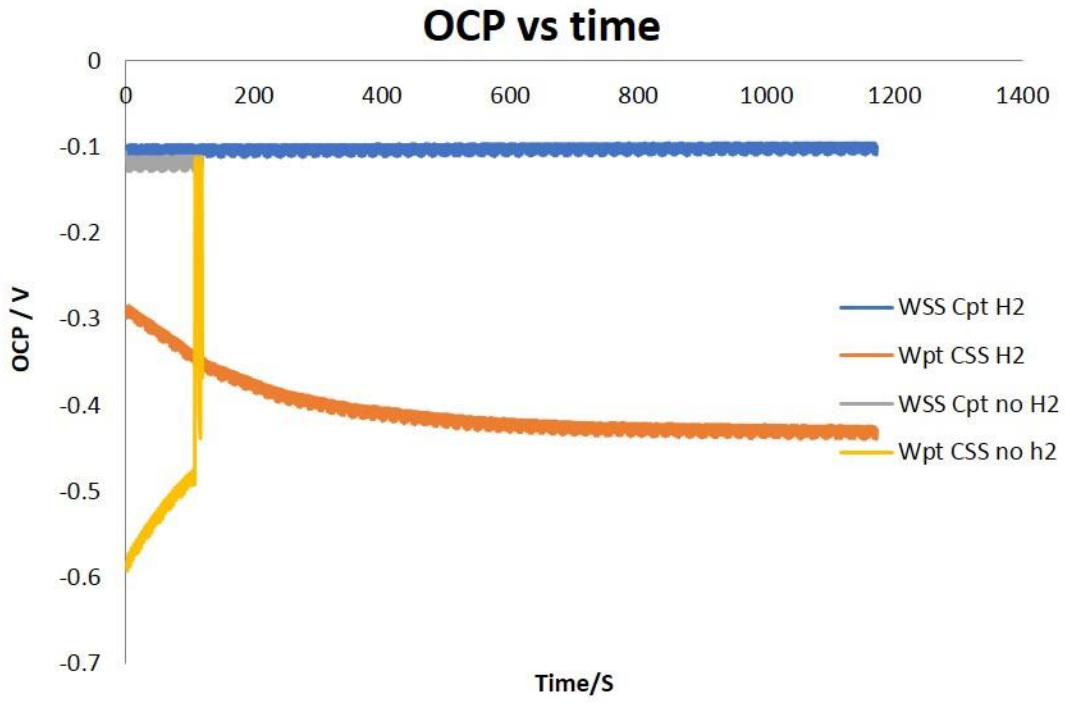

Appendix 3. OCP plot to show the OCP change with time and the injection of hydrogen

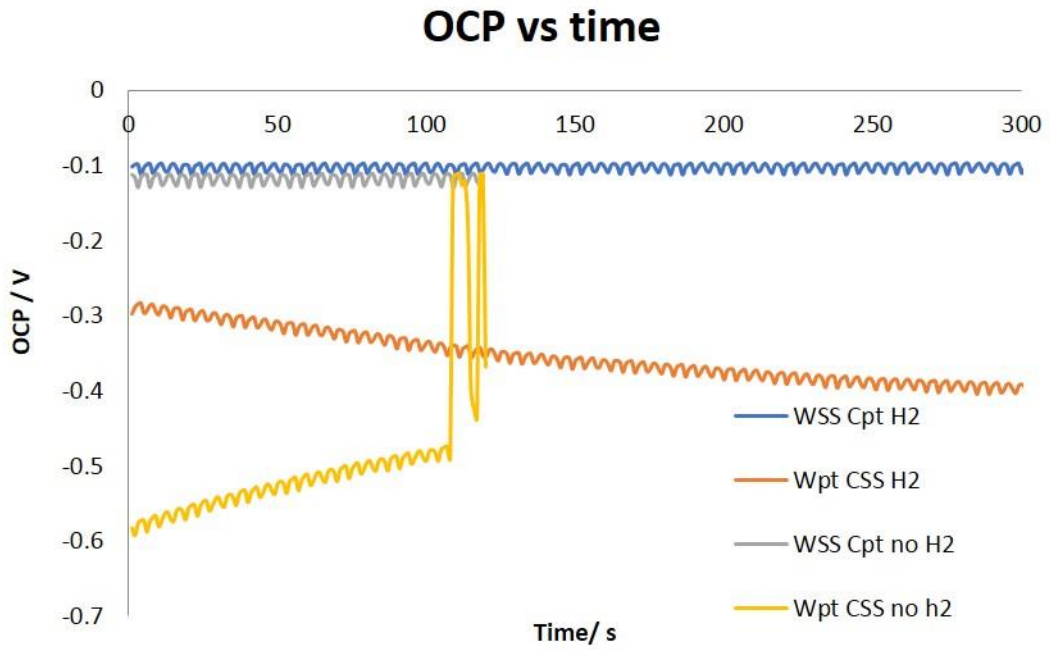

Appendix 4. Zoomed in plot to show the OCP change with time and the injection of hydrogen.

Appendix 3: Example of solid state dosimeter raw data and calculation.

Type and position	Thickness / cm	Λ (A_{max})	A	A/ cm	time/ min	Total Dose/ kGy	Dose Rate Gy/m
		603 nm					
Amber A	0.295		0.653	2.21	150	5.29	35.27
Amber B	0.295		0.802	2.72	150	6.6	44.00
Amber C	0.285		0.769	2.70	150	6.54	43.60
Amber A	0.295		8.21E-01	2.78	210	6.76	32.19
Amber B	0.285		0.846	2.97	210	7.27	34.62
Amber C	0.31		1.12	3.61	210	9.08	43.24
Amber A	0.295		1.22	4.14	270	10.69	39.59
Amber B	0.295		1.055	3.58	270	8.99	33.30
Amber C							
		651 nm					
Amber A	0.295		0.377	1.28	150	4.93	32.87
Amber B	0.295		0.46	1.56	150	6.11	40.73
Amber C	0.285		0.443	1.55	150	6.07	40.47
Amber A	0.295		4.83E-01	1.64	210	6.46	30.76
Amber B	0.285		0.498	1.75	210	6.94	33.05
Amber C	0.31		0.65	2.10	210	8.54	40.67
Amber A	0.295		0.701	2.38	270	9.88	36.59
Amber B	0.295		0.608	2.06	270	8.35	30.93
Average						**7.41**	**36.99**

Appendix 4: Examples of raw experimental data for corrosion tests

Examples of measurements for SEM thicknesses

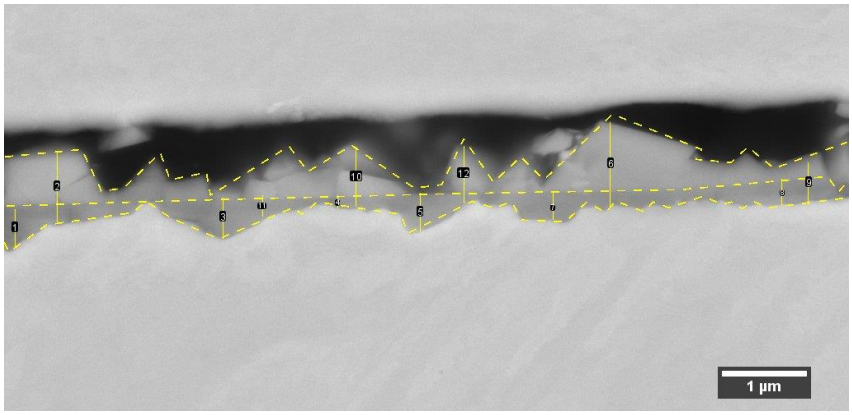

Appendix 5. Lines and lengths on unirradiated sample.

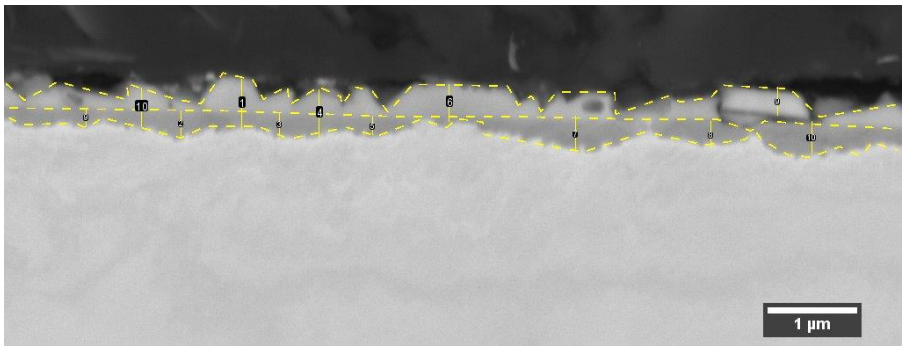

Appendix 6. Lines and lengths on irradiated sample.

Example of raw data and processing for the atomic concentrations and multiple EDS scans data

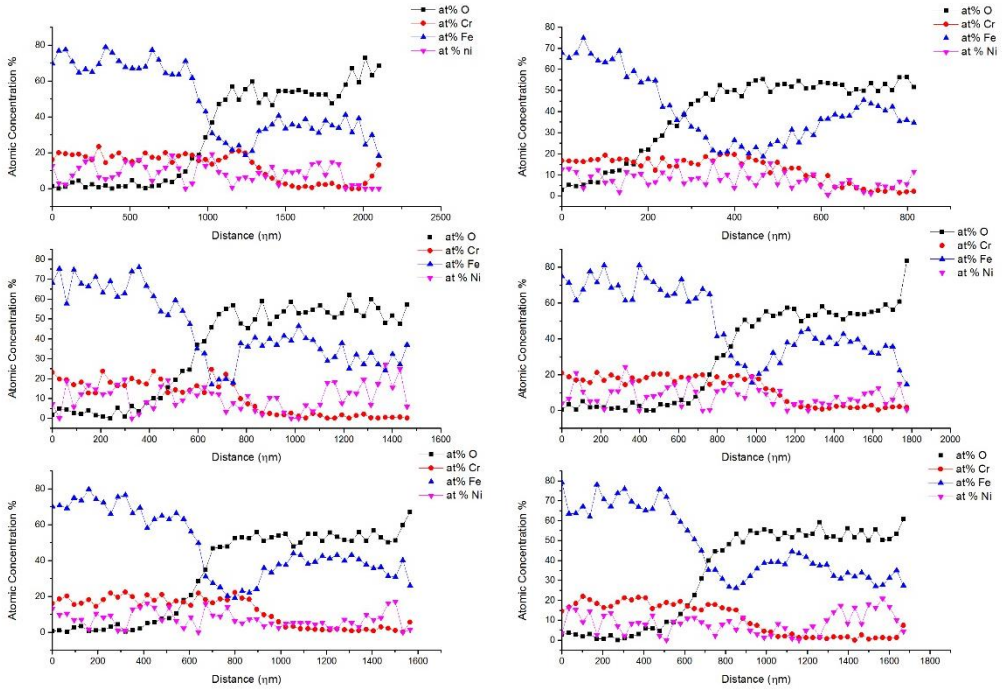

Appendix 7. Line scan data for multiple areas unirradiated sample.

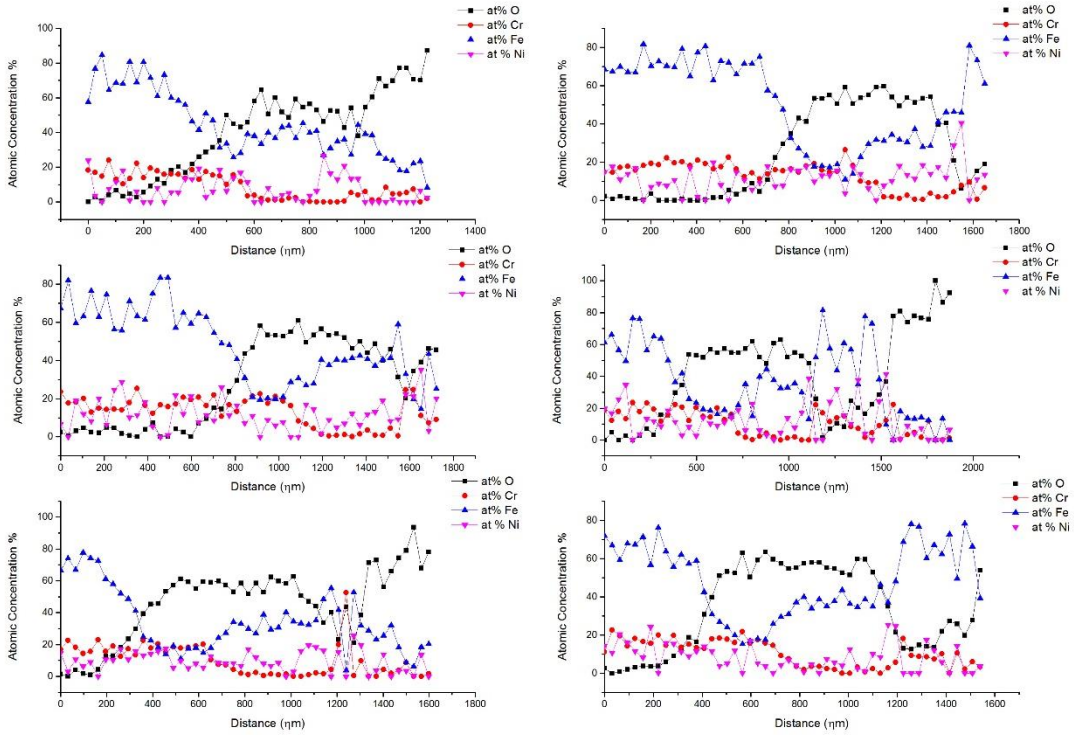

Appendix 8. Line scan data for multiple areas ɣ-irradiated sample.

Appendix 5: Example of raw data and processing for the atomic concentrations

Point	Distance (	Distance (\g(h)m)	O Wt%	wt%/at.w	at% O	Cr Wt%	wt%/at.w cr	at% Cr	Fe Wt%	wt%/at.w Fe	at% Fe	Ni Wt%	wt%/at.w ni	at % Ni	total wt/at w	at total	Total
		col(b)*1000		col(c)/16	(col(i1)/col(m1))*100		col(d)/52	(col(j1)/col(m1))*100		col(e)/55.85	(col(k1)/col(m1))*100		col(f)/58.69	(col(l1)/col(m1))*100	col(i1)+col(j1)+col(k1)+col(l1)	col(q1)+col(o1)+col(p1)+col(n1)	
1.00	0.00	0.00	0.81	0.05	2.75	13.91	0.27	14.52	81.38	1.46	79.12	3.90	0.07	3.61	1.84	100.00	100
2.00	0.03	34.09	1.14	0.07	3.86	15.82	0.30	16.47	65.48	1.17	63.47	17.56	0.30	16.20	1.85	100.00	100
3.00	0.07	68.17	0.80	0.05	2.72	17.52	0.34	18.36	65.14	1.17	63.56	16.54	0.28	15.36	1.84	100.00	100
4.00	0.10	102.26	0.53	0.03	1.81	20.99	0.40	22.02	68.67	1.23	67.06	9.81	0.17	9.12	1.83	100.00	100
5.00	0.14	136.34	0.91	0.06	3.09	19.53	0.38	20.37	63.82	1.14	61.99	15.74	0.27	14.55	1.84	100.00	100
6.00	0.17	170.43	0.22	0.01	0.76	17.41	0.33	18.39	79.41	1.42	78.09	2.96	0.05	2.77	1.82	100.00	100
7.00	0.20	204.52	0.23	0.01	0.79	15.36	0.30	16.32	71.33	1.28	70.56	13.09	0.22	12.32	1.81	100.00	100
8.00	0.24	238.60	0.66	0.04	2.26	16.14	0.31	16.97	68.42	1.23	67.00	14.78	0.25	13.77	1.83	100.00	100
9.00	0.27	272.69	0.00	0.00	0.00	17.97	0.35	19.12	74.46	1.33	73.75	7.57	0.13	7.13	1.81	100.00	100
10.00	0.31	306.77	0.28	0.02	0.96	20.10	0.39	21.15	77.47	1.39	75.89	2.15	0.04	2.00	1.83	100.00	100
11.00	0.34	340.86	0.57	0.04	1.94	19.24	0.37	20.18	71.23	1.28	69.55	8.96	0.15	8.33	1.83	100.00	100
12.00	0.37	374.95	0.88	0.06	2.98	20.64	0.40	21.47	68.99	1.24	66.82	9.48	0.16	8.74	1.85	100.00	100
13.00	0.41	409.03	1.79	0.11	5.92	20.81	0.40	21.17	68.79	1.23	65.15	8.61	0.15	7.76	1.89	100.00	100
14.00	0.44	443.12	1.77	0.11	5.89	15.53	0.30	15.90	68.94	1.23	65.72	13.76	0.23	12.48	1.88	100.00	100
15.00	0.48	477.20	1.41	0.09	4.70	16.89	0.32	17.34	79.29	1.42	75.77	2.41	0.04	2.19	1.87	100.00	100
16.00	0.51	511.29	2.86	0.18	9.20	19.13	0.37	18.93	78.01	1.40	71.87	0.00	0.00	0.00	1.94	100.00	100
17.00	0.55	545.38	2.80	0.18	9.07	17.94	0.35	17.88	68.57	1.23	63.62	10.68	0.18	9.43	1.93	100.00	100
18.00	0.58	579.46	4.18	0.26	13.09	20.08	0.39	19.35	66.04	1.18	59.26	9.71	0.17	8.29	2.00	100.00	100
19.00	0.61	613.55	5.69	0.36	17.29	18.03	0.35	16.86	63.06	1.13	54.90	13.21	0.23	10.94	2.06	100.00	100
20.00	0.65	647.63	7.72	0.48	22.48	17.70	0.34	15.86	60.53	1.08	50.50	14.06	0.24	11.16	2.15	100.00	100
21.00	0.68	681.72	11.44	0.72	30.90	18.09	0.35	15.03	58.10	1.04	44.96	12.37	0.21	9.11	2.31	100.00	100
22.00	0.72	715.81	16.24	1.02	40.01	23.60	0.45	17.89	49.84	0.89	35.18	10.31	0.18	6.92	2.54	100.00	100
23.00	0.75	749.89	18.93	1.18	44.41	24.77	0.48	17.88	52.72	0.94	35.43	3.57	0.06	2.28	2.66	100.00	100
24.00	0.78	783.98	19.24	1.20	45.08	22.57	0.43	16.27	45.83	0.82	30.76	12.36	0.21	7.89	2.67	100.00	100
25.00	0.82	818.06	21.24	1.33	48.21	22.19	0.43	15.50	41.04	0.73	26.69	15.53	0.26	9.61	2.75	100.00	100
26.00	0.85	852.15	24.98	1.56	53.34	23.06	0.44	15.15	42.71	0.76	26.13	9.25	0.16	5.38	2.93	100.00	100
27.00	0.89	886.24	21.73	1.36	49.13	15.61	0.30	10.86	44.09	0.79	28.56	18.57	0.32	11.45	2.76	100.00	100
28.00	0.92	920.32	25.99	1.62	54.89	12.63	0.24	8.21	53.24	0.95	32.21	8.14	0.14	4.69	2.96	100.00	100
29.00	0.95	954.41	24.98	1.56	53.56	11.30	0.22	7.46	58.55	1.05	35.97	5.16	0.09	3.02	2.91	100.00	100
30.00	0.99	988.49	26.34	1.65	55.38	7.08	0.14	4.58	64.18	1.15	38.66	2.40	0.04	1.38	2.97	100.00	100
31.00	1.02	1022.60	25.59	1.60	54.46	6.33	0.12	4.15	64.06	1.15	39.06	4.02	0.07	2.33	2.94	100.00	100
32.00	1.06	1056.70	22.59	1.41	50.60	2.73	0.05	1.88	61.39	1.10	39.40	13.29	0.23	8.12	2.79	100.00	100
33.00	1.09	1090.80	25.02	1.56	53.90	2.99	0.06	1.98	61.64	1.10	38.04	10.36	0.18	6.08	2.90	100.00	100
34.00	1.12	1124.80	23.54	1.47	51.71	4.44	0.09	3.00	70.72	1.27	44.51	1.30	0.02	0.78	2.85	100.00	100
35.00	1.16	1158.90	26.14	1.63	55.21	2.04	0.04	1.33	71.82	1.29	43.46	0.00	0.00	0.00	2.96	100.00	100
36.00	1.19	1193.00	23.88	1.49	52.35	1.91	0.04	1.29	66.37	1.19	41.68	7.83	0.13	4.68	2.85	100.00	100
37.00	1.23	1227.10	24.63	1.54	53.42	1.96	0.04	1.31	61.71	1.10	38.35	11.71	0.20	6.92	2.88	100.00	100
38.00	1.26	1261.20	29.35	1.83	59.19	2.16	0.04	1.34	65.09	1.17	37.60	3.40	0.06	1.87	3.10	100.00	100
39.00	1.30	1295.30	23.16	1.45	51.50	1.06	0.02	0.73	59.33	1.06	37.80	16.46	0.28	9.98	2.81	100.00	100
40.00	1.33	1329.40	23.46	1.47	52.00	2.28	0.04	1.56	50.76	0.91	32.23	23.51	0.40	14.21	2.82	100.00	100
41.00	1.36	1363.40	22.28	1.39	50.41	1.99	0.04	1.39	47.62	0.85	30.87	28.11	0.48	17.34	2.76	100.00	100
42.00	1.40	1397.50	26.72	1.67	56.17	2.60	0.05	1.68	56.17	1.01	33.83	14.51	0.25	8.32	2.97	100.00	100
43.00	1.43	1431.60	23.07	1.44	51.57	0.00	0.00	0.00	49.99	0.90	32.02	26.93	0.46	16.41	2.80	100.00	100
44.00	1.47	1465.70	25.97	1.62	55.17	4.07	0.08	2.66	55.73	1.00	33.92	14.24	0.24	8.25	2.94	100.00	100
45.00	1.50	1499.80	21.94	1.37	49.96	0.82	0.02	0.57	48.09	0.86	31.37	29.15	0.50	18.10	2.74	100.00	100
46.00	1.53	1533.90	26.08	1.63	55.60	1.70	0.03	1.12	44.28	0.79	27.04	27.94	0.48	16.24	2.93	100.00	100
47.00	1.57	1568.00	22.03	1.38	50.13	1.89	0.04	1.32	42.32	0.76	27.59	33.77	0.58	20.95	2.75	100.00	100
48.00	1.60	1602.00	22.53	1.41	50.78	1.40	0.03	0.97	48.75	0.87	31.47	27.31	0.47	16.78	2.77	100.00	100
49.00	1.64	1636.10	24.59	1.54	53.46	2.00	0.04	1.34	56.25	1.01	35.03	17.16	0.29	10.17	2.87	100.00	100
50.00	1.67	1670.20	30.92	1.93	60.81	12.13	0.23	7.34	48.69	0.87	27.43	8.25	0.14	4.42	3.18	100.00	100

Appendix 6: Examples of raw data for interactions studies

Example of absorbance graph for Ghormley calibration

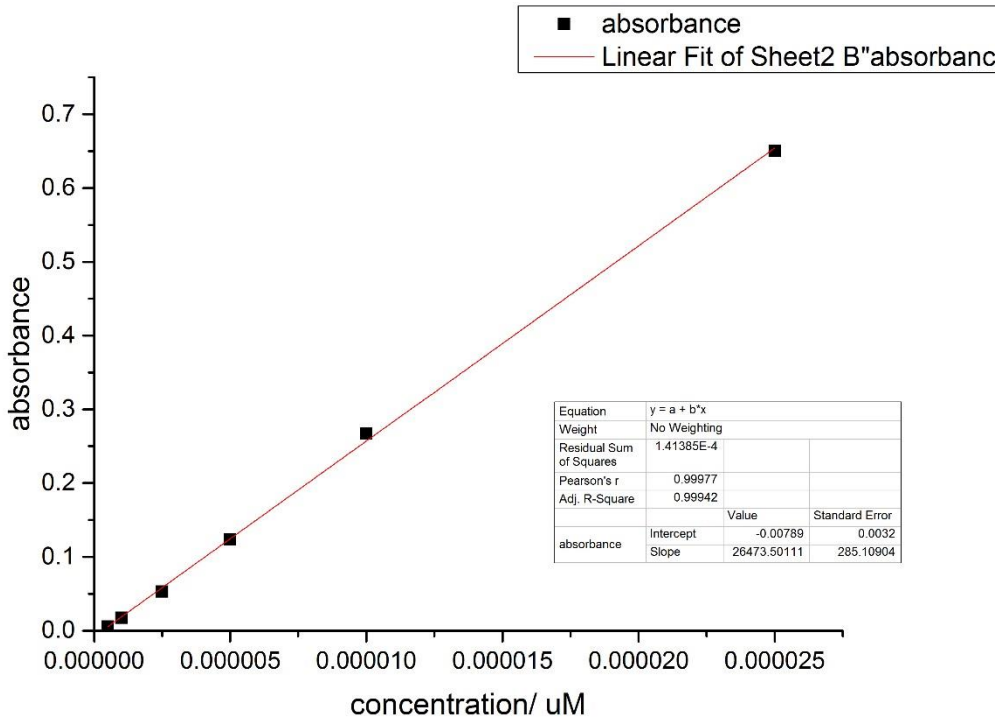

Appendix 7: Example of data processing for absorbance measurements to hydrogen peroxide concentration in the interactions studies for haematite systems

A	B	C	D	E	F	G	H	I	J	K	L	M	N	O	P
sample	Iron powd	W1	W2	Sample w	Degas tim	comment	Rad time/	dose rate	total dose	Exp time	ABS	abs*2			[H2O2]/ uM
				col(D)-col	6				291.34			col(l)*2	25408	col(m)/co	col(o)/1e-6
FE2O3 1 A-AO	Fe2O3	53.89717	54.15193	0.25476	6	--	21	--	291.34	--	0.68965	1.37929	25408	5.43E-05	54.28584
FE2O3 1 2 A-AO	Fe2O3	53.86256	54.14023	0.27767	6	--	21	--	291.34	--	0.88331	1.76663	25408	6.95E-05	69.53038
FE2O3 3 A-AO	Fe2O3	53.75912	54.01465	0.25553	6	--	21	--	291.34	--	0.54314	1.08628	25408	4.28E-05	42.75351
FE2O3 5 A-AO	Fe2O3	53.70619	53.95023	0.24404	6	--	0	--	--	--	0.02217	0.04434	25408	1.75E-06	1.74516
FE2O3 6 A-AO	Fe2O3	53.84361	54.113	0.26939	6	--	0	--	--	--	0.00192	0.00384	25408	1.51E-07	0.15112
FE2O3 7 A-AO	Fe2O3	53.65853	53.91082	0.25229	6	--	0		--	--	-0.00179	-0.00358	25408	-1.41E-07	-0.14082
fe2o3 7 a-a0	1.56012	53.74651	54.00406	0.25755	6	synthetic	21		290		1.56012	3.12023	25408	1.23E-04	122.80521
fe2o3 10 a-a0	1.31383	53.92044	54.16946	0.24902	6	synthetic	21		290		1.31383	2.62766	25408	1.03E-04	103.41879
fe2o3 8 a-a0	0.70346	53.79301	54.05905	0.26604	6	synthetic	21		290		0.70346	1.40692	25408	5.54E-05	55.37323

Appendix 8: Raw data and calculations for Redheads analysis

Redheads analysis Ed=RTp[Ln((Atp/B)-3.64)		R	8.314					
		A	1.00E+14					
		C to K	273.15					
		b	0.083					
		Kjmol to Ev	96.485					
Powder	Tp values / C	Tp Values / K	RTp	Ln(Atp/b)	Ln(Atp/b)-3.46	Ed	Ed / Kj/mol	ED / eV
FeO	277.36	550.51	4576.94014	41.03595109	37.39595109	171159	171.16	1.77
	365.26	638.41	5307.74074	41.18408668	37.54408668	199274.3	199.27	2.07
	154.15	427.3	3552.5722	40.78259232	37.14259232	131951.7	131.95	1.37
	57.01	330.16	2744.95024	40.52468336	36.88468336	101246.6	101.25	1.05
Fe2O3	227.91	501.06	4165.81284	40.94183183	37.30183183	155392.4	155.39	1.61
	159.63	432.78	3598.13292	40.79533549	37.15533549	133689.8	133.69	1.39
	103.62	376.77	3132.46578	40.65674089	37.01674089	115953.7	115.95	1.20
Fe3O4	238.54	511.69	4254.19066	40.96282495	37.32282495	158778.4	158.78	1.65
	96.45	369.6	3072.8544	40.63752731	36.99752731	113688	113.69	1.18

Appendix 9: Conferences and seminars

List of conferences and seminars attended, and any presentations or posters presented

- LLC, Bilboa 2014 ANT meeting (attendee)
- UNTF energy Materials, Oxford 2014 (Poster)
- Faraday Discussion Corrosion, London 2015 (Poster and 30 sec presentation)
- Manchester Performance centre seminar 2014 (oral presentation) 2015 (oral presentation)
- Nuclear PhD winter school Winter, Buxton 2014/2015 (poster presentation)
- EngD network conference, Derby 2014 (poster) 2015 (oral presentation)
- Nuclear Plant Chemistry Japan, 2014 (attendee) Brighton 2016 (poster)
- Nuclear Decommissioning authority meeting, 2015 (oral presentation)
- Dalton day seminar, 2016 (Poster)
- Cadarache International Nuclear PhD Workshop hosted by the CEA 2017 (poster)
- Miller conference 2017 (poster presentation)

The University of Manchester
Dalton Nuclear Institute

Corrosion and CRUD

The Effects of Radiation on Nickel Containing Alloys

Elizabeth Parker-Quaife
Dalton Cumbrian Facility

Elizabeth.parker-quaife@postgrad.manchester.ac.uk

What is CRUD?

Corrosion is the chemical degradation of a metal, it may occur through a series of reactions, the most significant contribution being oxidation. Corrosion affects most metals, including those present in a PWR reactor coolant system. The metal oxides produced may dissolved into and be transported around the PWR coolant system. Under the right conditions the metal oxides may deposit or precipitate out of solution. The deposition and accumulation of these corrosion products is known as CRUD.

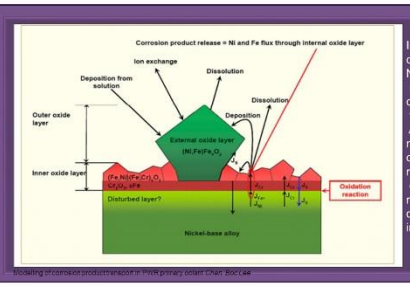

Image to model corrosion of a Ni alloy and how metal oxide can progress though the layer. Also shows the mechanism of oxide release and deposition. This release and deposition results in CRUD

The Importance of understanding CRUD

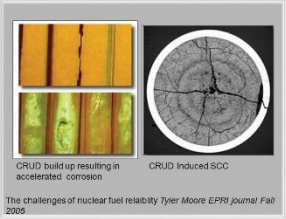

CRUD build up resulting in accelerated corrosion

CRUD Induced SCC

The challenges of nuclear fuel reliability *Tyler Moore EPRI journal Fall 2006*

Accumulation of CRUD can lead to reduction in plant life. CRUD can increase the corrosion rate of metal alloys, it may cause Stress Corrosion Cracking, and CRUD induced power shifts. It can also lead to increase out of system activity. Understanding the corrosion, dissolution and deposition mechanisms will allow for an overall understanding of CRUD. With this understanding issues with CRUD may be overcome, and this will increase plant efficiency and lifetime.

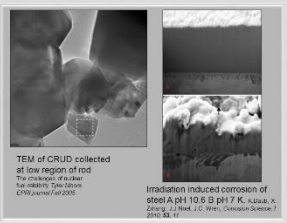

TEM of CRUD collected at low region of rod

Irradiation induced corrosion of steel A pH 10.6 B pH 7 K.

Research Direction

The design and implementation of experiments to investigate corrosion in a set of different metal alloys under PWR conditions. Use of ^{60}Co γ radiation and heavy ions to simulate reactor system radiation. To form an understanding of the effects radiation has on corrosion rate, in both static and flowing systems. Experiments will start at room temperature systems and progress to hot water systems.. These projects require the design and manufacture of autoclave systems that allow for PWR condition simulation.

Experimental variables:
- Metal type
- Radiation type
- Dose rate

Techniques:
- SEM
- Cyclic voltammetry
- TEM
- XPS spectroscopy
- pH monitoring
- Raman spectroscopy

Experimental set up:

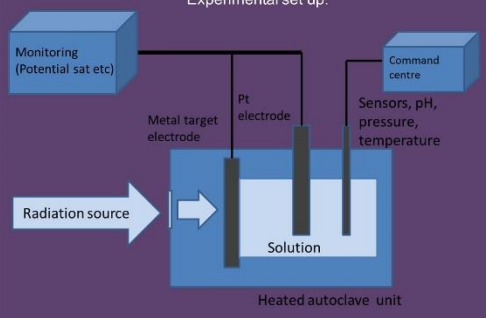

Diagram to show possible experimental set up, based on literature experiments by Wren and Corbel

The University of Manchester
Dalton Nuclear Institute

EPSRC
Engineering and Physical Sciences Research Council

Investigating the role of irradiation in corrosion simulated Light Water Reactor conditions

Elizabeth Parker-Quaife[1,3], Aliaksander Baidak[1,2], Jonathan Duff[3], Fabio Scenini[3] and Simon M. Pimblott[1,2]

[1]The University of Manchester, Dalton Cumbrian Facility, Westlakes Science & Technology Park, Moor Row, Cumbria, CA28 3HA.
[2]The University of Manchester, School of Chemistry, Oxford Road, Manchester, M13 9PL.
[3]The University of Manchester, School of Materials, Oxford Road, Manchester, M13 9PL.

elizabeth.parker-quaife@postgrad.manchester.ac.uk

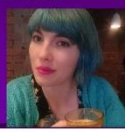

INTRODUCTION

The corrosion of primary circuit components and fuel clad is an important issue in reactor performance and lifetime extension. The harsh conditions within Pressurised Water Reactors (PWR), the high temperatures and pressures (HT/HP) along with the intense mixed radiation fields, lead to complex corrosion behaviour. Corrosion phenomena experienced within PWRs include stress corrosion cracking (SCC) and irradiation accelerated corrosion (IAC); which can lead to corrosion product accumulation elsewhere known as CRUD. CRUD can lead to changes in heat exchange efficiencies, flow behaviour and may even cause CRUD induced power shifts.

A research capability developed at the University of Manchester Dalton Cumbrian Facility (DCF) will allow for *in situ* radiolysis to support corrosion studies. This poster will introduce a PhD project investigating the role of irradiation in corrosion under simulated PWR conditions that utilises the HT/HP research capability.

PROJECT AIMS AND OBJECTIVES

Aims:

- To gain an understanding of how radiation effects corrosion of nuclear materials and corrosion products

Objectives:

- Develop experimental procedures that utilise the HT/HP research capability at the DCF
- Investigate effects of ionising radiation on corrosion using electrochemical techniques, surface techniques along with spectroscopic techniques; including but not limited to cyclic voltammetry, Electrochemical Impedance Spectroscopy (EIS), SEM and Raman spectroscopy
- Understand the effects of radiolysis on surface recombination reactions in relation to corrosion behaviour

WHAT IS RADIOLYSIS?

Radiolysis can be described as the dissociation of molecules by nuclear radiation. Radiolysis processes are very complex producing multiple primary products that have complex behaviour and many potential reactions. Water radiolysis is a concern in PWRs as water is the moderator and coolant. The complex behaviour of water can be seen in Figure 1[1].

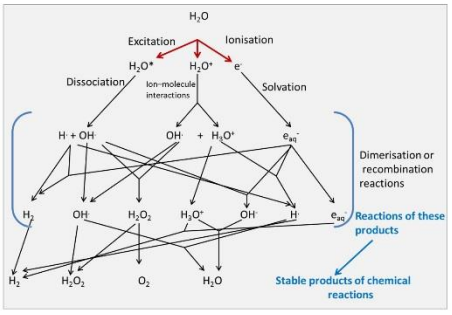

Figure 1 Water radiolysis cascade, showing the possible fates of water after experiencing ionising radiation

Primary products include radicals and molecule species which can be split into oxidising, reducing and neutral species. These species can interact with one another producing other reactive or neutral species[2]. Table 1 shows these primary products.

	Molecule	Radical
Oxidising	H_2O_2	$OH\bullet$ $HO_2\bullet$
Reducing		e^-_{aq} $H\bullet$
Neutral	H_2	

Table 1 Water radiolysis products defined by redox behaviour

The production of these species may alter the corrosion behaviour of the system depending on the concentration of each species. The material surface may also have an effect on the chemistry behaviour of the radiolysis products.

1 M. Spotheim-Maurizot, M. Mostafavi, T. Doüki and J. Belloni, *Radiation Chemistry: From Basics to Applications in Material and Life Sciences* (EDP Science France, 2008
2 M Wang, S Perrin, C Corbel, O Hénon, *Journal of Electroanalytical Chemistry* **737**, 2015

MONITORING CORROSION

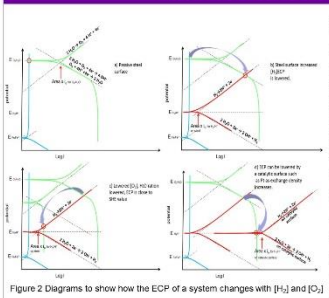

Figure 2 Diagrams to show how the ECP of a system changes with $[H_2]$ and $[O_2]$

It is possible to monitor corrosion behaviour using electrochemistry. The point at which anodic and cathodic potential curves overlap is the electrochemical corrosion potential (ECP). Lowering the ECP can help manage corrosion in reactors. The H:O ratio is increased by adding H_2, ideally gaining a 2:1 ratio. The graphs in Figure 2 show how ECP alters when $[H_2]$ is increased. The ECP will be lowered due to the recombination of $\frac{1}{2}O_2$ and H_2 leading to a reduced concentration of oxidising species.

EXPERIMENTAL CAPABILITIES

The HT/HP loop has been designed to simulate PWR conditions and is capable of operating at 200 atm. and 350 °C.

Reaction vessels that allow for the electrochemical monitoring of metallic samples in both an ion accelerator and a ^{60}Co source have been commissioned. The following test parameters and measurements are possible:

- Varied H_2 and O_2 concentration
- System temperature and pressure
- Water flows of up to 6 Lh^{-1}
- Dose rate for both the ion and ^{60}Co radiation
- Injection of chemical additives
- Conductance measurements
- Electrochemical measurements including ECP values
- Gaseous radiolysis products concentrations

This research capability allows for the study of PWR chemistry and corrosion studies with realistic flowing simulated conditions experiencing either gamma or proton irradiations.

EXPERIMENTAL TECHNIQUES

This project will incorporate the recirculation loop in corrosion studies. Figure 3 shows the outlined experiments.

Experimental variables:

- Metal type
- Radiation type
- Dose rate

Techniques:

- Open circuit potentials
- Cyclic voltammetry
- Impedance spectroscopy
- Surface techniques, TEM, SEM

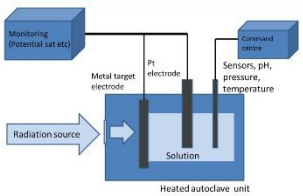

Figure 3 Proposed experimental set up, showing electrochemical monitoring during irradiation

ACKNOWLEDGEMENTS

The research described is supported by the Dalton Cumbrian Facility Project, a joint initiative of the University of Manchester and the Nuclear Decommissioning Authority. The EPSRC and the University of Manchester provide funding. Design and commissioning of the Hot water loop would not have been possible without the help of Cormet. Acknowledgements also include project supervisors Simon M. Pimblott and Fabio Scenini as well as Jonathan Duff and Aliaksander Baidak for help with experimental design and support.

Faculty of Engineering and Physical Sciences

www.materials.manchester.ac.uk

MANCHESTER 1824
The University of Manchester

Interactions of Corrosion Products with Radiolytic Species in PWR Primary Coolant

Elizabeth Parker-Quaife[1,2], Fabio Scenini[3], Andrew Banks[4], Andrew Powell[4] and Simon M. Pimblott[1,2]

[1]Dalton Cumbrian Facility, The University of Manchester, Moor Row, Cumbria, UK, [2]School of Chemistry, The University of Manchester, Manchester, UK, [3]School of Materials, The University of Manchester, Manchester, UK, [4]Rolls-Royce Plc, 62 Buckingham Gate, London SW1E 6AT

Introduction

Resolving the issues of material degradation is a major challenge in the continued safe and efficient operation of nuclear power plants. One major challenge is the corrosion and dissolution of structural materials leading to the deposition and build-up of corrosion products (CRUD). Corrosion and CRUD can lead to reduced reactor efficiency and plant lifetime. The ability to predict corrosion and CRUD behaviour would allow for the better design of operations and processes in reactor design and lifetime extension projects. The reactor environment is complex, experiencing temperature and pressure gradients as well as a mixed radiation field. These conditions present challenges that must be over come if a clear picture of corrosion and CRUD behaviour is to be gained. The results outlined in this poster represent some preliminary data from a research project that aims to investigate the interactions between the radiation environment and the corrosion products generated by the degradation of nuclear materials. The project attempts to link changes in the corrosion mechansim with radiolytically driven chemical processes that occur with in the primary coolant circuit of PWR systems.

Radiolysis and Corrosion

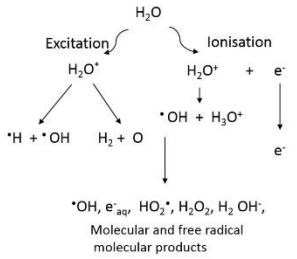

Water radiolysis produces redox active species that alter corrosion processes. H_2O_2 is a stable and highly oxidising species generated by radiolysis. In the presence of various surfaces it decomposes readily causing the radiolysis system to shift from a steady state. The decomposition products can interact with the surfaces, corrosion films, radiolysis products and solubilised corrosion products.

Investigations

Investigating the effects of γ-radiation on CRUD simulants and corrosion surfaces

- Samples were irradiated using Foss Therapy Services Model 812 Cobalt 60 shelf shielded irradiator
- Fe_3O_4 and Fe_2O_3 were irradiated in water
- No pre-treatment of powders
- Both aerated and deaerated were irradiated
- Total doses were varied
- $[H_2O_2]$ was determined using the Ghlormey triiodide method
- [Fe] determined using ICP- MS

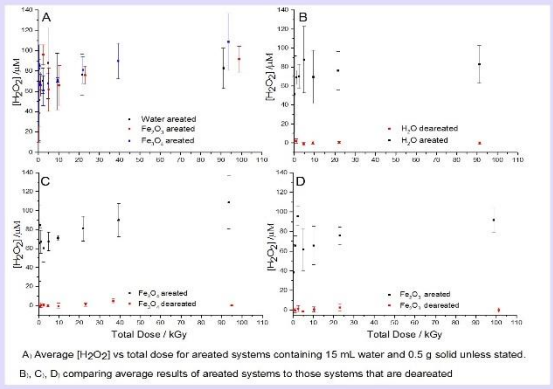

A, Average $[H_2O_2]$ vs total dose for areated systems containing 15 mL water and 0.5 g solid unless stated.
B, C, D comparing average results of areated systems to those systems that are deareated

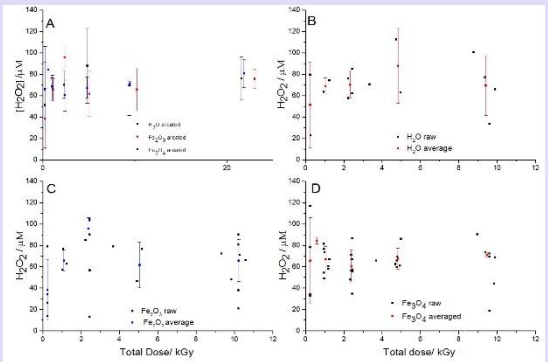

A, Average $[H_2O_2]$ vs total dose for areated systems containing 15 mL water and 0.5 g solid unless stated.
B, C, D, Comparsion of raw data to averages showing scatter within results.

Conclusions and Further Investigations

Conclusions

- When averaged the data shows no dependence of system on $[H_2O_2]$
- Comparing raw data to averaged data scatter shows some clustering
- The powders were no pre-treated so particle size and surface area could cause this scatter.
- $[H_2O_2]$ in deaerated was below detection limits for the Ghormley method, but is expected that $[H_2O_2]$ is low as O_2 can scavenge e^-_{aq}
- [Fe] investigations were inconclusive

Further work

- Effects of particle size and surface to be investigated and controlled
- Investigation of systems irradiated with known $[H_2O_2]$
- Spectroscopic determination of [Fe] using ferrozine
- Investigations of oxide films on corroded coupons of nuclear materials

Rolls-Royce

EPSRC
Engineering and Physical Sciences Research Council

Contact Details:

Elizabeth Paker-Quaife MCheM
School of Chemistry / Dalton Cumbrian Facility
The University of Manchester
Sackville Street
Manchester M13 9PL

Email: elizabeth.parker-quaife@postgrad.manchester.ac.uk

MANCHESTER 1824
The University of Manchester

Interactions of Corrosion Products with Radiolytic Species in PWR Primary Coolant

Elizabeth Parker-Quaife[1,2], Fabio Scenini[3], Andrew Banks[4], Andrew Powell[4], Jay A. LaVerne[5] and Simon M. Pimblott[1,2]

[1]Dalton Cumbrian Facility, The University of Manchester, Moor Row, Cumbria, UK, [2]School of Chemistry, The University of Manchester, Manchester, UK, [3]School of Materials, The University of Manchester, Manchester, UK, [4]Rolls-Royce Plc, 62 Buckingham Gate, London SW1E 6AT, [5]Radiation Laboratory, University of Notre Dame, Indiana, USA

Introduction and Project Aims

Resolving the issues of material degradation is a major challenge in the continued safe and efficient operation of nuclear power plants. One major challenge is the corrosion and dissolution of structural materials leading to the deposition and build-up of corrosion products (CRUD). Corrosion and CRUD can lead to reduced reactor efficiency and plant lifetime. The ability to predict corrosion and CRUD behaviour would allow for the better design of operations and processes.

Project aims

- To gain an understanding of how radiation affects corrosion of nuclear materials and corrosion products
- To enhance fundamental understanding of corrosion and CRUD mechanisms
- Understand the effects of radiolysis on surface recombination reactions in relation to corrosion behaviour

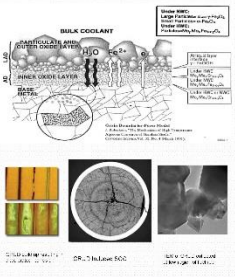

Radiolysis and Corrosion

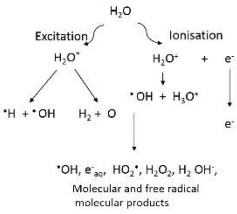

- H_2O_2 is a stable and highly oxidising species generated by radiolysis.
- H_2O_2 decomposes in presence of surfaces and shifts the radiolysis equilibrium from steady state conditions
- Interactions between corrosion and radiolysis products; surfaces, oxide films, and solubilised species will alter steady state behaviour further

Investigations

Investigating the effects of γ-radiation on CRUD simulants and corrosion surfaces

- Samples were irradiated using Cobalt 60 shelf shielded irradiators at the University of Notre Dame and The University of Manchester
- CRUD simulants (0.25 g, Fe_3O_4, Fe_2O_3, FeO) were irradiated in hydrogen peroxide (50 μM) in flame sealed vials after degassing (with argon or helium) varying total dose.
- $[H_2O_2]$ was determined using the Ghlormey triiodide method, which utilises the oxidation of iodine after (including non irradiated control samples, left for the same experimental time)
- Comparative studies were undertaken with long irradiations under deaerated (with argon) or aerated (synthetic air) conditions
- Powder characterisation methods included BET, analysis, SEM imaging and XPS analysis.

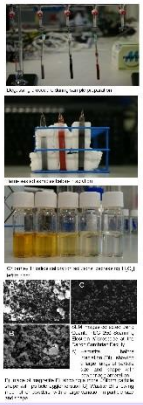

$[H_2O_2]$ vs Total Dose for CRUD Simulants

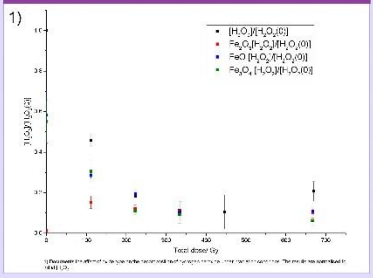

$[H_2O_2]$ Histogram for CRUD-H_2O_2 Systems Irradiated up to ~ 295 kGy

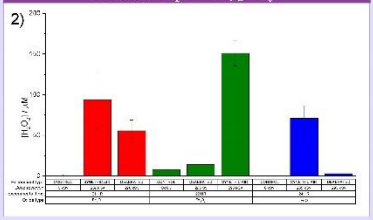

Figure 1) shows the effect of gamma dose on $[H_2O_2]$. It highlights different behaviours and reaction mechanisms for the different oxides, irrespective of irradiation dose. In the Fe_2O_3 system, there is an increase in $[H_2O_2]$ under irradiation compared to the control sample (which had a negligible $[H_2O_2]$). This result was unexpected so longer irradiations were undertaken.

The results of the longer irradiations are recorded in Figure 2). The Fe_2O_3 systems continue to have a higher comparative $[H_2O_2]$ under irradiation, suggesting there is a radiolytic pathway that allows for H_2O_2 build up during γ-irradiation. For instance if Fe_2O_3 is reduced to Fe_3O_4 during H_2O_2 decomposition, oxygen will be generated, allowing for additional H_2O_2 generation by water radiolysis. This production will may change redox behaviour of the oxide. It is clear the presences of the oxides changes the H_2O_2 decomposition mechanism but the nature of this change still requires further investigation to probe if it is a surface or bulk process or a combination the two.

Oxide Absorption Behaviour

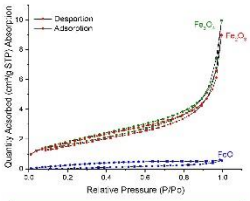

Oxide	BET surface area
Fe_2O_3	6.5235 ± 0.0277 m^2/g
Fe_3O_4	6.7927 ± 0.0182 m^2/g
FeO	1.4280 ± 0.0158 m^2/g

The BET analysis shows a type-II isotherm which is indicative of a nonporous or macroporous material. The lack of hysteresis loops in this data means that no conclusion about pore type can be drawn. The surface areas for Fe_2O_3 and Fe_3O_4 are very similar indicating the observed effects on H_2O_2 decomposition are due to different redox behaviour. FeO has a much lower surface area, but has similar reactivity towards H_2O_2 suggesting that surface area is not the driving factor.

Conclusions and Further Investigations

The current data set shows that CRUD simulant type has an effect on the $[H_2O_2]$ and potentially the mechanism for degradation. The data also suggests that γ-radiation has an effect on the hydrogen peroxide decomposition rate and mechanism, with γ-radiation having the biggest effect of the systems containing Fe_2O_3. This may be indicative of a change in the oxide itself and may be probed further using XPS and XRD analysis. Further Investigations should include:

- Agitated samples to probe is the mechanism for degradation is a bulk or surface effect
- Investigation of non irradiated systems further to gain further mechanistic understanding
- Kinetic modelling to gain mechanistic understanding

Rolls-Royce

EPSRC
Engineering and Physical Sciences Research Council

Contact Details:

Elizabeth Parker-Quaife MChem
School of Chemistry / Dalton Cumbrian Facility
The University of Manchester
Sackville Street
Manchester M13 9PL

Email: elizabeth.parker-quaife@postgrad.manchester.ac.uk